UNIVERSITY OF CALIFORNIA
RIVERSIDE

Development and Optimization of Chemically-Active Electrospun Nanofibers for Treatment of Impaired Water Sources

A Dissertation submitted in partial satisfaction
of the requirements for the degree of

Doctor of Philosophy

in

Chemical and Environmental Engineering

by

Michael Jean-Claude Nalbandian

December 2014

Dissertation Committee:

Dr. Nosang V. Myung, Chairperson
Dr. David Jassby
Dr. Mark R. Matsumoto

The Dissertation of Michael Jean-Claude Nalbandian is approved by:

_____

_____

_____

Committee Chairperson

University of California, Riverside

Acknowledgments

It is a pleasure to thank those who have made this project possible. First and foremost, I would like to thank God, my Heavenly Father, to whom I owe my very existence. I thank Him for His Son, Jesus, who was and is my source of joy, hope, strength, perseverance, peace and, above all else, salvation. I thank Him for science, a gift to man to be able to grasp just a glimpse of understanding all of His creations. "For in Him all things were created: things in heaven and on earth, visible and invisible…all things have been created through Him and for Him." (1 Corinthians 1:16) I thank Him for being able to work in such a dynamic field as engineering, and for putting me on a path of wisdom, discipline and success. Graduate school was easily the most difficult chapter in life so far. With days of breakthrough, there were always days of roadblocks. It was by His strength that I was able to persevere, despite my natural tendency to sulk in the roadblocks. "My grace is sufficient for you, for My power is made perfect in weakness." (2 Corinthians 12:9) His work in this season has produced and forged perseverance, persistence, patience, faith, wisdom, and leadership in my life. Altogether, these words are one more piece of evidence that, day after day and year after year, He was and is faithful. Thank you for everything.

I would like to thank my advisor, Dr. Nosang Myung. He has helped me become more hardworking, learn concepts outside of my field, and think like an independent researcher. He pushed me to go past my limits and boundaries to become the researcher he knew I could be. Thank you for your stern guidance.

I would like to thank my former advisor, Dr. David Cwiertny. As a professor and undergraduate research advisor, he taught me almost everything that I know about water treatment. My experiences with him helped me gain a great interest in this field and led me to pursue graduate school. Thank you for your continual mentorship and encouragement.

I would like to thank the other members of my committee, Dr. Mark Matsumoto and Dr. David Jassby, for their help with the project proposal. I would also like to thank Dr. Sharon Walker, Dr. Phil Christopher, Dr. Juchen Guo and Dr. Michael Anderson for their help and advice on this project.

I would like to thank my past and present colleagues in the Myung group. They provided great camaraderie and laboratory insight. My special thanks to Miluo Zhang, who basically taught me everything I needed to know about electrospinning, and Joel Sanchez, who made a large contribution to this work. I would also like to thank my past and present colleagues from the Cwiertny group. They have helped me when I had just begun as an undergraduate researcher and provided me with a knowledge base of laboratory work to pursue graduate school. My special thanks to Rebekah Oulton, who took me under her wing when I began doing research as an undergrad at UCR. Thank you to all who were involved in this work.

I would like to thank Ryan Honda for all his companionship as a fellow student. He has been a great friend of mine since the early years of our undergraduate careers at UCR. He was a great companion to be with throughout our entire environmental engineering curriculum. I wouldn't have picked a better partner to work with during our

senior design project. And after the departure of many friends from our graduating class, we managed to stay together to continue our academic careers in graduate school. We have spent a lot of time as friends and colleagues at UCR and I am grateful for every minute of it. Metagross, FTW!

I would like to thank my family. My parents have never stopped encouraging me to reach the top, especially in the academic realm. They wanted my sister and me to reach for things that they were not able to in their life. My sister took the first plunge into college and her hard work motivated me to be as great as she was. Leaving home to go to college wasn't so bad when I had my older sister there, who knew all the ropes of UC Riverside. Thank you for your love and support.

Last, but certainly not least, I would like to thank my best friend and my wife, Jenifer Natée Nalbandian. For the last 7 years, she has provided me with unyielding support, devotion, compassion, love, patience and pasta to get me through college and graduate school. As a fellow scientist who has gone through the Ph.D. program, she herself understands it all. She has been there through all the exams, projects, presentations, group meetings, and all the general ups and downs of graduate school life. I have no shadow of doubt that school would have been significantly more difficult if she wasn't in my life. I thank God everyday for placing that woman in front of my eyes that October evening in 2007. Jenifer, I am so enormously humbled and grateful to know you, let alone to have you in my life. You have made the past few years of my life at UCR the best years of my life, yet. Thank you for being you.

Dedication

This dissertation is dedicated to Jesus Christ, for everything.

"Give thanks to the LORD, for He is good;

His love endures forever."

(1 Chronicles 16:34)

This dissertation is also dedicated to my wife, Dr. Jenifer Nalbandian, for her love, support and faith in me.

ABSTRACT OF THE DISSERTATION

Development and Optimization of Chemically-Active Electrospun Nanofibers for Treatment of Impaired Water Sources

by

Michael Jean-Claude Nalbandian

Doctor of Philosophy, Graduate Program in Chemical and Environmental Engineering
University of California, Riverside, December 2014
Dr. Nosang Myung, Chairperson

To achieve sustainable water resources, new treatment technologies are needed that can be applied to a broad range of undesirable constituents in water over a broad range of water chemistries. In this project, nanomaterials were developed as building blocks for advanced treatment technologies through the controlled material synthesis technique of electrospinning. Electrospun nanofibers are promising materials for nano-integrated systems due to their simple tuning and production, large surface-area-to-volume ratio, and potential substrate integration to prevent incidental release into the environment.

In this work, electrospun metal oxide nanofibers were synthesized and optimized for their application in various aspects of water treatment, which include Ag-enriched TiO_2 nanofibers for UV-driven photocatalytic oxidation of organic microcontaminants, Al_2O_3-Fe_2O_3 composite nanofibers for adsorption of heavy metals, and $BiVO_4$ nanofibers for visible light-activated photocatalytic oxidation.

TiO_2 nanofibers were developed and tuned to alter morphological, dimensional and optical properties towards optimal photocatalytic performance of contaminant degradation. Electrospinning synthesis yielded nanofibers with controlled diameter, crystal phase, grain size, and band gap. Photoreactivity studies towards the model pollutant phenol showed that diameter and crystal phase composition were the two major factors in optimizing TiO_2 nanofibers performance. Additionally, the introduction of Ag led to further enhancement of photoreactivity, where optimization of the composite nanofibers was tied predominantly to Ag content.

Fe_2O_3 nanofibers were developed and tuned to alter morphological and dimensional properties towards optimal adsorption of heavy metals. Electrospinning synthesis yielded nanofibers with controlled diameter, crystal phase, grain size, and specific surface area. Chromate adsorption isotherm studies reveal increased sorption capacity with decreased diameter of the Fe_2O_3 nanofibers, attributed with the increased surface area. With the addition of Al, Al_2O_3-Fe_2O_3 composite nanofibers were produced with even greater sorption capacity due to further enhanced surface area.

$BiVO_4$ nanofibers were developed and tuned to control morphological, dimensional and optical properties towards optimal visible-light activated photocatalytic performance. Electrospinning synthesis yielded nanofibers with controlled diameter, crystal phase, grain size, and band gap. Photoreactivity studies towards phenol showed that reactivity increased with decreased nanofiber diameter. The addition of Ag and Au co-catalysts enhanced photoreactivity of the $BiVO_4$ nanofibers, outperforming TiO_2 nanomaterials under visible light irradiation.

Table of Contents

List of Figures

List of Tables

Chapter 1: Introduction

1.1 Emergence of Aquatic Contaminants

The primary motivation for this project is to alleviate the increasingly limited fresh water supply that is occurring not only in the United States but worldwide. The U.S. Department of the Interior has predicted that by the year 2025 large areas in the western half of the United States (especially around large cities such as Los Angeles, Phoenix and Denver) will potentially experience fresh water crises resulting from immense commercial, industrial, agricultural and ecological demands on existing water supplies.[1] To make matters worse, other sources report that an increased number of water sources are at risk due to industrial emissions into the atmosphere causing projected climate changes (Figure 1-1).[1] As populations increase worldwide, there is a sense of urgency for finding new water sources to meet the growing demand.

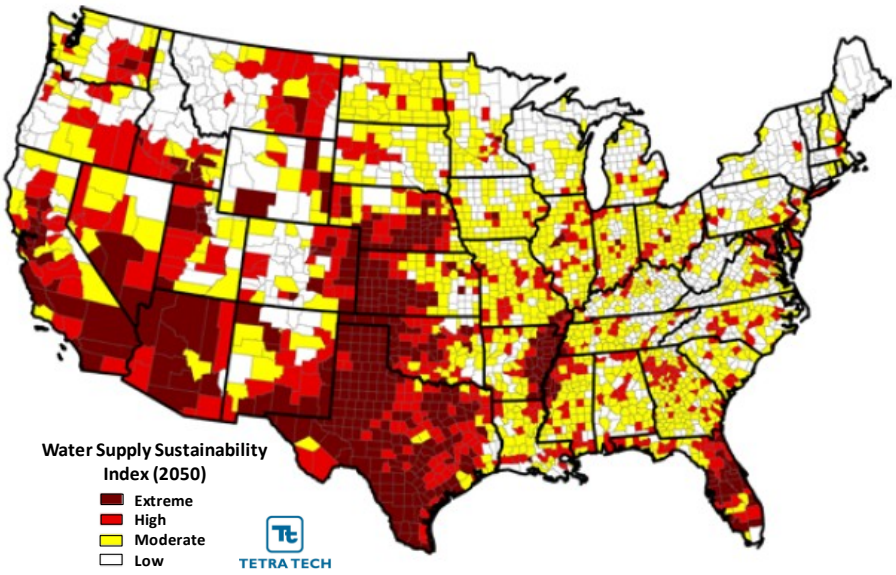

Figure 1-1: Risk to water supply sustainability by 2050 in the United States, color indexed by county.[1]

The shortage in fresh water supplies requires increased reliance on impaired water sources, in turn demanding new technologies to make these low quality supplies safe for reuse. Impaired water sources include polluted water sources and industrial and commercial wastewater. Recent research has shown that wastewater reuse has the greatest potential as an alternative source of water.[2],[3] Based on water usage in Southern California, the energy intensity required for the usage of reused water is significantly less than that for groundwater, surface water and ocean water.[4],[5] California and Florida are among the states that have in recent years implemented the reuse of millions of acre-feet of treated wastewater, with great potential for projected growth in the future.[6],[7] However, there are great concerns over wastewater reuse due to effluent organic matter and heavy metal contaminants.

Effluent organic matter includes biomolecules, soil organic matter, and anthropogenic organic matter, but most prominent are emerging contaminants called pharmaceuticals and personal care products (PPCPs). PPCPs are products, such as prescription and over-the-counter drugs, fragrances, cosmetics, and sun-screen products, used for personal health and cosmetic purposes.[8] Additionally, chemicals used in agribusiness for the enhancement of livestock commodities are also considered PPCPs.[9] PPCPs enter into wastewater via different pathways, mainly through domestic waste, washing, bathing and showering.[10] Altogether, the sources of these micropollutants are anthropogenic, whether through direct or indirect routes into the environment. Consequently, PPCPs have been found in surface waters and drinking water throughout the United States.[11] Such contaminants can enter these clean water sources via a variety

of routes, including leakage from septic tanks, waste storage tanks and landfills, output from sewers and wastewater treatment plants, and spray irrigation of raw and treated wastewater; however, the primary entry route into these systems is via effluent from wastewater treatment.[10] Heavy metals, such as arsenic (As), lead (Pb) and chromium (Cr), are classified as metals of environmental concern, having known adverse effects towards and human health.[12],[13] Although heavy metal use date back to Ancient Roman times, significant use sparked by the manufacturing boom of the Industrial Revolution has led to their entrance into the ambient environment.[14] Even today, due to poor maintenance, storage, and disposal practices of industrial process wastes, heavy metals continue to enter and persist, being found in groundwater sources used for public supply, usually as anionic ligands.[15],[16] Thus, an advanced treatment technology that targets various contaminants is necessary to promote wastewater reuse at best.

In order to meet the standard for implementation in treatment facilities, such a process must be efficient in terms of high contaminant removal, sustainable in terms of low energy demand, and have limited specificity to target a broad range of pollutants, ultimately yielding low-cost and high quality effluent. Unfortunately, present technologies are having difficulties dealing with the removal of emerging microcontaminants. For example, available data from a recent review suggests that a large fraction of PPCPs persist or are partially degraded after undergoing conventional treatment processes (Figure 1-2).[17] Alternatively, the review shows that advanced treatment methods, specifically chemical oxidation and membrane filtration, significantly improved PPCP removal. Despite the potential of these advanced treatment strategies for

the potable reuse of surface water and indirect potable reuse of wastewater, there are still some underlying challenges to overcome.

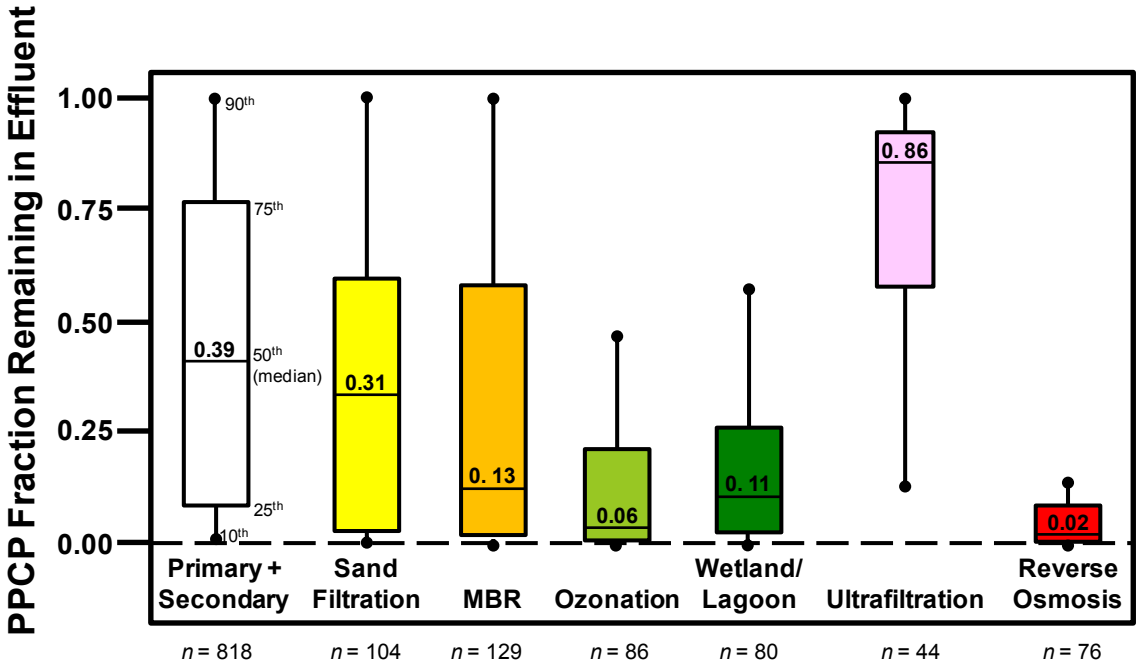

Figure 1-2: Box plot comparing PPCP removal efficiencies of the different wastewater treatment technologies.[17]

1.2 Water Treatment Challenges

There are several concerns regarding new treatment technologies to deal with emerging water contaminants. A recent review[18] noted that a major future challenge in water management is the development of new technologies that can control a broad array of chemically diverse pollutants and be applicable over a range of different water chemistries. Additionally, recent high profile reports[19]–[21] in the popular media emphasize the perceived failings in the ability of current technologies to provide safe water to the American public. Advanced treatment for water sources not only has to

deliver high quality effluent, but be aesthetically pleasing to the public, who despite the growing need for new water supply, have expressed displeasure over the idea of the water's origin.[22]

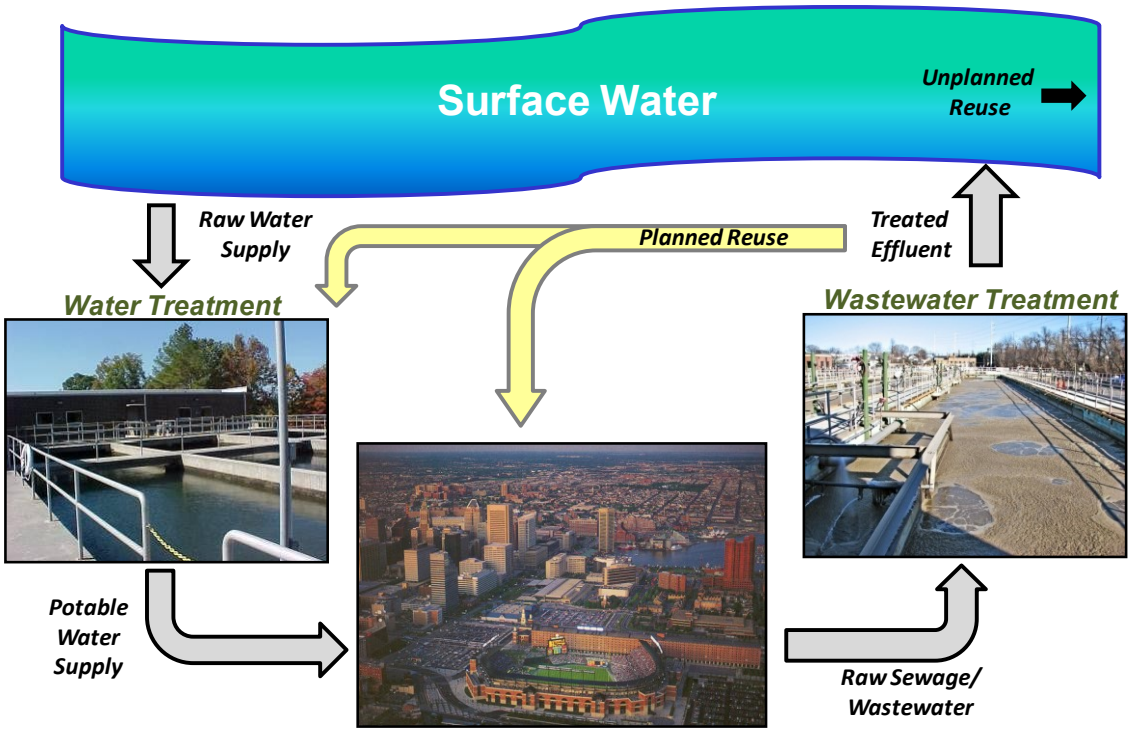

Figure 1-3: Schematic of the lifecycle of potable water.

However, the development of new technologies, while challenging at all scales, is particularly overwhelming for small public water systems.[23] Technologies must be of appropriate scale to serve small communities, simple to operate to minimize training requirements, robust to limit maintenance, and affordable to those with limited capital and revenue.[24] Above all, technologies must abide by the tenants of sustainable water resource management, which involves meeting needs reliably and equitably for current

and future generations by designing integrated and adaptable systems that optimize water use efficiency and preserve the natural ecosystem.[25] One of the most promising approaches to advanced treatment that has both impressive pollutant removal and scalable applicatory potential is nanotechnology-integrated treatment systems.

1.3 Nanotechnology

Nanotechnology is technology developed at the range of 1 to 100 nanometers, creating structures that bring innovative and practical properties due to their molecular-level dimensions.[26] As seen in Figure 1-4, nanostructures can vary in shape, from 0D nanoparticles and 1D nanotubes to 3D nanocomposites. The promise of nanotechnology-integrated water treatment is the ability to optimize process efficiency via unique material properties exhibited within the nanodomain while simultaneously reducing the footprint of engineered systems. Nevertheless, environmental engineers have been hesitant to embrace nanoengineered materials, primarily due to concerns over possible adverse effects upon their incidental release into the environment.[27] If such nanotechnologies are engineered safely and optimally, multi-functional nanostructures represent an innovative approach for the simultaneous treatment of undesirable constituents in water via operations and principles long exploited by water quality engineers. Nanotechnologies also hold the promise of being deployed across a range of treatment platforms, either as stand-alone technologies, integrated into conventional operations, or as point-of-use devices to polish tap water.[28] Nanoengineered treatment methods to deal with organic and heavy metal contaminants are photocatalysis and adsorption, respectively.

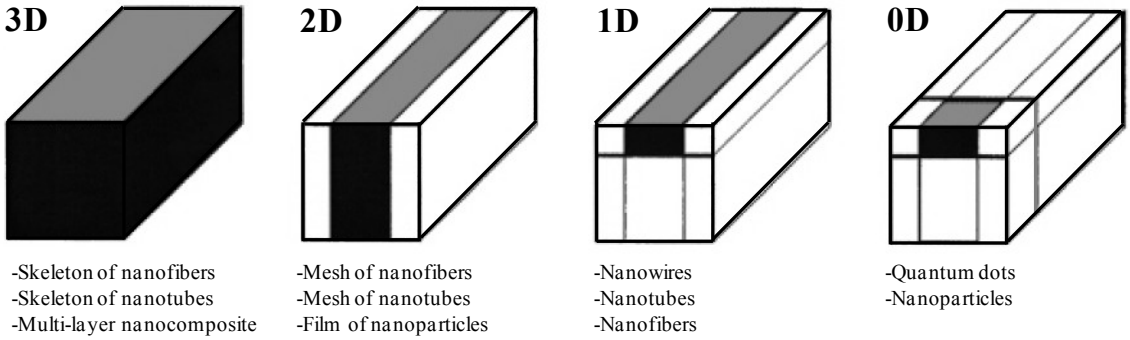

Figure 1-4: Different dimensional categories and their examples.[29],[30]

1.4 Photocatalysis

Photocatalysis in the environmental engineering field is considered an advanced oxidation process (AOP). AOPs are chemical processes that generate hydroxyl radical (•OH), known by many as the most powerful oxidant in water.[31] For example, the degradation rate of 17α-ethynylestradiol, a synthetic estrogen, is greatest with •OH over other common oxidants over a large pH range (Figure 1-5).[31] Other work has shown that •OH provides reaction rates in the order of 5 to 10 greater than that of ozone, one of the more popular oxidants used in water treatment, towards many different organic compounds.[32] AOPs have shown to be very effective in the degradation of organic pollutants in contaminated waters and soils, as well as gaseous effluents. AOPs are promising treatment technologies because •OH is non-selective, degrading most organic constituents in water ranging from bulk organic matter to micropollutants, such as pharmaceuticals,[17] pesticides,[33] and disinfection by-products (*e.g.*, NDMA).[34] Additionally, AOPs are capable of organic mineralization, where pollutants and their

intermediates are degraded into their simplest components, such as water (H_2O), carbon dioxide (CO_2) and inorganic ions (*i.e.*, NO_3^-, N_2).[32]

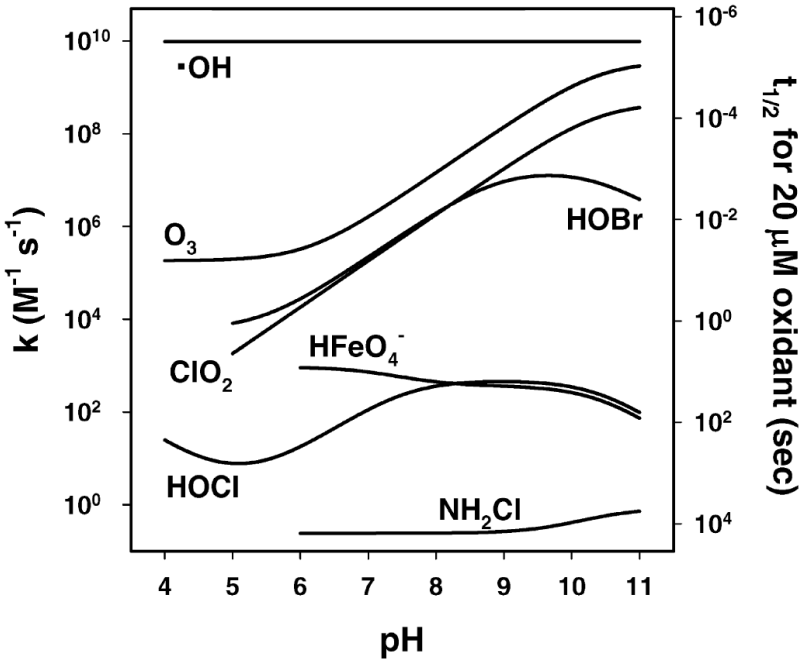

Figure 1-5: Kinetics of 17α-ethynylestradiol degradation by various oxidants versus pH.[31]

In the mechanism of $^{\bullet}OH$ oxidation, $^{\bullet}OH$ reacts with a large array of organic materials mainly by hydrogen abstraction:[32]

$$^{\bullet}OH + RH \longrightarrow R^{\bullet} + H_2O \qquad (1.1)$$

Organic compounds are designated by R, shown with an arbitrary H atom. The hydrogen abstraction by the $^{\bullet}OH$ produces organic radicals ($R^{\bullet}$) and H_2O molecules. In the presence of oxygen (O_2), the organic radicals $R^{\bullet}$ react quickly with O_2 to form organic peroxyl radicals ($RO_2^{\bullet}$):

$$R^{\bullet} + O_2 \longrightarrow RO_2^{\bullet} \quad (1.2)$$

With the initial attack by the $^{\bullet}OH$ in the presence of O_2, a complex chain of oxidative reactions lead to the mineralization of the organic compound,[32] where the radical oxidants continue to remove H atoms from the pollutant until it has been decimated into simpler components (e.g., H_2O, CO_2, inorganic ions). An example of organic mineralization can be seen in Figure 1-6, showing the oxidation of phenol.[35],[36]

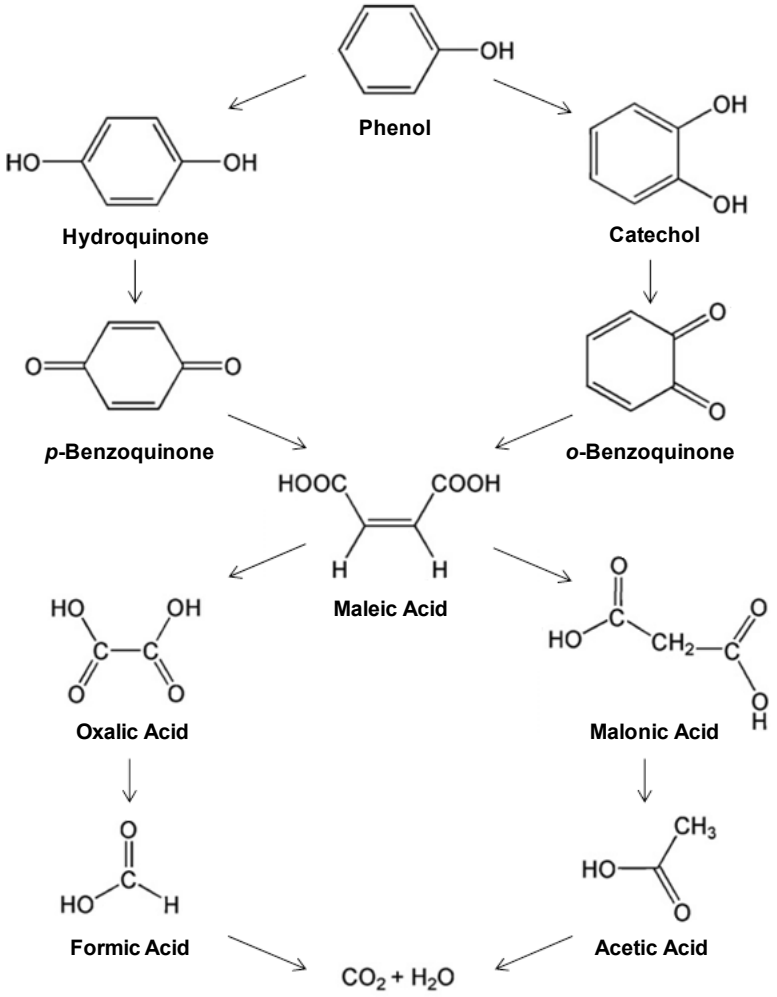

Figure 1-6: Scheme of the oxidation of phenol.

Conventional AOPs usually consist of a combination of ozone (O_3), hydrogen peroxide (H_2O_2), and ultra-violet light (UV).[25] Despite the amazing performance of these AOPs via $^{\bullet}OH$, however, concerns over the wide-spread application of AOPs are high energy demand, high chemical reagent costs, carbon footprint of reagents, undesired by-products primarily from O_3 oxidation, and variable treatment efficiency due to effluent $^{\bullet}OH$ scavengers. Photocatalytic AOPs,[32] such as titanium dioxide photo-oxidation (TiO_2/UV) and the photo-Fenton reaction (Fe^{2+}/H_2O_2/UV), offer a novel approach to traditional AOPs with use of nanostructured catalysts to not only combat high chemical reagent costs, but exploit photo-induced reactions for high $^{\bullet}OH$ generation as well as.

In particular, nanostructured photocatalysts are advantageous due to the shortcomings of traditional AOPs.[37],[38] Some advantages include its lower UV energy requirement than other AOPs, inhibition of by-product and intermediate formation, and additional oxidation pathways. It's most prominent advantage is its property manipulation for organic treatment efficiency. Use of conventional AOPs are hindered by their reagent and operation costs when higher dosages are necessary to deal with variable pollutant loads, thus high costs factor into very limited process advancements. Alternatively, photocatalysts can be tailored via physical modifications to change its optical and/or electrical properties and consequently enhance its photocatalytic activity.[39] In a way, tailoring photocatalysts can maximize pollutant removal while minimizing material and energy costs.[32] For example, one of the most noteworthy properties of TiO_2 that can be tailored is crystal structure; TiO_2 can be modified via calcination to crystallize into either the more thermodynamically stable rutile structure or

the more photoactive anatase structure, where a mixture of both structures have shown to optimize photocatalytic activity.[40],[41]

1.4.1 Photoactivation Mechanism

The mechanisms for the formation of •OH via photocatalysis are surface site limited, so understanding the nanoparticles in the colloidal dimensions is important to enhance surface site availability. Using TiO_2 as the example, photoactivation begins when the photocatalyst is exposed to a photon.[41] As a semiconductor, TiO_2 has low energy electrons in its valence band, and an empty high energy conduction band.[42] The incident photon will cause an electron in the valence band to be excited and move to a higher energy state in the conduction band, leaving a hole in the valence band.

$$TiO_2 + h\nu \longrightarrow e^-_{CB} + h^+_{VB} \tag{1.3}$$

The band gap energy for TiO_2 is 3.0 eV for the rutile structure and 3.2 eV for the anatase structure,[41] and mixed phase TiO_2 has shown to provide intermediate band gap values.[43] Based on the Plank-Einstein equation, the wavelength of light required to overcome the band gap is about ~410 and ~390 nm, respectively. Therefore, light with energy greater than that in the visible spectrum (*i.e.*, UVA light) is necessary to activate TiO_2. In retrospect, UV light used in combination with O_3 and/or H_2O_2 must be of greater energy, at the wavelength of 254 nm.

With the electron now in the conduction band, an electron hole is left in the valence band with a very high affinity to electrons in order to fill the hole and return to equilibrium. Recombination of the electron back to the valence band is feasible in the absence of electron scavengers.[41]

$$e_{CB}^{-} + h_{VB}^{+} \longrightarrow TiO_2 + \text{heat} \quad (1.4)$$

However, electron scavengers, such as oxygen (O_2), in the system will react with the conduction band electron to prolong recombination and continue successful photocatalysis.[41] Additionally, the presence of O_2 will cause the formation of superoxide radicals ($O_2^{\bullet -}$). The $O_2^{\bullet -}$ can further protonate to form hydroperoxyl radical ($HO_2^{\bullet}$), which itself can act as another electron scavenger to help inhibit recombination or transform into another reactive oxidation species, hydrogen peroxide (H_2O_2), through a secondary protonation.

$$O_2 + e_{CB}^{-} \longrightarrow O_2^{\bullet -} \quad (1.5)$$

$$O_2^{\bullet -} + H_2O \longrightarrow HO_2^{\bullet} + OH^{-} \quad (1.6)$$

$$HO_2^{\bullet} + e_{CB}^{-} \longrightarrow HO_2^{-} \quad (1.7)$$

$$HO_2^{-} + H^{+} \longrightarrow H_2O_2 \quad (1.8)$$

The electron hole, having a high redox potential (E^0 = 3.02 V), can react with organic micropollutants via direct oxidation.

$$h_{VB}^{+} + R \longrightarrow R^{+\bullet} \quad (1.9)$$

For the most part in photocatalysis, micropollutants undergo indirect oxidation, where they are attacked from $^{\bullet}OH$. One such way is by the electron hole reacting with surface or free hydroxides (OH^{-}):

$$h_{VB}^{+} + OH^{-} \longrightarrow {}^{\bullet}OH \quad (1.10)$$

$$^{\bullet}OH + RH \longrightarrow R^{\bullet} + H_2O \quad (1.11)$$

The micropollutant will then be degraded and mineralized by the newly formed $^{\bullet}OH$ as previously stated. Another way is by the electron hole reacting with water molecules to form $^{\bullet}OH$.

$$h_{VB}^{+} + H_2O \longrightarrow {}^{\bullet}OH + H^{+} \quad (1.12)$$

Altogether, these reactions are highly dependent on three main factors: the separation of photogenerated electron and hole carriers, the transport of these carriers to surface active sites and the surface chemical reactions between the carriers and the reagents.[44] These factors place great importance on comprehending photocatalysis process in the solid-liquid interface.

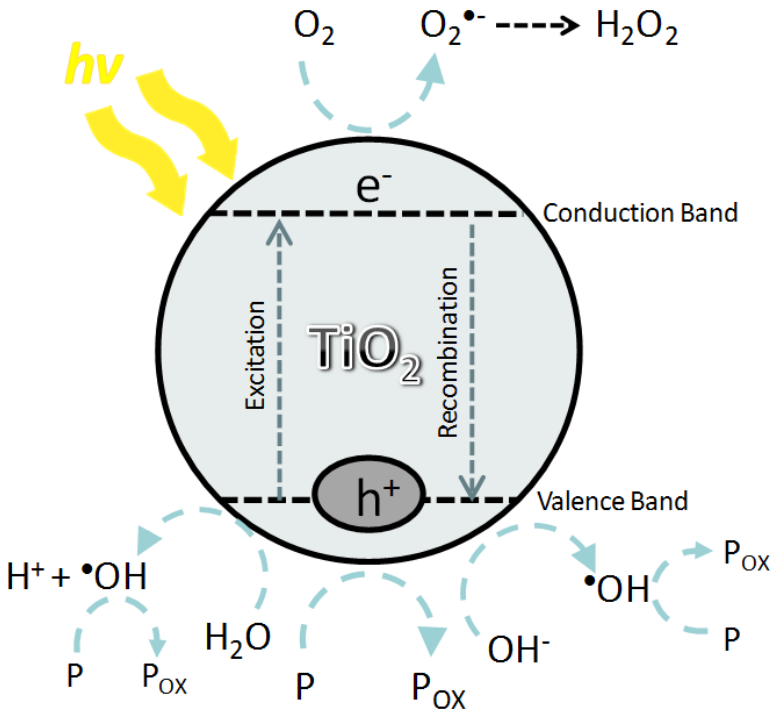

Figure 1-7: Diagram of TiO_2 photocatalysis.

1.5 Adsorption

Adsorption is a common treatment option for heavy metal removal in part by its low cost and simple implementation. Adsorption is a separation process in which organic or inorganic compounds are adsorbed from a solution onto a porous solid media with high surface area.[45] Adsorption can be categorized as physisorption, physical adsorption on the surface due to weak van der Waals forces, and chemisorption, adsorption caused by changes in electronic structures of atoms or molecules resulting from surface chemical reactions.[46] Specifically, removal of heavy metal contaminants via adsorption occurs through surface complexations, where heavy metal ligands are exchanged with surface function groups (e.g., OH^-), which will discussed in more detail below. Iron oxide

(Fe_2O_3), as well as alumina (Al_2O_3), is a one of the most commonly used adsorbent materials for heavy metal removal. Fe_2O_3 represents a model adsorbent because it is non-toxic, very abundant and inexpensive, and easily synthesizable. Additionally, the naturally high surface area and porosity of Fe_2O_3 yields great adsorption performance.

1.5.1 Adsorption Mechanisms

Fe_2O_3 nanomaterials have been used widely as a classic sorbent in adsorption studies.[47] Understanding the Fe_2O_3 adsorption mechanisms begins with understanding Fe_2O_3 suspensions in water. Surface Fe atoms in aquatic systems will draw in water molecules, where adsorbed water will undergo hydrolysis to create hydroxide complexes.[48] These hydroxide complexes comprise the surface functionality of Fe_2O_3. The basic reaction equation is as follows:

$$Fe^{3+} + H_2O \longrightarrow FeOH^{2+} + H^+ \tag{1.13}$$

A single surface iron hydroxide complex will be generalized as ≡FeOH from here on. As a trivalent atom, surface Fe atoms have the potential to be functionalized in different coordinations, with a single or multiple Fe atoms bonded to single or multiple hydroxyl groups. Additionally, the hydrolysis of water triggered by the surface Fe atoms will naturally lower the solution pH caused by the increasing concentration of protons (H^+). Therefore, the state of the iron hydroxide complexes and overall surface charge are

dependent on the pH of the aquatic environment. The equilibrium reactions of surface Fe complexes are attributed as the following:

$$\equiv \mathrm{FeOH_2^+} \;\rightleftarrows\; \equiv \mathrm{FeOH} + \mathrm{H^+} \quad (\mathrm{pK_{a1}} = 7.09) \tag{1.14}$$

$$\equiv \mathrm{FeOH} \;\rightleftarrows\; \equiv \mathrm{FeO^-} + \mathrm{H^+} \quad (\mathrm{pK_{a2}} = 11.11) \tag{1.15}$$

where $\equiv Fe^+$ is attributed as a single surface Fe valence bond of the potential three valences of a trivalent Fe atom (Fe^{3+}). Acidic conditions will contain higher concentrations of positively charged $\equiv FeOH_2^+$ complexes, moderate conditions will contain higher concentrations of neutral ≡FeOH complexes, and alkaline conditions will contain higher concentrations of negatively charged $\equiv FeO^-$ complexes. These surface hydroxyl groups posses a double pair electrons together with a dissociable hydrogen atom, enabling them to behave amphoterically.[47] Natural aquatic systems have a pH value of around 6-7 and, as stated earlier, trivalent Fe naturally acidifies aquatic environment, so $\equiv FeOH_2^+$ is typically the predominant iron hydroxide complex. But for the sake of simplicity, the subsequent adsorption reaction equations will utilize ≡FeOH to denote a surface iron hydroxide complex.

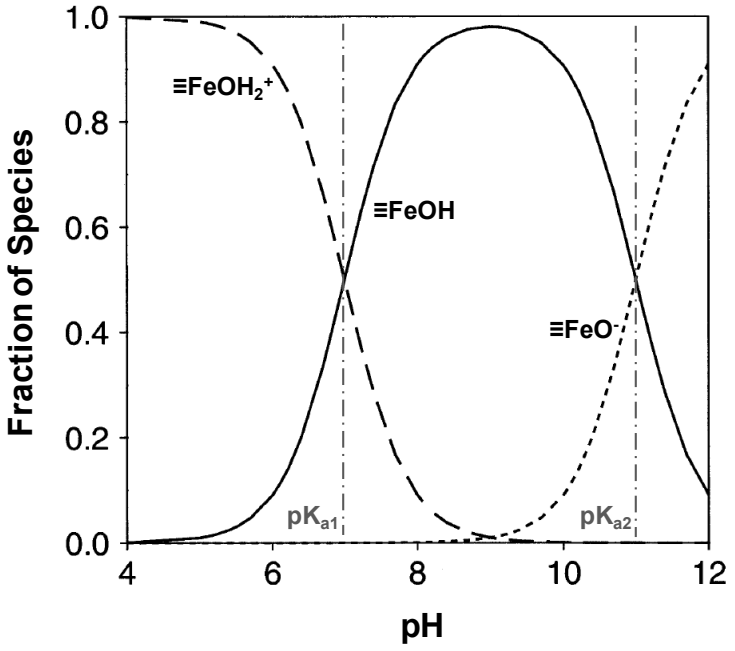

Figure 1-8: pC-pH diagram of surface hydroxyl groups on iron oxide surface.[47]

The adsorption of anionic ligands, negatively charged molecules such as CrO_4^{2-}, via Fe_2O_3 has been well investigated.[47] Concisely, the adsorption mechanism involves the replacement of the surface hydroxyl group with the adsorbing anionic ligand, denoted as L^-.

$$\equiv FeOH + L^- \rightleftarrows \equiv FeL + OH^- \quad (1.16)$$

$$\equiv (FeOH)_2 + L^- \rightleftarrows \equiv Fe_2L + 2\,OH^- \quad (1.17)$$

Due to the trivalency of Fe, the adsorption of anion ligands can form different species of coordination complexes, such as mononuclear monodentate, mononuclear bidentate and binuclear bidentate, based on the configuration of the surface Fe atoms and

O atoms of the anion.[47] Adsorption performance is at its maximum at low pH values and decreases with increasing pH, since the accumulation of $\equiv FeOH_2^+$ complexes at lower pH values promote attraction and subsequent adsorption of the anions on the surface.[47] According to authors, anion adsorption is considered to some extent irreversible, as the induction of desorption of the anions from the surface by means of changing the anion concentration or increasing the pH is very slow.[47]

1.6 Challenges of Nanotechnology

Despite the potential of these materials, nevertheless, obstacles surrounding nanostructures have still hindered the commercialization of nanoengineered treatment systems. Firstly, it is well recognized that many challenges hinder the application of TiO_2 nanoparticle photocatalysts in water treatment. Fundamentally, their inherent reactivity is relatively low compared to other AOPs (e.g., UV light in combination with O_3)[49] and they rely on high energy light (i.e., UVA with $\lambda < 390$ nm) that comprises only 5% of the solar spectrum. In complex water matrices fouling of TiO_2 surfaces and scavengers of photo-generated reactive oxygen species (e.g., $^{\bullet}OH$-scavenging carbonate and natural organic matter) can limit treatment efficiency.[50],[51] Consequently, while widely researched, TiO_2 has not yet been extensively commercialized or deployed for full-scale treatment. Furthermore, nanoparticle adsorbents like Fe_2O_3 are strictly surface-area driven, putting immense pressure on manipulating structure and porosity while bearing dimensional restrictions.

Perhaps of greater importance are the multitudes of practical hurdles associated with deployment of these nanoparticles. Amid rising concerns over the environmental release of engineered nanomaterials,[27],[52]–[54] a major design consideration is mitigating nanoparticle loss or leaching into the treated water supply.[55] Suspension instability is also a concern, with nanoparticles prone to aggregation that ultimately decreases reactive surface area.[56],[57] Moreover, proposed solutions to these issues (e.g., nanoparticle immobilization on a substrate) also adversely impact reactivity by sacrificing available surface sites.[41] Additionally, conventional synthesis methods (*e.g.*, sol-gel method, hydrothermal method, solvothermal method, and chemical vapor deposition)[37] used to prepare different nanostructures (e.g., nanoparticles, nanowires, nanorods, nanotubes, and nanoribbons)[29],[30],[40],[58] also offer challenges. These methods utilize expensive materials and equipment, require harsh and complicated conditions, and offer limited property manipulation and control. For this research, the nanostructures, specifically nanofibers, will be produced via the electrospinning process to avoid the drawbacks of conventional synthesis methods, as well as combating the aforementioned limitations of nanotechnology-based treatment systems.

1.7 Electrospinning

Electrospinning is an emerging electro-chemical process that produces solid nano-sized fibers from a liquid solution with the use of an electrical charge.[59]–[61] Considered a variant of electrospraying and originally called “electrostatic spinning”, electrospinning didn’t gain much interest in the research field until the early 1990s, where groups

demonstrated synthesis of fibers using a wide range of different organic polymers.[62] Shortly after, the number of publications on electrospinning increased exponential by the turn of the century. This cost-effective process is implemented with a simple apparatus at room-temperature, providing high yields of nanofiber mats that have shown to be very robust and stable.[61]

Although electrospinning can be conducted with a small and inexpensive apparatus, larger systems with a series of solution containers, spraying orifices and collectors can lead to heavy nanofiber production.[63] Based on dimensional geometries alone, nanofibers provide more surface area-to-volume ratio than commonly used nanoparticles, and the difference in this ratio gets larger when the nanofiber radius decreases. Recent work has shown that nanofibers, specifically TiO_2, perform greater than their nanoparticle counterparts due to their larger surface area (for greater surface site availability) and their greater photocurrent generation during photoexcitation (for greater electron transport).[64] Most notably, nanofiber mats are promising tools for filtration; they possess a larger surface area-to-volume ratio than conventional filters, are highly scalable, and tend to exhibit lower degrees of pressure drop.[61]

In the electrospinning process, as seen in Figure 1-9, a syringe is filled with a solution, containing a precursor of the nanofiber material and connecting polymer, and loaded onto a controlled syringe pump.[65] The syringe has an attached metallic needle that is connected to a high-voltage power supply. As the solution slowly moves through the metallic tip, the solution is electrified, forming a distorted conical shape, known as a Taylor cone, due to the solution overcoming its naturally high surface tension. From the

end of the Taylor cone, an electrified jet of fibers is released. As the solvent of the solution evaporates during travel time, the fibers solidify as it reaches a grounded collector. After a desired amount of electrospinning time, the collector contains a large mesh of nanofibers. For composite materials that include non-polymer reagents, the nanofibers can be subsequently annealed in a furnace to remove any polymer residue.

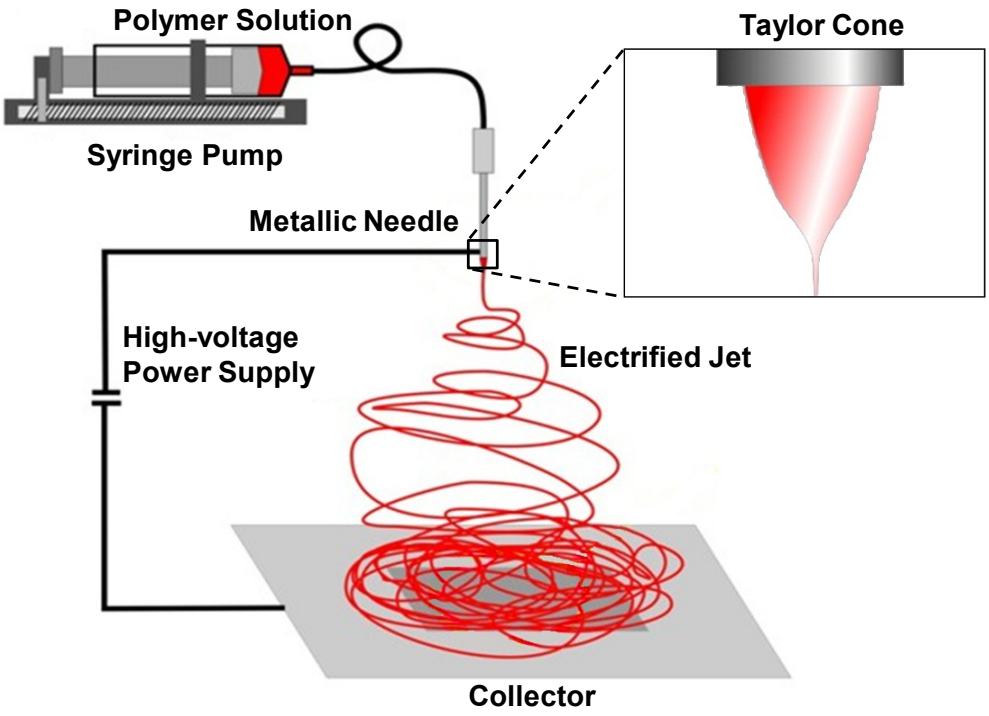

Figure 1-9: Schematic of electrospinning process.

With the use of electrospinning, the physical characteristics of synthesized nanofibers can be easily tuned by changing the parameters of the precursor solution, as well as parameters of the electrospinning process. The different parameters that can be altered for changing nanofiber characteristics are polymer concentration, precursor

concentration, applied voltage, travel distance, pump flow rate, annealing temperature, and annealing duration, as seen from recent research.[66] Additionally, nanofibers can also be easily doped during solution preparation with many different reagents to further enhance its material properties to increase overall performance.[67] Altogether, electrospinning provides easy preparation, synthesis and manipulation of nanofibers from large array of precursor and polymer materials.

Although the implementation of electrospinning is simple, the science behind it all is quite complex. In a general sense, the main mechanism that makes electrospinning feasible is merely caused by inducing an electric charge on the polymeric solution. The electric charge causes coulombic forces of repulsion between positive charges, which counteracts with the high surface tension of the solution. This results in the reduction of the surface tension, making the solution more subject to mechanical stretching. Through this stretching, the solution is distorted at the needle tip in the form of a Taylor cone, as previously stated. The narrowed segment at the end of the Taylor cone will undergo subsequent bending instabilities, causing the stream of the solution to stretch in a spiraling cone into the nano-dimension (Figure 1-10).[59] To the naked eye, the bending instabilities resemble a jet spray.[62] Despite the straightforward aspect of electrifying a solution to initiate electrospinning, there are many parameters that affect the entirety of this synthesis technique. The parameters can be separated into the categories of polymer solution parameters and processing parameters.[59]

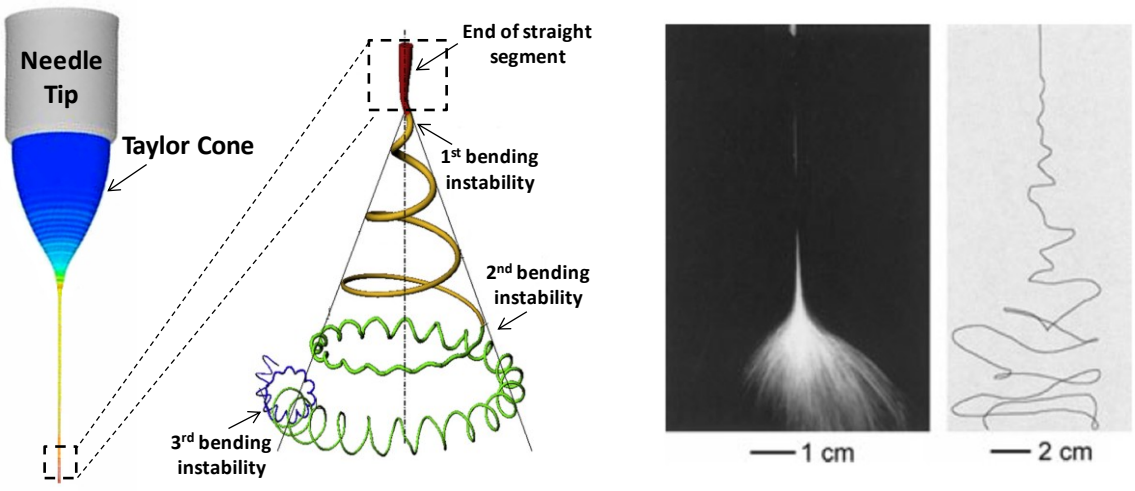

Figure 1-10: Schematic and SEM images of nanofiber bending instabilities.[62]

Polymer solution parameters, as the name suggests, are the parameters that are controlled during the preparation of the solution. The first, and most reasonable, parameter is the actually polymer. A polymer is a long chain of molecules with repeating units known as monomers. Polymers have low density so they can be easily molded, yet are strong enough to maintain their physical integrity and inert to prevent interreactions with other reagents. Not only do polymers vary in monomer chain and monomer functionality, but also in molecular weight, heat response, crystallinity and glass transition temperature, which can affect solution mobility and ductility[59]. Viscosity is the resistance of a fluid to physical deformation caused by stress. In a polymer solution, it is the degree of polymer molecule chain entanglement. The viscosity can be affected by the polymer concentration or polymer molecular weight. Solutions with higher polymer concentration or molecular weight have a higher probability of chain entanglement, and therefore higher viscosity. If the viscosity of the solution is too high, the solution cannot

be drawn out of the needle properly, possible causing clogging. If the viscosity is too low, the nanofibers can lose uniform smoothness and become beaded. The viscosity parameter can be related to the surface tension of the solution.

Surface tension is the tendency for the surface a fluid to resist external forces. In electrospinning, this constitutes the behavior between solvent and air molecules. As stated previously, the applied voltage induces a charge in the polymer solution, creating repulsive forces that reduce the surface tension. When there is a high concentration of free solvent molecules, there is a greater tendency for the solvent molecules to accumulate and form beaded structures, as seen in Figure 1-11.[59] For high viscosity solutions, there are more interactions between solvent and polymer molecules. Therefore, with the influence of coulombic forces stretching the solution, the solvent molecules will spread over the entangled polymer molecules evenly, preventing the formation of these beaded congregations.[59] Alternatively, low viscosity solutions will have a greater tendency to form beaded nanofibers. If the repulsive forces are not great enough to reduce the surface tension sufficiently, the jetted solution can break into droplets. If the surface tension is reduced too severely, the solution will drain freely, causing the formation of an unstable Taylor cone.

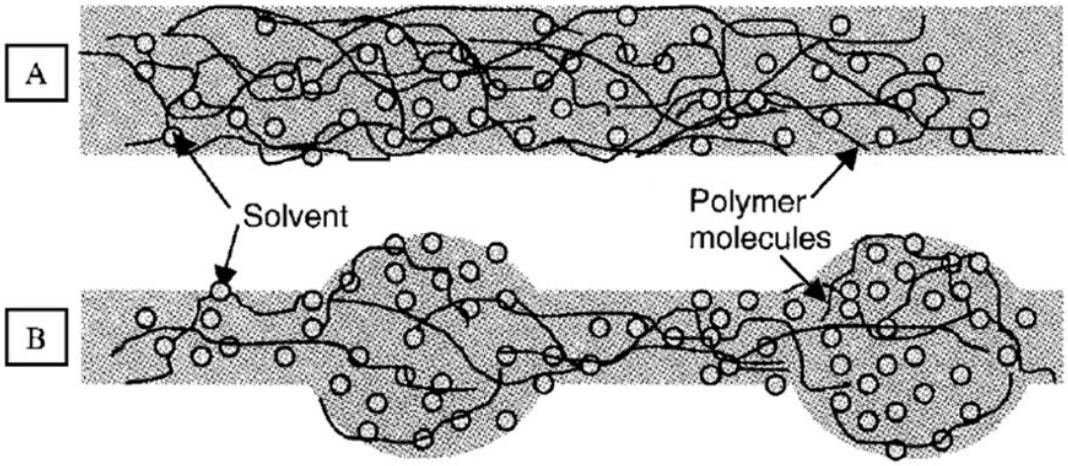

Figure 1-11: Formation of beaded nanofibers due to high surface tension (low polymer content) based on A) high viscosity and B) low viscosity.[59]

Electrical conductivity and dielectric property of the solvent are also important in the electrospinning, as they also work cooperatively. Electrical conductivity is the ability of a substance to conduct a flow of electric charge. Dielectric property is the capacity of a substance to carry electric charges. A solution with high electrical conductivity or a high dielectric constant will have the potential to accommodate a large concentration of electric charges. Therefore, this results in an increase in coulombic forces in the solution to overcome surface tension. High electrical conductivity or dielectric property leads to reduced bead formation, as well as increased bending instabilities, which results in reduced nanofiber diameter.[59] If the charge conductivity or capacity isn't great enough to overcome the solution's surface tension, there won't be enough force to stretch the solution for appropriate nanofiber uniformity. On the other hand, too high of charge

conductivity or capacity can cause a large accumulation of charge, leading to an unstable Taylor cone and preventing any synthesis of nanofibers.

Volatility of the solvent dictates the evaporation rate of the solution as the jet solidifies into nanofibers onto the collector. Many different factors affect volatility, such as boiling point, specific heat, heat of vaporization, and surface tension, but vapor pressure typically has the greatest effect.[59] The higher the vapor pressure of a solvent, the faster the evaporation rate. If the volatility is too high, the fibers can harden before reaching the nanoscale, leading to large diameters and possible needle clogging. If the volatility is too slow, the solvent won't evaporate by the time they reach the collector, leading to mesh of fused fibers.[59] In some cases, fused fiber synthesis can be sought after to create nanoweb scaffolds.

Lastly, polymer solubility is another important solution parameter, since a good solvent is considered one that is miscible with polymers and other reagents and also electrospinnable itself. High molecular weight and high crystalline polymers are more difficult to dissolve, as it takes longer for the solvent molecules to penetrate into the polymer bulk.[59] Heating the solution in a water bath can be helpful in encouraging polymer dissolution. Low polymer solubility will limit to amount of polymer content, leading to low viscosity solution. Polymer solubility can also be explained through Gibbs free energy, where a good solvent causes the polymer to expand, reducing the overall Gibbs free energy.[59] With solubility occurring when Gibbs free energy is negative and the terms of entropy of mixing and temperature together long thought to be positive,

Gibbs free energy is generally determined by enthalpy of mixing, which is a function of solute and solvent solubility parameters.[59]

Processing parameters are the parameters controlled during the actual electrospinning process. Applied voltage, possibly the most significant of parameters, is the induced charge used to create repulsive forces in the solution. Applied voltage dictates the electrostatic forces that combat the solution's surface tension as well as electric field that provides the acceleration for the jet spray.[59] Both the electrostatic force and electric field are responsible for turning the drop of solution at the needle tip to distort into the Taylor cone. There must be adequate power from the applied voltage to overcome the viscosity and surface tension of the solution and ultimate form and sustain the Taylor cone.[59] However, too high of an applied voltage will lead to an unstable Taylor cone, possibly leading to larger nanofibers.

Feedrate of the syringe pump determines the amount of polymer solution available for electrospinning. A certain applied voltage corresponds to a feedrate to maintain a stable Taylor cone. Increasing the feedrate results in large diameter fibers due to the greater volume of solution being drawn out.[59] However, too high of a feedrate doesn't give the solution sufficient time for evaporation, leading to fused nanofibers. If the feedrate is too low, broken nanofibers might result since there is less solution volume reaching the electric field with time. Travel distance, sometimes termed tip-to-collector distance (TCD), dictates the flight time of the nanofibers as well as the electric field strength.[59] The distance must be sufficient enough for the solvent to evaporate in time to form solid fibers. Longer distances increase evaporation time, leading to smaller diameter

nanofibers. Too large of a travel distance will weaken the electric field strength, leading to larger nanofibers. Shorter distances decrease evaporation time, leading to fused fibers, but too short of a travel distance could create sparks between electrodes, which is potentially dangerous.

Temperature of the electrospinning chamber is another parameter that can be controlled. Increased temperature increases evaporation rate and decreases viscosity, which is helpful for electrospinning solutions of high viscosity or of low vapor pressure.[59] Therefore, increased temperature can provide greater stretching of the solution, leading to smaller and more uniform nanofibers. However, increased temperatures are impractical for polymer solutions that contain biological substances. Temperature can also have an effect on the humidity of the electrospinning environment. Humidity is defined as the amount of water content in the air. High humidity leads to water condensing on the fiber surface, leading to porous structures.[59] A very humid environment might inhibit solvent evaporation, while a low humidity environment can cause premature hardening of the nanofibers before reaching the nanoscale.

Lastly, the needle tip and collector design are possible parameters than can be altered for desired synthesis. For needle tips, a smaller internal diameter reduces clogging because less solution is exposed to the atmosphere.[59] Additionally, smaller internal diameter also reduces the fiber diameter, as it decreases the jet acceleration allowing for more time for solution stretching. For collectors, many different shaped collectors, such as planar collectors, cylindrical drums, discs, and rotating wire drums, can be used for different applications, whether it is used for precision, yield or any other purpose.

Normally, a conductive collector that is grounded is used to provide a stable potential difference.[59] With a conductive collector, charges from the fibers are dissipated, allowing for more fiber collector and a more closely packed nanofiber film. For nonconductive collectors, the accumulation of charge on the collector causes slight repulsion forces, leading to 3D structures on the film.[59]

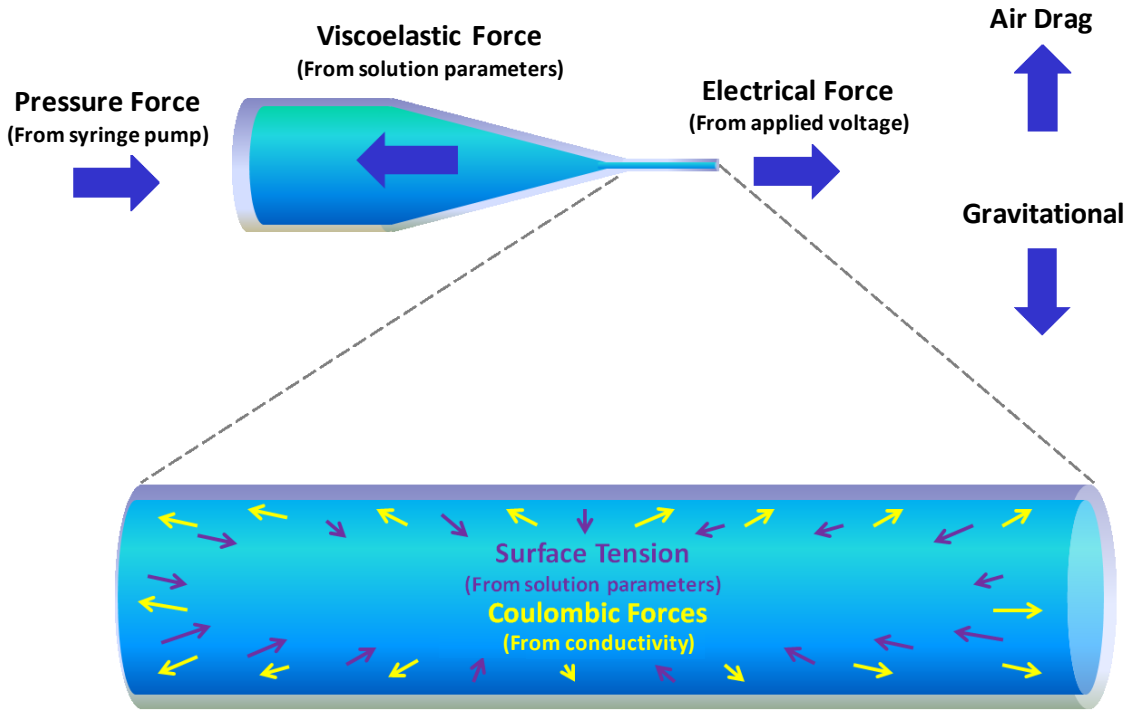

Figure 1-12: Diagram of forces associated with electrospinning.

Altogether, these parameters can be summed up into the forces that act on the solution during electrospinning, seen in Figure 1-12. The forces include pressure forces caused by the syringe pump to draw out the solution, viscoelastic forces from the solution's resistance to movement, surface tension forces from the cohesion of the

solvent molecules keeping the solution together, repulsive coulombic forces from the applied voltage stretching out the solution, electrical forces from the electric field providing the solution with acceleration towards the collector, and finally air drag and gravitation forces from the environment.[59] These forces can be used to model the behavior of jet flow trajectory, viscoeleastic properties, bending instabilities, as well as hypothesizing appropriate electrospinning parameters based on solution properties.

Electrospinning has already found numerous applications in catalysis, sensing, medicine and energy.[68] Examples of these applications include tissue engineering and drug delivery for bioengineering, protective cloths and composite reinforcement for defense and security, gas sensors and biosensors for sensing equipment, and batteries and capacitors for energy and electronics.[59] Researchers have recently turned to electrospinning as a viable route for the synthesis of inorganic nanofibers[64],[65] in a platform, a permeable two-dimensional nanofiber network, that may be more easily integrated into water treatment as reactive filtration materials.[61],[69]–[71] However, while many studies have demonstrated the synthesis and performance of such nanofibers, relatively little work has been geared toward optimizing structure, morphology and composition so as to improve their performance in simulated water treatment. Indeed, a major benefit of electrospinning is that the synthesis process is highly tunable, allowing nanofiber properties including diameter, grain size, phase composition and the presence and concentration of dopants or co-catalysts to be readily optimized for a targeted application.[66],[67] Altogether, current work on inorganic nanofibers do not offer extensive property modifications or establish clear links between material structure and reactivity,

information critical for optimizing their application for treatment of polluted water supplies. Further expansion of electropinning in the research field is essential for direct nanofiber applications in future water treatment systems.

1.8 Research Objectives

The primary goal of this study is to develop materials optimal for nanotechnology-enabled applications of micropollutant removal during water and wastewater treatment processes. Recent research in membrane technology has focused on composite membranes that incorporate nano-sized materials to not only increase membrane structure integrity, but also take advantage of key characteristics of the embedded materials for increased treatment efficiency.[72] Ultimately, these findings are the first step toward the development of nanofiber-enabled treatment technologies; this includes next-gen hybrid membranes, consisting of single or multi-component nanofiber mat-integrated ceramic membranes with the potential for multi-functional chemical (e.g., oxidation) and physical (e.g., filtration) treatment of impaired water supplies, as seen in Figure 1-13. Specifically, filtration by the ceramic membrane can occur concurrently with the treatment provided by the different nanofiber materials via strongly oxidizing microenvrionments or highly adsorbent surface sites. By taking advantage of the single- or multi-component nanofiber mat as a collective filtration membrane itself, there is the possibility of increased contact time, and consequently increased pollutant removal during influent movement, as well as synergies among the materials that can enhance performance.

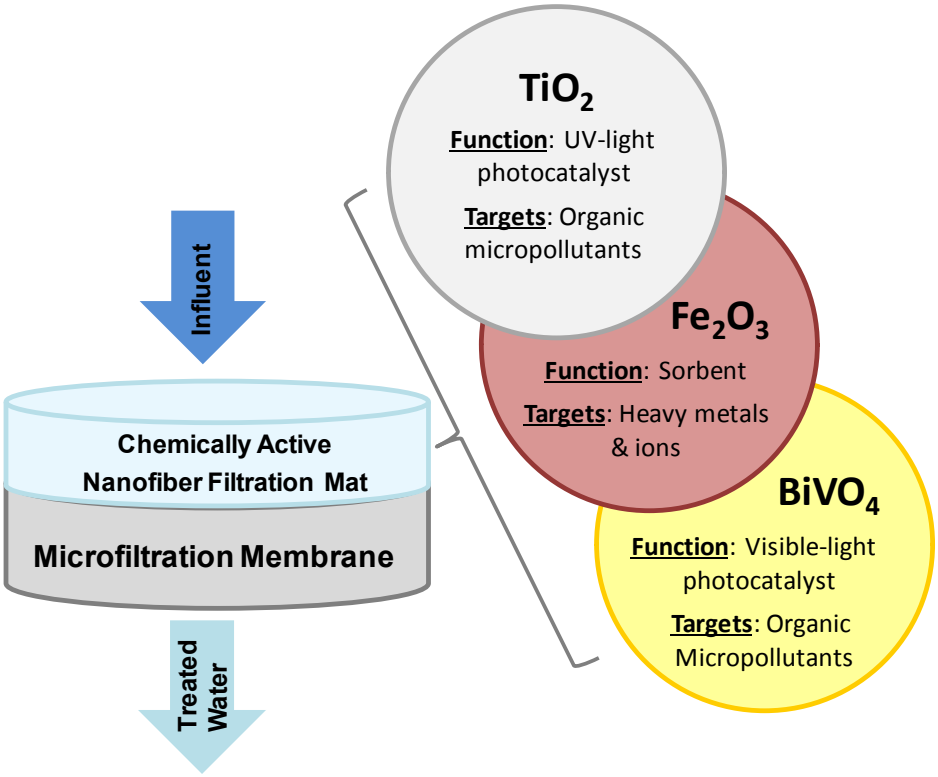

Figure 1-13: Conceptual electrospun nanofiber-integrated hybrid filter.

The project encompasses the synthesis and optimization of electrospun metal oxide nanofibers for the potential treatment of impaired water sources via photocatalysis and adsorption. The specific aims of this work were the following:

1) Determine the tunability of TiO_2 nanofiber characteristics based on electrospinning parameters and its impact on photochemical oxidation of micropollutants through photoreactivity studies. TiO_2 nanofibers have been synthesized for sensing, catalysis and filtration applications[65]. Based on different synthesis parameters, TiO_2 nanofibers can be tuned by dimensional

and morphological manipulation for specific treatment. Additionally, co-catalysts have been used to increase photocatalytic performance of pollutant degradation.[73]–[77] Therefore, nanofiber tuning could be controlled towards optimizing different characteristics for increased photoreactivity of pollutants in aquatic environments while characterizing physical, optical and electrical properties to analyze their effects on reactivity.

2) Determine the tunability of $BiVO_4$ nanofiber characteristics based on electrospinning parameters and its impact on visible light-induced photochemical oxidation of micropollutants through photoreactivity studies. $BiVO_4$ has shown to be an emerging non-titania semiconductor candidate for visible light-activated photocatalysis.[78] Although having been used in different applications such as gas sensors and batteries, $BiVO_4$ has seen some relevance in the field of photocatalytic degradation of aquatic pollutants.[79],[80] $BiVO_4$, due to its shorter band gap than TiO_2 (2.4 eV vs. 3.2 eV), is capable of photoactivation in the visible light region, decreasing the energy costs related to UV illumination.[81]–[83] Since work on electrospun $BiVO_4$ nanofibers has just been recently published, and therefore extremely limited,[84],[85] synthesis optimization and property-to-performance trends are currently unavailable. Thus, this work will provide substantial insight for future $BiVO_4$ nanofiber research in a range of suitable applications. $BiVO_4$ nanofibers will be synthesized with the objective of optimizing its visible light photocatalytic performance.

3) Determine the tunability of Fe_2O_3 nanofiber characteristics based on electrospinning parameters and its impact on surface site availability and surface chemistry for heavy metal adsorption. Extensive research has been performed on the adsorption properties of different iron oxides for heavy metal treatment of water sources.[15],[16] Hematite (α-Fe_2O_3) has shown the most promise for water treatment applications due to its non-toxicity, mineral stability, and great sorption capacity.[12] Hematite nanofibers have been successfully synthesized, primarily for magnetic applications.[86]–[88] Thus, these results can be applied towards hybrid membranes for water treatment. Iron oxide nanofibers will be synthesized by tuning dimensions and morphology to increase surface area-to-volume ratio to optimize available surface sites for heavy metal sorption. Additionally, metal oxides at controlled content levels will be implemented to further increase specific surface area for enhanced sorption performance.[89]

1.9 References

[1] Roy, S. B.; Chen, L.; Girvetz, E.; Edwin, P.; Mills, W. B.; Grieb, T. M. Evaluating Sustainability of Projected Water Demans under Future Climate Change Scenarios. **2010**, *Tetra Tech*.

[2] Tchobanoglous, G.; Burton, F. L.; Stensel, H. D. *Wastewater Engineering: Treatment and Reuse*; Fourth Edi.; Metcalf & Eddy: New York, 2002.

[3] Hermanowicz, S. W.; Takashi, A. Abel Wolman's "The Metabolism of Cities" Revised: A Case for Water Recycling and Reuse. *Water Science and Technology* **1999**, *40*, 29–36.

[4] Larson, D.; Lee, C.; Tellinghuisen, S.; Keller, A. California's Energy-Water Nexus : Water Use in Electricity Generation. *Southwest Hydrology* **2007**, *6*, 21–30.

[5] Wilkinson, R. C. Analysis of the Energy Intensity of Water Supplies for West Basin Municipal Water District. *West Basin Municipal Water District* **2007**.

[6] State of California Department of Water Resources. *California Water Plan Update 2005*; 2005.

[7] State of Florida Department of Environmental Protection. *2010 Reuse Inventory*; 2011.

[8] Daughton, C. G.; Ternes, T. A. Pharmaceuticals and Personal Care Products in the Environment: Agents of Subtle Change? *Environmental Health Perspectives* **1999**, *107*, 907–938.

[9] Boyd, G. R.; Reemtsma, H.; Grimm, D. A.; Mitra, S. Pharmaceuticals and Personal Care Products (PPCPs) in Surface and Treated Waters of Louisiana, USA and Ontario, Canada. *The Science of the Total Environment* **2003**, *311*, 135–149.

[10] Ternes, T. A.; Joss, A.; Siegrist, H. Scrutinizing Pharmaceuticals and Personal Care Products in Wastewater Treatment. *Environmental Science & Technology* **2004**, *38*, 392A–399A.

[11] Benotti, M. J.; Trenholm, R. A.; Vanderford, B. J.; Holady, J. C.; Stanford, B. D.; Snyder, S. A. Pharmaceuticals and Endocrine Disrupting Compounds in U.S. Drinking Water. *Environmental Science & Technology* **2009**, *43*, 597–603.

[12] Giménez, J.; Martínez, M.; de Pablo, J.; Rovira, M.; Duro, L. Arsenic Sorption onto Natural Hematite, Magnetite, and Goethite. *Journal of Hazardous Materials* **2007**, *141*, 575–80.

[13] Narayana, B.; Cherian, T.; Mathew, M.; Pasha, C. Spectrophotometric Determination of Arsenic in Environmental and Biological Samples. *Indian Journal of Chemical Technology* **2006**, *13*, 36–40.

[14] Jarup, L. Hazards of Heavy Metal Contamination. *British Medical Bulletin* **2003**, *68*, 167–182.

[15] Chowdhury, S. R.; Yanful, E. K. Arsenic and Chromium Removal by Mixed Magnetite-Maghemite Nanoparticles and the Effect of Phosphate on Removal. *Journal of Environmental Management* **2010**, *91*, 2238–2247.

[16] Ramos, M. A. V; Yan, W.; Li, X.; Koel, B. E.; Zhang, W. Simultaneous Oxidation and Reduction of Arsenic by Zero-Valent Iron Nanoparticles : Understanding the Significance of the Core-Shell Structure. *Journal of Physical Chemistry C Letters* **2009**, *113*, 14591–14594.

[17] Oulton, R. L.; Kohn, T.; Cwiertny, D. M. Pharmaceuticals and Personal Care Products in Effluent Matrices: A Survey of Transformation and Removal during Wastewater Treatment and Implications for Wastewater Management. *Journal of Environmental Monitoring* **2010**, *12*, 1956–1978.

[18] Schwarzenbach, R. P.; Escher, B. I.; Fenner, K.; Hofstetter, T. B.; Johnson, C. A.; von Gunten, U.; Wehrli, B. The Challenge of Micropollutants in Aquatic Systems. *Science* **2006**, *313*, 1072–1077.

[19] Donn, J.; Mendoza, M.; Pritchard, J. An AP Investigation: Pharmaceuticals Found in Drinking Water. *Assoc. Press* **2008**.

[20] Sutton, R. Chromium-6 in U.S. Tap Water. *Environmental Working Group* **2010**.

[21] Leonnig, C. D. CDC Misled District Residents about Lead Levels in Water, House Probe Finds. *Washington Post* **2010**.

[22] Hartley, T. W. Public Perception and Participation in Water Reuse. *Desalination* **2006**, *187*, 115–126.

[23] Brass, I.; Chirigotis, A.; Engelberg, D.; Pelczarski, F. Much Effort and Resources Needed to Help Small Drinking Water Systems Overcome Challenges. *U.S. Environmental Protection Agency, Report No. 2006-P-00026* **2006**.

[24] National Research Council. *Safe Water from Every Tap: Improving Water Service to Small Communities*; National Academies Press: Washington D.C., 1996.

[25] Takashi, A.; Burton, F. L.; Leverenz, H. L.; Tsuchihashi, R.; Tchobanoglous, G. *Water Reuse: Issues, Technologies and Applications*; First Edit.; Metcalf & Eddy: New York, 2007.

[26] National Science and Technology Council. *National Nanotechnology Initiative: The Initiative and Its Implementation Plan*; 2000.

[27] Wiesner, M. R.; Lowry, G. V.; Alvarez, P.; Dionysiou, D.; Biswas, P. Assessing the Risks of Manufactured Nanomaterials. *Environmental Science & Technology* **2006**, *40*, 4336–4345.

[28] Qu, X.; Alvarez, P. J. J.; Li, Q. Applications of Nanotechnology in Water and Wastewater Treatment. *Water Research* **2013**, *47*, 3931–46.

[29] Pokropivny, V. V.; Skorokhod, V. V. Classification of Nanostructures by Dimensionality and Concept of Surface Forms Engineering in Nanomaterial Science. *Materials Science and Engineering: C* **2007**, *27*, 990–993.

[30] Klabunde, K. J. *Nanoscale Materials in Chemistry*; John Wiley & Sons, Inc.: New York, 2001.

[31] Lee, Y.; Escher, B. I.; von Gunten, U. Efficient Removal of Estrogenic Activity during Oxidative Treatment of Waters Containing Steroid Estrogens. *Environmental Science & Technology* **2008**, *42*, 6333–6339.

[32] Munter, R. Advanced Oxidation Processes - Current Status and Prospects. *Proceedings of the Estonian Academy of Sciences, Chemistry* **2001**, *20*, 59–80.

[33] Chiron, S.; Fernandez-alba, A.; Rodriguez, A. Pesticide Chemical Oxidation: State-of-the-Art. *Water Research* **2000**, *34*, 366–377.

[34] Lee, C.; Yoon, J.; Von Gunten, U. Oxidative Degradation of N-Nitrosodimethylamine by Conventional Ozonation and the Advanced Oxidation Process Ozone/hydrogen Peroxide. *Water Research* **2007**, *41*, 581–590.

[35] Liotta, L. F.; Gruttadauria, M.; Di Carlo, G.; Perrini, G.; Librando, V. Heterogeneous Catalytic Degradation of Phenolic Substrates: Catalysts Activity. *Journal of hazardous materials* **2009**, *162*, 588–606.

[36] Soria-Sánchez, M.; Maroto-Valiente, a.; Álvarez-Rodríguez, J.; Muñoz-Andrés, V.; Rodríguez-Ramos, I.; Guerrero-Ruíz, a. Carbon Nanostrutured Materials as

Direct Catalysts for Phenol Oxidation in Aqueous Phase. *Applied Catalysis B: Environmental* **2011**, *104*, 101–109.

[37] Carp, O.; Huisman, C. L.; Reller, A. Photoinduced Reactivity of Titanium Dioxide. *Progress in Solid State Chemistry* **2004**, *32*, 33–177.

[38] Gaya, U. I.; Abdullah, A. H. Heterogeneous Photocatalytic Degradation of Organic Contaminants over Titanium Dioxide: A Review of Fundamentals, Progress and Problems. *Journal of Photochemistry and Photobiology C: Photochemistry Reviews* **2008**, *9*, 1–12.

[39] Wold, A. Photocatalytic Properties of TiO_2. *Chemistry of Materials* **1993**, *5*, 280–283.

[40] Hurum, D. C.; Agrios, A. G.; Gray, K. A.; Rajh, T.; Thurnauer, M. C. Explaining the Enhanced Photocatalytic Activity of Degussa P25 Mixed-Phase TiO_2 Using EPR. *Journal of Physical Chemistry B* **2003**, *107*, 4545–4549.

[41] Chong, M. N.; Jin, B.; Chow, C. W. K.; Saint, C. Recent Developments in Photocatalytic Water Treatment Technology: A Review. *Water Research* **2010**, *44*, 2997–3027.

[42] Lu, S.-Y.; Wu, D.; Wang, Q.-L.; Yan, J.; Buekens, A. G.; Cen, K.-F. Photocatalytic Decomposition on Nano-TiO_2: Destruction of Chloroaromatic Compounds. *Chemosphere* **2011**, *82*, 1215–24.

[43] Toyoda, T.; Tsuboya, I. Apparent Band-Gap Energies of Mixed TiO_2 Nanocrystals with Anatase and Rutile Structures Characterized with Photoacoustic Spectroscopy. *Review of Scientific Instruments* **2003**, *74*, 782.

[44] Zawadzki, P.; Laursen, A. B.; Jacobsen, K. W.; Dahl, S.; Rossmeisl, J. Oxidative Trends of TiO_2—hole Trapping at Anatase and Rutile Surfaces. *Energy & Environmental Science* **2012**, *5*, 9866–9869.

[45] Jeong, Y.; Fan, M.; Singh, S.; Chuang, C.-L.; Saha, B.; Hans van Leeuwen, J. Evaluation of Iron Oxide and Aluminum Oxide as Potential arsenic(V) Adsorbents. *Chemical Engineering and Processing: Process Intensification* **2007**, *46*, 1030–1039.

[46] Oura, K.; Lifshits, V. G.; Saranin, A.; Zotov, A. V.; Katayama, M. *Surface Science: An Introduction*; Springer: Berlin, 2003; p. 440.

[47] Cornell, R. M.; Schwertmann, U. *The Iron Oxides: Structure, Properties, Reactions, Occurences and Uses*; Second Edi.; Wiley-VCH: Weinheim, 2003; pp. 3–527.

[48] Schwertmann, U.; Cornell, R. M. *Iron Oxides in Laboratory: Preparation and Characterization*; Second Edi.; Wiley-VCH: Weinheim, 2000; Vol. 156.

[49] Ruppert, G.; Bauer, R. UV-O_3, UV-H_2O_2, UV-TiO_2 and the Photo-Fenton Reaction - Comparison of Advanced Oxidation Processes for Wastewater Treatment. *Chemosphere* **1994**, *28*, 1447–1454.

[50] Thiruvenkatachari, R.; Ouk Kwon, T.; Shik Moon, I. Application of Slurry Type Photocatalytic Oxidation-Submerged Hollow Fiber Microfiltration Hybrid System for the Degradation of Bisphenol A (BPA). *Separation Science and Technology* **2005**, *40*, 2871–2888.

[51] Carbonaro, S.; Sugihara, M. N.; Strathmann, T. J. Continuous-Flow Photocatalytic Treatment of Pharmaceutical Micropollutants: Activity, Inhibition, and Deactivation of TiO_2 Photocatalysts in Wastewater Effluent. *Applied Catalysis B: Environmental* **2013**, *129*, 1–12.

[52] Gardea-Torresdey, J. L.; Rico, C. M.; White, J. C. Trophic Transfer, Transformation, and Impact of Engineered Nanomaterials in Terrestrial Environments. *Environmental Science & Technology* **2014**, *48*, 2526–2640.

[53] Andon, F. T.; Fadeel, B.; Torres, F. Programmed Cell Death: Molecular Mechanisms and Implications for Safety Assessment of Nanomaterials. *Accounts of Chemical Research* **2013**, *46*, 733–742.

[54] Powers, C. M.; Bale, A. S.; Kraft, A. D.; Makris, S. L.; Trecki, J.; Cowden, J.; Hotchkiss, A.; Gillespie, P. a Developmental Neurotoxicity of Engineered Nanomaterials: Identifying Research Needs to Support Human Health Risk Assessment. *Toxicological Sciences* **2013**, *134*, 225–242.

[55] Kiser, M. a; Westerhoff, P.; Benn, T.; Wang, Y.; Pérez-Rivera, J.; Hristovski, K. Titanium Nanomaterial Removal and Release from Wastewater Treatment Plants. *Environmental Science & Technology* **2009**, *43*, 6757–6763.

[56] Zhang, Y.; Chen, Y.; Westerhoff, P.; Hristovski, K.; Crittenden, J. C. Stability of Commercial Metal Oxide Nanoparticles in Water. *Water Research* **2008**, *42*, 2204–2212.

[57] Keller, A. a; Wang, H.; Zhou, D.; Lenihan, H. S.; Cherr, G.; Cardinale, B. J.; Miller, R.; Ji, Z. Stability and Aggregation of Metal Oxide Nanoparticles in

Natural Aqueous Matrices. *Environmental Science & Technology* **2010**, *44*, 1962–1967.

[58] Yuan, Z.; Su, B. Titanium Oxide Nanotubes, Nanofibers and Nanowires. *Colloids and Surfaces A: Physicochemical Engineering Aspect* **2004**, *241*, 173–183.

[59] Ramakrisha, S.; Fujuhara, K.; Teo, W.-E.; Lim, T.-C.; Ma, Z. *An Introduction to Electrospinning and Nanofibers*; World Scientific Publishing Co.: Singapore, 2005.

[60] Dai, Y.; Liu, W.; Formo, E.; Sun, Y.; Xia, Y. Ceramic Nanofibers Fabricated by Electrospinning and Their Applications in Catalysis, Environmental Science, and Energy Technology. *Polymers for Advanced Technologies* **2011**, *22*, 326–338.

[61] Thavasi, V.; Singh, G.; Ramakrishna, S. Electrospun Nanofibers in Energy and Environmental Applications. *Energy & Environmental Science* **2008**, *1*, 205–221.

[62] Li, D.; Xia, Y. Electrospinning of Nanofibers: Reinventing the Wheel? *Advanced Materials* **2004**, *16*, 1151–1170.

[63] Persano, L.; Camposeo, A.; Tekmen, C.; Pisignano, D. Industrial Upscaling of Electrospinning and Applications of Polymer Nanofibers: A Review. *Macromolecular Materials and Engineering* **2013**, *298*, 504–520.

[64] Choi, S. K.; Kim, S.; Lim, S. K.; Park, H. Photocatalytic Comparison of TiO_2 Nanoparticles and Electrospun TiO_2 Nanofibers: Effects of Mesoporosity and Interparticle Charge Transfer. *Journal of Physical Chemistry C* **2010**, *114*, 16475–16480.

[65] Li, D.; Xia, Y. Fabrication of Titania Nanofibers by Electrospinning. *Nano Letters* **2003**, *3*, 555–560.

[66] Lee, J.-S.; Lee, Y.-I.; Song, H.; Jang, D.-H.; Choa, Y.-H. Synthesis and Characterization of TiO_2 Nanowires with Controlled Porosity and Microstructure Using Electrospinning Method. *Current Applied Physics* **2011**, *11*, S210–S214.

[67] Mowbray, D. J.; Martinez, J. I.; Thygesen, K. S.; Jacobsen, K. W. Stability and Electronic Properties of TiO_2 Nanostructures With and Without B and N Doping. *Journal of Physical Chemistry C* **2009**, *113*, 12301–12308.

[68] Ramakrishna, S.; Jose, R.; Archana, P. S.; Nair, a. S.; Balamurugan, R.; Venugopal, J.; Teo, W. E. Science and Engineering of Electrospun Nanofibers for Advances in Clean Energy, Water Filtration, and Regenerative Medicine. *Journal of Materials Science* **2010**, *45*, 6283–6312.

[69] Wang, X.; Choi, J.; Mitchell, D. R. G.; Truong, Y. B.; Kyratzis, I. L.; Caruso, R. A. Enhanced Photocatalytic Activity: Macroporous Electrospun Mats of Mesoporous Au/TiO_2 Nanofibers. *ChemCatChem* **2013**, *5*, 2646–2654.

[70] Zhang, X.; Xu, S.; Han, G. Fabrication and Photocatalytic Activity of TiO_2 Nanofiber Membrane. *Materials Letters* **2009**, *63*, 1761–1763.

[71] Gao, P.; Tai, M. H.; Sun, D. D. Hierarchical TiO_2 /V_2O_5 Multifunctional Membrane for Water Purification. *ChemPlusChem* **2013**, *78*, 1475–1482.

[72] Mauter, M. S.; Elimelech, M. Environmental Applications of Carbon-Based Nanomaterials. *Environmental Science & Technology* **2008**, *42*, 5843–5859.

[73] Zaleska, A. Characterics of Doped-TiO_2 Photocatalysts. *Physicochemical Problems of Mineral Processing* **2008**, *42*, 211–221.

[74] Zhu, W.; Qiu, X.; Iancu, V.; Chen, X.-Q.; Pan, H.; Wang, W.; Dimitrijevic, N.; Rajh, T.; Meyer, H.; Paranthaman, M.; et al. Band Gap Narrowing of Titanium Oxide Semiconductors by Noncompensated Anion-Cation Codoping for Enhanced Visible-Light Photoactivity. *Physical Review Letters* **2009**, *103*, 226401.

[75] Madhusudan Reddy, K.; Baruwati, B.; Jayalakshmi, M.; Mohan Rao, M.; Manorama, S. V S-, N- and C-Doped Titanium Dioxide Nanoparticles: Synthesis, Characterization and Redox Charge Transfer Study. *Journal of Solid State Chemistry* **2005**, *178*, 3352–3358.

[76] Di Paola, A.; Marci, G.; Palmisano, L.; Schiavello, M.; Uosaki, K.; Ikeda, S.; Ohtani, B. Preparation of Polycrystalline TiO_2 Photocatalysts Impregnated with Various Transition Metal Ions: Characterization and Photocatalytic Activity for the Degradation of 4-Nitrophenol. *Journal of Physical Chemistry B* **2001**, *106*, 637–645.

[77] Bouras, P.; Stathatos, E.; Lianos, P. Pure versus Metal-Ion-Doped Nanocrystalline Titania for Photocatalysis. *Applied Catalysis B: Environmental* **2007**, *73*, 51–59.

[78] Zhang, L.; Long, J.; Pan, W.; Zhou, S.; Zhu, J.; Zhao, Y.; Wang, X.; Cao, G. Efficient Removal of Methylene Blue over Composite-Phase $BiVO_4$ Fabricated by Hydrothermal Control Synthesis. *Materials Chemistry and Physics* **2012**, *136*, 897–902.

[79] Zhang, X.; Ai, Z.; Jia, F.; Zhang, L.; Fan, X.; Zou, Z. Selective Synthesis and Visible-Light Photocatalytic Activities of $BiVO_4$ with Different Crystalline Phases. *Materials Chemistry and Physics* **2007**, *103*, 162–167.

[80] Zhou, L.; Wang, W.; Zhang, L.; Xu, H.; Zhu, W. Single-Crystalline $BiVO_4$ Microtubes with Square Cross-Sections: Microstructure, Growth Mechanism, and Photocatalytic Property. *Journal of Physical Chemistry C* **2007**, *111*, 13659–13664.

[81] Walsh, A.; Yan, Y.; Huda, M. N.; Al-Jassim, M. M.; Wei, S.-H. Band Edge Electronic Structure of $BiVO_4$: Elucidating the Role of the Bi S and V D Orbitals. *Chemistry of Materials* **2009**, *21*, 547–551.

[82] Kudo, A.; Omori, K.; Kato, H. A Novel Aqueous Process for Preparation of Crystal Form-Controlled and Highly Crystalline $BiVO_4$ Powder from Layered Vanadates at Room Temperature and Its Photocatalytic and Photophysical Properties. *Journal of the American Chemical Society* **1999**, *121*, 11459–11467.

[83] Park, Y.; McDonald, K. J.; Choi, K.-S. Progress in Bismuth Vanadate Photoanodes for Use in Solar Water Oxidation. *Chemical Society Reviews* **2013**, *42*, 2321–2337.

[84] Liu, G.; Liu, S.; Lu, Q.; Sun, H.; Xiu, Z. $BiVO_4$/cobalt Phthalocyanine (CoPc) Nanofiber Heterostructures: Synthesis, Characterization and Application in Photodegradation of Methylene Blue. *RSC Advances* **2014**, *4*, 53402–53406.

[85] Liu, G.; Liu, S.; Lu, Q.; Sun, H.; Xiu, Z. Synthesis and Characterization of $Bi(VO_4)_{1-m}(PO_4)_m$ Nanofibers by Electrospinning Process with Enhanced Photocatalytic Activity under Visible Light. *RSC Advances* **2014**, *4*, 33695–33701.

[86] Zhu, Y.; Zhang, J. C.; Zhai, J.; Jiang, L. Preparation of Superhydrophilic Alpha-Fe_2O_3 Nanofibers with Tunable Magnetic Properties. *Thin Solid Films* **2006**, *510*, 271–274.

[87] Zheng, W.; Li, Z.; Zhang, H.; Wang, W.; Wang, Y.; Wang, C. Electrospinning Route for Alpha-Fe_2O_3 Ceramic Nanofibers and Their Gas Sensing Properties. *Materials Research Bulletin* **2009**, *44*, 1432–1436.

[88] Shao, H.; Zhang, X.; Liu, S.; Chen, F.; Xu, J.; Feng, Y. Preparation of Pure Iron Nanofibers via Electrospinning. *Materials Letters* **2011**, *65*, 1775–1777.

[89] Li, R.; Li, Q.; Gao, S.; Shang, J. K. Enhanced Arsenite Adsorption onto Litchi-Like Al-Doped Iron Oxides. *Journal of the American Ceramic Society* **2011**, *94*, 584–591.

Chapter 2: Synthesis and Optimization of TiO_2 Nanofibers

2.1 Abstract

Although still in development, nanotech-integrated advanced treatment systems have shown to be the future remedy for combating the emergence of organic microcontaminants in water sources. In this study, titanium dioxide (TiO_2) nanofibers were synthesized via electrospinning, while structure and composition were tailored to optimize photocatalytic treatment efficiency. Through systematic tuning of the parameters during electrospinning, TiO_2 nanofibers of controlled diameter (ranging from 33-209 nm), crystallinity (anatase, rutile and mixed phases), grain size (ranging from 19-49 nm), and band gap (ranging from 3.02 to 3.21 eV) were developed. Additionally, their reactivity was then examined in batch suspensions toward the model pollutant phenol to quantify photoactive performance. Photocatalytic studies revealed enhancement in performance with decreased average diameter due to increased reactive surface sites, as well as an optimal mixed phase composition leading to the greatest reactivity. Dimension and crystal phase composition showed to heave the greatest effect in enhancing TiO_2 photoreactivity. Optimal TiO_2 nanofibers tailored via electrospinning, having an average diameter of 33 nm and mixed phase composition of 26/74 (±0.5) % rutile/anatase, exceeded the performance of traditional photocatalysts (e.g., Aeroxide® P25). Ultimately, TiO_2 nanofibers appear most promising for use as reactive filtration materials because their performance was invariant with water quality, although future efforts must increase the strength of TiO_2 nanofiber mats to realize such applications.

2.2 Introduction

2.2.1 Titanium Dioxide (TiO_2)

Titanium (Ti), the world's fourth most abundant metal and ninth most abundant element, was discovered in 1791 by Reverend William Gregor.[1] Titanium dioxide (TiO_2), the most commonly used compound of titanium, comprises of approximately 95% of the world's titanium consumption.[2] Because of its bright white pigmentation and high refractive index, TiO_2 is used in paints, plastics, paper as major end-use sectors, but has also been used in foods, textiles, pharmaceuticals and cosmetics.[1] In addition to those main properties, TiO_2's chemical stability, non-toxicity and low cost helped it garner a great amount of attention in the field on nanotechnology. As a result, TiO_2 has been heavily investigated in applications of dye-sensitized solar cells, gas sensors, biomaterials, and especially, catalysts. Scientific studies of TiO_2 date back to the early part of the 20^{th} century,[3] but it wasn't until the late 1960s where the photocatalysis of TiO_2 in the presence of UV light was discovered and investigated, which was later to be called the Honda-Fujishima effect.[4]

In a general sense, semiconductors are materials with electron conductivity properties between that of a metal and an insulator. Instead of having a valence and conduction band that overlap, thus having free electron movement within the material, a semiconductor has a band gap separating the valence band and conduction band.[5] Absorption of incident photons by a semiconductor with energy equal or greater than the band gap energy can induce charge carrier movement within the material.[5] Among the semiconductor catalysts, TiO_2 has by far received the greatest interest in the

photocatalysis field because of its high photoactivity and photoefficiency in the UV spectrum.[6]

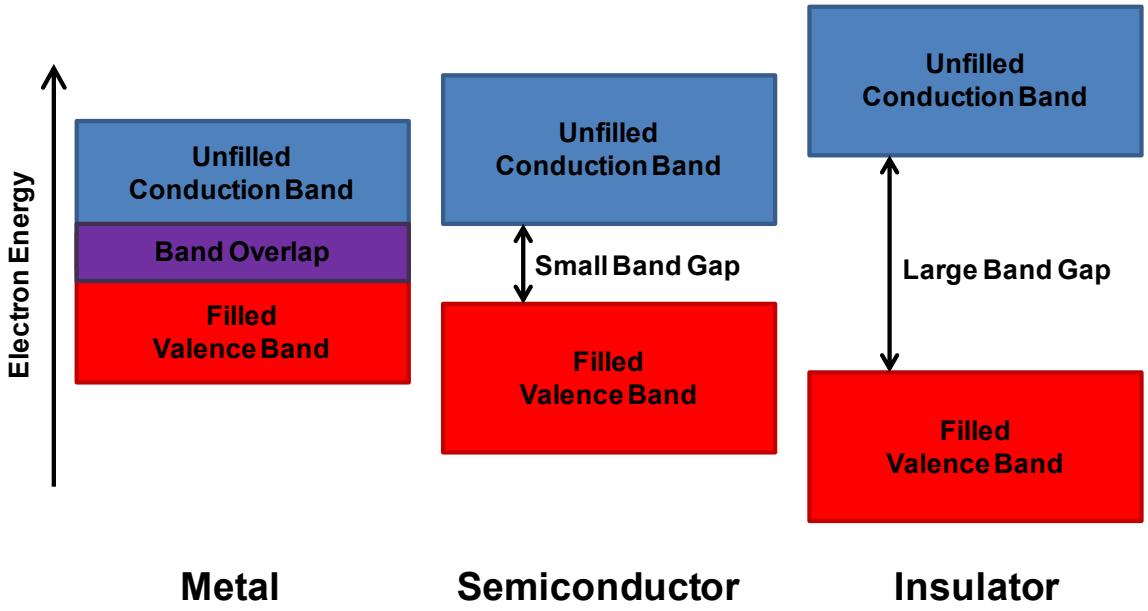

Figure 2-1: Comparison of the electronic band structures of metals, semiconductors and insulators.

Despite it having poor performance in the presence of visible light, TiO_2 is an ideal semiconductor because it is chemically and biologically inert, photocatalytically stable, relatively easy to produce and to use, able to efficiently catalyze reactions, cheap and without risks to the environment or humans.[6] In the sphere of the environmental remediation field, TiO_2 has been significantly studied and manipulated for decades as a promoter of oxidative radical species, such as hydroxyl radical ($^{\bullet}OH$), for the degradation of aqueous micropollutants.[7] This extensive research has shown that its photocatalytic properties are influenced by many physicochemical variables, such as size, pore volume, surface area, and crystallinity.[8] Altogether, the physical parameters of TiO_2 collectively

have a great effect on the ultimate photoelectrochemical mechanisms of the semiconductor's photoactivity.

2.2.2 TiO_2 Nanofibers

Since TiO_2 photocatalysts have been heavily studied for years, there is a large list of work on different structured TiO_2, including nanoparticles, nanowires, nanorods, nanotubes, and nanoribbons.[9]–[12] But as previously discussed, electrospun nanofibers, as they offer advantages in terms of easy of synthesis and tuning, photocatalytic performance, and system integratability.[13]–[16]

Doh et al.[17] reported on electrospun TiO_2 nanofibers with varied electric field and solution flow rate. Based on the different synthesis parameters, TiO_2 nanofibers were fabricated with average diameters ranging from 150 to 400 nm. Additionally, annealing temperature tuning from 250 to 850 °C showed control of crystal phase composition. Lee et al.[18] reported on electrospun nanofibers with varied polymer content and applied voltage. Synthesis with different electrospinning parameters led to nanofibers with various diameters from 50 to 100 nm. Calcination temperature was tuned from 400 to 800 °C, controlling crystal phase composition. Li et al.[19] reported on electrospun TiO_2 nanofibers controlled by several tuning parameters. By varing polymer ceontration Ti precursor concentration, electric field and feeding rate, the TiO_2 nanofibers had diameters ranging from 30 to 200 nm. Watthanaarun et al.[20] reported on electrospun TiO_2 nanofibers with varied polymer content, applied voltage and calcination temperature, yielding diameters ranging from 100 to 200 nm. Sarlak et al[21]. reported on electrospun

TiO_2 nanofibes with several tuned parameters, including applied voltage, flow rate, electrospun distance, polymer content, Ti precursor content, and solution pH. Based on experimental design of these parameters, the TiO_2 nanofibers varied in diameter from 200 to 2000 nm.

Du et al.[22] reported on electrospun TiO_2 nanofibers with an average diameter of 100 nm, outperforming zinc oxide (ZnO) nanofibers based on the photocatalytic degradation of Rhodamine B. Di Camilluo et al.[23] reported on electrospun TiO_2 nanofibers, having diameters with a range of 300 to 400 nm and only modified by nitrogen (N) doping. Choi et al.[24] reported on electrospun TiO_2 nanofibers with an average diameter of 500 nm, outperforming TiO_2 nanoparticles based on photocatalytic activity. Pan et al.[25] reported on electrospun TiO_2 nanofibers with an average diameter ranging from 200 to 300 nm and only modified by surface functionalization of gold (Au). Zhang et al.[26] reported on electrospun TiO_2 nanofibers with an average diameter from 100 to 150 nm and only modified by tin dioxide (SnO_2) beads. Liu et al.[27] reported on electrospun TiO2 nanofibers with an average diameter of 300 nm and modified only by the addition of carbon nanospheres for increased porosity. While substantial work on TiO_2 nanofibers is available, lack of extensive property modifications towards dimensional optimization and links between material structure and reactivity presents obstacles to the progression of these novel materials for nanoengineered treatment systems.

The overall objective of this study is to synthesize TiO_2 nanofibers and optimize their photocatalyic activity for the oxidation of organic micropollutants in water.

Through the versatile nanofiber synthesis process of electrospinning, TiO_2 nanofiber dimension (*i.e.,* diameter) and material properties (*e.g.*, crystal structure, and grain size) can be tuned by varying synthesis parameters (*e.g.*, applied voltage and annealing temperature). Synthesized nanofibers were characterized via various techniques, such as SEM, XRD and diffuse reflectance, to first relate observed changes in nanofiber properties to specific adjustments in our electrospinning procedure. Subsequently, performance of these nanofibers were analyzed in model laboratory systems for degradation of phenol, a model pollutant with functional moieties often encountered in common organic micropollutant classes. Based on their photoreactivity, the structural modifications critical to optimizing treatment efficiency were identified.

2.3 Experimental Methods

2.3.1 Reagents

All chemicals were reagent grade or better and used as received. The synthesis of the TiO_2 nanofibers involved titanium tetraisopropoxide (TTIP) (Sigma Aldrich, 97%), ethanol (Fisher Scientific, anhydrous), acetic acid (Fisher Scientific, glacial 99.7%) and polyvinylpyrrolidone (PVP) (Sigma Aldrich, MW: 1,300,000 g/mol).

A buffer prepared from 5 mM potassium phosphate monobasic (Fisher Scientific, 99.3%) and 5 mM sodium chloride (NaCl) (Sigma Aldrich, >99.0%) was used in all photochemical experiments. A buffer prepared from 10 mM NaCl was used in all zeta potential experiments. Aeroxide® P25 (Acros Organics) was used as a commercially available TiO_2 photocatalyst for treatment efficiency comparison. Phenol (Sigma-

Aldrich, >99%) was used as a model organic micropollutant in all photoactivity studies. The eluent for HPLC analysis of phenol used sodium acetate (Sigma Aldrich, anhydrous) and acetonitrile (ACN) (Fisher Scientific, 99.9%). All solutions were prepared in deionized (DI) water (Millipore, Milli-Q).

2.3.2 Synthesis of TiO_2 Nanofibers

The synthesis of TiO_2 nanofibers began with the preparation of two separate solutions, the titanium precursor solution containing TTIP, and the polymer solution containing PVP. A designated amount (12-15 wt.%) of PVP and 4.5 mL of ethanol were added in a 50 mL glass beaker and stirred with a magnetic stirrer at a rate of 300 rpm for at least 2 hours, insuring that all of the PVP has dissolved. Additionally, 1.68 mL of TTIP, 3 mL of ethanol and 3 mL of acetic acid were added in a 50 mL glass beaker and stirred at a rate of 300 rpm for 10 minutes. After both solutions dissolved completely, they were mixed together for an hour, creating the desired electrospinning solution.

For the electrospinning process, the precursor solution was transferred into a syringe that was subsequently loaded onto a syringe driver (Braun Perfusor, Inc.). The syringe was connected to a metallic adapter with 25 gauge plastic needle tip (NanoNC, Inc. from Korea) and situated 10 cm away from an aluminum foil-covered rotating drum (SPG Co., Ltd; Korea), which acted as the grounded collector. The metal adapter was connected to an Acopian (Easton, PA) high-voltage power supply, and a range of applied voltages (12-18 kV) were utilized. As the solution progressed through the system (0.3

mL/hr) it became electrified. The tip of the resulting Taylor cone expelled an electrified jet of fibers, forming a fibrous mesh on the grounded collector.

After 3 hours, the electrospinning was ceased and the Al foil coated with the nanofibers was removed and inserted into a drying oven (Yamato DVS 402) at 60 °C overnight. After this low heating, the nanofiber mat (typically 0.13 x 0.28 m^2) was peeled off and placed into a ceramic bowl for subsequent annealing/calcination in a box furnace (Thermolyne; Thermo Scientific) for polymer removal and TiO_2 crystallization. The furnace was heated to the desired temperature from room temperature at a rate of 3 °C/min, maintained at a temperature for a desired period of time, and cooled down to room temperature. The annealing process was set at different temperatures from 500 °C, the lowest temperature to both completely remove PVP and crystallize the nanofibers to the anatase phase, to 800 °C, the temperature at which only rutile phase is present.

After annealing, typically 20-25 mg of nanofibers were produced and combined with a designated amount of DI water to create a 1 g/L TiO_2 stock and sonicated in a Branson sonicator to disperse the nanofibers into a homogenous suspension.

2.3.3 Nanofiber Characterization

TiO_2 nanofibers were characterized using several different techniques to quantify their size, and morphological and optical properties. Nanofiber diameter was examined by a Phillips XL30 FEG scanning electron microscopy (SEM). For SEM, samples were prepared by placing approximately a 0.5 cm x 0.5 cm area of nanofibers onto a SEM

sample holder. SEM imaging of n = 100 nanofibers yielded average diameters (with standard deviation) that were used to create sizing histograms.

Crystal phase, crystal orientation and average grain size were determined by a Bruker D8 Advance x-ray diffraction (XRD) analyzer. XRD samples were prepared by depositing a 1 x 1 cm^2 area of nanofibers onto a glass slide. Samples were analyzed from 20° to 80° for the Bragg angle with an interval of 0.03°. The motivation for crystal phase tuning is that Aeroxide® P25, a mixed phase TiO_2 with an anatase to rutile ratio of 70-80:20-30[6],[9], outperforms both pure phases in reactivity studies[28]. Moreover, grain size tuning represents a means to control crystallinity, which strongly influences the recombination rate of photogenerated holes and electrons. Using the XRD spectra data, the rutile percent composition was calculated by means of equation 2.10:[29]

$$R(\%) = \frac{0.79\left(\frac{IR}{IA}\right)}{1 + \left(0.79\left(\frac{IR}{IA}\right)\right)} \tag{2.1}$$

where *IR* is the intensity of the rutile peak (1 1 0) at 2θ = 27.5° and *IA* is the intensity of the anatase peak (1 0 1) at 2θ = 25.4°. The average grain size was calculated by the Scherrer-Debye equation, as seen in equation 2.11:[29]

$$D = \frac{k\lambda}{B cos\theta} \tag{2.2}$$

where D is the average grain size in nm, k is the shape factor constant (0.9), λ is the wavelength used by XRD (0.154 nm), B is the broadening of the diffraction line measured by the full width at half maximum of the peak and θ is the Bragg angle of the peak from the XRD spectrum.

The texture coefficient of nanofibers was also determined from XRD spectra to verify random or preferential crystal orientation. The texture coefficient (TC) equation is defined as[30]:

$$TC(hlk) = \frac{\frac{I(hkl)}{I_0(hkl)}}{\sum_n \frac{I(hkl)}{I_0(hkl)}} \; x \; 100\% \tag{2.3}$$

where $I(hkl)$ is the measured relative intensity of a plane (hkl) and $I_0(hkl)$ is the standard intensity of the plane (hkl) taken from the JCPDS data. A $TC(hkl)$ value of 1 represents randomly oriented nanofibers, while higher values indicate the abundance of crystals oriented in a given (hkl) direction. Three peaks were used in both anatase and rutile calculations. Anatase peaks used were (1 0 1) at 2θ = 25.4°, (0 0 4) at 2θ = 37.8° and (2 0 0) at 2θ = 48.1°, and rutile peaks used were (1 1 0) at 2θ = 27.5°, (1 0 2) at 2θ = 36.1° and (2 1 1) at 2θ = 54.3°.

Zeta potential was determined by a Brookhaven Instrumental Corporation ZetaPALS zeta potential analyzer. Zeta potential analyses were conducted to examine the nanofiber's electrical potential and describe the electrostatic interaction near the surface of the TiO_2 nanofibers. Based on previous research,[31],[32] 100 μL of the 1 g/L TiO_2 stock

suspension was added to 3.5 mL of 10 mM NaCl set at various pH values between 4 and 8. The solution was then added to plastic cuvettes for subsequent analysis, in which values of zeta potential represent an average and standard deviation of 5 runs per sample. The point of zero charge (pzc) was calculated by interpolation between data points in which a zeta potential equal to 0 was achieved.

Band gap energy was determined by a Thermo Scientific Evolution 300 UV-Vis spectrophotometer with a Praying Mantis diffuse reflectance infrared Fourier transform spectroscopy (DRIFTS) accessory. For analysis, the TiO_2 samples were irradiated by light over a wavelength scan from 200 to 800 nm and absorbance was measured. Values of absorbance were then converted into reflectance by means of equation 2.13:

$$A = \log\left(\frac{1}{R}\right) \tag{2.4}$$

where A is the measured absorbance and R is the reflectance. The Kubelka-Munk formula was then used to convert reflectance into a function F equivalent to the absorption coefficient α, seen as the following equation:[33],[34]

$$F = \frac{(1-R)^2}{2R} \tag{2.5}$$

The band gap was obtained by plotting $(Fhv)^{1/2}$ versus hv, which involves converting the wavelength (nm) into band gap energy (eV) via the Planck relation:

$$E = h\nu = \frac{hc}{\lambda} \tag{2.6}$$

where E is the energy of a photon, h is Planck's constant (4.14 x 10-15 eV•s), c is the speed of light (3.0 x 10^8 m/s), ν is frequency and λ is wavelength. Through this plot, extrapolating the linear portion of the graph at $(Fh\nu)^{1/2} = 0$ yielded band gap energy.

Surface area was determined by BET analysis via Micromeritics ASAP 2020 Physisorption Analyzer in order to investigate any surface property change towards enhancement of photoactivity. Due to the amount of mass required for accurate analysis, BET was only conducted on select samples. All samples were degassed at 300 °C for 3 hours prior to analysis.

Sedimentation studies were conducted to explore the stability of nanofiber and Aeroxide® P25 suspensions. Prior to analysis, a 1 g/L stock solution of either pure TiO_2 nanofibers (12 kV, 650 °C, d = 33 nm) or Aeroxide® P25 was sonicated for 1 hr. Afterwards, a solution of 0.1 g/L catalyst was created for both NFs and Aeroxide® NPs, where 100 □L of the 1 g/L stock was added to 900 □L of DI water for a total volume of 1 mL (pH ~7). The solution was mixed thoroughly for homogeneity and pipetted in a 1.5 mL cuvette with a path length of 1 cm. Absorbance due to particles in the suspension was then monitored at a wavelength of 400 nm in 5 min intervals over one hour.

2.3.4 Photocatalysis Experiments

Reactivity experiments were conducted in batch systems using a commercially available 1000 W Xenon arc lamp (Newport Corporation). The light was first passed

through a water filter to remove infrared (IR) radiation, reflected off a 90° full reflectance beam turning mirror, and then passed through a 305 nm long-pass filter to better simulate the spectrum of light available at earth's surface. Reactivity studies were conducted within a jacketed photoreactor containing catalyst suspensions (0.1 g/L) prepared at pH 7 (using 5 mM buffer) and maintained at 25 °C with a recirculating water bath. All experiments were conducted at the same initial concentration (100 μM). Often, a Langmuir Hirshelwood kinetic model is applied to the TiO_2 mediated photocatalytic degradation of aqueous phase pollutants,[35]–[37] that accounts for surface adsorption and reaction during transformation. However, the focus of this initial work was optimizing photocatalytic activity based on structural modifications to TiO_2 nanofibers, although there was no indication of sorption of phenol onto the nanofibers based on comparison of initial phenol concentration measurements made in control reactors without nanofibers.

After dispersion of nanofibers via sonication, suspensions were irradiated and aliquots were withdrawn over time to measure change in phenol concentration over time. Samples were centrifuged at 10,000 rpm for 8 min in the dark to allow extraction of the supernatant. The supernatant was transferred to a 1.5 mL amber autosampler vial for subsequent analysis via high performance liquid chromatography with photodiode array detector (1200 Series Agilent HPLC-DAD) equipped with an Eclipse XDB-C18 column (4.6 × 50 mm, 1.8 μm particle size). The HPLC method of analysis for phenol was based on previous work and employed a mobile phase of 65:35 1 mM sodium acetate: ACN at pH 3, a flow rate of 0.75 mL/min, an injection volume of 20 μL and a 254 nm detection wavelength.[38]–[40]

2.4 Results and Discussion

2.4.1 Nanofiber Characterization

Variations in polymer concentration and applied voltage during synthesis adjusted the diameter of resulting nanofibers. Based on the histograms shown in Figure 2-2, decreasing the PVP polymer concentration from 15 to 12 wt. % and increasing the applied voltage from 8 to 12 kV produced a decrease in the average diameter of the TiO_2 nanofibers from 209 (±37) to 33 (±10) nm. These observations are consistent with the decrease in polymer concentration and increase in applied voltage reduce the surface tension, thereby stretching the nanofibers from the electrified Taylor cone more thinly during electrospinning.[21] Thus, electrospinning provides a relatively simple route to maximizing the surface area-to-volume ratio of the nanofibers, in turn enhancing the available reactive surface area during irradiation. As a point of reference,[8] nanoparticulate Aeroxide® P25, a commonly utilized TiO_2 photocatalyst, has an average size of ~25 nm. From here on, TiO_2 nanofibers will be referenced as 209, 146, 63 and 33 nm in average diameter.

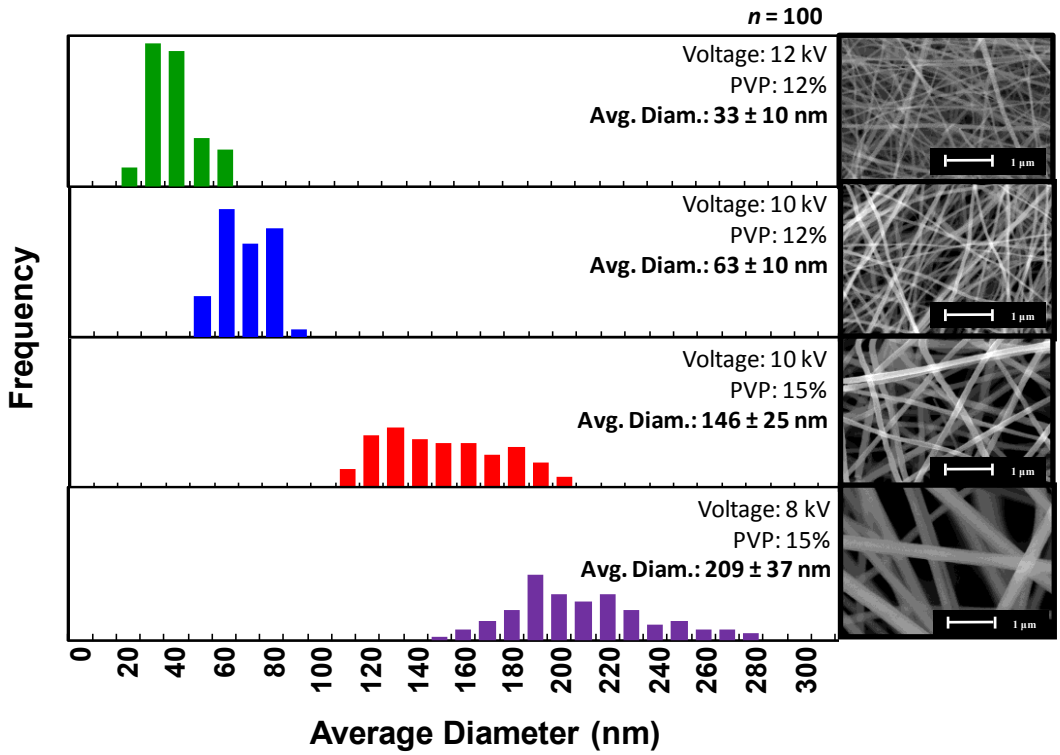

Figure 2-2: Histogram of TiO_2 nanofiber diameter with associated SEM image.

The annealing process was found to alter crystal structure and grain size. For a fixed ramping rate (3 °C/min) and annealing duration (3 hours) of the 33 nm sized nanofibers, a general increase in rutile composition was observed at higher annealing temperatures, as seen by the emergence of rutile peaks in Figure 2-3. These results are expected because as the more thermodynamically favorable phase, the rutile phase is preferred at higher annealing temperatures and over longer annealing time. Figure 2-4 provides 3D surface plots of the rutile percent composition and average grain size for nanofibers with an average diameter of 33 nm. These data are presented as a function of annealing temperature (500-800 °C) and annealing time (1-6 hours). By increasing both the annealing temperature and annealing duration, rutile composition and the average

grain size were increased. As observed via XRD analysis, the rutile composition can be tuned from 0-100% (±0.5%) with average grain sizes from 19-49 (±0.5) nm. These trends of crystal phase composition and average grain size also hold true for the large TiO_2 nanofibers, as nanofiber dimension had no significant effect on any property tuning from annealing treatment.

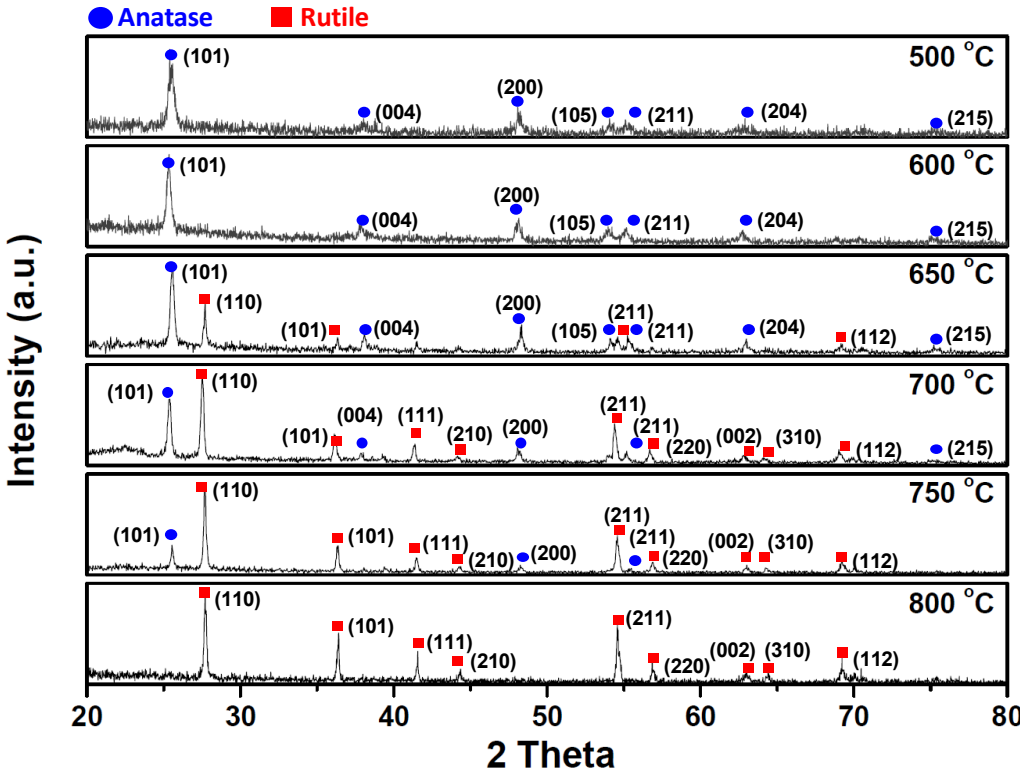

Figure 2-3: XRD spectra of synthesized TiO_2 nanofibers after annealing at different temperatures.

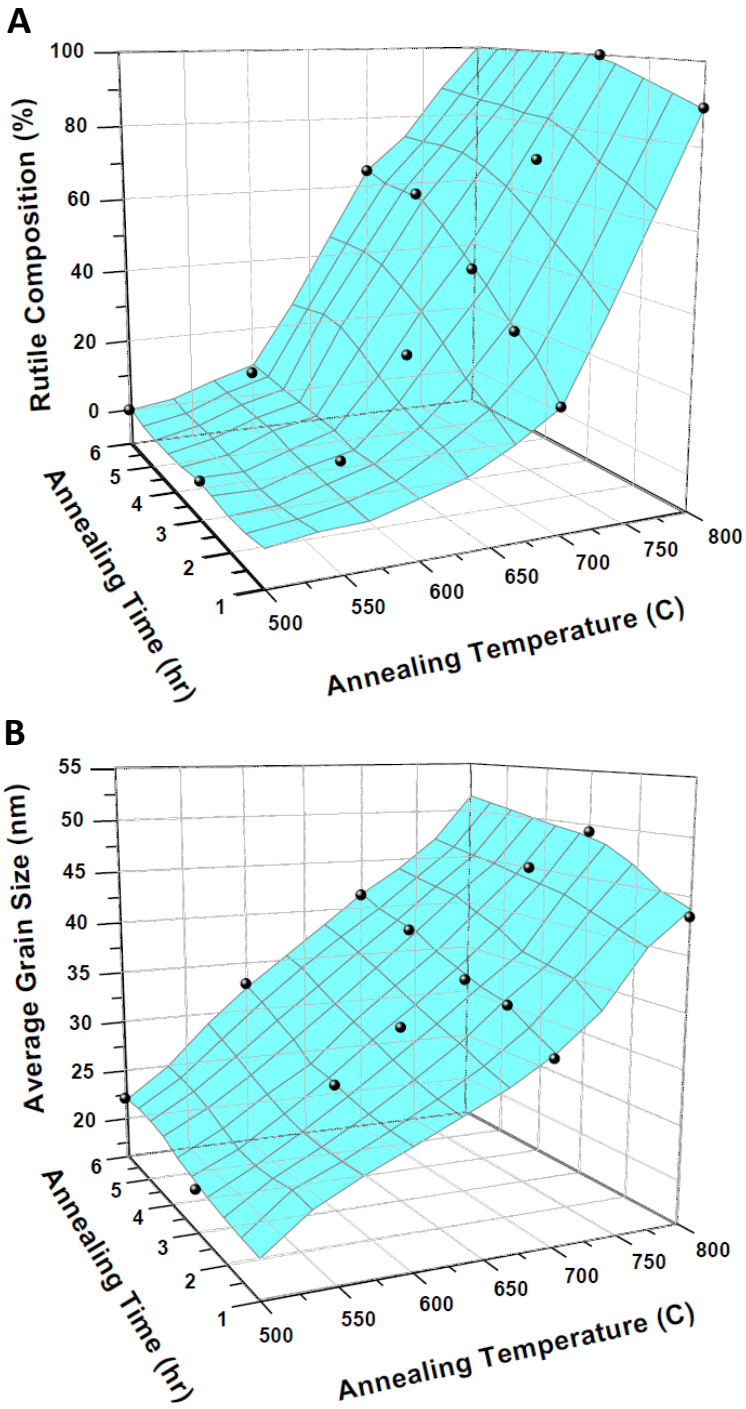

Figure 2-4: A) Rutile composition and B) average grain size 3D surface plots as a function of annealing temperature and time.

Diffuse reflectance analysis showed a strong correlation between band gap energy and crystal phase composition, seen in Figure 2-5. Identical to accepted values,[1],[6] the band gap energies of pure anatase (500-600 °C) and pure rutile phase (800 °C) TiO_2 nanofibers were found to be 3.21 and 3.02 eV, respectively. Additionally, band gap steadily increased with increasing anatase content, with values similar to existing publication,[41] as the mixed phase materials yielded intermediate band gap energies. As expected, no change band gap was observed as a function of average diameter since the Bohr radius of TiO_2 (~2 nm) is significantly smaller than the synthesized nanofiber size.[42],[43]

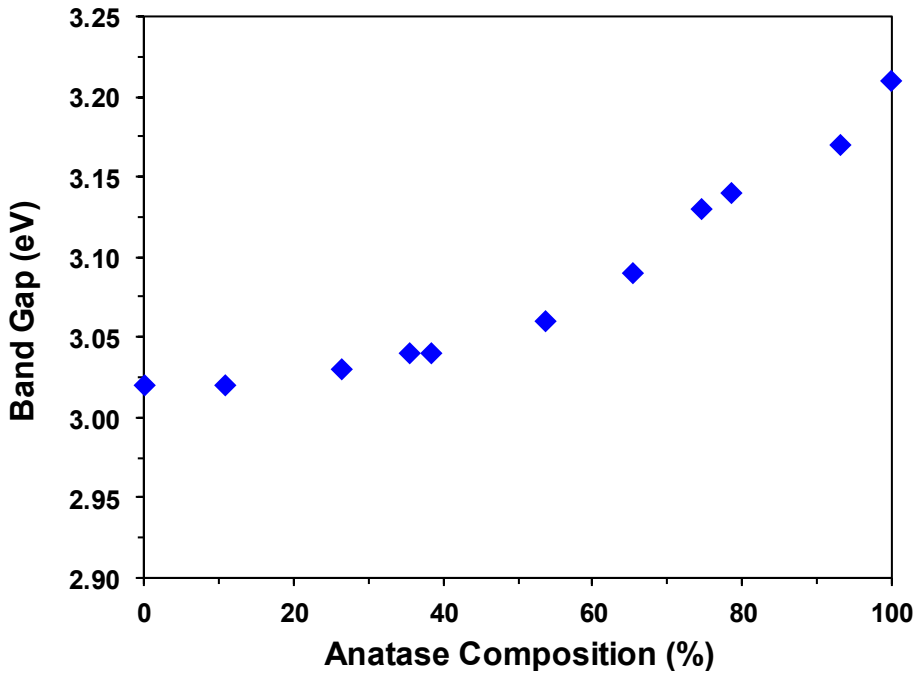

Figure 2-5: Band gap as a function of anatase composition of the TiO_2 nanofibers.

Based on measured zeta potential values (Figure 2-6), the pH-dependent surface chemical activity of the TiO_2 nanofibers were essentially invariant over the entire range of synthesis conditions and nearly identical to the behavior of commercially available Aeroxide® P25. The pH of the point of zero charge for all of the analyzed materials was ~5.2 (±0.1), which signifies negatively charged behavior in photoreactivity experiments that were conducted at pH 7. These results are comparable to earlier investigations[44]–[46] of Aeroxide® P25, having a pzc range of ~5-6. Additionally, texture coefficient calculations yielded random crystal orientation, which also correlates with the commercial TiO_2 photocatalyst[47],[48]. BET measurements yielded surface area values in the range of 10-20 m^2/g for the 33 nm sized TiO_2 nanofibers, yet these values were notably smaller than that of commercial Aeroxide® P25 (52 m^2/g).

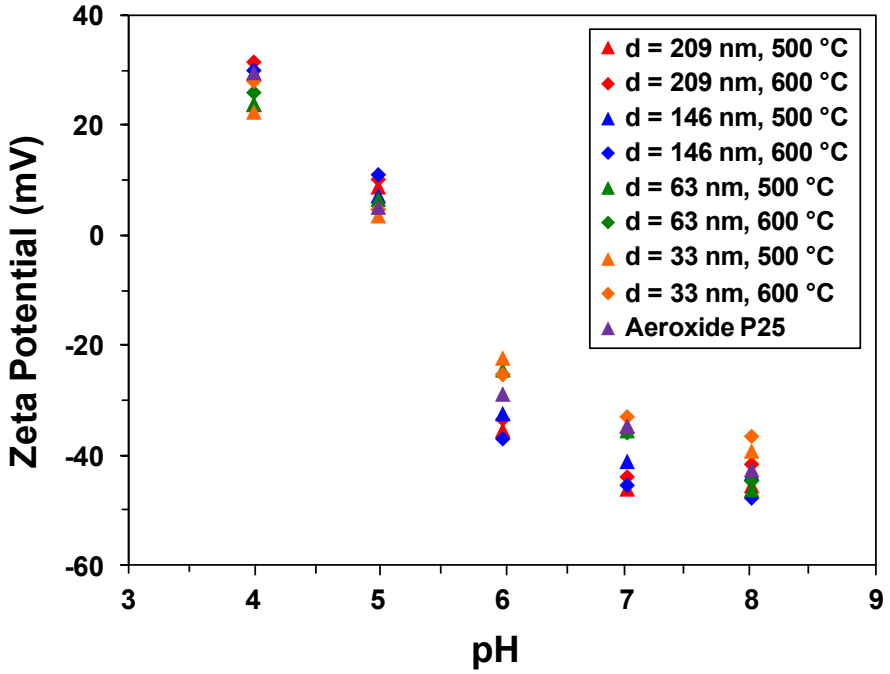

Figure 2-6: Zeta potential analysis of TiO_2 nanofibers at different diameters and Aeroxide® P25.

Table 2-1: Texture coefficient calculations of TiO_2 nanofibers at different annealing temperatures.

XRD Parameters			Annealing Temperature (C)					
Peak	2θ	Intensity	500	600	650	700	750	800
A (100)	25.281	100	1.10356	1.0559	1.06537	1.16743	1.07783	-
A (004)	37.800	29	0.81098	0.98127	0.90336	0.96135	0.91873	-
A (200)	48.049	35	1.08546	0.96283	1.03127	0.87122	1.00344	-
R (110)	27.446	100	-	-	1.32017	1.00862	1.24842	0.95141
R (102)	36.085	50	-	-	0.93935	0.82759	0.82595	1.08951
R (211)	54.322	60	-	-	0.74048	1.16379	0.92563	0.95908

Lastly, sedimentation studies were conducted with Aeroxide P25 and dispersed nanofibers (d = 33 nm) to analyze photocatalyst stability. As seen in Figure 2-7, normalized absorbance decreased relatively quickly with the commericial photocatalyst nanoparticles compared to the synthesized nanofibers, which indicates greater suspension instability (i.e., aggregation) for the nanoparticles relative to nanofibers.

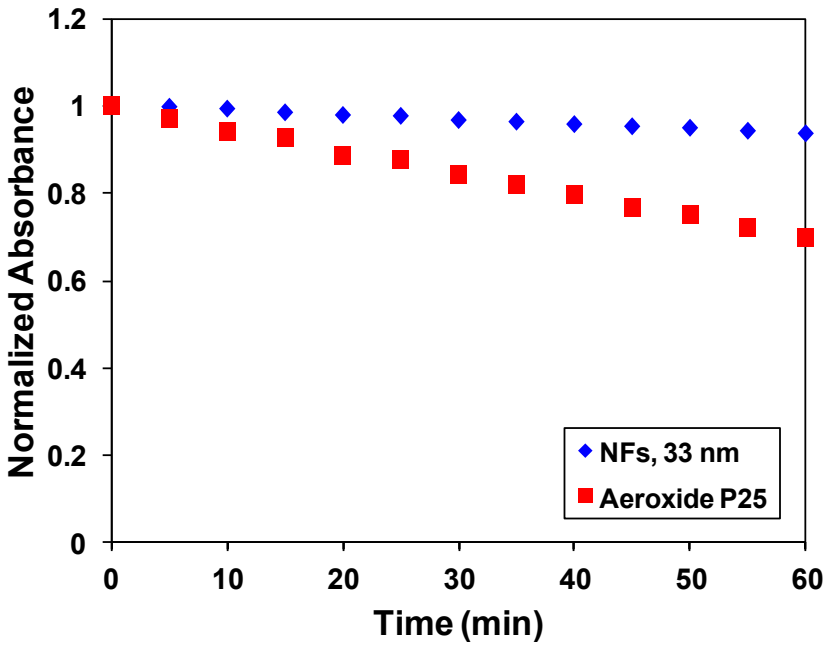

Figure 2-7: Sedimentation data for TiO_2 nanofibers and Aeroxide® P25 at pH 7. Absorbance was monitored at 400 nm in 0.1 g/L suspensions of each photocatalyst.

2.3.2 Photocatalysis of TiO_2 Nanofibers

Using the probe compound phenol, reactivity trends as a function of nanofiber diameter, phase, and grain size were developed. In all nanofiber systems, phenol followed exponential decay (Figure 2-8) and hence pseudo-first-order rate constants (i.e., k_{obs} values) were reported as a metric for TiO_2 nanofiber reactivity. Figure 2-9 shows average k_{obs} values (from triplicate analyses) for phenol decay as a function of annealing temperature for nanofibers with different diameters. For all annealing temperatures, nanofiber reactivity increased with decreasing diameter, consistent with a positive effect of increased reactive surface sites on photoreactivity. Additionally, a maximum peak in reactivity is observed at the annealing temperature of 650 °C for the two smallest diameter nanofibers (d = 33, 63 nm), indicating an optimal mixed phase composition. Altogether, the smallest sized fibers of d = 33 nm showed the greatest reactivity, with the 650 °C annealed nanofibers (k_{obs} = (9.7 ± 0.4) x 10^{-2} min^{-1}) outperforming Aeroxide® P25 TiO_2 nanoparticles (k_{obs} = (8.0 ± 0.1) x 10^{-2} min^{-1}) by 20 percent per unit mass of photocatalyst.

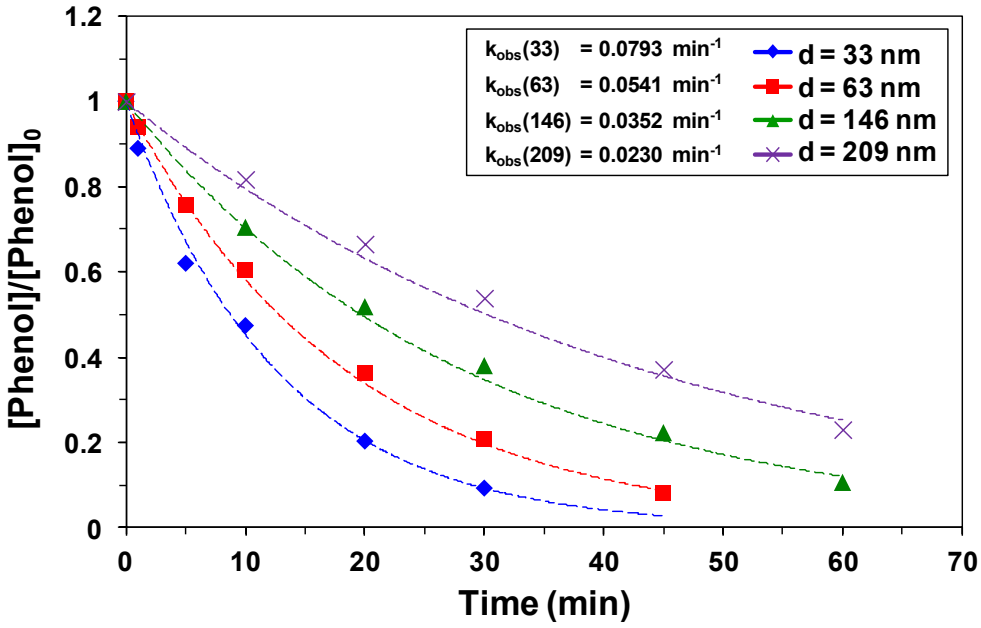

Figure 2-8: Representative first-order kinetics phenol decay curves during photocatalytic reaction with TiO_2 nanofibers, annealed at 500 °C for 3 hours.

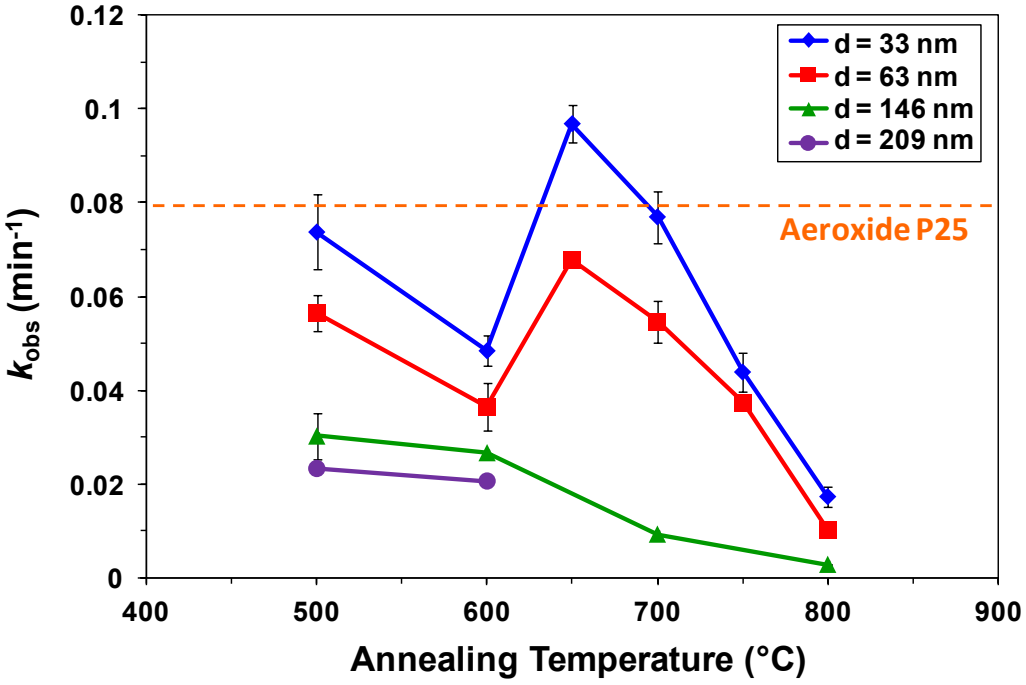

Figure 2-9: Average phenol decay rate constant as a function of annealing temperature for TiO_2 nanofibers with different diameters.

Results in Figure 2-9 indicate that available nanofiber surface area is a dominant control on photoreactivity, as expected for catalytic nanomaterials. In fact, the smallest nanofibers (d = 33 nm) possess a diameter on par with the particle size of P25 (~25 nm), consistent with their essentially equivalent per mass reactivity. Notably, however, BET measurements for these 33 nm nanofibers yield a specific surface area (~15 m^2/g) considerably smaller than that of commercial P25 (52 m^2/g), suggesting an advantage of nanofibers on the basis of surface-area-normalized rate constants (k_{SA} values). The roughly 3-fold greater k_{SA} value for nanofibers (i.e., d = 33 nm resulted in k_{SA} = 5.40 x 10^{-2} $L \cdot m^{-2} \cdot min^{-1}$, whereas P25 resulted in k_{SA} = 1.54 x 10^{-2} $L \cdot m^{-2} \cdot min^{-1}$) is speculated to be the result of more extensive aggregation of P25 nanoparticles in suspension (Figure 2-7), as has previously been invoked in instances where smaller nanomaterials exhibit less reactivity per unit surface area.[49] Because the pH-dependent surface charge on nanofibers (pH_{zpc} ~5.2 (±0.1)) was essentially identical to that of Aeroxide P25 (Figure 2-6), these differences in aggregation likely result from the different particle morphologies of P25 and nanofibers.

Because crystal phase and grain size are both dependent on annealing conditions, their respective influence on reactivity was explored at a fixed nanofiber diameter (d = 33 nm; Figure 2-10). Optimal reactivity was observed at a mixed phase composition [26/74 (±0.5) % rutile/anatase], a phase ratio comparable to that of P25.[50] As has been explained previously,[9],[51] the enhanced photocatalytic activity observed for a mixed rutile/anatase materials is most often attributed to an electron trapping mechanism. Specifically, energy levels in anatase act as an electron trap in mixed phase TiO_2, holding

photogenerated electrons until they encounter appropriate scavengers (e.g., O_2).[9],[51] Otherwise, rutile, as a solitary phase, acts as an inferior semiconductor in part from its high recombination rate. Photocatalytic activity was generally observed to increase with decreasing grain size, with the greatest reactivity observed for nanofibers prepared with an average grain size of 32 nm and at the optimal rutile/anatase ratio. These nanofiber properties could both be achieved via annealing at 650 °C for 3 hours.

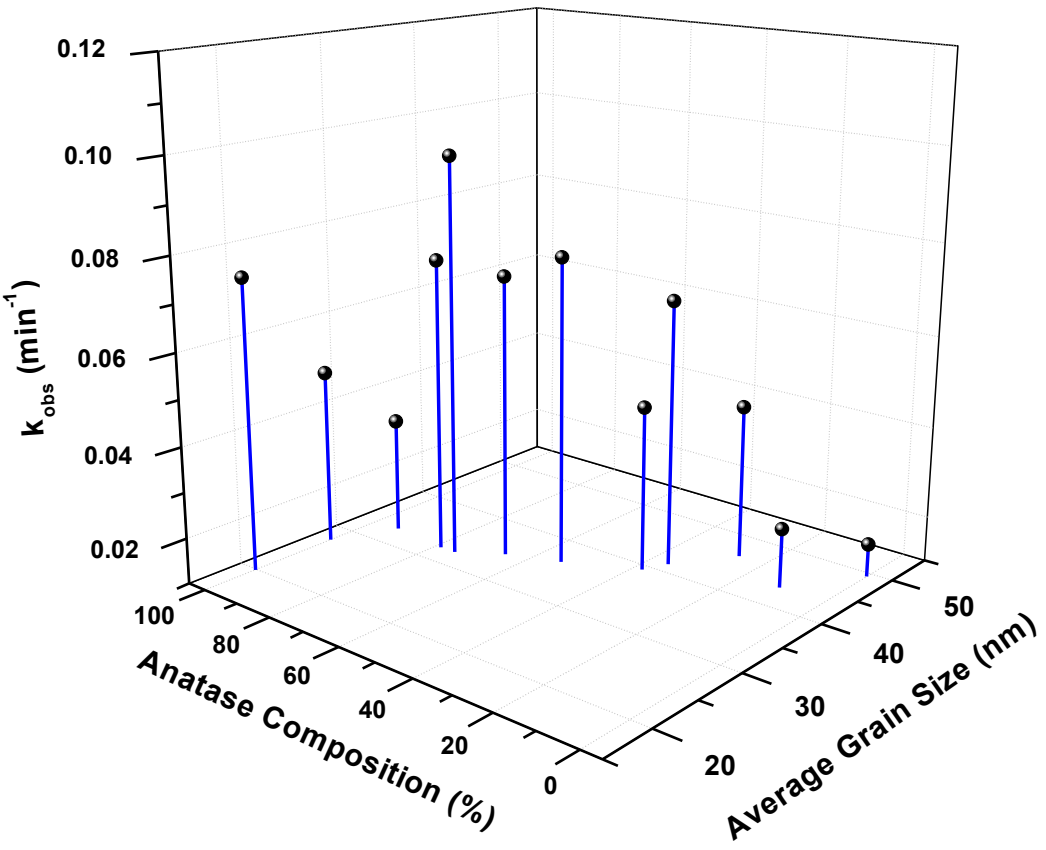

Figure 2-10: Average phenol decay rate constant as a function of the average grain size and rutile percent composition for TiO_2 nanofibers.

2.5 Conclusion

Growing interest in nanotechnology has led to significant advances in material synthesis, which in turn has produced a plethora of uniquely structured nanomaterials often touted as next-generation water treatment options. However, although there is little doubt as to the significant promise nanomaterials possess for water treatment applications, it is often unclear whether innovative, highly tailored nanostructures can ever be viable alternatives in practice.

This study attempted to bridge the existing gap between fundamentals and practice for electrospun TiO_2 nanofibers, an emerging synthesis route for nanomaterials given the high degree of tailoring it affords to nanomaterial structure and composition. We show that the performance of TiO_2 nanofiber photocatalyts is largely governed by the same material, physical, chemical and optical properties established for more traditional nanoparticle TiO_2 photocatalysts (e.g., P25). Accordingly, electrospun nanofibers are perhaps an ideal focal point for future technology development based on the advantages this approach provides, specifically the ability to fabricate nanomaterials with tunable properties that can be easily integrated into treatment as a reactive nanofiber networks, mats or coatings.

TiO_2 nanofibers with average diameters ranging from 209 to 33 nm, full spectrum of anatase and rutile composition and average grain size ranging from 19 to 49 nm were developed. Lastly, photoreactivity studies were performed to relate dimensional and morphological properties toward TiO_2 photo-oxidation. Results show the TiO_2 nanofibers with average diameter of 33 nm and anatase to rutile composition of 75/25 provided the

greatest phenol degradation, outperforming commerical Aeroxide® P25. The use of electrospun nanofibers present the potential for engineered nanofiber mat applications unobtainable by the suspension-driven commercial TiO_2 catalyst. However, the performance of these nanofibers needs to be explored over longer timescales and in flow through system more representative of their intended application platform.

2.6 References

[1] Carp, O.; Huisman, C. L.; Reller, A. Photoinduced Reactivity of Titanium Dioxide. *Progress in Solid State Chemistry* **2004**, *32*, 33–177.

[2] Bedinger, G. M. Titanium. In *United States Geological Survey 2011 Minerals Yearbook*; 2013.

[3] Hashimoto, K.; Irie, H.; Fujishima, A. TiO_2 Photocatalysis: A Historical Overview and Future Prospects. *Japanese Journal of Applied Physics* **2005**, *44*, 8269–8285.

[4] Honda, K.; Fujishima, A. Electrochemical Photolysis of Water at a Semiconductor Electrode. *Nature* **1972**, *238*, 37–38.

[5] Akpan, U. G.; Hameed, B. H. The Advancements in Sol–gel Method of Doped-TiO_2 Photocatalysts. *Applied Catalysis A: General* **2010**, *375*, 1–11.

[6] Chong, M. N.; Jin, B.; Chow, C. W. K.; Saint, C. Recent Developments in Photocatalytic Water Treatment Technology: A Review. *Water Research* **2010**, *44*, 2997–3027.

[7] Ye, M.; Vennerberg, D.; Lin, C.; Lin, Z. Nanostructured TiO_2 Architectures for Environmental and Energy Applications. *Journal of Nanoscience Letters* **2012**, *2:1*, 1–35.

[8] Raj, K. J. A.; Viswanathan, B. Effect of Surface Area , Pore Volume and Particle Size of P25 Titania on the Phase Transformation of Anatase to Rutile. *Indian Journal of Chemistry* **2009**, *48A*, 1378–1382.

[9] Hurum, D. C.; Agrios, A. G.; Gray, K. A.; Rajh, T.; Thurnauer, M. C. Explaining the Enhanced Photocatalytic Activity of Degussa P25 Mixed-Phase TiO_2 Using EPR. *Journal of Physical Chemistry B* **2003**, *107*, 4545–4549.

[10] Yuan, Z.; Su, B. Titanium Oxide Nanotubes, Nanofibers and Nanowires. *Colloids and Surfaces A: Physicochemical Engineering Aspect* **2004**, *241*, 173–183.

[11] Pokropivny, V. V.; Skorokhod, V. V. Classification of Nanostructures by Dimensionality and Concept of Surface Forms Engineering in Nanomaterial Science. *Materials Science and Engineering: C* **2007**, *27*, 990–993.

[12] Klabunde, K. J. *Nanoscale Materials in Chemistry*; John Wiley & Sons, Inc.: New York, 2001.

[13] Thavasi, V.; Singh, G.; Ramakrishna, S. Electrospun Nanofibers in Energy and Environmental Applications. *Energy & Environmental Science* **2008**, *1*, 205–221.

[14] Wang, X.; Choi, J.; Mitchell, D. R. G.; Truong, Y. B.; Kyratzis, I. L.; Caruso, R. A. Enhanced Photocatalytic Activity: Macroporous Electrospun Mats of Mesoporous Au/TiO_2 Nanofibers. *ChemCatChem* **2013**, *5*, 2646–2654.

[15] Zhang, X.; Xu, S.; Han, G. Fabrication and Photocatalytic Activity of TiO_2 Nanofiber Membrane. *Materials Letters* **2009**, *63*, 1761–1763.

[16] Gao, P.; Tai, M. H.; Sun, D. D. Hierarchical TiO_2 /V_2O_5 Multifunctional Membrane for Water Purification. *ChemPlusChem* **2013**, *78*, 1475–1482.

[17] Doh, S. J.; Kim, C.; Lee, S. G.; Lee, S. J.; Kim, H. Development of Photocatalytic TiO_2 Nanofibers by Electrospinning and Its Application to Degradation of Dye Pollutants. *Journal of Hazardous Materials* **2008**, *154*, 118–127.

[18] Lee, J.-S.; Lee, Y.-I.; Song, H.; Jang, D.-H.; Choa, Y.-H. Synthesis and Characterization of TiO_2 Nanowires with Controlled Porosity and Microstructure Using Electrospinning Method. *Current Applied Physics* **2011**, *11*, S210–S214.

[19] Li, D.; Xia, Y. Fabrication of Titania Nanofibers by Electrospinning. *Nano Letters* **2003**, *3*, 555–560.

[20] Watthanaarun, J.; Pavarajarn, V.; Supaphol, P. Titanium(IV) Oxide Nanofibers by Combined Sol–gel and Electrospinning Techniques: Preliminary Report on Effects of Preparation Conditions and Secondary Metal Dopant. *Science and Technology of Advanced Materials* **2005**, *6*, 240–245.

[21] Sarlak, N.; Nejad, M. A. F.; Shakhesi, S.; Shabani, K. Effects of Electrospinning Parameters on Titanium Dioxide Nanofibers Diameter and Morphology: An Investigation by Box–Wilson Central Composite Design (CCD). *Chemical Engineering Journal* **2012**, *210*, 410–416.

[22] Du, P.; Song, L.; Xiong, J.; Cao, H. Photocatalytic Degradation of Rhodamine B Using Electrospun TiO_2 and ZnO Nanofibers: A Comparative Study. *Journal of Materials Science* **2013**, *48*, 8386–8392.

[23] Di Camillo, D.; Ruggieri, F.; Santucci, S.; Lozzi, L. N-Doped TiO_2 Nanofibers Deposited by Electrospinning. *Journal of Physical Chemistry B* **2012**, *116*, 18427–18431.

[24] Choi, S. K.; Kim, S.; Lim, S. K.; Park, H. Photocatalytic Comparison of TiO_2 Nanoparticles and Electrospun TiO_2 Nanofibers: Effects of Mesoporosity and

Interparticle Charge Transfer. *Journal of Physical Chemistry C* **2010**, *114*, 16475–16480.

[25] Pan, C.; Dong, L.; Gu, Z.-Z. Surface Functionalization of Electrospun TiO_2 Nanofibers by Au Sputter Coating for Photocatalytic Applications. *International Journal of Applied Ceramic Technology* **2010**, *7*, 895–901.

[26] Zhang, R.; Wu, H.; Lin, D.; Pan, W. Preparation of Necklace-Structured TiO_2/SnO_2 Hybrid Nanofibers and Their Photocatalytic Activity. *Journal of the American Ceramic Society* **2009**, *92*, 2463–2466.

[27] Liu, S.; Liu, B.; Nakata, K.; Ochiai, T.; Murakami, T.; Fujishima, A. Electrospinning Preparation and Photocatalytic Activity of Porous TiO_2 Nanofibers. *Journal of Nanomaterials* **2012**, *2012*, 1–5.

[28] Ding, Z.; Lu, G. Q.; Greenfield, P. F. Role of the Crystallite Phase of TiO_2 in Heterogeneous Photocatalysis for Phenol Oxidation in Water. **2000**, 4815–4820.

[29] Hosseini, S. N.; Borghei, S. M.; Vossoughi, M.; Taghavinia, N. Immobilization of TiO_2 on Perlite Granules for Photocatalytic Degradation of Phenol. *Applied Catalysis B: Environmental* **2007**, *74*, 53–62.

[30] Ilican, S.; Caglar, M.; Caglar, Y. Determination of the Thickness and Optical Constants of Transparent Indium-Doped ZnO Thin Films by the Envelope Method. *Materials Science-Poland* **2007**, *25*, 709–718.

[31] Liu, G. J.; Zhang, X. R.; McWilliams, L.; Talley, J. W.; Neal, C. R. Influence of Ionic Strength, Electrolyte Type, and NOM on As(V) Adsorption onto TiO_2. *Journal of environmental science and health. Part A, Toxic/hazardous substances & environmental engineering* **2008**, *43*, 430–6.

[32] Boncagni, N. T.; Otaegui, J. M.; Warner, E.; Curran, T.; Marta, M.; Cortalezzi, F. D. E. Exchange of TiO_2 Nanoparticles between Streams and Streambeds. *Environmental Science & Technology* **2009**, *43*, 7699–7705.

[33] Tunc, I.; Bruns, M.; Gliemann, H.; Grunze, M.; Koelsch, P. Bandgap Determination and Charge Separation in $Ag@TiO_2$ Core Shell Nanoparticle Films. *Surface and Interface Analysis* **2010**, *42*, 835–841.

[34] Pal, M.; Pal, U.; Jiménez, J. M. G. Y.; Pérez-Rodríguez, F. Effects of Crystallization and Dopant Concentration on the Emission Behavior of TiO_2:Eu Nanophosphors. *Nanoscale Research Letters* **2012**, *7*, 1.

[35] Yu, K.; Lee, G. Decomposition of Gas-Phase Toluene by the Combination of Ozone and Photocatalytic Oxidation Process (TiO_2/UV, TiO_2/UV/O_3, and UV/O_3). *Applied Catalysis B: Environmental* **2007**, *75*, 29–38.

[36] Tôrres, A. R.; Azevedo, E. B.; Resende, N. S.; Dezotti, M. A Comparison between Bulk and Supported TiO_2 Photocatalysts in the Degradation of Formic Acid. *Brazilian Journal of Chemical Engineering* **2007**, *24*, 185–192.

[37] Sopyan, I.; Hafizah, N.; Jamal, P. Immobilization of TiO_2 with Cement : Photocatalytic Degradation of Phenol and Its Kinetic Studies. *Indian Journal of Chemical Technology* **2011**, *18*, 263–270.

[38] Guo, Z.; Ma, R.; Li, G. Degradation of Phenol by Nanomaterial TiO_2 in Wastewater. *Chemical Engineering Journal* **2006**, *119*, 55–59.

[39] Araña, J.; Doña-Rodríguez, J. M.; Portillo-Carrizo, D.; Fernández-Rodríguez, C.; Pérez-Peña, J.; González Díaz, O.; Navío, J. a.; Macías, M. Photocatalytic Degradation of Phenolic Compounds with New TiO_2 Catalysts. *Applied Catalysis B: Environmental* **2010**, *100*, 346–354.

[40] Parra, S.; Olivero, J.; Pacheco, L.; Pulgarin, C. Structural Properties and Photoreactivity Relationships of Substituted Phenols in TiO_2 Suspensions. *Applied Catalysis B: Environmental* **2003**, *43*, 293–301.

[41] Toyoda, T.; Tsuboya, I. Apparent Band-Gap Energies of Mixed TiO_2 Nanocrystals with Anatase and Rutile Structures Characterized with Photoacoustic Spectroscopy. *Review of Scientific Instruments* **2003**, *74*, 782.

[42] Yang, X. H.; Li, Z.; Liu, G.; Xing, J.; Sun, C.; Yang, H. G.; Li, C. Ultra-Thin Anatase TiO_2 Nanosheets Dominated with {001} Facets: Thickness-Controlled Synthesis, Growth Mechanism and Water-Splitting Properties. *CrystEngComm* **2011**, *13*, 1378–1383.

[43] Pradhan, S.; Ghosh, D.; Chen, S. Janus Nanostructures Based on Au-TiO_2 Heterodimers and Their Photocatalytic Activity in the Oxidation of Methanol. *ACS Applied Materials & Interfacespplied materials & interfaces* **2009**, *1*, 2060–2065.

[44] Chong, M. N.; Lei, S.; Jin, B.; Saint, C.; Chow, C. W. K. Optimisation of an Annular Photoreactor Process for Degradation of Congo Red Using a Newly Synthesized Titania Impregnated Kaolinite Nano-Photocatalyst. *Separation and Purification Technology* **2009**, *67*, 355–363.

[45] Ko, K. H.; Lee, Y. C.; Jung, Y. J. Enhanced Efficiency of Dye-Sensitized TiO_2 Solar Cells (DSSC) by Doping of Metal Ions. *Journal of Colloid and Interface Science* **2005**, *283*, 482–487.

[46] Qamar, M.; Muneer, M. A Comparative Photocatalytic Activity of Titanium Dioxide and Zinc Oxide by Investigating the Degradation of Vanillin. *Desalination* **2009**, *249*, 535–540.

[47] Tirosh, S.; Dittrich, T.; Ofir, A.; Grinis, L.; Zaban, A. Influence of Ordering in Porous TiO_2 Layers on Electron Diffusion. *Journal of Physical Chemistry B Letters* **2006**, *110*, 16165–16168.

[48] Ting, C.; Chen, S.; Liu, D. Preferential Growth of Thin Rutile TiO_2 Films upon Thermal Oxidation of Sputtered Ti Films. *Thin Solid Films* **2002**, *402*, 290–295.

[49] Cwiertny, D. M.; Handler, R. M.; Schaefer, M. V.; Grassian, V. H.; Scherer, M. M. Interpreting Nanoscale Size-Effects in Aggregated Fe-Oxide Suspensions: Reaction of Fe(II) with Goethite. *Geochimica et Cosmochimica Acta* **2008**, *72*, 1365–1380.

[50] Ohtani, B.; Prieto-Mahaney, O. O.; Li, D.; Abe, R. What Is Degussa (Evonik) P25? Crystalline Composition Analysis, Reconstruction from Isolated Pure Particles and Photocatalytic Activity Test. *Journal of Photochemistry and Photobiology A: Chemistry* **2010**, *216*, 179–182.

[51] Scanlon, D. O.; Dunnill, C. W.; Buckeridge, J.; Shevlin, S. a; Logsdail, A. J.; Woodley, S. M.; Catlow, C. R. a; Powell, M. J.; Palgrave, R. G.; Parkin, I. P.; et al. Band Alignment of Rutile and Anatase TiO_2. *Nature Materials* **2013**, *12*, 798–801.

Chapter 3: Synthesis and Optimization of Ag-TiO_2 Composite Nanofibers

3.1 Abstract

In this work, Ag-TiO_2 composite nanofibers were developed through the electrospinning process while characterizing their dimensional, morphological and optical properties to assess the effects of Ag co-catalysts. Additionally, their photocatalytic activity was tested toward phenol as a model pollutant. Characterization revealed a slight increase in nanofiber diameter, inhibition of anatase-to-rutile phase transformation and a decrease in band gap from 3.21 down to 2.79 eV due to the presence of bulk–embedded Ag nanoparticles. The reactivity of 0.5 at.% Ag-TiO_2 nanofibers was the greatest, outperforming both unmodified TiO_2 electrospun nanofibers and commercially available TiO_2 Aeroxide® P25 by a factor of ~3.

The high reactivity of the low content Ag-TiO_2 nanofibers can be attributed to the addition of electron traps, which provide efficient carrier separation and, therefore, decreased recombination. However, further increase in Ag content led to lower photoreactivity, most likely due to the growth of the Ag nanoparticles, which suggests an optimal size of 2 to 3 nm for the Ag nanoparticles at 0.5 at.% provided the greatest photoreactivity. Ag-TiO_2 nanofibers show great promise as innovative and highly performing nanomaterials for future nanotechnology-based treatment systems, particularly when the photoreactivity demonstrate herein is used in synergy with the established antimicrobial activity of nano-Ag.

3.2 Introduction

3.2.1 TiO_2 Photocatalysts

TiO_2 is an ideal semiconductor of choice for numerous applications because it is chemically and biologically inert, photocatalytically stable, and relatively easy to produce and to use.[1],[2] Accordingly, TiO_2 has been widely used in dye-sensitized solar cells, gas sensors, biomaterials, and, most notably, as a photocatalyst because of its high photoactivity and photoefficiency in the UV spectrum.[1] In the sphere of environmental remediation, TiO_2 has been significantly studied and manipulated for decades as a source of reactive oxygen species (ROS), such as hydroxyl radical ($^{\bullet}OH$), for the degradation of aquatic micropollutants as an advanced oxidation process (AOP).[3] Prior research has established that its photocatalytic properties are influenced by physicochemical variables, such as size, pore volume, surface area, and crystallinity.[4] Collectively, the physical parameters of TiO_2 greatly affect the photoelectrochemical phenomena responsible for semiconductor's photocatalytic activity.

In light of the many different applications of TiO_2 (i.e. photooxidation, water splitting, solar cells) due to its attractive features, including its non-toxicity, great chemical and thermal stability, and above all its high photocatalytic efficiency,[2] there is a still a large force in research to further enhance TiO_2 photoactivity. For successful photocatalytic transformation, energy transfer must be efficient during the separation of the electron-hole pairs, the carrier transport to surface active sites and the actual surface chemical reactions.[5] Modifications of TiO_2 nanostructures via the introduction of metal and nonmetal additives have been widely reported in efforts to enhance the performance

of the photocatalyst. Various methods of TiO_2 modifications have been explored to improve photoactivity, especially towards water treatment applications.

3.2.2 Modified TiO_2 Photocatalysts

Modification of TiO_2 (i.e. crystal lattice, co-catalysts, composite materials) has been generalized into the term doping. Doping is the intentional introduction of impurities or defects into a pure semiconductor for the manipulation of the material's electrical properties.[6] Adding impurities can increase the quantity of electrons or holes, also known as charge carriers, in the semiconductor. P-type semiconductors contain an excess of holes, while n-type semiconductors contain an excess of electrons. The property changes depend on the semiconductor material, the dopant material and the dopant content. There are three main mechanisms in which doping can enhance the performance of TiO_2: band gap narrowing, surface plasmon resonance, and electron trapping. Band gap narrowing involves defect formation via Ti or O atom replacement and electron configurations with that of the dopants, narrowing the band between the conduction and valence band and causing shorter pathways for electron movements. The shorter energy band will then have implications on the wavelength requirement for electron excitation, where light with a lower energy demand can be used to induce photoactivation. Surface plamon resonance involves the use of noble metals, primarily Au and Ag, where the surface electrons of the noble metals oscillate due to the frequency from incident photons.[7] The stimulation of resonant oscillation would likely enhance surface electron excitation.

Lastly, electron trapping involves the retaining of electrons in the irregularities or defects in the material's morphology during photoexcitation. This will induce electrons movement within the material towards the conduction band while remaining near the traps, keeping electron-hole separation and preventing recombination.[8] After the electron-hole split during photoexcitation, the electron will move within the material towards either shallow or deep traps. Some electrons will migrate towards deep traps, where relatively high activation energy (~1 to 3 meV) traps keep the electrons stable to the conduction band, while other electron migrate towards lower activation energy (< 1 meV) shallow traps, where they are likely to undergo trap-to-trap hopping towards the conduction band until they reach a deep trap. The electron trapping provides transport of the electrons towards the conduction band and minimizing recombination due to the activation energy required to remove the electrons from the traps.[8]

a. Nonmetal-doped TiO_2

Despite the reputation of TiO_2 as a great photocatalyst, it is still restricted by its relatively large band gap (3.2 eV). Light necessary to excite the electrons within the semi-conductor must be of a wavelength of around ~400 nm or smaller, right at the transition of UV to visible light, in order to achieve photoactivation. Considering that just under 5% of total solar irradiation (sunlight that reaches the earth's surface) is UV light, UV lamps are necessary to initiate photoactivation of TiO_2 for efficient photooxidation. Nonmetal doping of TiO_2, which involves the addition of nonmetals such as C, N, and S into the photocatalyst, has been heavily reported to increase photoactivity via band gap

reduction[9] by the shifting of the valence band energy level. Such reduction not only enhances UV reactivity, but also has the potential to facilitate photoactivation using visible light.

Nitrogen has shown to be the most promising of the nonmetal dopants for visible light active photocatalysis. Gombac et al.[10] reported on N-doped TiO_2 nanopowders synthesized via sol-gel method utilizing HNO_3 as the N source. Their doped TiO_2 was synthesized having 100% anatase crystal phase, crystallite size of 13 nm, and surface area around 85 m^2/g. Photoreactivity studies against methyl orange showed enhanced performance of N-doped TiO_2 compared to bare synthesized powder under visible light irradiation. Liu et al.[11] synthesized TiO_2 via hydrothermal method and doped the material by annealing in an ammonia atmosphere. Based on photoreactions with rhodamine B under UV and visible light irradiation, they reported that N-doping increased the reactivity of bare titania.

Cong et al.[12] worked on TiO_2 prepared by microemulsion-hydrothermal method and doped with various N sources, including triethylamine, urea, thiourea, and hydrazine hydrate, at different dopant loadings. Their findings resulted in reduction of the photocatalysts band gap from 3.2 eV down to 2.7 eV for the highest content doping. Based on photoreactivity studies against rhodamine B and 2,4-dichlorophenol under both UV and visible light irradiation, N-doped TiO_2 performed better than its bare counterpart, where triethylamine with a N:Ti mole ratio of 2:1 provided the greatest organic decomposition. Nolan et al.[13] reported sol-gel synthesis of N-doped TiO_2 using 1,3-diaminopropane as the N source. Diffuse reflectance data showed visible light absorption,

but calcinations of the N-doped TiO_2 had a strong effect on the formation of the rutile phase. Photoreactivity of methylene blue showed enhancement due to N-doping, but reactivity studies also showed inhibition at higher temperatures most likely due to the greater rutile content.

Yang et al.[14] synthesized N-doped TiO_2 via solvothermal method using ethylenediamine as the N source. N-doped TiO_2 yielded crystallite size ranging from 8-16 nm and showed great visible light absorbance, as well as reducing the bang gap energy down to 3.0 eV. N-doped TiO_2 showed considerably greater photoactivity than the bare TiO_2 photocatalyst based on photooxidation of methylene blue and methyl orange under visible light irradiation. Gai et al.[15] reported on TiO_2 nanorods synthesized via hydrolysis and doped by the addition of hydrazine, followed by ultrasonication and autoclaving. N-doping by hydrazine led to reduced anatase content, reduced surface area, and reduced band gap to 2.9 eV. Photoreactivity studies towards methyl orange and 4-chlorphenol resulted in greater performance of the N-doped TiO_2 nanorods at all levels of dopant content. Buzby et al.[16] investigated N-doped TiO_2 nanoparticles synthesized via plasma-assisted metal organic chemical vapor deposition. NH_3 gas was used as the N source, since initial experiments with N_2 and NO gases were unsuccessful in doping the nanoparticles with N. Characterization showed that N-doping had no effect on the crystallite size (roughly 20 nm in size) and the crystal phase was anatse rich. Photoreactivity against 2-chlorophenol showed that N-doping improved the performance of the TiO_2, where photocatalytic kinetics increased with increasing N content.

Of all the nonmetal anions, N has shown to be the best nonmetal dopant towards enhancing TiO_2 photoreactivity. Based on these reports,[10]–[16] N-doping has the potential to increase on TiO2 observed rate constant (k_{obs}) by a factor of 9 and surface area-normalized rate constant (k_{SA}) by a factor of 6. Band gap reduction was the prominent mechanism caused by N-doping, as reports indicated band gap narrowing due to valence band movement leading to band gap energies as low as 2.6 eV.

b. Transition Metal-doped TiO_2

Similar to nonmetal doping of TiO_2, transition metal doping has also seen its fair share of research for their contribution in band gap reduction. Similar to nonmetals replacing O atoms, transition metals, such as Fe, Zn, and Co, create impurities near the conduction band by replacing Ti atoms in the crystal lattice to facilitate a conduction band energy shift and reduce the band gap. Kumbhar et al.[17] studied Fe-doped TiO_2 nanoparticles synthesized via modified sol-gel method. Diffuse reflectance analysis showed a sharp red shift in the band gap transition, attributed to the incorporation of Fe(III) ions in the titania matrix. XRD characterization resulted in crystallized anatase crystal phase of the photocatalysts, as well as the larger agglomerations of small TiO_2 particles due to lattice distortion cause by the Fe(III) ions. Photoreactivity studies towards the dye pollutant sulforhodamine-B under visible light irradiation resulted in moderate degradation with Fe-doped TiO_2 but no degradation whatsoever with unmodified TiO_2.

Luu et al.[18] worked on Fe-doped TiO_2 photocatalysts synthesized via sol-gel method. XRD analysis showed an increase in rutile content with the incorporation of Fe,

from 7% to a range of 18-40%, as well as a slight decrease in crystallite size, from 30 nm for the unmodified TiO_2 to as low as 19.5 nm for the 2 mol.% doped TiO_2. Diffuse reflectance analysis showed a red shift in the light absorption of the Fe-doped TiO_2 nanoparticles. The red shift was more prominent with increasing dopant content, resulting in a decreassed band gap from 3.20 eV to as low as 2.67 eV. Additionally, BET characterization showed that Fe doping decreased the surface area of the photocatalyst from 45 m^2/g to a range of 10-43 m^2/g. Photoreactivity studies towards p-xylene showed that Fe doping increased degradation of the pollutant in the presence of UV and LED light.

Nguyen et al.[19] reported on Fe-doped TiO_2 photocatalysts synthesized via hydrothermal method. HR-TEM imagery indicated that morphology of the Fe-doped TiO_2 was similar to that of the unmodified TiO_2. XRD analysis resulted in only crystalline anatase phase for both doped and unmodified TiO_2. UV-Vis spectra of the Fe-doped TiO_2 show a more pronounced red shift and an increased absorbance of the visible range with increased Fe dopant content. The authors attributed this to the formation of dopant energy levels within the band gap of TiO_2, causing charge-transfer transitions between the Fe ions and the TiO_2 conduction band, and thus effectively causing a red shift in the band edge adsorption threshold. Photoreactivity studies towards methylene orange showed increased performance of all the Fe-doped TiO_2 samples under sunlight and halogen lamp irradiation, with the 0.3 wt.% Fe content level yielding the greatest reactivity.

Deng et al.[20] studied TiO_2 nanopowders synthesized via sol-gel method doped with various levels of Mn (0.1-12 at.%). XRD characterization determined that both the unmodified and doped powders were crystallized in pure anatase phase. Additionally, average grain size slightly decreased with increasing Mn content, from 7.5 nm of the pure TiO_2 to 6.8 nm for the highest doping of 12 at.%, which was confirmed by TEM imaging. Diffuse reflectance analysis showed a large red shift of the Mn-doped TiO_2 as well as increased absorption of light in the visible and even infrared spectral regions. Photoreactivity studies towards methylene blue resulted in greater performance of all the Mn-doped TiO_2 over the unmodified TiO_2, with the greatest reactivity resulting from the 0.2 at.% Mn-doped TiO_2 nanopowder.

Liu et al.[21] reported on Zn-doped TiO_2 synthesized via sol-gel and solid phase reaction methods. TEM images showed that the sol-gel method had little influence on the particle size (20-30 nm), while the solid phase reaction method greatly reduced the particle size to about 10 nm. XRD characterization showed no effect on the crystal phase of the TiO_2 nanoparticles by either method. Photoreactivity studies towards Rhodamine B showed little change in performance from the sol-gel synthesized Zn-doped TiO_2, but increased performance for the solid phase reaction method synthesized Zn-doped TiO_2, where optimal performance was observed at 0.5 mol.% Zn doping and an annealing temperature of 500 °C.

Despite the manipulation of band gap energy, some publications have reported inhibition of photoreactivity due to transition metal doping. Colmenares et al.[22] worked on TiO_2 photocatalysts doped with Fe, Zn and Zr, as well as some noble metals. BET

analysis showed increase in surface area due to transition metal doping. Diffuse reflectance characterization showed no reduction of band gap for the Zn- and Zr-doped TiO_2, but a slight decrease in band gap down to 3.15 eV was observed in the Fe-doped TiO_2. XRD analysis showed no significant change in crystal phase (100% anatase) and a slight decrease in crystallite size from 28 nm to an average of 24 nm. Photoreactivity studies toward 2-propanol showed no improvement in performance for the Zn-doped TiO_2, and also decreased performance for the Fe- and Zr- doped TiO_2 nanoparticles.

Di Paola et al.[23] reported their findings of TiO_2 nanoparticles doped with various transition metals (Co, Cr, Cu, Fe, Mo, V, and W) at various content levels (0.3-5 mol. %) via wet impregnation method. XRD analysis revealed that transition metal doping had little effect on the crystal phase, as the anatase and rutile diffraction patterns had minimal change compared to that of the unmodified TiO_2. BET characterization showed little to no reduction of the surface area of the all photocatalysts. Diffuse reflectance analysis revealed a red shift in the band gap transition, resulting in increased light absorption of the doped TiO_2. Photooxidation studies towards 4-nitrophenol showed that all the transition metal doped-TiO_2 nanoparticles (excluding W-doped TiO_2) yielded reduced photoactivity, where performance decreased with increasing dopant content. They investigated electron-hole recombination kinetics via femtosecond pump-probe diffuse reflectance spectroscopy and observed increased second-order recombination rate constants in all the transition metal-doped photocatalysts. The authors concluded that although the presence of these transition metal dopants can shift the energy levels of the band edges, they might be isolated far from the surface with little chance of transferring

trapped charge carriers to the reaction interface, causing the metal ions to act more like recombination centers than trap sites.[24]

Although transition metals have shown enhancement of photocatalytic reactivty in some instances, significant reports show inhibition of reactivity in the presence of these dopants. Findings show that despite decreasing the band gap, transition metal ions in the TiO_2 interfere with the electron-hole separation and increase recombination kinetics.[23] Figure 3-1 shows the range kinetic rate constants of the transition metal-doped TiO_2 from the review[22]–[28] normalized to their respective unmodified TiO_2 counterpart. As seen with k_{obs} and k_{SA}, photocatalytic kinetics in both cases were reduced significantly due to the addition of transition metal dopants, with some results showing doped TiO_2 materials yielding reactivity as low as 10% of the unmodified TiO_2.

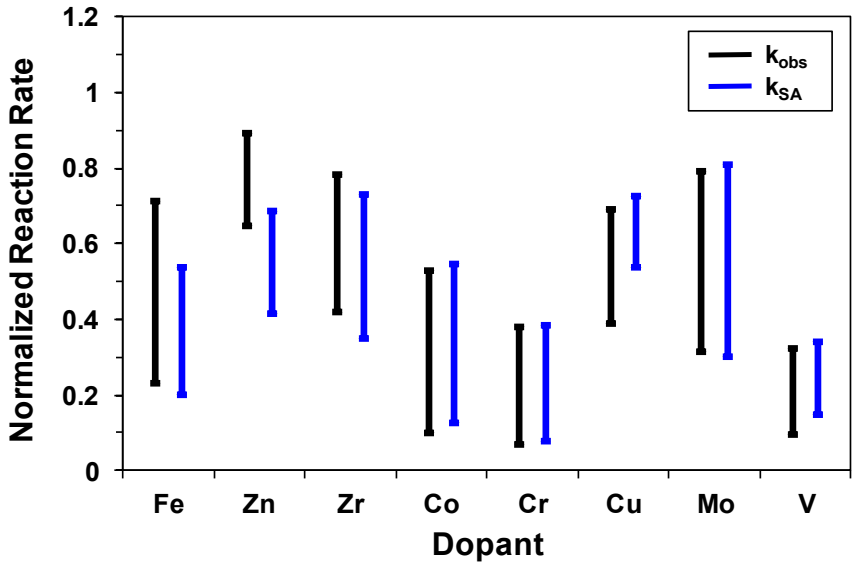

Figure 3-1: Normalized k_{obs} and k_{SA} of transition metal-doped TiO_2[22]–[28].

d. Rare Earth Metal-doped TiO_2

There has also been some work on incorporating rare earth metals into TiO_2 to improve photoactivity. Although there is very limited work on rare earth metal-doped TiO_2, such few reports in literature have shown that rare earths behave as electron sinks, enhancing charge-transfer efficiency. Xu et al.[29] reported on TiO_2 photocatalysts doped with La, Ce, Er, Pr, Gd, Nd and Sm via sol-gel method. XRD and BET characterization of the doped materials showed no change in crystal phase (100% anatase), a slight decrease in particle size from 20 to a range of 13-17 nm, and a slight increase in surface area from 36 m^2/g to a range of 37-45 m^2/g. Diffuse reflectance analysis observed a red shift in the band gap transition of the rare earth metal-doped TiO_2 and increased light absorbance with increasing rare earth content. Photoreactivity studies based on nitrate degradation were performed with Sm- and Gd-doped TiO_2, which showed that rare earth metal-doped TiO_2 at all content loadings outperformed unmodified TiO_2 nanoparticles.

Stengl et al.[30] studied the photocatalytic activity of TiO_2 nanoparticles doped with Nd, Ce^{3+}, Ce^{4+}, Pr, Sm, Gd, Eu, Dy, and Ly. BET analysis showed that in majority, the rare earth metal dopant increased the surface area and pore volume of the doped nanoparticles. Additionally, band gap reduction was observed, where the presence of rare earths slightly lowered the band gap to an average of 3.10 eV, while the more effective dopants lowered the band gap to 2.7 eV. Photoactivity studies towards Orange II dye at different wavelengths within the UV and visible light range showed improved reactivity of the rare earth metal-doped TiO_2 over unmodified TiO_2.

Rare earth dopants have shown to provide enhance photoreactivity of TiO_2 due to increased carrier traps, but don't offer as great of photocatalytic enhancement as other additives. Figure 3-2 provides the normalized rate constants of the rare earth metal-doped TiO_2 based on reports.[29],[30] where average photocatalytic activity was improved by factor of ~2.

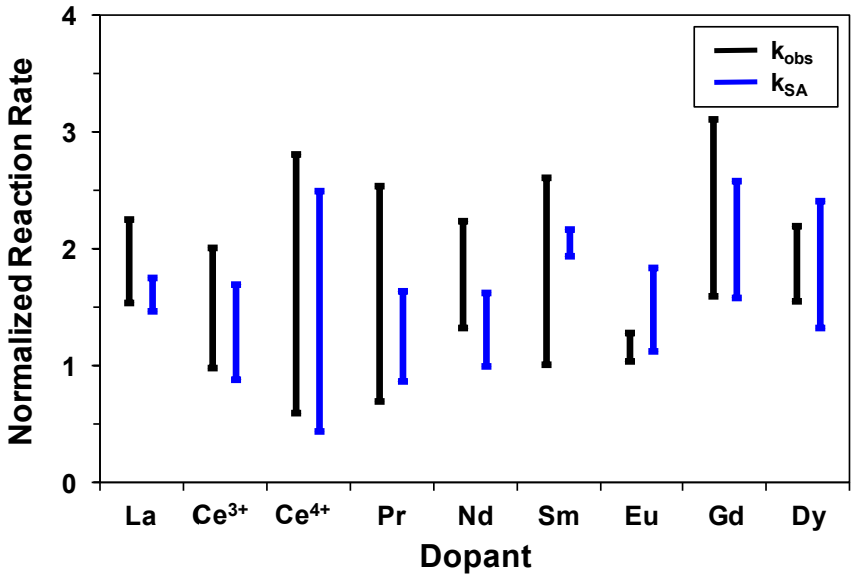

Figure 3-2: Normalized k_{obs} and k_{SA} of rare earth metal-doped TiO_2[29],[30].

c. Noble Metal-doped TiO_2

Noble metals are considered the most popular of additives used with TiO_2 due to the vast reports of their improvement towards photodegradation of pollutants. Noble metals have proven to be effective co-catalysts for enhancing TiO_2 photoreactivity because they can function as electron sinks. In all semiconductors, the mechanism of electron excitation from the valence band to the conduction band can also lead to

potential recombination of the electron and hole, which lowers photoefficiency. Noble metal co-catalysts including gold (Au), silver (Ag), palladium (Pd), and platinum (Pt) serve as electron traps near the conduction band to promote carrier transfer and prevent recombination with the valence band holes, thereby facilitating electron-hole separation and enhancing TiO_2 photoactivity.[31] Other mechanisms for the enhanced reactivity of noble metal-incorporated TiO_2 include extending the light absorption of the semiconductor into the visible range, enhancing surface electron excitation by plasmon resonances excited by visible light, and modifying the surface properties of photocatalysts.[32] With all of these benefits, noble metal-doped TiO_2 has been heavily investigated by researchers. Colmenares et al.[22] reported on sol-gel synthesized TiO_2 doped with Ag, Pd, and Pt. The synthesis of the doped TiO_2 was carried out by two methods: ultrasonic irradiation and magnetic stirring. The addition of noble metals had little effect on band gap energy (3.1-3.2 eV) or crystal phase (100% anatase). Additonally, noble metal doping slightly decreased the crystallite size from 28 nm to a range of 21-26 nm. Based on photoreactivity studies with 2-propanol, the doped TiO_2 with Ag, Pt and Pd all outperformed unmodified TiO_2 nanoparticles in either synthesis process, where the magnetic stirring synthesis yielded greater performance.

Moonsiri et al.[33] studied Pt- and Ag-doped TiO_2 via sol-gel method. Characterization analysis revealed that the presence of noble metals did not significantly affect crystal phase or surface area, but did slightly decrease the crystallite size of the TiO_2 from around 12 nm to an average of 10 nm. Both the addition of Pt and Ag improved the photocatalytic reactivity of 4-chlorophenol, where the highest reactivity

was obtained from 1.0 wt.% Pt-TiO_2 and 0.5 wt.% Ag-TiO_2. Loganathan et al.[34] investigated sol-gel synthesized TiO_2 nanoparticles doped with Ag, Au and Pt. XRD analysis showed that the dopants had no effect on the crystal phase, which was pure anatase for all 3 noble metals and content levels. Crystallite size did increase slightly with the addition of the dopant, increasing from 8 nm for the unmodified TiO_2 to around 12, 15 and 20 nm for Ag, Pt and Au, respectively. Additionally, the noble metal dopants did promote slight band gap reduction, going down to as low as 3.07 eV. Based on the degradation of 4-chlorophenol, noble metal doping enhanced photoreactivity, where the activity order was as follows: Au-TiO_2 > Pt-TiO_2 > Ag-TiO_2 > unmodified TiO_2. You et al.[35] reported on TiO_2 nanoparticles doped with Ag (1-4 wt.%) synthesized by deposition precipitation method. Characterization analysis revealed that Ag had no effect on crystal phase (100% anatase) or crystallite size (12 nm). Photocatalytic reactivity studies against methyl orange showed that Ag enhanced the performance of the photocatalyst at all content levels, where the 2 wt.% Ag content level yielded the greatest reactivity.

Seery et al.[36] investigated Ag-doped TiO_2 via sol-gel method by two routes: UV irradiation and direct calcinations. XRD analysis showed that by either doped method, the doped and unmodified TiO_2 nanoparticles crystallized to pure anatase at an annealing temperature of 600 °C. When annealed at 700 °C, the unmodified TiO_2 had yielded a high amount of the rutile crystal phase, while the presence of Ag in the doped TiO_2 suppressed the formation of rutile. Higher Ag loadings (3 wt.%) showed the beginning of very small rutile crystal phase formation. Additionally, the addition of Ag slightly

decreased the crystallite size compared to the unmodified TiO_2, but increasing the Ag content had no significant effect on the crystallite size. Diffuse reflectance analysis also showed higher visible absorbance capacity due to the addition of Ag. Photoreactivity studies against rhodamine 6G revealed that Ag greatly enhanced the performance of TiO_2, where Ag reduction via direct calcination yielded greater reactivity than UV irradiation.

Paramasivam et al.[37] reported on the electrochemical synthesis of TiO_2 nanotubes doped with Ag and Au. Based on SEM images, 10 nm sized Ag and 30 nm sized Au nanoparticles were observed on the surface of 100 nm sized TiO_2 nanotubes for Ag- and Au-doped TiO_2, respectively. Evaluation of the photocatalytic activity against Acid orange 7 showed that the noble metals enhanced the performance of the photocatalyst, where the greatest decomposition was associated with Ag. Zang et al.[38] reported on sol-gel synthesized TiO_2 doped with Pt, Pd and Au, as well as some transition metals. The noble metal-doped TiO_2 materials were more heavily emphasized than the others because of their greater contribution to photoreactivity enhancement. Based on degradation of 4-chlorophenol upon illumination of UV and visible light, the noble metals played a large role on enhancing photocatalytic performance, with the greatest performance associated with Pt.

Sakthivel et al.[39] investigated Pd, Au and Pt doping of commercially-available TiO_2 via impregnation method. Diffuse reflectance analysis resulted in light absorbance of the doped TiO_2 with no apparent change to band gap. XRD analysis resulted in no change in the crystal phase composition between the unmodified and doped TiO_2. Grain size of the anatase phase was unaffected by the addition of the noble metals (22 nm),

while rutile grain size did decrease from 33 nm to a range of 26-29 nm. Photocatalytic reactivity studies against Acid green 16 showed that all 3 noble metals enhanced degradation kinetics of the TiO_2, where Pt and Au had an exceptionally greater effect than Pd.

Sobana et al.[32],[40] worked on TiO_2 nanoparticles doped by Ag via photoreduction. Diffuse reflectance analysis showed greater absorption of visible light due to the presence of the Ag. Since a strong band associated with surface plasmon absorption did not appear, the authors concluded that the Ag caused band gap absorption. XRD characterization reported that the Ag-doped and unmodified TiO_2 were fully anatase, while crystallite size increased from 21 nm to an average 34 nm due to the addition of Ag. Photocatalytic reactivity studies against azo dyes Direct red 23 and Direct blue 53 revealed that Ag-doped TiO_2 outperformed unmodified TiO_2 at all content loadings (0.5-2.5 wt.%). Organicc degradation was optimal at 1.5 and 2 wt.% Ag for Direct red 23 and Direct blue 5, respectively.

Iliev et al.[41] investigated the modification of commercially-available TiO_2 with Pt and Ag particles by photoreduction. BET analysis showed no significant change in surface area due to noble metal doping, ranging from 48-50 m^2/g. Photocatalytic studies against oxalic acid showed enhanced performance of the TiO_2 with the addition of Pt and Ag. Barakat et al.[42] reported results from Ag-doping of TiO_2 nanofibers syntheseized via electrospinning. XRD characterization showed that the Ag-doped TiO_2 nanofibers were fully anatase at Ag content levels of 1, 1.5 and 2 wt.%. They also reported that at larger Ag loadings (3 and 5 wt.% Ag), rutile formation became more apparent and rutile content

increased from 3 to 5 wt.% Ag loading. Additionally, the higher Ag content loadings also hindered the integrity of the nanofibers, creating broken nanorods. Photocatalytic reactivity results against methylene blue revealed that the addition of Ag enhanced performance of organic degradation.

Of all the additives mentioned, noble metals are most sought after because of their effectiveness in enhancing the photocatalytic performance of TiO_2. Figure 3-3 shows normalized rate constants of the reviewed data,[31]–[43] where performance can reach up to 4 times that of pure TiO_2.While all noble metals have shown significant enhancement in photocatalytic performance, Ag, in particular, has attracted much interest because of its superior performance in the destruction of aqueous phase pollutants over other noble metals co-catalysts[22]–[28],[33],[37] and additional antibacterial activity.[32],[43]

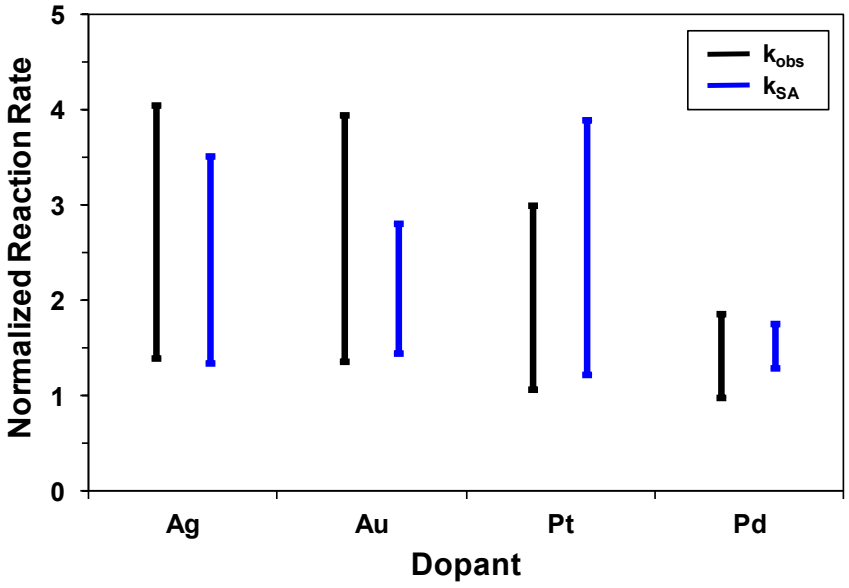

Figure 3-3: Normalized k_{obs} and k_{SA} of noble metal-doped TiO_2.[31]–[43]

The overall objective of this study is to synthesize Ag-TiO_2 composite nanofibers and optimize their photocatalyic activity for the oxidation of organic micropollutants in water. The synthesis of the nanofibers was conducted via electrospinning, a facile and cost-effective process that yields solid nanoscale fibers from a sol-gel solution with the use of an electrical charge.[44]–[46] In addition to having greater photocatalytic performance than conventional nanoparticles,[47] electrospun nanofiber mats can be very robust and stable and are well suited for filtration/membrane applications.[46] Synthesized nanofibers were characterized via various techniques, such as SEM, XRD and diffuse reflectance, to identify observed changes in nanofiber properties resulting from the presence of the Ag nanoparticles. Subsequently, we analyzed the performance of these nanofibers in laboratory systems for degradation of phenol, a model pollutant with functional moieties typical of common organic micropollutants, to quantify the effect of the Ag co-catalyst on photocatalytic treatment efficiency.

3.3 Experimental Methods

3.3.1 Reagents

All chemicals were reagent grade or better and used as received. The synthesis of the TiO_2 nanofibers involved titanium tetraisopropoxide (TTIP) (Sigma Aldrich, 97%), ethanol (Fisher Scientific, anhydrous), acetic acid (Fisher Scientific, glacial 99.7%) and polyvinylpyrrolidone (PVP) (Sigma Aldrich, MW: 1,300,000 g/mol). Additionally, silver nitrate ($AgNO_3$) (Fisher Scientific) was used as the Ag precursor during solution

preparation. The content levels of Ag were calculated based on atomic percentage (at.%) of TiO_2.

A buffer prepared from 5 mM potassium phosphate monobasic (Fisher Scientific, 99.3%) and 5 mM sodium chloride (NaCl) (Sigma Aldrich, >99.0%) was used in all photochemical experiments. A buffer prepared from 10 mM NaCl was used in all zeta potential experiments. Aeroxide® P25 (Acros Organics) was used as a commercially available TiO_2 photocatalyst for treatment efficiency comparison. Phenol (Sigma-Aldrich, >99%) was used as a model organic micropollutant in all photoactivity studies. The eluent for HPLC analysis of phenol used sodium acetate (Sigma Aldrich, anhydrous) and acetonitrile (ACN) (Fisher Scientific, 99.9%). All solutions were prepared in deionized (DI) water (Millipore, Milli-Q).

3.3.2 Synthesis of Ag-TiO_2 nanofibers

The electrospinning solution was prepared by creating two separate solutions, a polymer and precursor solution. The polymer solution was made by mixing 0.45 g of PVP and 4.5 mL of ethanol for 2 hours, while the precursor solution was made my mixing 1.68 mL of titanium precursor solution (TTIP), 3 mL of ethanol and 3 mL of acetic acid for 10 minutes. After both solutions dissolved completely, they were blended together for an hour, creating the desired electrospinning solution. $AgNO_3$ was incorporated in the polymer solution at levels between 0.25 and 10 at. % prior to the combination of the two solutions.

The precursor solution was transferred into a syringe that was subsequently loaded onto a syringe driver (Braun Perfusor, Inc.). The syringe was connected to a metallic adapter with 25 gauge plastic needle tip (NanoNC, Inc. from Korea) and situated 10 cm away from an Al foil-covered rotating drum (SPG Co., Ltd; Korea), which acted as the grounded collector. The metal adapter was connected to an Acopian (Easton, PA) high-voltage power supply, and a range of applied voltages (12-18 kV) were utilized. As the solution progressed through the system (0.3 mL/hr) it became electrified. The tip of the resulting Taylor cone expelled an electrified jet of fibers, forming a fibrous mesh on the grounded collector.

After 3 hours, the electrospinning was ceased and the Al foil coated with the nanofibers was removed and inserted into a drying oven (Yamato DVS 402) at 60 °C overnight. After this low heating, the nanofiber mat (typically 0.13 x 0.28 m^2) was peeled off and placed into a ceramic bowl for subsequent annealing/calcination in a box furnace (Thermolyne; Thermo Scientific) at 650 °C for 3 hours for polymer removal and TiO_2 crystallization. Additionally, the annealing process provided thermal decomposition of the $AgNO_3$ to Ag_2O and finally to Ag.[36] The Ag-TiO_2 composite nanofibers were then recalcinated at 700 °C, 3 °C/min at various durations to control the crystal phases, crystallinity and grain size, referred to as 0.5-R Ag-TiO_2. The motivation for such phase tuning is Aeroxide® P25, a mixed phase TiO_2 photocatalyst with a anatse to rutile ratio of 70-80%-to-20-30%[1],[48] that outperforms both pure phases in reactivity studies.[49] Additionally, this finding had also been observed in our work with unmodified TiO_2 nanofibers (Chapter 2). After annealing, typically 20-25 mg of nanofibers were produced

and combined with a designated amount of DI water to create a 1 g/L TiO_2 stock and sonicated in a Branson sonicator to disperse the nanofibers into a homogenous suspension.

3.3.3 Nanofiber characterization

Ag-TiO_2 nanofibers were characterized using several different techniques to quantify their size, morphological and optical properties. Nanofiber diameter was examined by a Phillips XL30 FEG scanning electron microscopy (SEM). For SEM, samples were prepared by placing approximately a 0.5 cm x 0.5 cm area of nanofibers onto a SEM sample holder. SEM imaging of n = 100 nanofibers yielded average diameters (with standard deviation) that were used to create sizing histograms. Transmission electron microscopy (TEM) and scanning transmission electron microscopy (STEM) were used to analyze Ag nanoparticle size and distribution in composites. Additionally, the presence of Ag nanoparticles was analyzed by energy dispersive X-ray spectroscopy (EDX) following SEM and selected area diffraction (SAED) analysis following TEM.

Crystal phase and average grain size were determined by a Bruker D8 Advance x-ray diffraction (XRD) analyzer. XRD samples were prepared in the same manner as described for the TiO_2 nanofibers. The 1 x 1 cm^2 samples were analyzed from 20° to 80° for the Bragg angle with an interval of 0.03°. Crystal phase composition was quantified by means of equation that analyzes the ratio of the main diffraction peak intensities of anatase and rutile.[50] Grain size was quantified by means of the Scherrer-Debye equation, which relates grain size to the diffraction peak properties.[50]

Band gap energy was quantified by a Thermo Scientific Evolution 300 UV-Vis spectrophotometer via diffuse reflectance infrared Fourier transform spectroscopy (DRIFTS). For analysis, the dry Fe_2O_3 samples were analyzed over a wavelength scan from 200 to 800 nm and absorbance was measured. The band gap was calculated by inserting the absorbance dataset of the nanofibers as a function of wavelength into the Kubelka-Munk method.[51],[52]

3.3.4 Photocatalysis experiments

Reactivity experiments were conducted in batch systems using a commercially available 1000 W Xenon arc lamp (Newport Corporation). The light was first passed through a water filter to remove infrared (IR) radiation, reflected off a 90° full reflectance beam turning mirror, and then passed through a 305 nm long-pass filter to better simulate the spectrum of light available at earth's surface. Reactivity studies were conducted within a jacketed photoreactor containing catalyst suspensions (0.1 g/L) prepared at pH 7 (using 5 mM buffer) and maintained at 25 °C with a recirculating water bath.

Similar to the studies conducted in Chapter 2, reactivity of TiO_2 nanofibers, Ag-TiO_2 composite nanofibers and commercial P25 nanoparticles was explored toward phenol at an initial concentration of 100 μM to identify the optimal diameter, grain size, and Ag content level. After dispersion of nanofibers via sonication, suspensions were irradiated and aliquots were withdrawn over time to measure change in phenol concentration over time. Samples were centrifuged at 10,000 rpm for 8 min in the dark to allow extraction of the supernatant because filtration resulted in the loss of some analytes

by sorption. The supernatant was transferred to a 1.5 mL amber autosampler vial for subsequent analysis via high performance liquid chromatography with photodiode array detector (1200 Series Agilent HPLC-DAD). The 1200 Series Agilent HPLC-DAD was equipped with an Eclipse XDB-C18 column (4.6 × 50 mm, 1.8 μm particle size). The HPLC method of analysis for phenol was based on previous work and employed a mobile phase of 65:35 1 mM sodium acetate: ACN at pH 3, a flow rate of 0.75 mL/min, an injection volume of 20 μL and a 254 nm detection wavelength.[53]–[55]

3.4 Results and Discussion

3.4.1 Nanofiber characterization

The Ag content in the TiO_2 nanofibers was adjusted by controlling the amount of $AgNO_3$ in the sol-gel solution prior to electrospinning, as confirmed by SEM-EDX analysis (Figure 3-4). While the unmodified TiO_2 was white, a very light grayish tint was observed with increasing Ag content. SEM analysis (Figure 3-5) of Ag-TiO_2 nanofibers indicated that the presence of Ag may slightly increase average nanofiber diameter at low content levels (≤ 1 at.%), but all measured diameters were still within one standard deviation of the diameter of unmodified TiO_2 nanofibers (33±10 nm). For 5 and 10 at.%, the average diameter increased significantly, reaching 68±20 and 92±25 nm, respectively. This can be attributed to the inclusion of the $AgNO_3$, which not only increased total metal content in the electrospinning solution, but also increased the solution viscosity, which can affect the nanofiber diameter size.[56]

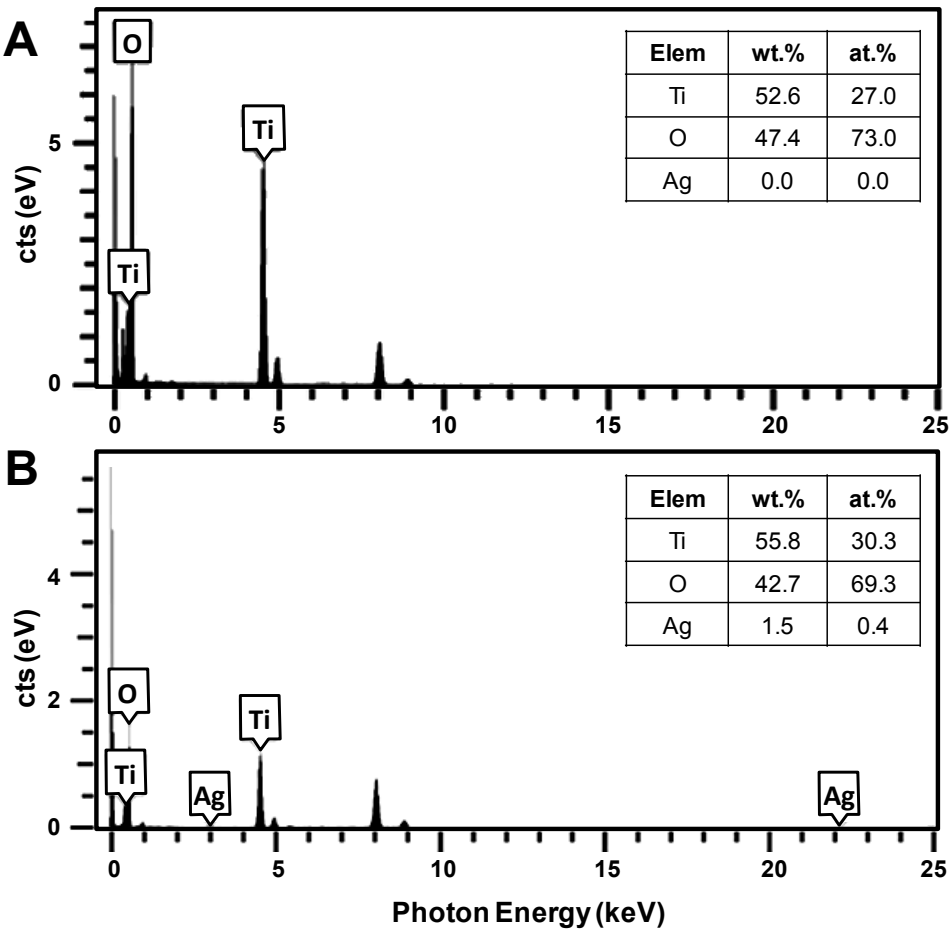

Figure 3-4: EDX spectra of A) 0 and B) 0.5 at.% Ag-TiO_2 nanofibers.

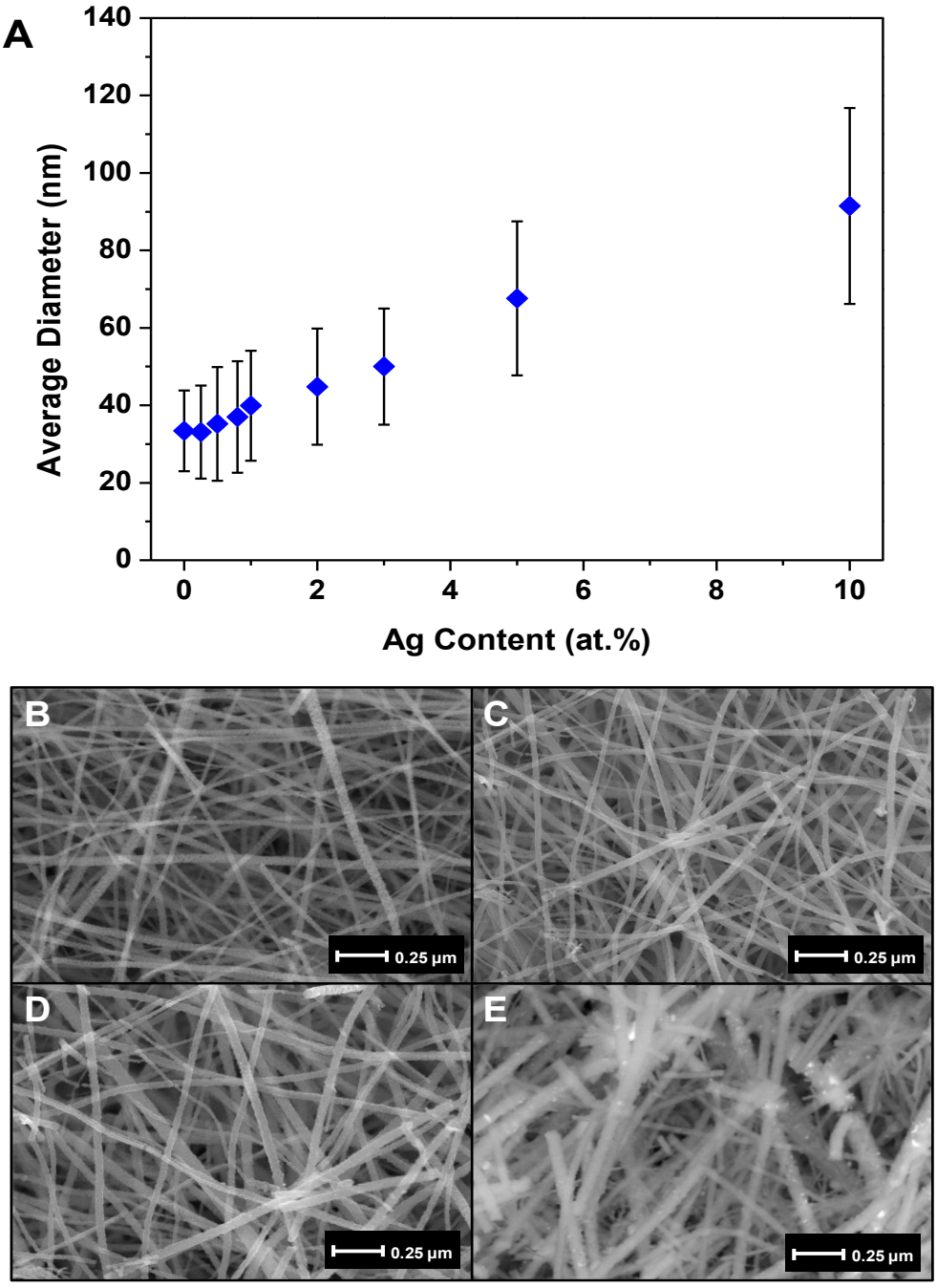

Figure 3-5: A) Average diameter as a function of Ag content for the Ag-TiO_2 nanofibers. Corresponding SEM images: B) 0 C) 0.5 D) 2 and E) 5 at.% Ag.

TEM analysis (Figure 3-6) was performed on unmodified and 0.5 at.% Ag-TiO_2 to examine the Ag formation in the TiO_2 nanofibers. Small Ag nanoparticles approximately 2 to 3 nm in size were uniformly distributed in the Ag-TiO_2 nanofibers (Figure 3-6-B), although sparingly, compared to the pristine TiO_2 nanofibers (Figure 3-6-E). The electron diffraction pattern from SAED analysis confirms that the TiO_2 nanofibers are polycrystalline with diffraction rings that correspond to those of anatase for both unmodified (Figure 3-6-C) and 0.5 at.% Ag-TiO_2 (Figure 3-6-F) nanofibers. Additionally, an extra diffraction ring can be seen in the 0.5 at.% Ag pattern corresponding with the crystalline Ag in the (111) orientation.

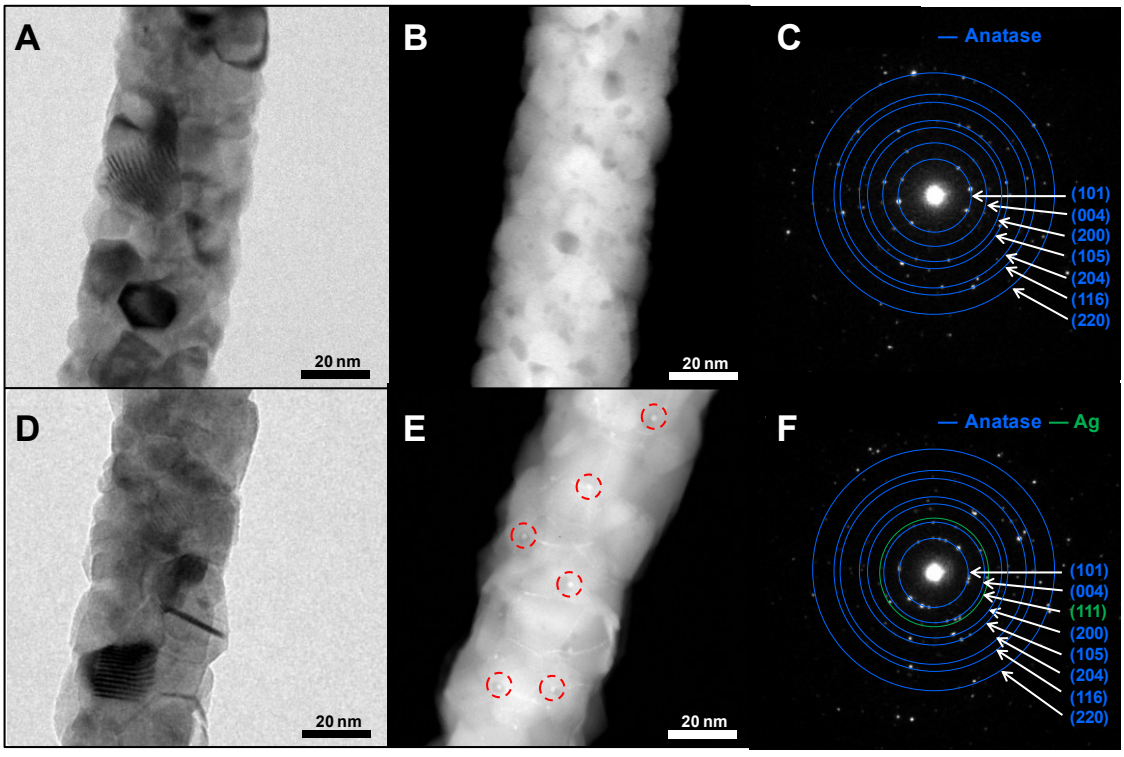

Figure 3-6: TEM, STEM and SAED images of unmodified (A, B, C) and 0.5 at.% Ag-TiO_2 nanofibers (D, E, F). Red dashed circles in STEM images indicate Ag nanoparticles in TiO_2 nanofiber bulk. Blue and green circles in SAED images indicate anatase TiO_2 and metal Ag diffraction peaks, respectively.

To compare the effect of the co-catalyst without variation of size, the applied voltage was increased from 12 to 18 kV for 5 at. % Ag-TiO_2 to produce nanofibers with an average diameter of 35±11 nm (Figure 3-7-A, B). For future reference, these materials will be referred to as 5-S Ag-TiO_2 nanofibers. Other characteristics of the 5 at.% Ag-TiO_2 nanofibers (grain size, band gap, etc.) remained unaltered.

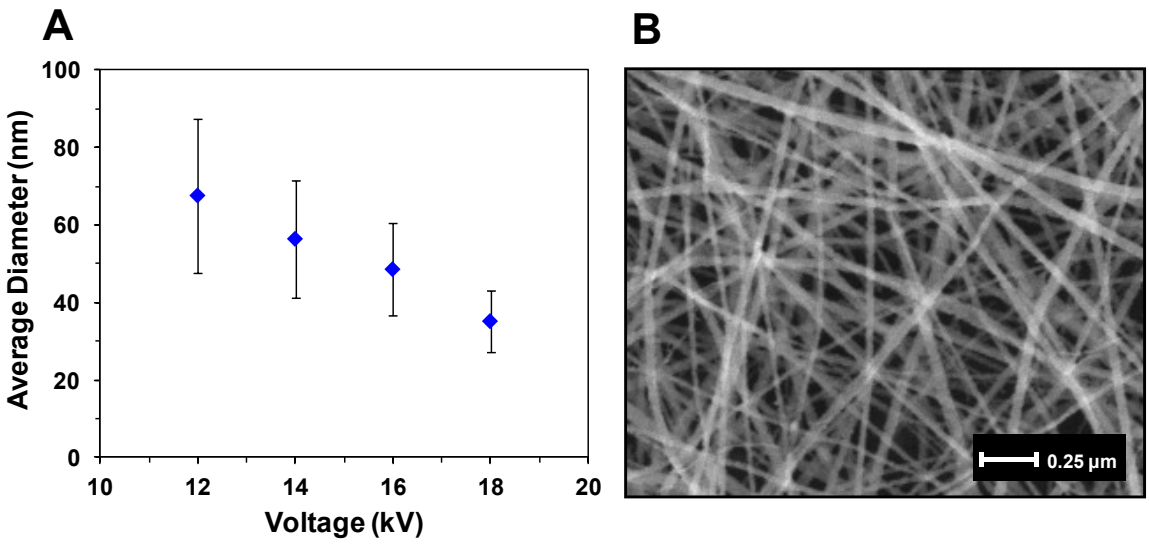

Figure 3-7: A) Average diameter as a function of applied voltage for the 5 at.% Ag-TiO_2 nanofibers and B) SEM image of 5 at.% Ag-TiO_2 electrospun at 18 kV.

XRD spectra of the Ag-TiO_2 nanofibers illustrate the disappearance of rutile peaks with increasing Ag content (Figure 3-8), implying that the anatase-to-rutile transformation is inhibited by the presence of Ag. XRD analysis indicates that most of the Ag-incorporated samples were pure anatase phase after annealing. Figure 3-9-A shows that starting at 75% with the unmodified TiO_2 nanofibers, the anatase composition increased to 89% with 0.25 at.% Ag and afterwards, the composite nanofibers are 100% anatase, signifying rutile growth inhibition in the presence of Ag, up to 10 at.% Ag,

where the anatase composition decreased to 87.5%. Additionally, very small Ag peaks are observable in the XRD spectra at the 3 at.% Ag level and above, although the (111) Ag peak was in fact visible in the SAED pattern at lower content (0.5 at.% Ag).

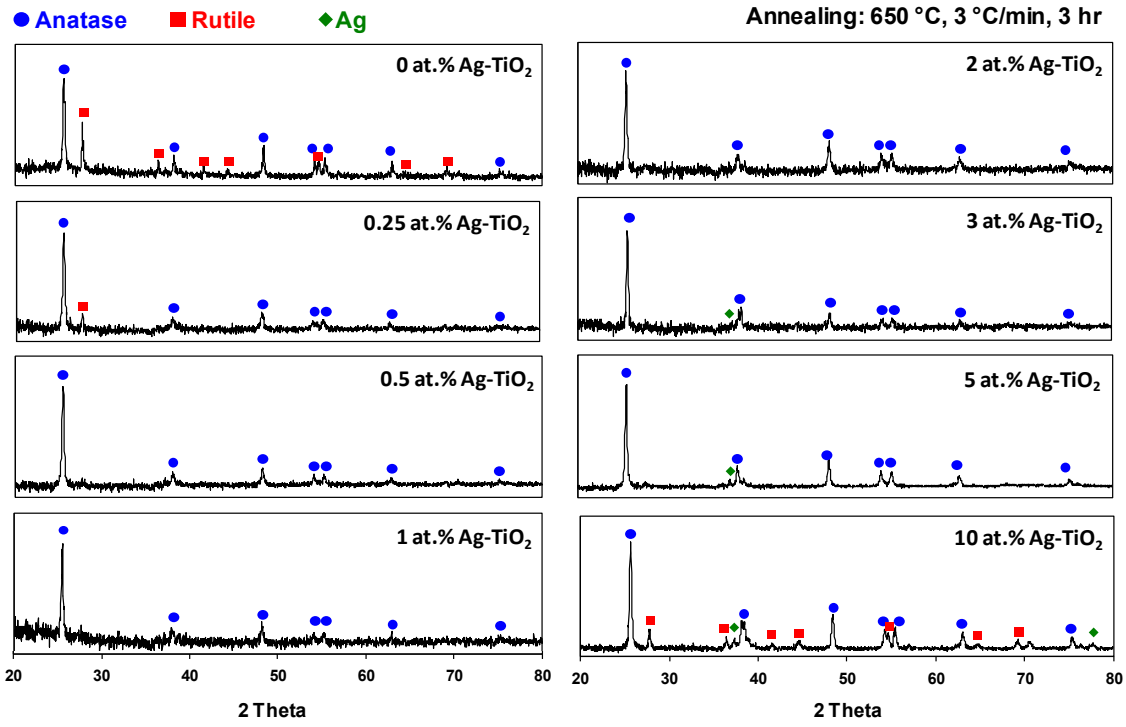

Figure 3-8: XRD pattern of the Ag-TiO_2 nanofibers at different Ag content levels.

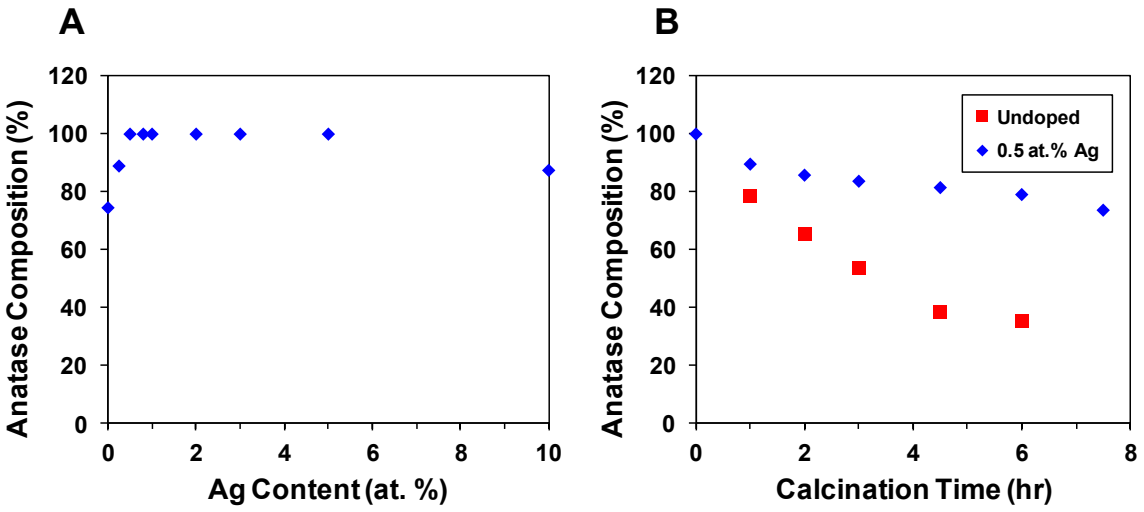

Figure 3-9: A) Anatase composition as a function of Ag content and B) rutile composition as a function of calcination time for Ag-TiO_2 nanofibers.

For the 0.5-R Ag-TiO_2 nanofibers (Figure 3-10), rutile peaks observably increased with increasing annealing duration, without an apparent Ag peak. However, XRD analysis (Figure 3-9-B) revealed that rutile growth in the Ag-TiO_2 nanofibers was inhibited relative to unmodified TiO_2. Furthermore, we note that average grain size, which was essentially constant (~32 nm) for all Ag loadings (Figure 3-11-A), slightly increased during recalcination due to the heat treatment (Figure 3-11-B).

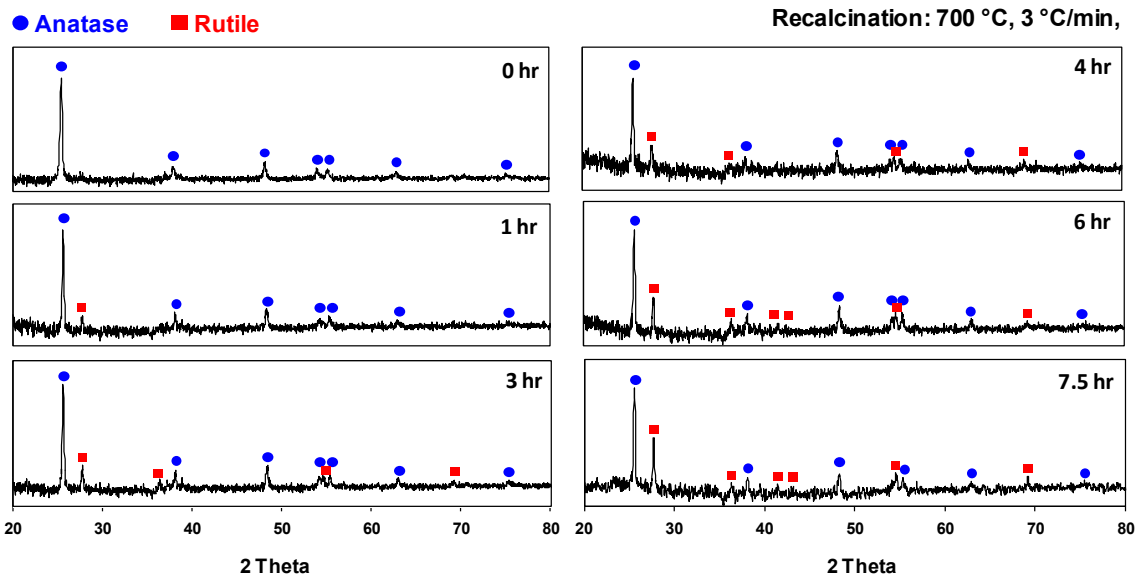

Figure 3-10: XRD pattern of the 0.5 at.% Ag-TiO_2 nanofibers recalcined at different time durations.

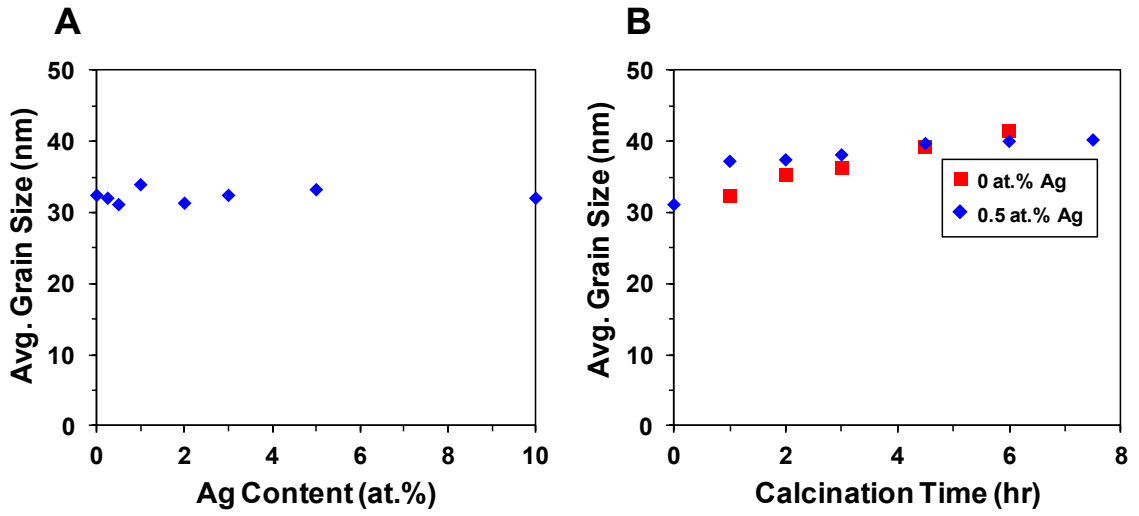

Figure 3-11: Average grain size as a function of A) Ag content and B) calcination time for Ag-TiO_2 nanofibers.

The band gap energies of the nanofibers with various Ag contents were calculated using the Kubelka-Munk method from the absorbance curves collected via diffuse

reflectance spectroscopy. As shown in Figure 3-12-A, the band gap of the Ag-TiO_2 nanofibers decreased from 3.21 eV to 2.79 eV as the Ag content increased from 0 to 10 at.%. This steady decrease in band gap with Ag content has been observed in previous reports of Ag-TiO_2 composites.[34],[57] A sharp decrease in the band gap energy was observed for Ag content less than 2 at.%. This may be attributed to the overlap of the wavefunctions of the electrons, which bind to the impurity (i.e., Ag) atoms as the density of the impurity increases.[58] Band gap energies for 0.5-R Ag-TiO_2 nanofibers, as well as unmodified TiO_2 nanofibers, are plotted on the basis of crystal phase composition in Figure 3-12-B. Starting at 3.21 eV for a pure anatase phase, the band gap of the unmodified TiO_2 nanofibers steadily decreased with increasing rutile content down to 3.02 eV for a pure rutile phase, with values similar to existing publication.[59] Interestingly, this same trend, not previously reported before in Ag-TiO_2 composites, can be seen with the 0.5 at.% Ag-TiO_2 nanofibers, where band gap decreases with increasing rutile composition.

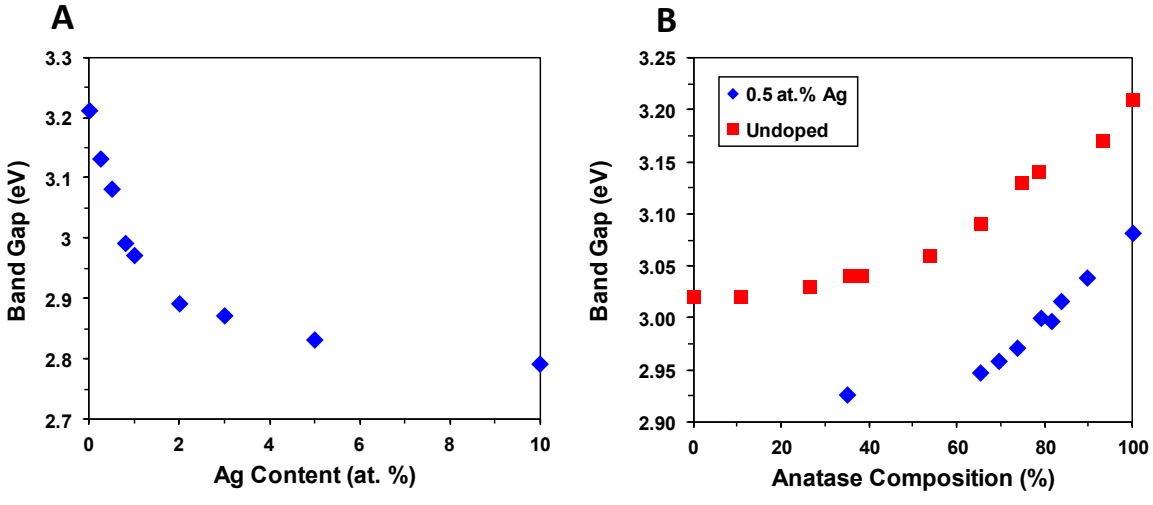

Figure 3-12: Band gap energy as a function of A) Ag content and B) anatase composition for unmodified and 0.5 at.% Ag-TiO_2 nanofibers.

3.4.2 Photocatalysis of Ag-TiO_2 nanofibers

In irradiated Ag-TiO_2 suspensions, phenol degradation followed exponential decay, for which we report pseudo-first-order rate constants for the phototransformation reaction (k_{obs} values; see Figure 3-13). As seen in Figure 3-14, the presence of Ag improved the reactivity of the nanofibers, where the optimal content of 0.5 at.% Ag (k_{obs} = (2.7 ± 0.1) x 10^{-1} min^{-1}) enhanced reactivity per unit mass by almost 3 times that of the optimal unmodified nanofibers (k_{obs} = (9.7 ± 0.4) x 10^{-2} min^{-1}). If compared by crystal phase composition, the 0.5 at.% Ag at 100% anatase performed a factor of ~3.6 greater than the pure anatase nanofibers (k_{obs} = (7.4 ± 0.8) x 10^{-2} min^{-1}) (Figure 3-15). After the peak, reactivity steadily decreased, where 5 at.% (k_{obs} = 8.2 x 10^{-2} min^{-1}) performed comparably to unmodified TiO_2 nanofibers and Aeroxide P25 whereas 10 at.% (k_{obs} = 5.7 x 10^{-2} min^{-1}) actually performed worse than unmodified TiO_2 nanofibers. However, the poor reactivity could possibly stem from the larger average diameter or the relatively larger sized Ag nanoparticles (8-12 nm) at the higher content levels (5-10 at.%) (Figure 3-16).[36]

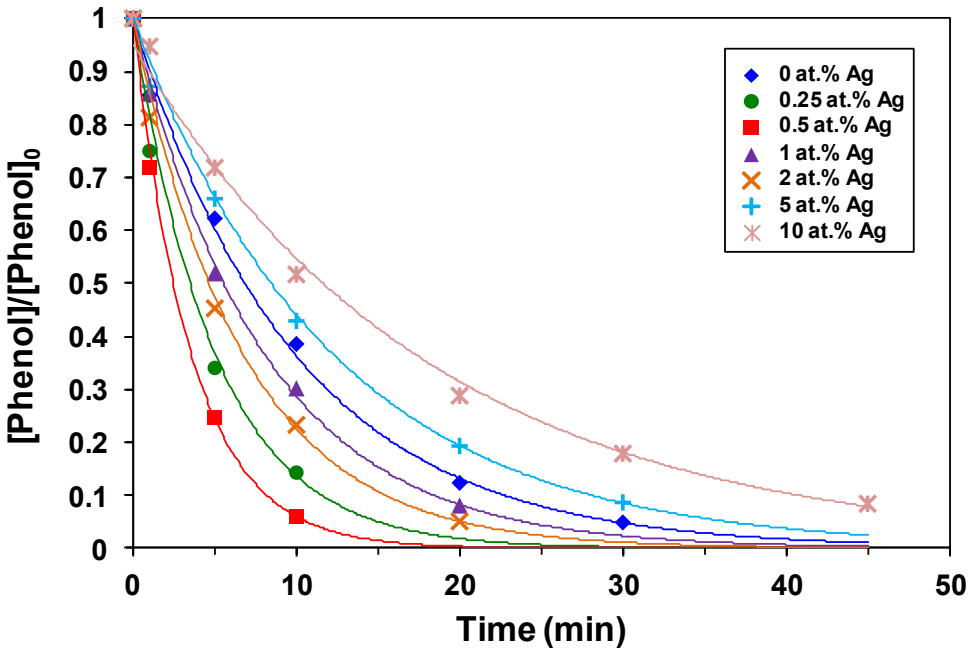

Figure 3-13: Normalized phenol concentration as a function of time from reactivity studies of Ag-TiO_2 nanofibers.

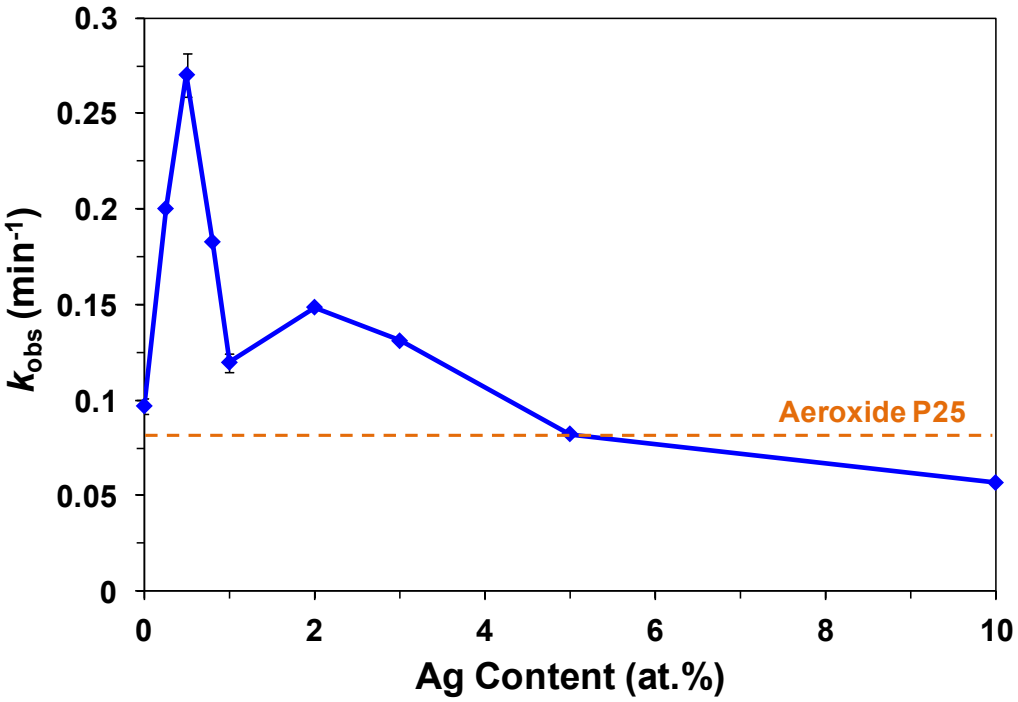

Figure 3-14: Average phenol decay rate constant as a function of Ag content for the Ag-TiO_2 nanofibers. Orange dotted line indicates rate constant of Aeroxide P25 commercial TiO_2 nanoparticles.

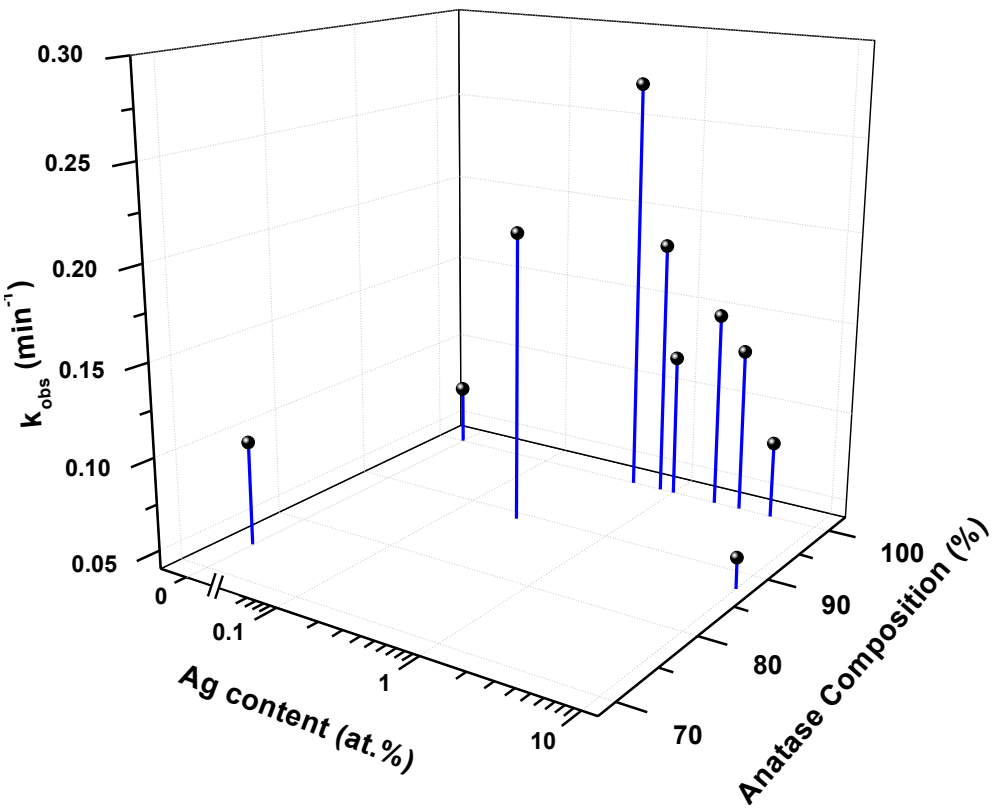

Figure 3-15: Average phenol decay rate constant as a function of Ag content and anatase composition for the Ag-TiO_2 nanofibers.

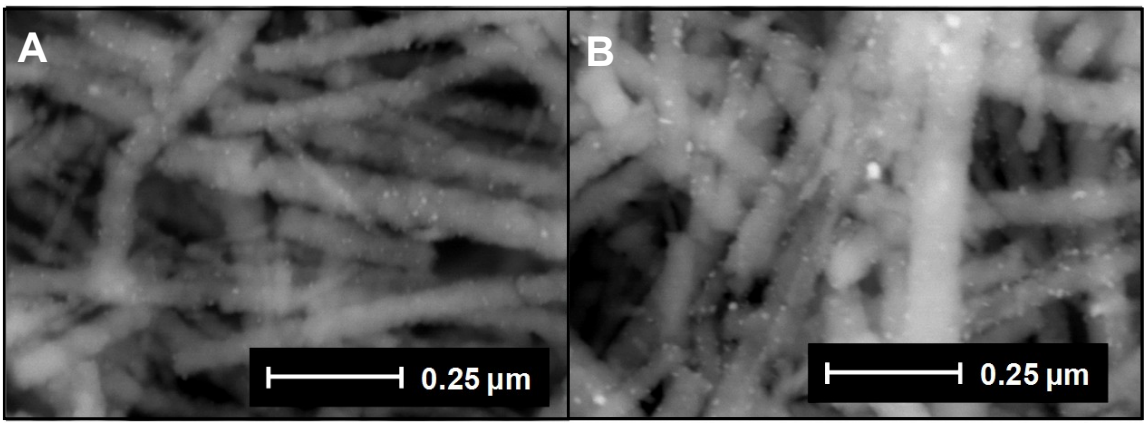

Figure 3-16: SEM images of A) 5 and B) 10 at.% Ag-TiO_2 nanofibers.

The 5-S Ag-TiO_2 nanofibers were also used in reactivity studies to explore whether the observed photoreactivity decline is due to dimensional change or co-catalyst mechanism. Figure 3-17 shows a 3D plot of photoreactivity as a function of Ag content and average diameter. The plot shows that the reactivity of the 5-S Ag-TiO_2 nanofibers increased with decreasing diameter, with the 35 nm sample having the greatest reaction rate of all the 5-S Ag samples (k_{obs} = (1.2 x 10^{-1} min^{-1}). However, the most reactive 5-S Ag sample still had lower reactivity than the composite nanofibers with less Ag content, keeping the trend of the optimal at 0.5 at.% and reactivity decreasing with increasing Ag content. Thus, the evidence of maximum reactivity at 0.5 at.% suggests the presence of an optimal size or surface area-to-volume ratio of the Ag nanoparticles, factors known to have significant effects on performance in addition to composite diameter.[60]

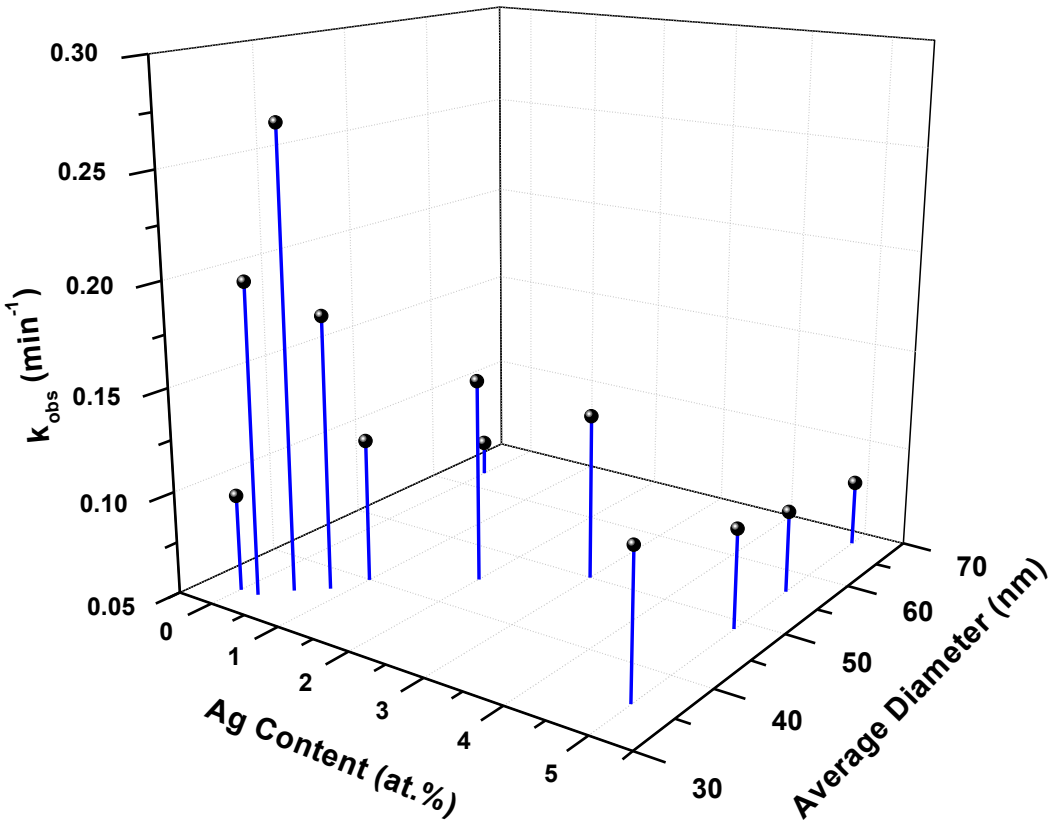

Figure 3-17. Average phenol decay rate constant as a function of Ag content and average diameter of the Ag-TiO_2 nanofibers.

Figure 3-18 shows a 3D plot comparing k_{obs} values for unmodified and 0.5 at.% Ag-TiO_2 nanofibers as a function of anatase composition and band gap energy, two key factors in photocatalyst performance. Overall, the primary parameter that dictates photoreactivity differs between the unmodified and Ag-TiO_2 nanofibers. For the unmodified nanofibers, crystal phase had the greatest influence on reactivity, whereas grain size and band gap energy had very little effect on performance. Specifically, the TiO_2 material with 75% anatase outperformed other nanofiber materials with smaller

average grain sizes (Chapter 2). Additionally, despite rutile having the lower band gap, its low photoactivity prevents it from being an efficient semiconductor phase.

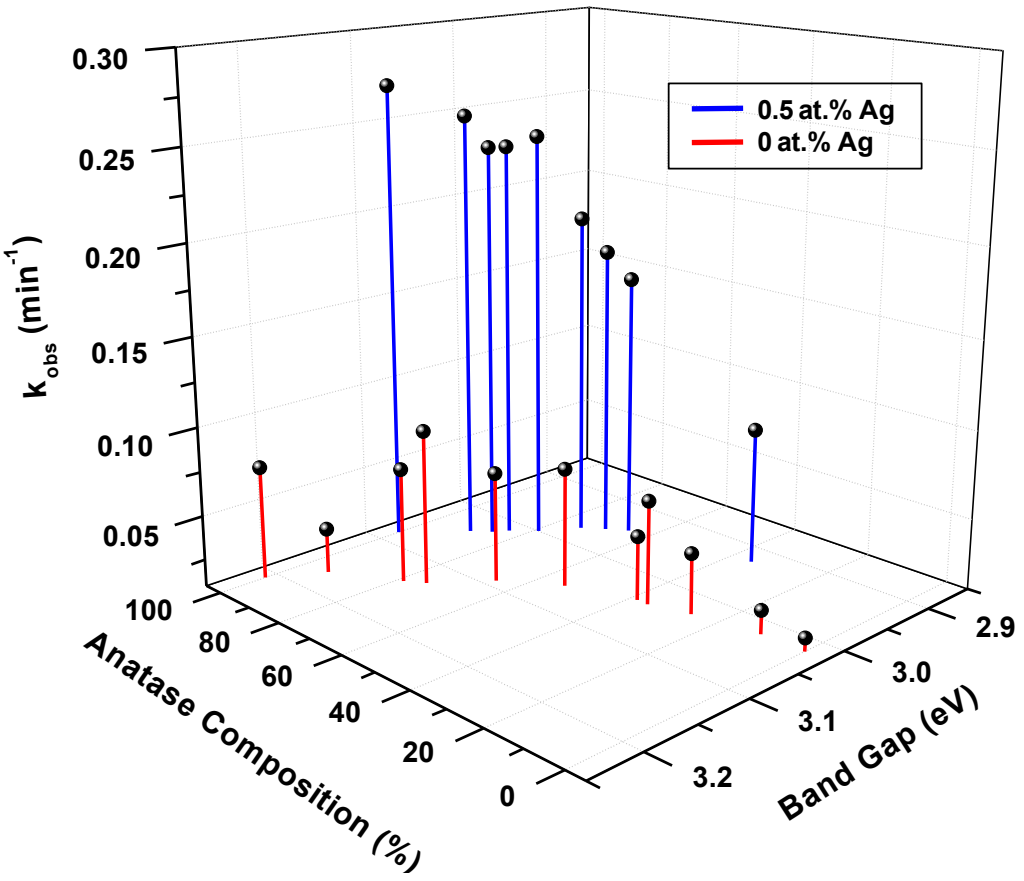

Figure 3-18. Average phenol decay rate constant of unmodified and 0.5 at.% Ag-TiO_2 nanofibers as a function of anatase composition and band gap energy.

For the Ag-TiO_2 composite nanofibers, the incorporation of the co-catalyst was clearly the greatest contributor to reactivity. The 0.5 at.% Ag material exhibited the greatest reactivity, despite having the largest bang gap level (3.08 eV) compared to other Ag-incorporated nanofibers (2.78-3.04 eV). Additionally, the introduction of rutile phase in the 0.5 at.% Ag-TiO_2 nanofibers actually inhibited reactivity, counter to the reactivity

benefits afforded by mixed phase TiO_2, where reactivity decreases steadily with increasing rutile composition. These results suggest that unlike unmodified TiO_2, which performs optimally with mixed phase, Ag-TiO_2 performs optimally in solely anatase phase. Therefore, co-catalyst level represents the parameter with the strongest effect for optimizing photoreactivity.

3.4.3 Mechanistic details

Based on the photoactivity studies, it is suggested that the electron trapping mechanism is the primary attributor to the enhanced performance of the Ag-TiO_2 composite nanofibers. Surface plasmon resonance was not a feasible option based on several parameters. Diffuse reflectance analysis showed no visible light absorption peaks, which is the most significant indicator of plasmon effect. Moreover, the Ag-TiO_2 nanofibers at all Ag content levels had very poor photocatalytic reactivity when illuminated by only the visible light spectrum ($\lambda > 395$ nm), having k_{obs} values of roughly 0.5% the UV rate constant values across the board. Band gap narrowing was also not a probable phenomenon attributed to enhanced reactivity since the addition of the co-catalyst did not narrow the band gap significantly (2.8-3.1 eV). Additionally, the more reactive of the Ag-TiO_2 nanofibers (0.25-1 at.% Ag) had higher values of band gap energy (3.08-3.13 eV) and were well within the range of pure anatase and rutile TiO_2 nanofibers (3.00-3.21 eV).

Electron trapping that occurs via Ag-incorporation is similar to the mechanism that naturally occurs in unmodified TiO_2. The photoexcited electrons expelled from the

valence band either undergo recombination with vacant electron holes or become ensnared in sinks, known as electron traps, at or near the surface.[8] These electron traps are either deep traps, where carriers effectively remain until encountering an electron scavenger (i.e. O_2), or shallow traps, where carriers can move between via trap-to-trap hopping process until they encounter a deep trap, an electron scavenger or an electron hole.[8] In mixed phase TiO_2, the anatase/rutile interface provides scavenging of rutile electrons from photons and facilitates electron transfer from rutile to anatase trapping sites, leading to greater stabilized charge separation and decreased recombination.[48] Therefore, anatase activation of rutile yields greater photoreactivity due to the stabilized charge separation. In terms of the Ag-TiO_2 composites, the Ag nanoparticles act as electron sinks, facilitating electron-hole separation and promoting electron transfer for increased photoreactivity.[31] The photoreactivity studies of the Ag-TiO_2 nanofibers demonstrated the performance of the Ag nanoparticles as efficient electron sinks according to the significant reactivity enhancement. The phenomenon suggests that Ag plays a prominent role as the antennae for electron-hole separation, assisting in surface carrier reactions and minimizing recombination kinetics. However, the presence of the rutile phase in the mixed phase Ag-TiO_2 nanofibers led to a decrease in reactivity, as the photoreactivity diminished with increasing rutile content. This is likely because the Ag nanoparticle-anatase phase interface functioned as the main route to facilitate carrier separation and efficient surface carrier transport, while the rutile phase functioned solitarily. Without the synergistic activation from anatase, rutile behaved as a lone ineffective semiconductor due to its high recombination kinetics. Although observable,

the decline in reactivity of the Ag-TiO_2 nanofibers due to rutile phase should not be considered significant since, for example, the Ag-TiO_2 sample with the highest rutile content (65% rutile, 35% anatase) still behaved comparable to the optimal unmodified TiO_2 nanofibers, as clearly seen in Figure 3-18.

3.5 Conclusion

While TiO_2 nanofibers could be optimized via changes in diameter and crystal phase, photocatalytic reactivity could be further optimized by incorporating Ag as a co-catalyst. Dimensional and morphological properties from the original unmodified form were intentionally replicated while the incorporation of Ag was conducted in order provide greater reactivity. Nanofiber diameter was not significantly altered with the addition of Ag until higher levels of incorporation ($\geq$ 2 at.%). We found that inhibition of the anatase-to-rutile phase transformation through the addition of Ag led to most of the composite samples to be purely anatase, although grain size was not affected. Additionally, the band gap was reduced with increasing Ag content, dropping to a value of 2.8 eV with 10 at.% Ag. Lastly, photoreactivity studies were performed to establish the influence of Ag on TiO_2 photooxidation processes. Results show the presence of the Ag co-catalyst enhanced reactivity, with an optimal loading of 0.5 at.% Ag outperforming its unmodified nanofiber counterpart by nearly a factor of 3. Above this loading, the photoreactivity decreased with increasing Ag content. We attribute this reactivity increase to the role of Ag as an electron sink that inhibits carrier recombination, but based on the observed optimum in activity, the size of the Ag is a was critical determinant of

photoreactivity. The use of electrospun nanofibers allow for application of nanofiber mats to harness the reactivity of nanomaterials that might otherwise be unobtainable by suspension-driven processes (e.g., the use of commercial TiO_2 catalyst nanoparticles in water treatment). Altogether, these results show the promise of Ag-TiO_2 nanofibers as efficient nanotechnology for aquatic treatment systems due to their enhanced photocatalytic performance and their synergistic potential with antimicrobial properties.

3.6 References

[1] Chong, M. N.; Jin, B.; Chow, C. W. K.; Saint, C. Recent Developments in Photocatalytic Water Treatment Technology: A Review. *Water Research* **2010**, *44*, 2997–3027.

[2] Grabowska, E.; Reszczyńska, J.; Zaleska, A. Mechanism of Phenol Photodegradation in the Presence of Pure and Modified-TiO_2: A Review. *Water Research* **2012**, *46*, 5453–5471.

[3] Ye, M.; Vennerberg, D.; Lin, C.; Lin, Z. Nanostructured TiO_2 Architectures for Environmental and Energy Applications. *Journal of Nanoscience Letters* **2012**, *2:1*, 1–35.

[4] Raj, K. J. A.; Viswanathan, B. Effect of Surface Area , Pore Volume and Particle Size of P25 Titania on the Phase Transformation of Anatase to Rutile. *Indian Journal of Chemistry* **2009**, *48A*, 1378–1382.

[5] Zawadzki, P.; Laursen, A. B.; Jacobsen, K. W.; Dahl, S.; Rossmeisl, J. Oxidative Trends of TiO_2—hole Trapping at Anatase and Rutile Surfaces. *Energy & Environmental Science* **2012**, *5*, 9866–9869.

[6] Erwin, S. C.; Zu, L.; Haftel, M. I.; Efros, A. L.; Kennedy, T. a; Norris, D. J. Doping Semiconductor Nanocrystals. *Nature* **2005**, *436*, 91–94.

[7] Liang, A.; Liu, Q.; Wen, G.; Jiang, Z. The Surface-Plasmon-Resonance Effect of Nanogold/silver and Its Analytical Applications. *Trends in Analytical Chemistry* **2012**, *37*, 32–47.

[8] Ke, S.-C.; Wang, T.-C.; Wong, M.-S.; Gopal, N. O. Low Temperature Kinetics and Energetics of the Electron and Hole Traps in Irradiated TiO_2 Nanoparticles as Revealed by EPR Spectroscopy. *Journal of Physical Chemistry* **2006**, *110*, 11628–11634.

[9] Pelaez, M.; Nolan, N. T.; Pillai, S. C.; Seery, M. K.; Falaras, P.; Kontos, A. G.; Dunlop, P. S. M.; Hamilton, J. W. J.; Byrne, J. A.; O'Shea, K.; et al. A Review on the Visible Light Active Titanium Dioxide Photocatalysts for Environmental Applications. *Applied Catalysis B: Environmental* **2012**, *125*, 331–349.

[10] Gombac, V.; De Rogatis, L.; Gasparotto, A.; Vicario, G.; Montini, T.; Barreca, D.; Balducci, G.; Fornasiero, P.; Tondello, E.; Graziani, M. TiO_2 Nanopowders Doped with Boron and Nitrogen for Photocatalytic Applications. *Chemical Physics* **2007**, *339*, 111–123.

[11] Liu, G.; Zhao, Y.; Sun, C.; Li, F.; Lu, G. Q.; Cheng, H.-M. Synergistic Effects of B/N Doping on the Visible-Light Photocatalytic Activity of Mesoporous TiO_2. *Angewandte Chemie (International ed. in English)* **2008**, *47*, 4516–4520.

[12] Cong, Y.; Zhang, J.; Chen, F.; Anpo, M. Synthesis and Characterization of Nitrogen-Doped TiO_2 Nanophotocatalyst with High Visible Light Activity. *Journal of Physical Chemistry C* **2007**, *111*, 6976–6982.

[13] Nolan, N. T.; Synnott, D. W.; Seery, M. K.; Hinder, S. J.; Van Wassenhoven, A.; Pillai, S. C. Effect of N-Doping on the Photocatalytic Activity of Sol-Gel TiO_2. *Journal of Hazardous Materials* **2012**, *211-212*, 88–94.

[14] Yang, G.; Jiang, Z.; Shi, H.; Xiao, T.; Yan, Z. Preparation of Highly Visible-Light Active N-Doped TiO_2 Photocatalyst. *Journal of Materials Chemistry* **2010**, *20*, 5301–5309.

[15] Gai, L.; Duan, X.; Jiang, H.; Mei, Q.; Zhou, G.; Tian, Y.; Liu, H. One-Pot Synthesis of Nitrogen-Doped TiO_2 Nanorods with Anatase/brookite Structures and Enhanced Photocatalytic Activity. *CrystEngComm* **2012**, *14*, 7662–7671.

[16] Buzby, S.; Barakat, M. a.; Lin, H.; Ni, C.; Rykov, S. a.; Chen, J. G.; Ismat Shah, S. Visible Light Photocatalysis with Nitrogen-Doped Titanium Dioxide Nanoparticles Prepared by Plasma Assisted Chemical Vapor Deposition. *Journal of Vacuum Science & Technology B: Microelectronics and Nanometer Structures* **2006**, *24*, 1210–1214.

[17] Kumbhar, A.; Chumanov, G. Synthesis of Iron(III)-Doped Titania Nanoparticles and Its Application for Photodegradation of Sulforhodamine-B Pollutant. *Journal of Nanoparticle Research* **2005**, *7*, 489–498.

[18] Luu, C. L.; Nguyen, Q. T.; Ho, S. T. Synthesis and Characterization of Fe-Doped TiO_2 Photocatalyst by the Sol–gel Method. *Advances in Natural Sciences: Nanoscience and Nanotechnology* **2010**, *1*, 015008.

[19] Nguyen, V. N.; Nguyen, N. K. T.; Nguyen, P. H. Hydrothermal Synthesis of Fe-Doped TiO_2 Nanostructure Photocatalyst. *Advances in Natural Sciences: Nanoscience and Nanotechnology* **2011**, *2*, 035014.

[20] Deng, Q. R.; Xia, X. H.; Guo, M. L.; Gao, Y.; Shao, G. Mn-Doped TiO_2 Nanopowders with Remarkable Visible Light Photocatalytic Activity. *Materials Letters* **2011**, *65*, 2051–2054.

[21] Liu, G.; Zhang, X.; Xu, Y.; Niu, X.; Zheng, L.; Ding, X. The Preparation of Zn^{2+}-Doped TiO_2 Nanoparticles by Sol-Gel and Solid Phase Reaction Methods

Respectively and Their Photocatalytic Activities. *Chemosphere* **2005**, *59*, 1367–1371.

[22] Colmenares, J. C.; Aramendía, M. a.; Marinas, a.; Marinas, J. M.; Urbano, F. J. Synthesis, Characterization and Photocatalytic Activity of Different Metal-Doped Titania Systems. *Applied Catalysis A: General* **2006**, *306*, 120–127.

[23] Di Paola, A.; Marci, G.; Palmisano, L.; Schiavello, M.; Uosaki, K.; Ikeda, S.; Ohtani, B. Preparation of Polycrystalline TiO_2 Photocatalysts Impregnated with Various Transition Metal Ions: Characterization and Photocatalytic Activity for the Degradation of 4-Nitrophenol. *Journal of Physical Chemistry B* **2001**, *106*, 637–645.

[24] Litter, M. I.; Navfo, J. A. Photocatalytic Properties of Iron-Doped Titania Semiconductors. *Journal of Photochemistry and Photobiology A: Chemistry* **1996**, *98*, 171–181.

[25] Cong, Y.; Zhang, J.; Chen, F.; Anpo, M.; He, D. Preparation, Photocatalytic Activity, and Mechanism of Nano-TiO_2 Co-Doped with Nitrogen and Iron (III). *Journal of Physical Chemistry C* **2007**, *111*, 10618–10623.

[26] Štengl, V.; Bakardjieva, S.; Murafa, N.; Oplustil, F. Zirconium Doped Titania : Destruction of Warfare Agents and Photocatalytic Degradation of Orange 2 Dye. *The Open Process Chemistry Journal* **2008**, *1*, 1–7.

[27] Litter, M. Heterogeneous Photocatalysis Transition Metal Ions in Photocatalytic Systems. *Applied Catalysis B: Environmental* **1999**, *23*, 89–114.

[28] Chennan, L.; Srinivasan, S.; Algarin, P.; Kislov, N.; Phani, A.; Stefanakos, E.; Goswami, Y. Increasing the Photocatalytic Activity by Mechano-Chemically Milling on Zn-Doped TiO_2. *Materials Research Society Symposium Proceedings* **2010**, *1217*.

[29] Xu, a The Preparation, Characterization, and Their Photocatalytic Activities of Rare-Earth-Doped TiO_2 Nanoparticles. *Journal of Catalysis* **2002**, *207*, 151–157.

[30] Štengl, V.; Bakardjieva, S.; Murafa, N. Preparation and Photocatalytic Activity of Rare Earth Doped TiO_2 Nanoparticles. *Materials Chemistry and Physics* **2009**, *114*, 217–226.

[31] Lee, M. S.; Hong, S.-S.; Mohseni, M. Synthesis of Photocatalytic Nanosized TiO_2–Ag Particles with Sol–gel Method Using Reduction Agent. *Journal of Molecular Catalysis A: Chemical* **2005**, *242*, 135–140.

[32] Sobana, N.; Muruganadham, M.; Swaminathan, M. Nano-Ag Particles Doped TiO_2 for Efficient Photodegradation of Direct Azo Dyes. *Journal of Molecular Catalysis A: Chemical* **2006**, *258*, 124–132.

[33] Moonsiri, M.; Rangsunvigit, P.; Chavadej, S.; Gulari, E. Effects of Pt and Ag on the Photocatalytic Degradation of 4-Chlorophenol and Its by-Products. *Chemical Engineering Journal* **2004**, *97*, 241–248.

[34] Loganathan, K.; Bommusamy, P.; Muthaiahpillai, P.; Velayutham, M. The Syntheses, Characterizations, and Photocatalytic Activities of Silver, Platinum, and Gold Doped TiO_2 Nanoparticles. *Environmental Engineering Research* **2011**, *16*, 81–90.

[35] You, X.; Chen, F.; Zhang, J.; Anpo, M. A Novel Deposition Precipitation Method for Preparation of Ag-Loaded Titanium Dioxide. *Catalysis Letters* **2005**, *102*, 247–250.

[36] Seery, M. K.; George, R.; Floris, P.; Pillai, S. C. Silver Doped Titanium Dioxide Nanomaterials for Enhanced Visible Light Photocatalysis. *Journal of Photochemistry and Photobiology A: Chemistry* **2007**, *189*, 258–263.

[37] Paramasivam, I.; Macak, J. M.; Schmuki, P. Photocatalytic Activity of TiO_2 Nanotube Layers Loaded with Ag and Au Nanoparticles. *Electrochemistry Communications* **2008**, *10*, 71–75.

[38] Zang, L.; Macyk, W.; Lange, C.; Maier, W. F.; Antonius, C.; Meissner, D.; Kisch, H. Visible-Light Detoxification and Charge Generation by Transition Metal Chloride Modified Titania. *Chemistry – A European Journal* **2000**, *6*, 379–384.

[39] Sakthivel, S.; Shankar, M. V; Palanichamy, M.; Arabindoo, B.; Bahnemann, D. W.; Murugesan, V. Enhancement of Photocatalytic Activity by Metal Deposition: Characterisation and Photonic Efficiency of Pt, Au and Pd Deposited on TiO_2 Catalyst. *Water Research* **2004**, *38*, 3001–3008.

[40] Sobana, N.; Selvam, K.; Swaminathan, M. Optimization of Photocatalytic Degradation Conditions of Direct Red 23 Using Nano-Ag Doped TiO_2. *Separation and Purification Technology* **2008**, *62*, 648–653.

[41] Iliev, V.; Tomova, D.; Bilyarska, L.; Eliyas, A.; Petrov, L. Photocatalytic Properties of TiO_2 Modified with Platinum and Silver Nanoparticles in the Degradation of Oxalic Acid in Aqueous Solution. *Applied Catalysis B: Environmental* **2006**, *63*, 266–271.

[42] Barakat, N. A. M. Influences of Silver-Doping on the Crystal Structure, Morphology and Photocatalytic Activity of TiO_2 Nanofibers. *Materials Sciences and Applications* **2011**, *02*, 1188–1193.

[43] Liu, Y.; Liu, C.; Rong, Q.; Zhang, Z. Characteristics of the Silver-Doped TiO_2 Nanoparticles. *Applied Surface Science* **2003**, *220*, 7–11.

[44] Ramakrisha, S.; Fujuhara, K.; Teo, W.-E.; Lim, T.-C.; Ma, Z. *An Introduction to Electrospinning and Nanofibers*; World Scientific Publishing Co.: Singapore, 2005.

[45] Dai, Y.; Liu, W.; Formo, E.; Sun, Y.; Xia, Y. Ceramic Nanofibers Fabricated by Electrospinning and Their Applications in Catalysis, Environmental Science, and Energy Technology. *Polymers for Advanced Technologies* **2011**, *22*, 326–338.

[46] Thavasi, V.; Singh, G.; Ramakrishna, S. Electrospun Nanofibers in Energy and Environmental Applications. *Energy & Environmental Science* **2008**, *1*, 205–221.

[47] Choi, S. K.; Kim, S.; Lim, S. K.; Park, H. Photocatalytic Comparison of TiO_2 Nanoparticles and Electrospun TiO_2 Nanofibers: Effects of Mesoporosity and Interparticle Charge Transfer. *Journal of Physical Chemistry C* **2010**, *114*, 16475–16480.

[48] Hurum, D. C.; Agrios, A. G.; Gray, K. A.; Rajh, T.; Thurnauer, M. C. Explaining the Enhanced Photocatalytic Activity of Degussa P25 Mixed-Phase TiO_2 Using EPR. *Journal of Physical Chemistry B* **2003**, *107*, 4545–4549.

[49] Ding, Z.; Lu, G. Q.; Greenfield, P. F. Role of the Crystallite Phase of TiO_2 in Heterogeneous Photocatalysis for Phenol Oxidation in Water. **2000**, 4815–4820.

[50] Hosseini, S. N.; Borghei, S. M.; Vossoughi, M.; Taghavinia, N. Immobilization of TiO_2 on Perlite Granules for Photocatalytic Degradation of Phenol. *Applied Catalysis B: Environmental* **2007**, *74*, 53–62.

[51] Tunc, I.; Bruns, M.; Gliemann, H.; Grunze, M.; Koelsch, P. Bandgap Determination and Charge Separation in $Ag@TiO_2$ Core Shell Nanoparticle Films. *Surface and Interface Analysis* **2010**, *42*, 835–841.

[52] Pal, M.; Pal, U.; Jiménez, J. M. G. Y.; Pérez-Rodríguez, F. Effects of Crystallization and Dopant Concentration on the Emission Behavior of TiO_2:Eu Nanophosphors. *Nanoscale Research Letters* **2012**, *7*, 1.

[53] Guo, Z.; Ma, R.; Li, G. Degradation of Phenol by Nanomaterial TiO_2 in Wastewater. *Chemical Engineering Journal* **2006**, *119*, 55–59.

[54] Araña, J.; Doña-Rodríguez, J. M.; Portillo-Carrizo, D.; Fernández-Rodríguez, C.; Pérez-Peña, J.; González Díaz, O.; Navío, J. a.; Macías, M. Photocatalytic Degradation of Phenolic Compounds with New TiO_2 Catalysts. *Applied Catalysis B: Environmental* **2010**, *100*, 346–354.

[55] Parra, S.; Olivero, J.; Pacheco, L.; Pulgarin, C. Structural Properties and Photoreactivity Relationships of Substituted Phenols in TiO_2 Suspensions. *Applied Catalysis B: Environmental* **2003**, *43*, 293–301.

[56] Sarlak, N.; Nejad, M. A. F.; Shakhesi, S.; Shabani, K. Effects of Electrospinning Parameters on Titanium Dioxide Nanofibers Diameter and Morphology: An Investigation by Box–Wilson Central Composite Design (CCD). *Chemical Engineering Journal* **2012**, *210*, 410–416.

[57] Kočí, K.; Matějů, K.; Obalová, L.; Krejčíková, S.; Lacný, Z.; Plachá, D.; Čapek, L.; Hospodková, A.; Šolcová, O. Effect of Silver Doping on the TiO_2 for Photocatalytic Reduction of CO_2. *Applied Catalysis B: Environmental* **2010**, *96*, 239–244.

[58] Bart Van Zeghbroeck *Principles of Semiconductor Devices*; <http://ece-www.colorado.edu/~bart/book/>, 2011.

[59] Toyoda, T.; Tsuboya, I. Apparent Band-Gap Energies of Mixed TiO_2 Nanocrystals with Anatase and Rutile Structures Characterized with Photoacoustic Spectroscopy. *Review of Scientific Instruments* **2003**, *74*, 782.

[60] Kaur, R.; Pal, B. Size and Shape Dependent Attachments of Au Nanostructures to TiO_2 for Optimum Reactivity of Au–TiO_2 Photocatalysis. *Journal of Molecular Catalysis A: Chemical* **2012**, *355*, 39–43.

Chapter 4: Synthesis and Optimization of $BiVO_4$ and Co-catalyzed $BiVO_4$ Nanofibers

4.1 Abstract

Due to the limited photoefficeincy of TiO_2 under solar irradiation, non-titania semiconductors, such as bismuth vanadate ($BiVO_4$), have been gaining attention for use as visible light (VL) photocatalysts. In this work, electrospun $BiVO_4$ nanofibers were synthesized as photocatalysts for VL-induced photo-oxidation of organic pollutants. $BiVO_4$ nanofibers of varied average diameters (33 to 71 nm) were characterized to observe morphological, dimensional and optical properties and tested in aqueous solutions containing a model pollutant to analyze their photocatalytic activity under solar and VL irradiation conditions. Based on phenol degradation studies at pH 7, k_{obs} of the $BiVO_4$ nanofibers increased with decreasing diameter, with the 33 nm sized nanofibers slightly outperforming TiO_2 nanomaterials under VL irradiation. Additionally, Ag and Au co-catalyzed $BiVO_4$ nanofibers were developed, showing greater photocatalytic performance. Ag-$BiVO_4$ showed enhancement due to increased carrier traps, where as Au-$BiVO_4$ showed enhancement due to both carrier traps and surface plasmon resonance. Both co-catalyzed $BiVO_4$ nanofibers strongly outperformed TiO_2 nanomaterials under VL irradiation, with the greatest coming from 2 at.% Au-$BiVO_4$. Electrospun $BiVO_4$ nanofibers have potential to become efficient VL-activated photocatalysts for a low-energy alternative for the removal of emerging organic contaminants.

4.2 Introduction

4.2.1 Bismuth Vanadate ($BiVO_4$)

In lieu of TiO_2's great performance as stated earlier, its relatively large band gap of 3.2 eV provides little visible light (VL) absorption (< 380 nm). Additionally, the amount of photons from direct sunlight that can photoactivate TiO_2 is drastically small (< 5%).[1] In effort to capture VL photons, which constitutes a majority of solar irradiance (~42%),[1] recent research has moved towards modified TiO_2 as well as non-titania based semiconductors with narrower band gaps for VL-driven photocatalysis.[2] For instance, the valence bands of ternary metal oxide semiconductors consist of hybridizations of transition-metal orbitals, and this hybridization can increase the valence band level, thus resulting in the narrow band gap.[3] Among the group of new VL-active photocatalysts, bismuth vanadate ($BiVO_4$) has been reported to have narrow band gaps and exhibit good photocatalytic performance.

$BiVO_4$ was first reported in a medical patent for pharmaceutical purposes in 1924, but significant development of this material didn't occur until the mid 1970s.[4],[5] With its relatively recent discovery, $BiVO_4$ has been heavily manufactured for its initial use as a bright yellow pigment, as seen in Figure 4-1. Due to its non toxicity, environmentally-friendly $BiVO_4$-based paints have recently replaced paints containing toxic pigments such as lead chromate ($PbCrO_4$) and cadmium sulfide (CdS).[6] In addition to its popularity as a high performance pigment, $BiVO_4$ has been utilized in other useful applications due to additional attractive properties, including its ferroelastic, acousto-optical, ionic conductive and photocatalytic properties.[7],[8] Since its inaugural work by Kudo et al. as a

photocatalyst for O_2 evolution in 1999,[9] $BiVO_4$ has been widely used in gas sensors, posistors, batteries, electrolytes, water splitting and other applications.[8],[10] With the growth of nanomaterial research in the environmental field, $BiVO_4$, as a semiconductor, has found great relevance as an effective photocatalyst for pollutant degradation.

Figure 4-1: $BiVO_4$ powder.

Similar to TiO_2, the photocatalytic performance of $BiVO_4$ is heavily influenced by its crystal structure[2]. $BiVO_4$ has three main crystal structures: zircon-tetragonal, scheelite-tetragonal, and scheelite-monoclinic. Zircon-tetragonal phase can be formed from via low temperature (~100 °C) synthesis, while scheelite-monoclinic can be formed via high temperature (400-600 °C) synthesis.[10] Moreover, phase transformation between scheelite-monoclinic and scheelite-tetragonal can occur reversibly at 255 °C.[11] Based on extensive photocatalytic research, sheelite-monoclinic is observed as the most active $BiVO_4$ structure under VL irradiation.[2] The greater reactivity could be associated with the energy band structure, since monoclinic and tetragonal $BiVO_4$ have band gap energies of 2.4 and 2.9 eV, respectively (Figure 4-2).[9],[12],[13]

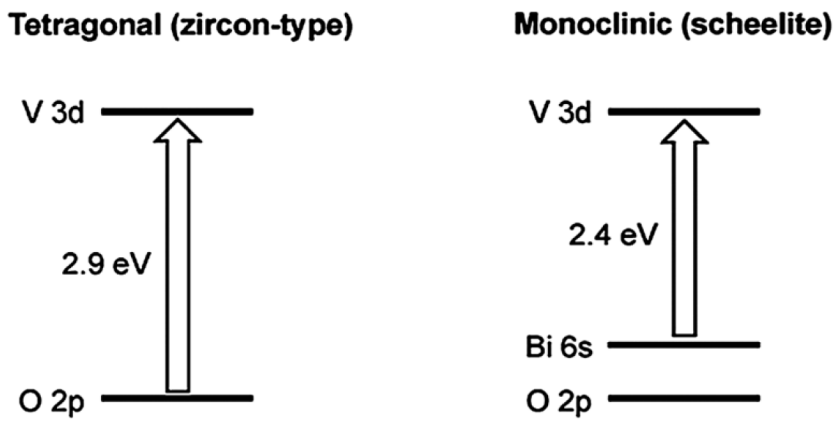

Figure 4-2: Diagram of band structures for tetragonal and monoclinic $BiVO_4$.[12],[13]

4.2.2 $BiVO_4$ Nanostructures

With the rise of $BiVO_4$ applications, researchers have experimented with different morphologies for their suitable applications, including remediation based photocatalysis. There has been substantial work on the synthesis of $BiVO_4$ photocatalysts by various preparation methods, as well as performance experiments towards the degradation of aqueous pollutants. Normally, $BiVO_4$ nanostructures are synthesized by the 1:1 molar combination of a bismuth precursor (i.e. $Bi(NO_3)_3$) and a vanadium precursor (i.e. NH_4VO_3) and subsequently heat treated for crystallization[9].

Hou et al.[3] reported on $BiVO_4$ nanorods synthesized by hydrothermal method. Another $BiVO_4$ sample was synthesized by solid-state reaction for comparison. BET surface area measurements showed greater surface area from the nanorods (10.7 m^2/g) compared to the nanoparticles synthesized by solid-state reaction (0.75 m^2/g). Photocatalytic studies were conducted against methylene blue under VL irradiation at a cutoff of 450 nm as well as under natural sunlight. Based on the photocatalytic

experiments, the $BiVO_4$ nanorods outperformed the $BiVO_4$ nanoparticles on both photodegradation and adsorption removal of methylene blue under both light conditions. Total removal under artificial VL was 81.2% for the nanorods, 17.3% for the nanoparticles, and 9.8% for Aeroxide® P25, which was conducted for TiO_2 comparison. Total removal under natural sunlight was 98.8% for the nanorods, 23.1% for the nanoparticles, and 14.2% for Aeroxide® P25.

Zhou et al.[8] reported on $BiVO_4$ microtubes synthesized by reflux method. A solution with $Bi(NO_3)_3$ and NH_4VO_3 dissolved in water was heated at 80 °C in a reflux system with varying times from 2 to 15 hours. The precipitate was subsequently collected and dried. $BiVO_4$ synthesized by solid-state reaction was prepared for comparison. Monoclinic $BiVO_4$ microtubes were synthesized by the 6 hour reaction, while the 2 hour reaction yielded tetragonal phase. Increased reaction time also created larger multi-tube flower-like structures, also noting the presence of $NaHCO_3$ being crucial in the forming of these structures. Photocatalytic reactions with Rhodamine B under VL at a cutoff of 400 nm showed significantly greater performance from the $BiVO_4$ microtubes over the solid-state reaction synthesized $BiVO_4$. Although not indicating which $BiVO_4$ microtube sample used in the photoreactions, the authors suggest the novel square tubular structure and/or the flowerlike morphology attributed to the enhanced photoreactivity.

Zhang et al.[10] reported on $BiVO_4$ nanoparticles synthesized via hydrothermal method. A suspension of $Bi(NO_3)_3$ and NH_4VO_3 was created and autoclaved at room temperature, 140 160, 180 and 200 °C for 24 hours under autogenous pressure. Based on XRD characterization, the autoclave temperature was used to alter the crystal phase

composition, where the room temperature reaction led to pure tetragonal phase and increased temperature led to more monoclinic phase content. By 180 °C, pure monoclinic phase formed. Additionally, increased reaction time also led to larger branches on the nanoparticles. BET analysis showed that surface area drastically decreased when the reaction was conducted with heat (140-200 °C) compared to that of the room temperature material, from 9.11 m^2/g down to a range 1.57-2.07 m^2/g. Band gap of $BiVO_4$ decreased steadily with increased reaction temperature, from 3.1 eV at room temperature down to 2.3 eV at 200 °C. Photocatalytic reactions with Rhodamine B under VL at a cutoff of 400 nm were conducted for the $BiVO_4$ nanoparticles, as well as Aeroxide® P25 for TiO_2 comparison. Their results revealed that monoclinic $BiVO_4$ showed very high photocatalytic activity, outperforming Aeroxide® P25, while tetragonal $BiVO_4$ reactivity was negligible.

Zhou et al.[14] also reported on $BiVO_4$ nanoparticles synthesized via sonochemical method. A solution containing $Bi(NO_3)_3$ and NH_4VO_3 dissolved in water was exposed to high-intensity ultrasound irradiation and the precipitate was centrifuged, collected and dried. Another sample of $BiVO_4$ was synthesized by solid state reaction for comparison. XRD characterization showed that increased sonication time increased the monoclinic content, where 30 minute sonication led to 47% monoclinic and 60 minute sonication, which was used for performance analysis, led to pure monoclinic. Additionally, ultrasonication showed smaller crystal phase and larger surface area than the $BiVO_4$ synthesized by solid-state reaction, while band gap was roughly the same. Based on photocatalytic studies with methyl orange under VL at a cutoff of 400 nm, the

ultrasonicated $BiVO_4$ showed greater degradation (90% removal) than that of the solid-state reaction $BiVO_4$ (8% removal), which performed similar to Aeroxide® P25 (6%) that was tested for TiO_2 comparison.

Fan et al.[11] reported on $BiVO_4$ nanoparticle synthesis via coprecipitation method. The $Bi(NO_3)_3$ and NH_4VO_3 precursors were dissolved in DI water and the subsequent precipitation was collected. The as-collected material was considered pure tetragonal and heat treatment at 500 C for 4 hours led to pure monoclinic. A second synthesis that included $LiNO_3$ salt was created for a composite material, having a 25.3% monoclinic phase. Based on photocatalytic reactions with methylene blue under VL at a cutoff wavelength of 400 nm, the pure monoclinic $BiVO_4$ nanoparticles performed significantly better than the pure tetragonal, where as the mixed phase only did slightly better than the tetragonal. Based on transient photovoltage and surface photovoltage characterization, the authors theorized the performance of the $BiVO_4$ being dependent on the accumulation of either photoinduced electrons or holes on the surface.

Wang et al.[15] reported on monoclinic $BiVO_4$ of different morphologies synthesized by solvothermal method. These structures include nanorods, nanofibers, bundle-like nanostructures and microrods. A suspension of $Bi(NO_3)_3$ and NH_4VO_3 in ethylene glycol and water (35:5 by volume) was created and autoclaved at 180 °C at various time scales. The $BiVO_4$ morphology was controlled by varying the reaction time, as well as the presence of sodium oleate. Based on photocatalytic reactions with Rhodamine B under VL with a cutoff at 380 nm, the $BiVO_4$ nanorods performed the best, followed by nanofibers and lastly microrods.

Li et al.[16] reported on monoclinic $BiVO_4$ of different morphologies synthesized by hydrothermal method. These structures include nano-sized cuboid-like, plate-like and flower-like nanostructures. The $Bi(NO_3)_3/NH_4VO_3$ solution was pH adjusted to 7, 9 and 11 to alter the morphology to nanocuboids, nanoplates and nanoflowers, respectively. All the nanostructures were pure monoclinic phase and had band gaps around 2.4 eV. Photocatalytic studies with methyl orange were conducted under sunlight irradiation. The studies show that the nanoflowers had the greatest photocatalytic degradation of methyl orange, followed by the nanoplates and then nanocuboids. The authors suggest that the high surface area from the nanoflowers led to the greatest photocatalytic performance. Additionally, Aeroxide® P25 was analyzed similarly and was outperformed by all the synthesized $BiVO_4$ nanostructures.

Similarly, Jiang et al.[17] reported on monoclinic $BiVO_4$ micro-sized structures of different morphologies synthesized by hydrothermal method. The $Bi(NO_3)_3/NH_4VO_3$ solution was created in the presence and absence of poly(vinyl pyrrolidone) as a surfactant to create porous nanostructures. The $BiVO_4$ with the surfactant came out as porous spheres, while the $BiVO_4$ in the absence of the surfactant came out as flowers-like structures. The porous $BiVO_4$ nanostructures naturally had greater surface area (5-8 m^2/g) than the non-porous $BiVO_4$ (2-3 m^2/g), and all had band gap energy of around 2.5 eV. Based on photocatalytic studies with methyl orange under visible radiance with a cutoff at 400 nm, the porous spheres performed better than the flower-like structures, naturally due to the greater surface area. Additionally, all the $BiVO_4$ samples performed better than Aeroxide® P25.

Pookmanee et al.[18] reported on $BiVO_4$ needle-shaped nanostructures synthesized via hydrothermal method. The samples were then calcined at 100 °C for 2, 4, and 6 hours. The needle-like nanostructures had sizes of 0.3 μm in width and 1.5 μm in length for 2 hour calcination, 0.5 μm in width and 2 μm in length for 4 hour calcination, and 1 μm in width and 4 μm in length for 6 hour calcinations. Based on photocatalytic studies with methylene blue under VL irradiation, performance increased with increased calcination time. Authors suggest that crystal phase had a larger impact on dictating photoactivity, since the 6 hour sample is the only pure monoclinic $BiVO_4$ synthesized.

Yu et al.[19] reported on nanofibrous $BiVO_4$ via hydrothermal synthesis. A suspension of NH_4VO_3 in HNO_3 was created and mixed with solution of heptane and hexanol (20:6 by volume). A solution of $Bi(NO_3)_3$ was added dropwise will stirring and the solution was subsequently and autoclaved at 160 °C for 48 hours. The $BiVO_4$ nanofibers had an average diameter of 100 nm and a surface area of 13 m^2/g, much larger than the surface area of bulk $BiVO_4$ at 0.5 m^2/g. The $BiVO_4$ nanofibrous structures were not analyzed for their VL photocatalytic activity.

To the best of my knowledge, only Liu et al. have reported on the synthesis $BiVO_4$ nanofibers via electrospinning, which has only been recently published.[20],[21] They reported on $BiVO_4$ nanofibers doped with phosphate (PO_4) and cobalt phthalocyanine (CoPc) for enhanced photocatalytic performance. Based on photocatalytic studies with methylene blue under VL irradiation with a cutoff at 400 nm, the two modified $BiVO_4$ nanofiber samples outperformed the unmodified $BiVO_4$ nanofibers. Although they have fabricated effective $BiVO_4$ nanofibers, their work, however, lacks

optimization of any sort. Firstly, their $BiVO_4$ nanofibers have an average diameter of 200 nm, which leaves much room for improvement to maximize surface area-to-volume ratio. Extensive synthesis tuning studies is also necessary to understand the boundaries and limitations of synthesizing a complex ternary metal oxide as $BiVO_4$. Finally, property-to-performance trends are important to understand links between material structure and reactivity and identify the major factor or factors that lead to the greatest photocatalytic performance. Altogether, these studies are currently unavailable and are essential for comprehending and developing $BiVO_4$ nanofibers as novel and effective VL photocatalysts.

In this work, $BiVO_4$ nanofibers were synthesized for the degradation of aqueous organic contaminants as a viable VL-active alternative to TiO_2. $BiVO_4$ nanofibers would be more beneficial towards future photocatalytic treatment systems, as they potentially provide greater performance than their nanoparticles counterparts, as well as having the potential for membrane integration. Optimization of this material was run in a similar fashion as with TiO_2, where morphology and dimension were altered and characterized to maximize photocatalytic performance. Prior to knowledge of recent $BiVO_4$ nanofiber work, a review was done on the synthesis of bismuth oxide (Bi_2O_3) and vanadium oxide (V_2O_5) nanofibers. Synthesis protocols from Wang et al.[22] for Bi_2O_3 and from Wang et al.[23] for V_2O_5 were used since the precursors of both metal oxides were dissolvable in a common solvent. Additionally, co-catalyzed $BiVO_4$ composite nanofibers were synthesized to enhance photocatalytic activity through increased carrier separation and create an improved VL-activated photocatalyst.[24]–[30]

4.3 Experimental Methods

4.3.1 Reagents

All chemicals were reagent grade or better and used as received. The synthesis of the $BiVO_4$ nanofibers involved bismuth(III) nitrate pentahydrate, ($Bi(NO_3)_3$) (Sigma Aldrich, 98%), vanadyl acetylacetonate, ($VO(C_5H_7O_2)_2$) (Sigma Aldrich, 98%), dimethylformamide (DMF) (Fisher Scientific) and polyvinylpyrrolidone (PVP) (Sigma Aldrich, MW: 1,300,000 g/mol). Additionally, pyridinium formate buffer ($C_6H_6NO_2$) (Santa Cruz Biotechnology, Inc.) and BYK-377 (BYK USA, Inc.) were used to alter solution electrical conductivity and surface tension, respectively, and added during solution preparation when indicated. Silver nitrate ($AgNO_3$) (Fisher Scientific) and gold(III) chloride trihydrate ($HAuCl_4 \cdot 3H_2O$) (Sigma Aldrich, >99.9%) were used as co-catalysts to enhance photocatalytic reactivity and introduced during solution preparation, calculated based on atomic percentage (at.%) of $BiVO_4$.

Similar to the TiO_2 work in Chapters 2 and 3, a buffer prepared from 5 mM potassium phosphate monobasic (Fisher Scientific, 99.3%) and 5 mM sodium chloride (NaCl) (Sigma Aldrich, >99.0%) was used in all photochemical experiments. A buffer prepared from 10 mM NaCl was used in all zeta potential experiments. Aeroxide® P25 (Acros Organics), as well as synthesized TiO_2 nanofibers, was used as a TiO_2 photocatalyst for treatment efficiency comparison. Phenol (Sigma-Aldrich, >99%) was used as a model organic micropollutant in all photoactivity studies. The eluent for HPLC analysis of phenol used sodium acetate (Sigma Aldrich, anhydrous) and acetonitrile

(ACN) (Fisher Scientific, 99.9%). All solutions were prepared in deionized (DI) water (Millipore, Milli-Q).

4.3.2 Synthesis of $BiVO_4$ Nanofibers

The synthesis of $BiVO_4$ nanofibers used 0.364 g of $Bi(NO_3)_3$, 0.2 g of $VO(C_5H_7O_2)_2$, a designated amount (7-8 wt. %) of PVP and 4.85 mL of DMF. The solution was mixed placed in a 20 mL glass beaker and stirred with a magnetic stirrer at a rate of 300 rpm for at least 2 hour. The addition of the volatile conductive buffer and surfactant were added, as indicated, at 1 and 0.5 wt.%, respectively. After thorough mixing, the electrospinning solution would have a deep blue color. The same electrospinning setup previously described in the TiO_2 and Fe_2O_3 nanofiber synthesis was used. The needle was set at a distance of 10 cm from the drum collector, the feed rate was varied from 0.2 to 0.5 mL/hr and the voltage was varied from 15 to 24 kV. Additionally, the electrospinning chamber was preheated at 40 °C. The $Bi(NO_3)_3/VO(C_5H_7O_2)_2$/PVP nanofiber film that was collected was very light blue in color. The $Bi(NO_3)_3/VO(C_5H_7O_2)_2$/PVP nanofibers were annealed at 350 °C at rate of 3 °C/min and held for 10 hours. After annealing, the $BiVO_4$ nanofibers were kept as dry samples in 20 mL glass vials for characterization and were later used to make 1 g/L stock suspensions in DI water for performance tests. The $BiVO_4$ nanofibers had a very bright yellow hue after annealing as expected. Co-catalyzed $BiVO_4$ nanofibers were synthesized in the same manner, where the metal salts, $AgNO_3$ and $HAuCl_4 \cdot 3H_2O$, were added during solution preparation at levels between 0.5 and 10 at. %.

4.3.3 Nanofiber Characterization

$BiVO_4$ nanofibers were characterized using several different techniques to quantify their size, morphological and optical properties. Nanofiber diameter was examined by a Phillips XL30 FEG scanning electron microscopy (SEM). For SEM, samples were prepared by placing approximately a 0.5 cm x 0.5 cm area of nanofibers onto a SEM sample holder. SEM imaging of $n = 40$ nanofibers yielded average diameters (with standard deviation) that were used to create sizing histograms. Additionally, Bi and V composition was analyzed by energy dispersive X-ray spectroscopy (EDX) following SEM analysis.

Crystal phase and average grain size were determined by a Bruker D8 Advance x-ray diffraction (XRD) analyzer. XRD samples were prepared in the same manner as described for the TiO_2 nanofibers. The 1 x 1 cm^2 samples were analyzed from 20° to 80° for the Bragg angle with an interval of 0.03°. Grain size was quantified by means of the Scherrer-Debye equation, which relates grain size to the diffraction peak properties.[31] The prominent monoclinic peak (121) was used for this calculation.

Band gap energy was quantified by a Thermo Scientific Evolution 300 UV-Vis spectrophotometer via diffuse reflectance infrared Fourier transform spectroscopy (DRIFTS). For analysis, the dry $BiVO_4$ samples were analyzed over a wavelength scan from 200 to 800 nm and absorbance was measured. The band gap was calculated by inserting the absorbance dataset of the nanofibers as a function of wavelength into the Kubelka-Munk method.[32],[33]

4.3.4 Photocatalysis Experiments

Reactivity experiments were conducted in batch systems using a commercially available 1000 W Xenon arc lamp (Newport Corporation). The light was first passed through a water filter to remove infrared (IR) radiation, reflected off a 90° full reflectance beam turning mirror, and then passed through a 305 nm long-pass filter to better simulate the spectrum of light available at earth's surface. In addition, a 395 nm filter as used to analyze photoreactivity in the presence of solely VL. Reactivity studies were conducted within a jacketed photoreactor containing catalyst suspensions (0.1 g/L) prepared at pH 7 (using 5 mM buffer) and maintained at 25 °C with a recirculating water bath.

After dispersion of nanofibers via sonication, suspensions were irradiated and aliquots were withdrawn over time to measure change in phenol concentration over time. Samples were centrifuged at 10,000 rpm for 8 min in the dark to allow extraction of the supernatant because filtration resulted in the loss of some analytes by sorption. The supernatant was transferred to a 1.5 mL amber autosampler vial for subsequent analysis via high performance liquid chromatography with photodiode array detector (1200 Series Agilent HPLC-DAD). The 1200 Series Agilent HPLC-DAD was equipped with an Eclipse XDB-C18 column (4.6 × 50 mm, 1.8 μm particle size). The HPLC method of analysis for phenol was based on previous work and employed a mobile phase of 65:35 1 mM sodium acetate: ACN at pH 3, a flow rate of 0.75 mL/min, an injection volume of 20 μL and a 254 nm detection wavelength.[34]–[36]

4.4 Results and Discussion

4.4.1 Nanofiber Characterization

The $BiVO_4$ nanofibers were synthesized based on solution chemistry and electrospinning parameters to minimize nanofiber diameter. Firstly, solution properties were independently controlled via polymer content for viscosity, addition of pyridinium formate buffer for electrical conductivity and addition of BYK-377 for surface tension. As seen in Table 4-1, viscosity was reduced from 46 to 36 cP (8 and 7 wt.% respectively), electrical conductivity increased from about 4 to 6 mS/cm (0 and 1 wt.% pyridinium formate buffer), and surface tension was reduced from 37 to 24 dynes/cm (0 and 0.5 wt.% BYK-377). Based on a review of Bi_2O_3 and V_2O_5 nanofibers,[22][23] an initial electrospinning protocol (8 wt.% PVP, 20 kV, 0.5 mL/hr, 10 cm) was utilized. Experimental design was performed for systematic testing and revealed that the control solution (Sample 2) yielded uniform nanofibers with an average diameter of 56 ± 10 nm. Electrospinning was unsuccessful at the lower PVP loading (Samples 1 and 3), yielding a rough film with spherical mounds. The addition of pyridium formate buffer didn't hinder the synthesis of nanofibers, but showed no significant change in average diameter. Lastly, the addition of the surfactant BYK-377 lowered the diameter of the 8% PVP samples (Samples 6 and 8) from about 60 to 40 nm and also led to the formation of nanofibers in the 7% samples. Despite having small sized nanofibers (~37 nm), the 7% samples (Samples 5 and 7) were heavily beaded (~1000 nm in width), indicating that 8% is the minimum limit in polymer content to maintain nanofiber uniformity. Altogether, surface

tension and viscosity had shown to be the two prominent solution properties in developing small nanofibers.

Table 4-1: Experimental design table of $BiVO_4$ nanofibers based on solution properties.

Samples		Solution Parameters			Solution Properties			Nanofiber Properties	
Number	DOE	PVP (%)	Pyridin. Formate (%)	BYK 337 (%)	Viscosity (cP)	Conductivity (mS/cm)	Surface Tension (dynes/cm)	Avg Diam. (nm)	Morphology
1	---	7	0	0	36	3.905	36.8	X	Film
2	+--	8	0	0	46	3.621	37.2	56.0	Uniform
3	-+-	7	1	0	37	6.195	37.0	X	Film
4	++-	8	1	0	46	6.062	37.1	60.9	Uniform
5	--+	7	0	0.5	36	3.915	23.9	38.1	Beaded
6	+-+	8	0	0.5	47	3.576	24.2	43.4	Uniform
7	-++	7	1	0.5	37	6.183	23.9	36.9	Beaded
8	+++	8	1	0.5	46	5.986	23.8	44.7	Uniform

Next, a new experimental design was constructed for the electrospinning parameters, as indicated in Figure 4-3. From the previous experimental design, the protocol of 8 wt.% PVP was utilized while altering applied voltage and feedrate as the electrospinning parameters; additionally, studies were conducted in the presence and absence of BYK-377, as surface tension had shown to be a significant factor. Applied voltage was varied from 15 to 24 kV and feedrate was altered from 0.2 to 0.5 mL/hr. The experimental design revealed that, with either the standard solution or the surfactant-containing solution, increased voltage to 20 kV led to smaller nanofibers sized nanofibers. Further increase in voltage led to larger nanofibers, indicating that 20 kV is the optimal voltage level to provide the smallest nanofibers. Moreover, decreased feedrate to 0.3 mL/hr led to smaller nanofibers for the BYK solution, where as the standard solution yielded films similar to the previous studies (Table 4-1). Below a

feedrate of 0.3 mL/hr, the average diameter steadily increased, possibly due to an unstable Taylor cone at such high voltage. Altogether, the nanofiber diameter as a function of voltage and feedrate yielded a bowl-shape function. The smallest nanofiber size of 33 nm was formed from a voltage of 20 kV and a feedrate of 0.3 mL/hr. Additionally, it was observed that the range of voltage and feedrate used to synthesize nanofibers with BYK-377 is extended due to reduction in surface tension, where solutions synthesized without BYK-377 did not yield nanofibers at similar electrospinning parameters. From these experiments, five samples were selected at different diameter levels for further characterization and performance studies. The histograms and SEM images of the select samples, which will be described henceforth as d = 33, 43, 51, 61, and 71 nm, can be seen in Figure 4-4. EDX analysis revealed that the $BiVO_4$ nanofibers maintained a 1:1 Bi to V atomic ratio, as expected. Additional studies had shown that increased temperature showed no significant change in nanofiber diameter, while slight increase humidity was detrimental to the morphology of nanofibers. Ag and Au co-catalyzed nanofibers were also successfully synthesized. While the unmodified $BiVO_4$ nanofibers were bright yellow, the Ag-$BiVO_4$ nanofibers had a faint gray tint that increased with increasing Ag content. The Au-$BiVO_4$ nanofibers maintained the yellow color, having a subtle green tint at higher Au content levels. The addition of Ag and Au co-catalysts in the $BiVO_4$ nanofibers showed little variability in average diameter at low content levels (0.5-2 at.%), but steadily increased with increasing co-catalyst content, with the 10 at.% nanofibers yielding diameters of 72 and 76 nm for Ag- and Au-$BiVO_4$, respectively (Figure 4-5).

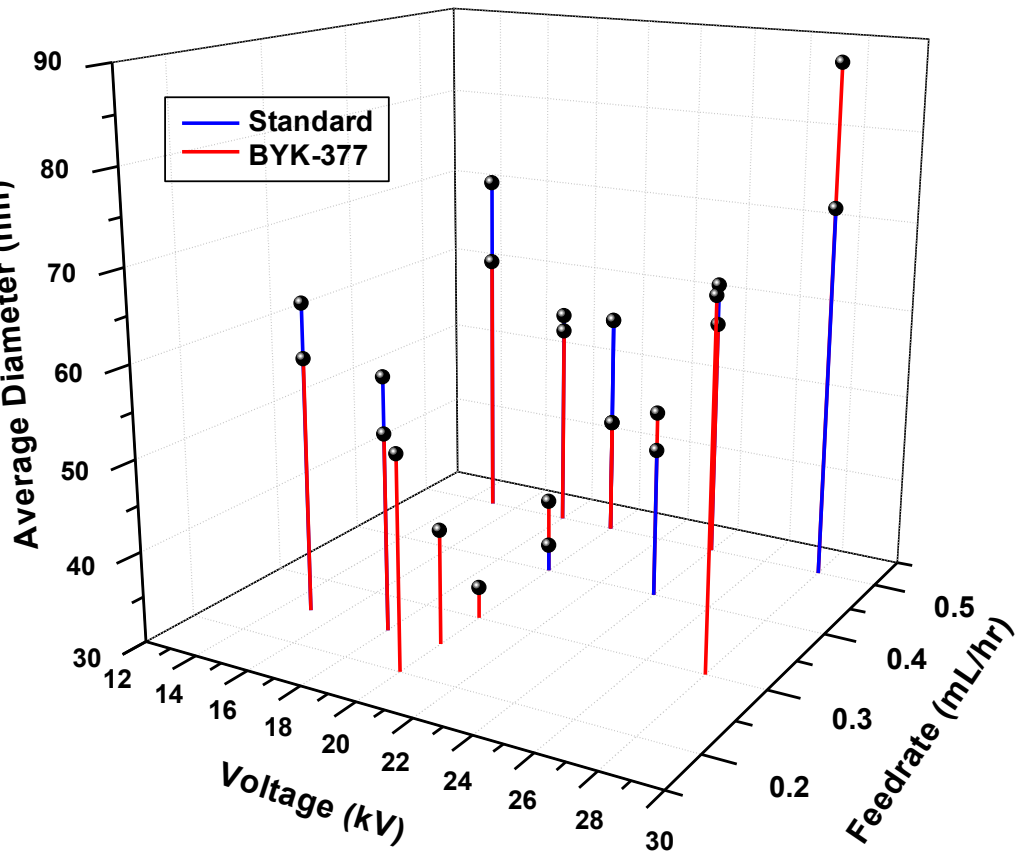

Figure 4-3: 3D surface plot of average diameter of $BiVO_4$ nanofibers as a function of voltage and feedrate with and without the surfactant BYK-377.

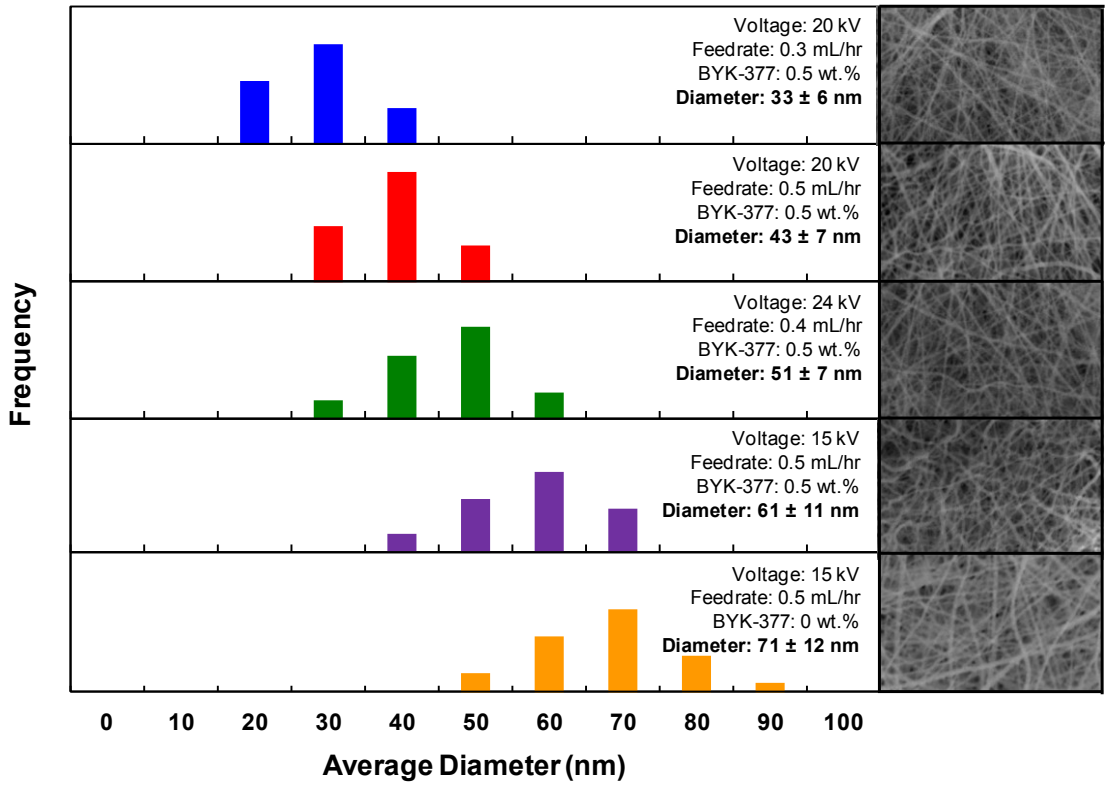

Figure 4-4: Histogram of $BiVO_4$ nanofiber average diameter with associated SEM images.

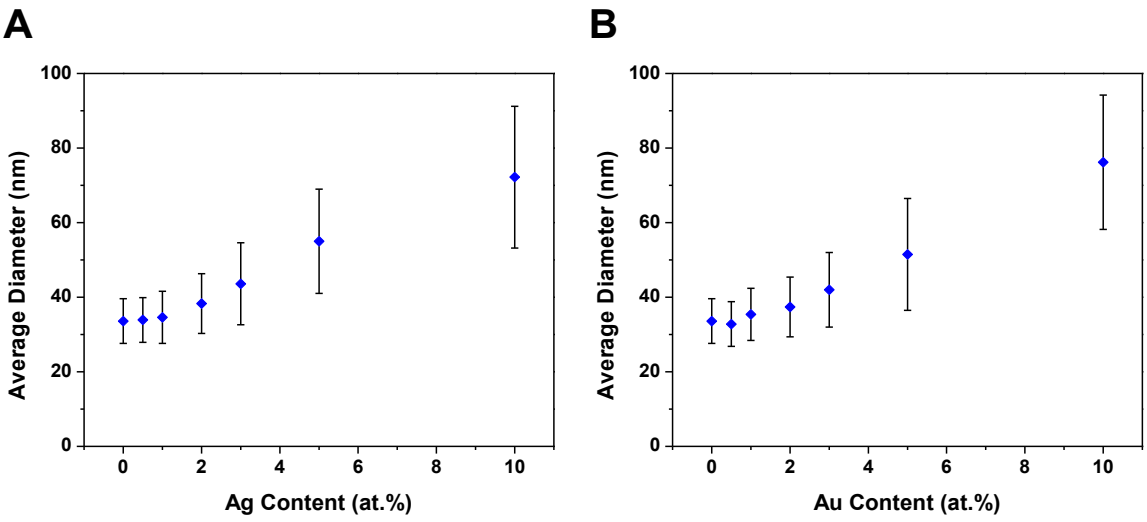

Figure 4-5: Average diameter as a function of co-catalyst content of A) Ag-$BiVO_4$ and B) Au-$BiVO_4$ nanofibers.

XRD characterization was conducted on the $BiVO_4$ nanofibers to analyze crystallinity. XRD spectra confirmed crystallization of the monoclinic phase (JCPDS #14-0688) independent of nanofiber diameter, as seen in Figure 4-6. Crystallization of the monoclinic crystal phase was targeted because of its superior performance over tetragonal and mixed phase $BiVO_4$. Additionally, average grain size was calculated via the Scherrer equation and determined to be stable at 23.4 ± 0.5 nm (Figure 4-7). Another set of materials were studied, designated as $BiVO_4$-G hereafter, synthesized with an average diameter of 33 nm yet annealed at varying durations to study grain size-dependent trends towards photocatalytic activity. Figure 4-8 shows that average grain size increased with increasing annealing duration time until reaching a plateau at about 27 nm. This phenomenon is suggested to be caused by the dimension confinement of the nanofiber diameter. Lastly, the XRD spectra of Ag- and Au-$BiVO_4$ nanofibers can be seen in Figure 4-9 and Figure 4-10, respectively. The addition of Ag and Au co-catalysts in the $BiVO_4$ nanofibers had little effect on the crystallinity of the monoclinic phase. Additionally, grain size slightly increased with the addition of the co-catalysts Ag or Au and remained stable regardless of co-catalyst content, having an average of 24.4 ± 0.4 nm for both Ag and Au co-catalyzed nanofibers. Small peaks around 38 degrees were observed for both Ag- and Au-$BiVO_4$ nanofibers at higher co-catalyst content levels (3 at.% for Ag-$BiVO_4$ and 5 at.% for Au-$BiVO_4$), which correlates with the prominent (111) of elemental Ag and Au, respectively.

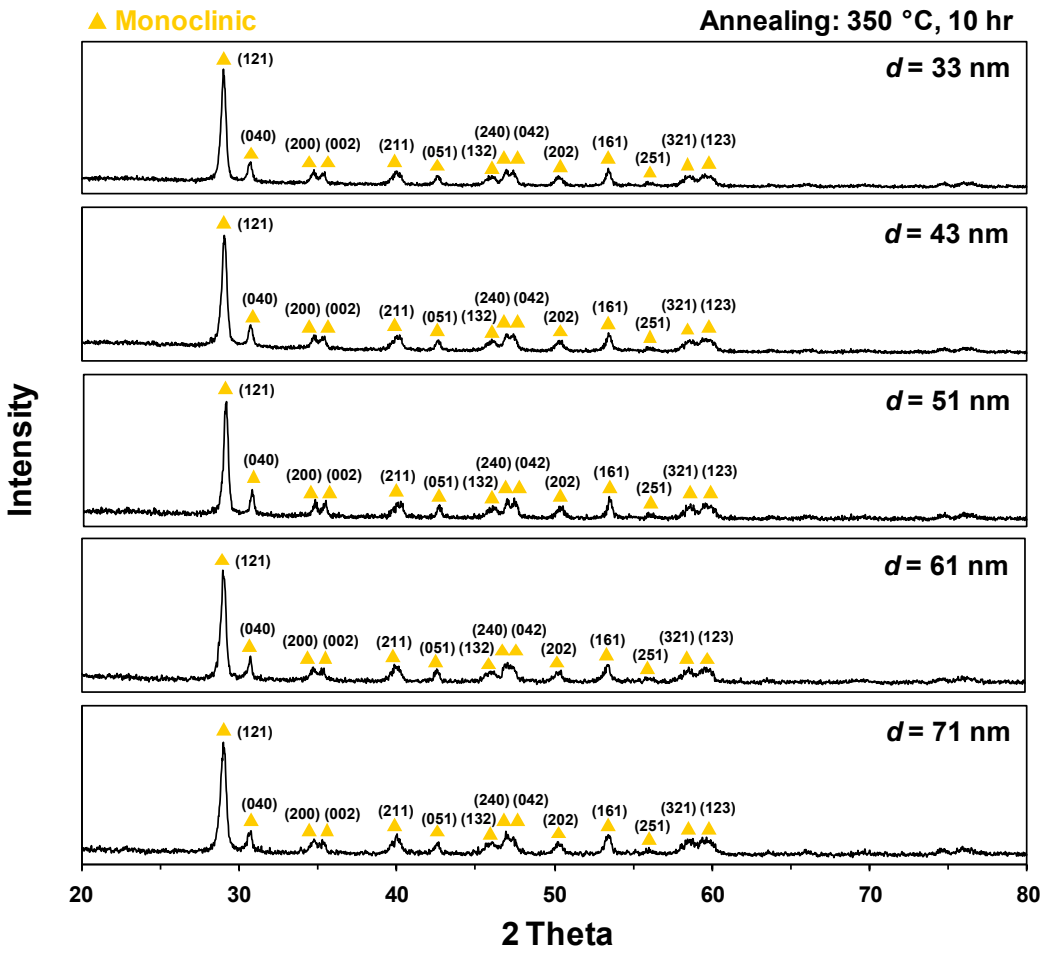

Figure 4-6: XRD patterns of the $BiVO_4$ nanofibers at different average diameter sizes.

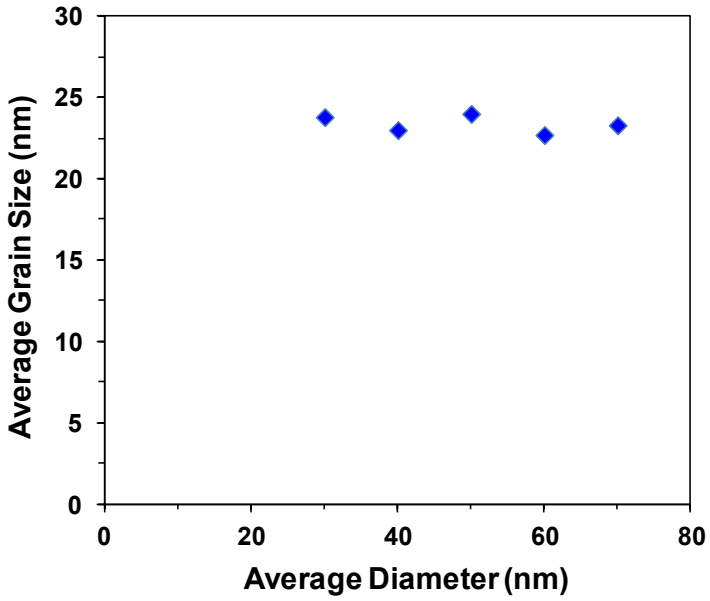

Figure 4-7: Average grain size as a function of $BiVO_4$ nanofiber diameter.

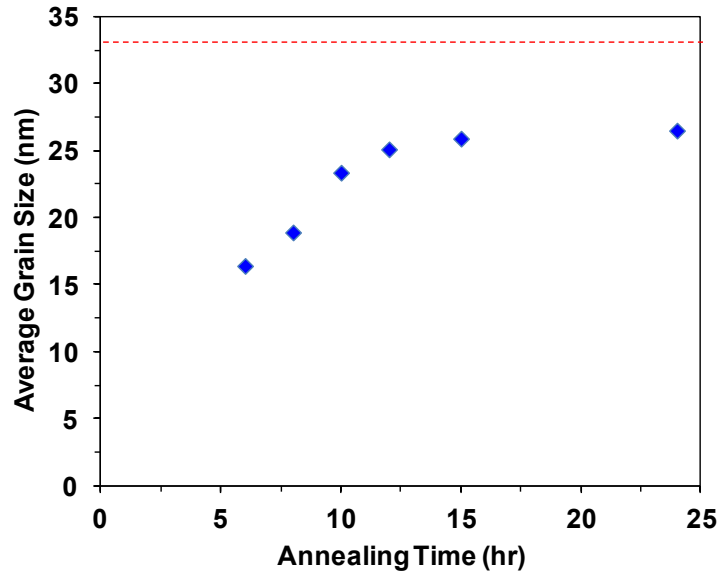

Figure 4-8: Average grain size of d = 33 nm $BiVO_4$ nanofiber as a function of annealing time.

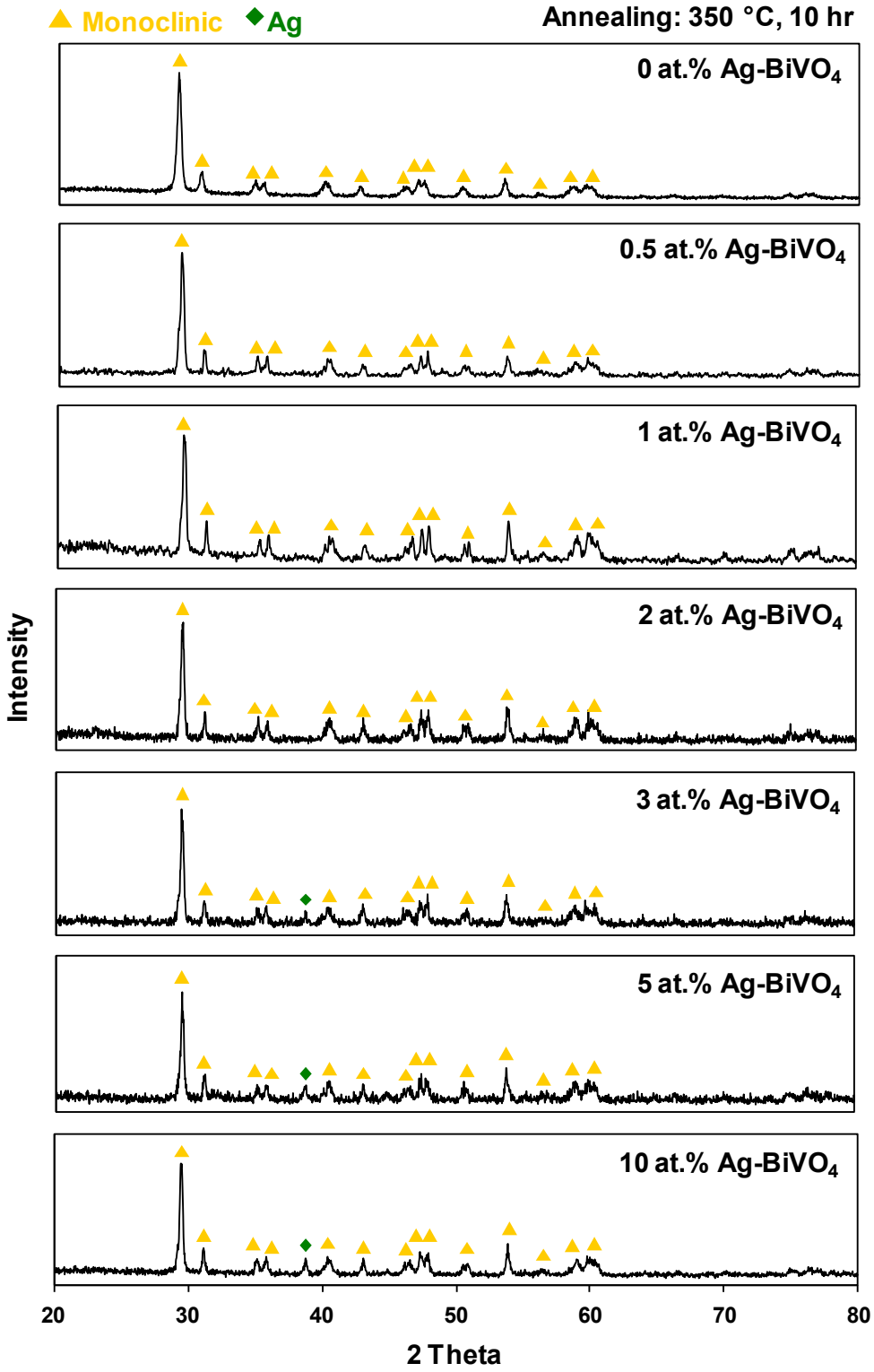

Figure 4-9: XRD patterns of the Ag-$BiVO_4$ nanofibers at different Ag content levels.

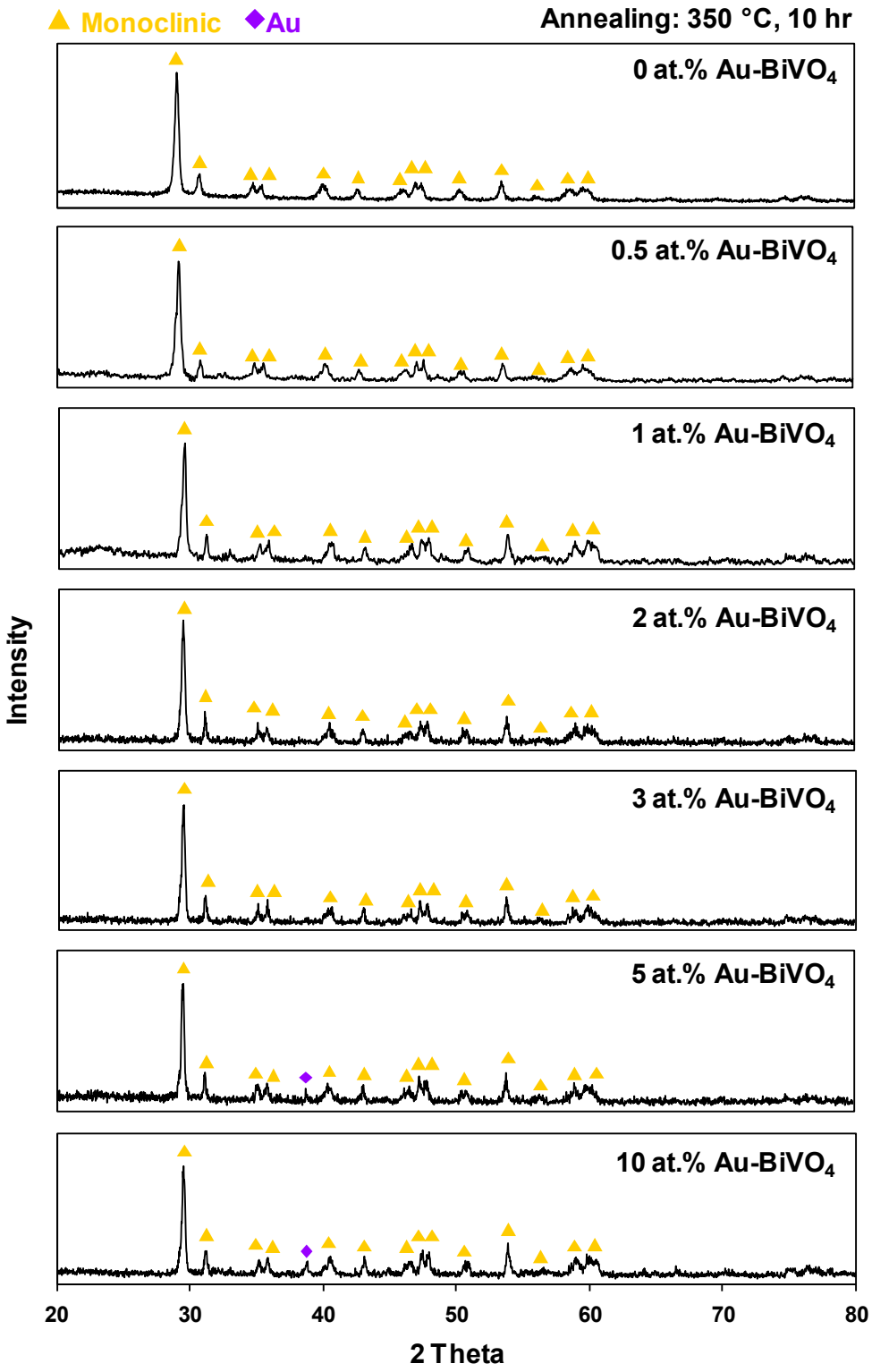

Figure 4-10: XRD patterns of the Au-$BiVO_4$ nanofibers at different Au content levels.

Diffuse reflectance analysis, configured with the Kubelka-Munk method, showed that the $BiVO_4$ nanofibers had an average band gap of 2.39 ± 0.1 eV (Figure 4-11), in accord with previous studies.[9],[12],[13] The value of band gap was stable regardless of the variance in average diameter, which was expected since the Bohr radius of both Bi_2O_3 and V_2O_5 are below ~10 nm.[37]–[41] The addition of Ag and Au co-catalysts in the $BiVO_4$ nanofibers lead to a decrease in band gap value, as seen in Figure 4-12 and Figure 4-13 respectively. Adsorption of VL increased and band gap steadily decreased with increased co-catalyst content, indicating improved VL response of the co-catalyzed nanofibers.[42],[43] Additionally, the presence of a small peak at ~630 nm was observed in the Au-$BiVO_4$ nanofibers at all content levels, indicating surface plasmon resonance from the Au nanoparticles. The surface plasmon peak for Au was observed at a larger wavelength than reported (~520 nm) because of the high refractive index of $BiVO_4$, similar to TiO_2.[44] The surface plasmon peak shifted to longer wanvelengths with Au content, denoting a possible increase in Au nanoparticle size.[27] Based on Kubelka-Munk calculations, band gap decreased steadily with increased co-catalyst content for both composite nanofibers, from 2.39 eV at 0 at.% to 2.24 and 2.23 eV at 10 at.% Ag and Au, respectively.

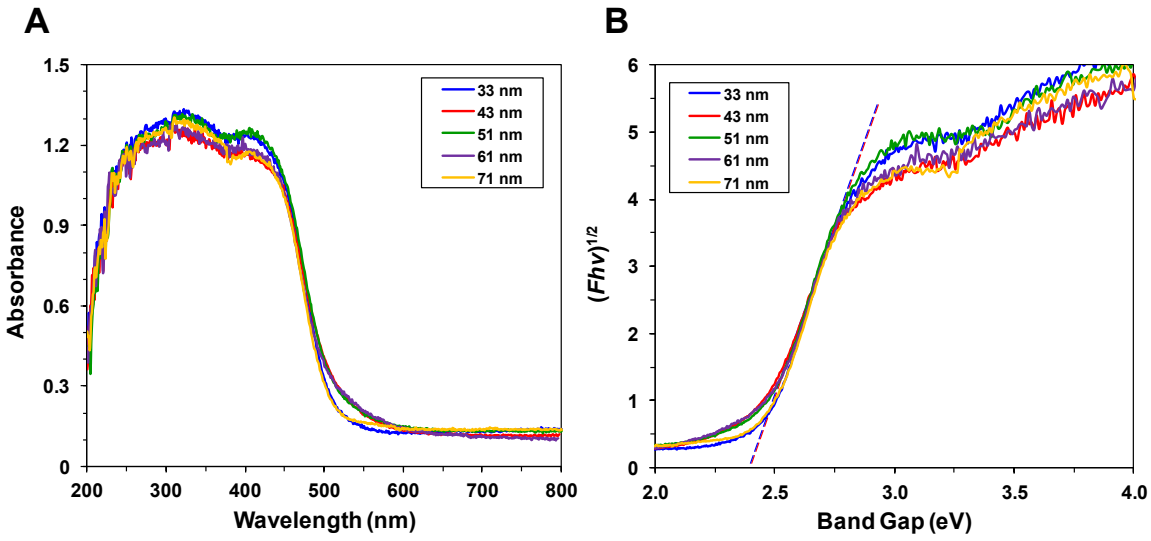

Figure 4-11: A) Diffuse reflectance absorbance curves of different nanofiber diameter and B) Kubelka-Munk function as a function of band gap of $BiVO_4$ nanofibers.

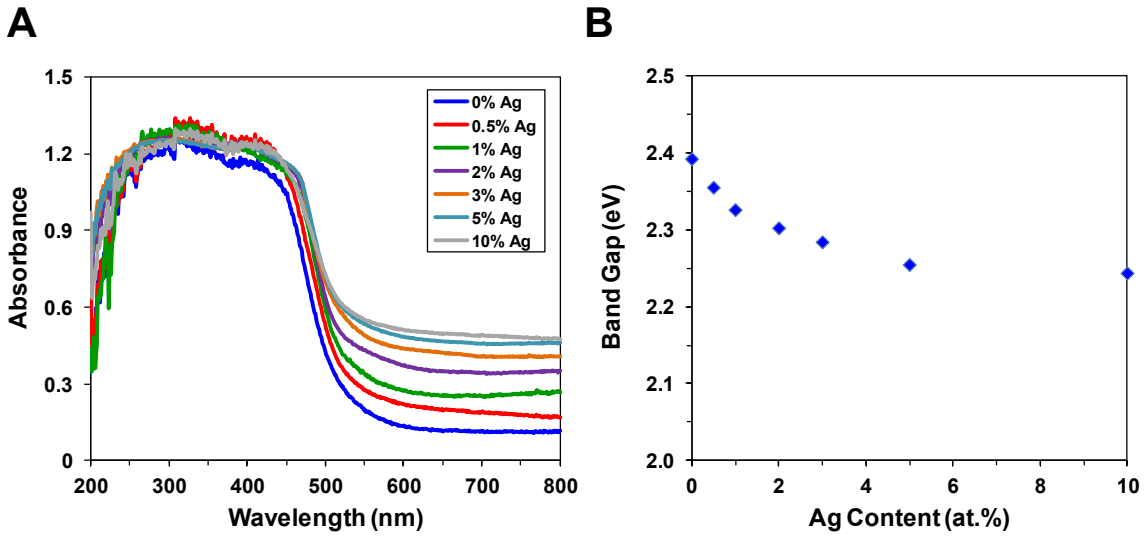

Figure 4-12: A) Diffuse reflectance absorbance curves of Ag-$BiVO_4$ nanofibers at different Ag content levels and B) Kubelka-Munk calculated band gap as a function of Ag content.

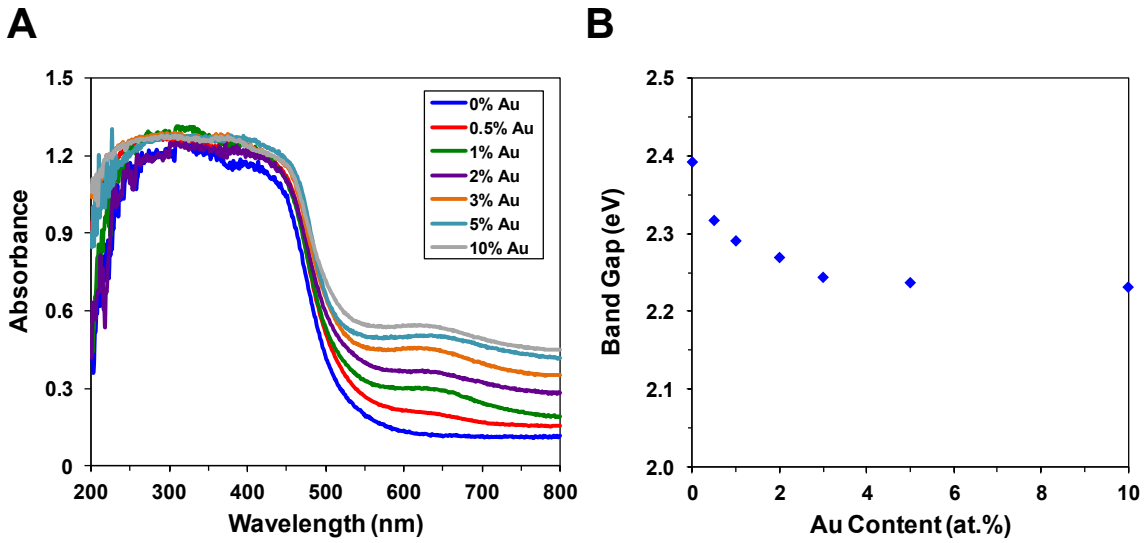

Figure 4-13: A) Diffuse reflectance absorbance curves of Au-$BiVO_4$ nanofibers at different Au content levels and B) Kubelka-Munk calculated band gap as a function of Au content.

Zeta potential analysis, seen in Figure 4-14, revealed that the pzc of the $BiVO_4$ nanofibers averaged to a value of 3.91 ± 0.1, which rests within the accepted range of 3-5.[45]–[48] Zeta potential analysis was not conducted on the co-catalyzed $BiVO_4$ nanofibers, since surface charge is not expected to change with the addition of co-catalysts based on work from Chapter 3. Lastly, specific surface area of the $BiVO_4$ nanofibers, characterized by BET analysis, increased from 4.2 to 21.1 m^2/g with decreasing diameter. The surface area was relatively larger than reported $BiVO_4$ nanomaterials (1-8 m^2/g),[9],[17],[49],[50] possibly due to the fiber morphology's higher surface-to-volume ratio, yet lower than conventional photocatalysts (Aeroxide® P25 TiO_2, 52 m^2/g). Additionally, the addition of Ag and Au (up to 2 at.%) had minimal effect on the surface area (~21-22 m^2/g), similar to previous reports.[24],[28],[51] Any reactivity enhancement from the co-catalysts would not be attributed to surface area or porosity.

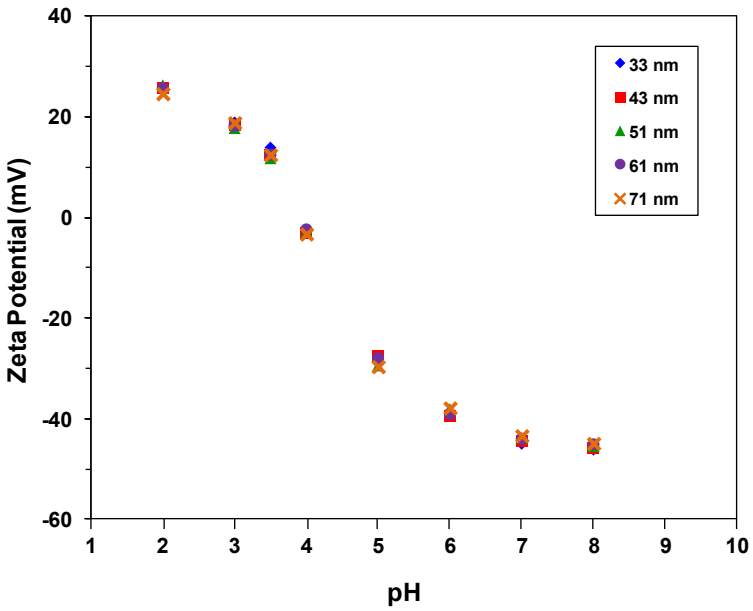

Figure 4-14: Zeta potential of $BiVO_4$ nanofibers at different average diameters.

4.4.2 Photocatalysis of $BiVO_4$ Nanofibers

For the photocatalytic studies of $BiVO_4$, the nanofiber materials were run against the pollutant phenol under both solar ($\lambda > 305$ nm) and VL ($\lambda > 395$ nm) irradiation. The average k_{obs} values for phenol decay were compared based on nanofiber property and light spectrum, as well as compared to commercially-available powders. Figure 4-15 shows reactivity as a function of nanofiber diameter, where reactivity increased with decreasing average diameter. Normalized by surface area, reactivity was roughly stable with diameter ($(7.31 \pm 0.28) \times 10^{-5}$ $m^2/g \cdot min$), confirming the surface area-to-volume ratio effect. Additionally, it can be seen that reactivity was reduced in the presence of VL only ($\lambda > 395$ nm). Reactivity was optimal at the smallest diameter ($d = 33$ nm), having a reaction rate constant k_{obs} of $(1.42 \pm 0.04) \times 10^{-3}$ and $(1.04 \pm 0.06) \times 10^{-3}$ min^{-1} under solar and VL irradiation, respectively. In comparison with TiO_2 photocatalysts, which

include electrospun TiO_2 and 0.5% Ag-TiO_2 nanofibers (Chapter 3) and commercially-available Aeroxide® P25, the $BiVO_4$ nanofibers performed poorly under solar irradiation conditions (Figure 4-16-A). On the contrary, the $BiVO_4$ nanofibers outperformed Aeroxide® P25 (8.87×10^{-4} min^{-1}) and TiO_2 nanofibers (7.66×10^{-4} min^{-1}) under VL irradiation while still being outshined by the Ag-TiO_2 nanofibers (1.26×10^{-3} min^{-1}; Figure 4-16-B). Altogether, the reactivity of TiO_2 photocatalysts was reduced by ~99% in the presence of VL, where the reduction was only ~30% for $BiVO_4$ nanofibers, indicating effective VL photocatalysis. The photocatalytic reactions of the $BiVO_4$-G samples showed no visible trend between grain size and photoreacticity, as the rate constants were relatively stable as a function of average grain size (Figure 4-17).

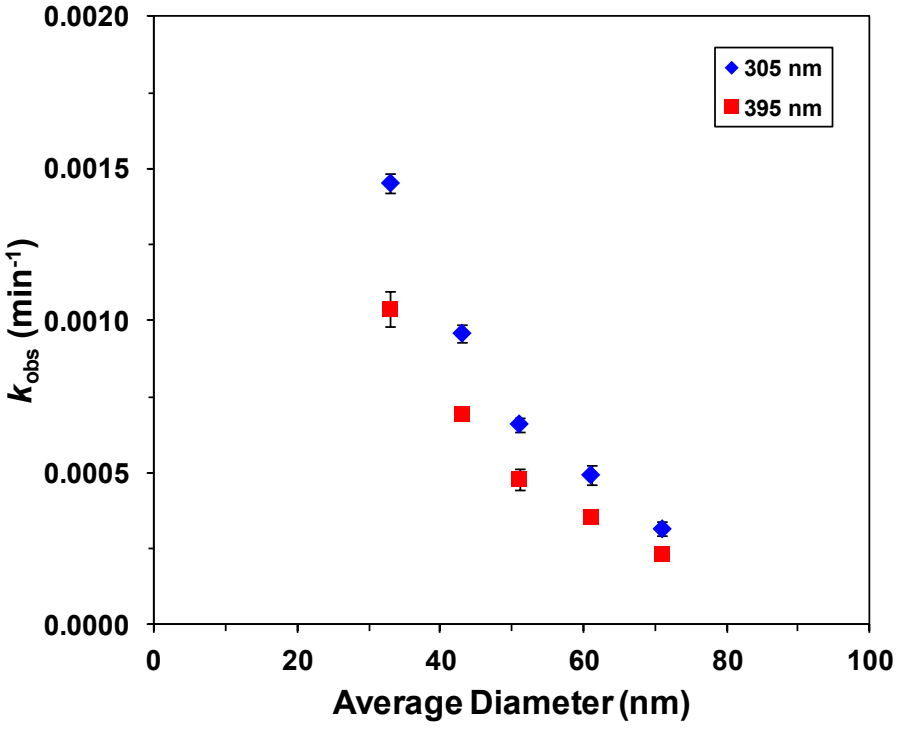

Figure 4-15: First order reaction rate constant (k_{obs}) as a function of average diameter of $BiVO_4$ nanofibers at different irradiation conditions.

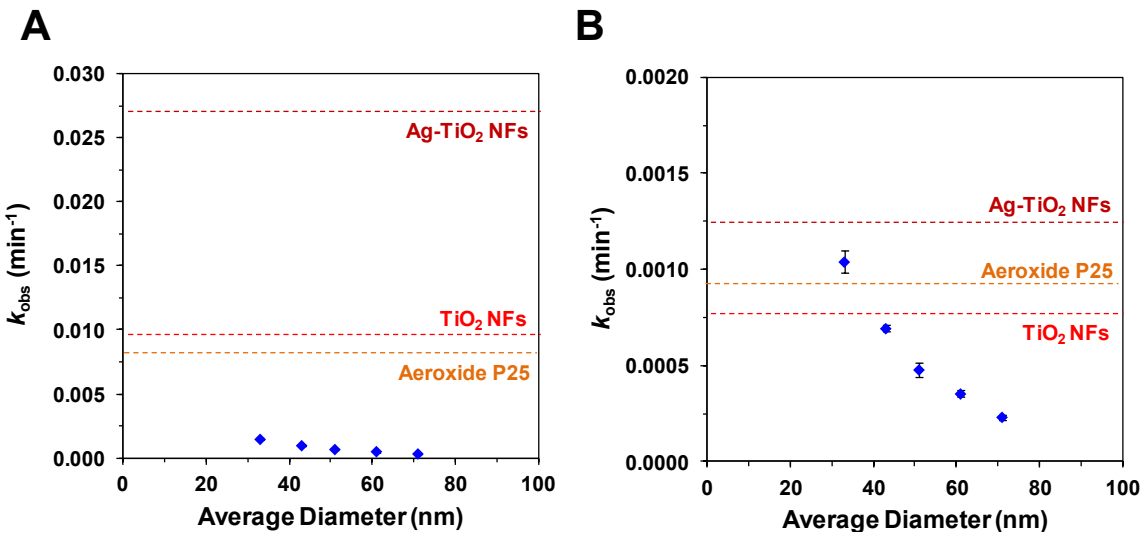

Figure 4-16: First order reaction rate constant (k_{obs}) as a function of average diameter of $BiVO_4$ nanofibers under A) solar irradiation (λ > 305 nm) and B) VL irradiation (λ > 395 nm). Dotted lines indicate k_{obs} of several TiO_2 photocatalysts for comparison.

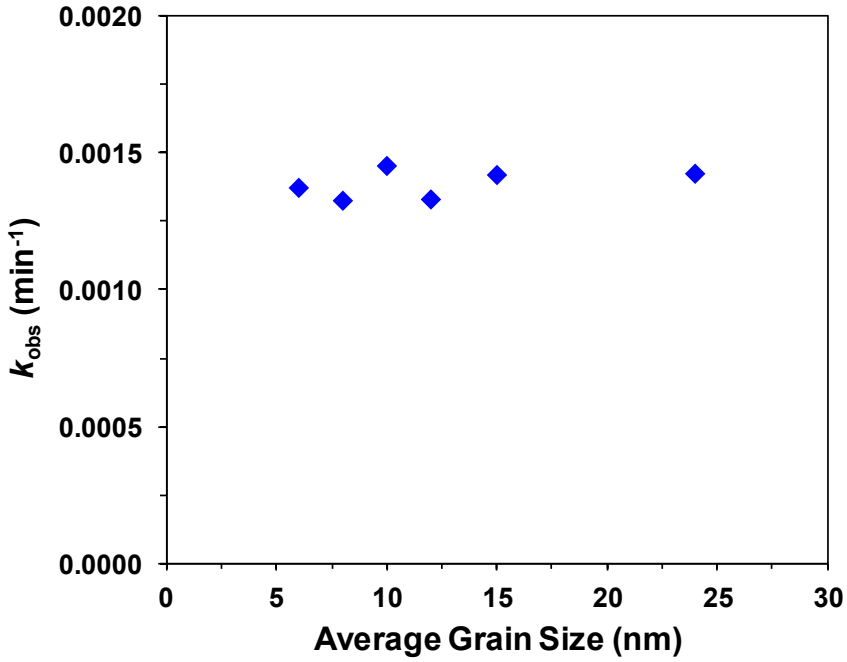

Figure 4-17: First order reaction rate constant (k_{obs}) as a function of average grain size of $BiVO_4$ nanofibers under solar irradiation (λ > 305 nm) conditions.

The introduction of both Ag and Au co-catalysts to the $BiVO_4$ nanofibers showed improved photocatalystic activity. Under solar irradiation, rate constant of the Ag-$BiVO_4$ nanofibers initially increased with increased Ag content, reaching a maximum at 1 at.% Ag ((2.34 ± 0.15) x 10^{-3} min^{-1}) (Figure 4-18). Afterwards, reactivity decreased when Ag content was greater than 1 at.% Ag, indicating an optimal Ag content level for enhanced reactivity. The Au-$BiVO_4$ nanofibers also outperformed unmodified $BiVO_4$ under solar irradiation conditions, but not to the extent of the Ag-$BiVO_4$ nanofibers. Similar to the Ag-$BiVO_4$ nanofibers, the optimal performance was seen 1 at.% Au ((1.79 ± 0.04) x 10^{-3} min^{-1}). Still, their performance was unsatisfactory compared to TiO_2 photocatalysts under solar irradiation from Figure 4-16.

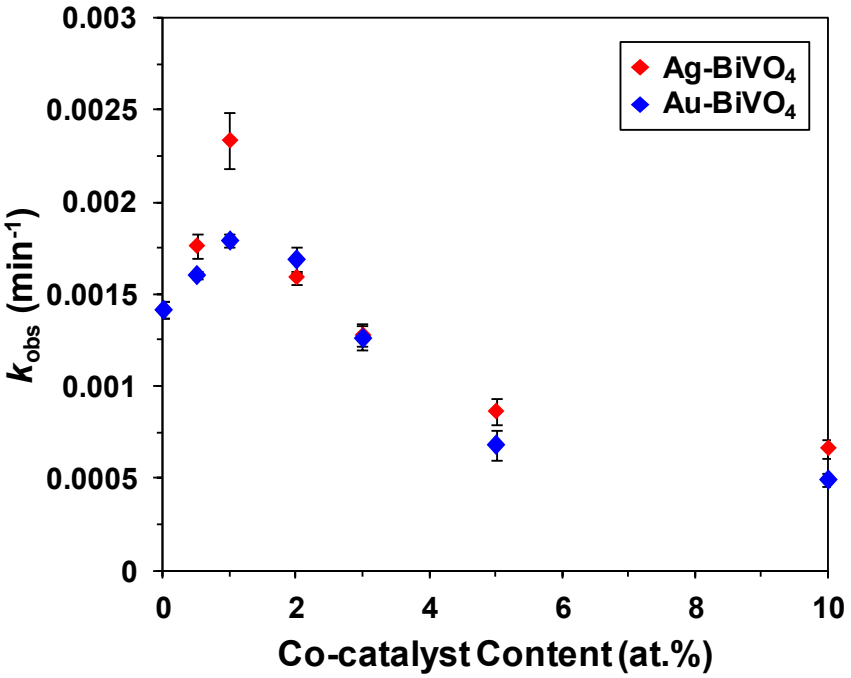

Figure 4-18: First order reaction rate constant (k_{obs}) as a function of co-catalyst content of Ag- and Au-$BiVO_4$ nanofibers under solar irradiation (λ > 305 nm) conditions.

Reactivity of the Ag-$BiVO_4$ nanofibers under VL irradiation (Figure 4-19-A) resulted in a trend similar to the outcome under solar irradiation, where reactivity was optimal at 1 at.% Ag ((1.55 ± 0.07) x 10^{-3} min^{-1}). Considering that reactivity trends of solar and VL irradiation were similar, the enhanced photocatalytic performance of the Ag-$BiVO_4$ nanofibers is attributed to increased carrier traps by the Ag nanoparticles, promoting greater electron-hole separation and reducing carrier recombination.[52],[53] Under VL irradiation, reactivity of the Au-$BiVO_4$ increased rapidly with increased Au content, surpassing the solar irradiated kinetics (Figure 4-19-B). This indicates strong surface plasmon resonance from the Au nanoparticles.[54]–[56] The optimal performance under VL irradiation was seen from 2 at.% Au ((2.12 ± 0.06) x 10^{-3} min^{-1}), outperforming the unmodified $BiVO_4$ nanofibers by a factor of 2. An optimum found in both composite nanofiber trends denotes an optimal size or surface area-to-volume ratio of the co-catalyst nanoparticles, similar to the results in Chapter 3.[57] Although the addition of the co-catalysts reduced band gap, optimal reactivity was observed in the samples with larger band gaps, not indicative of the band gap narrowing mechanism. Additionally, the decrease in reactivity with increased co-catalyst content can stem from either the increase in co-catalyst nanoparticle size or the increase in the nanofiber diameter (Figure 4-20).[58] Altogether, the Ag-$BiVO_4$ nanofibers saw enhanced reactivity due to increased carrier traps that help facilitate electron-hole separation and reduce carrier recombination,[53],[59],[60] while the Au-$BiVO_4$ nanofibers saw enhanced reactivity due to both carrier traps for electron-hole separation and local surface plasmon resonance that concentrate VL photons to promote increased electron excitation.[55],[56],[61],[62]

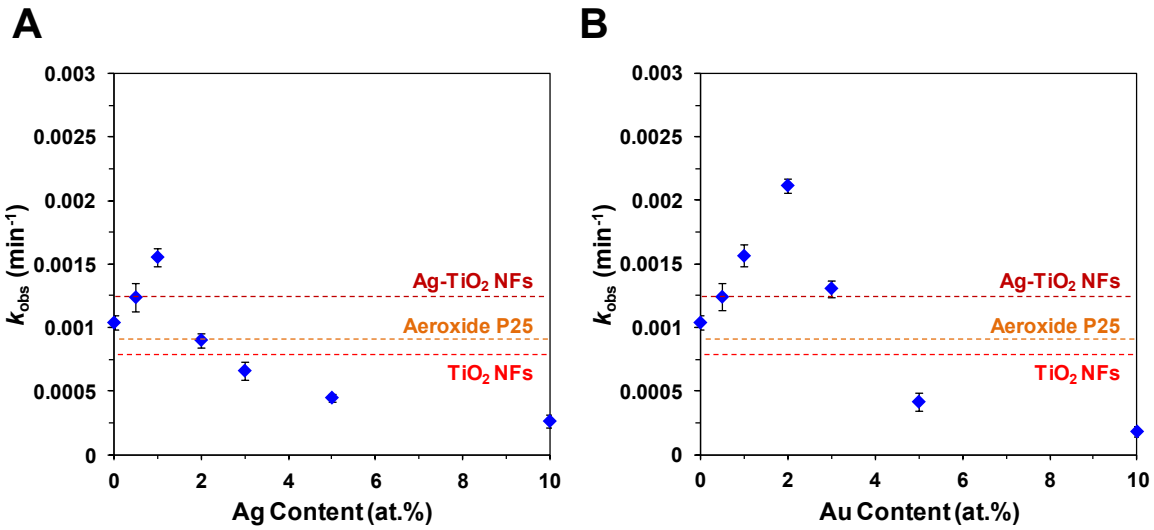

Figure 4-19: First order reaction rate constant (k_{obs}) as a function of co-catalyst content of A) Ag-$BiVO_4$ and B) Au-$BiVO_4$ nanofibers under VL irradiation ($\lambda > 395$ nm). Dotted lines indicate k_{obs} of several TiO_2 photocatalysts for comparison.

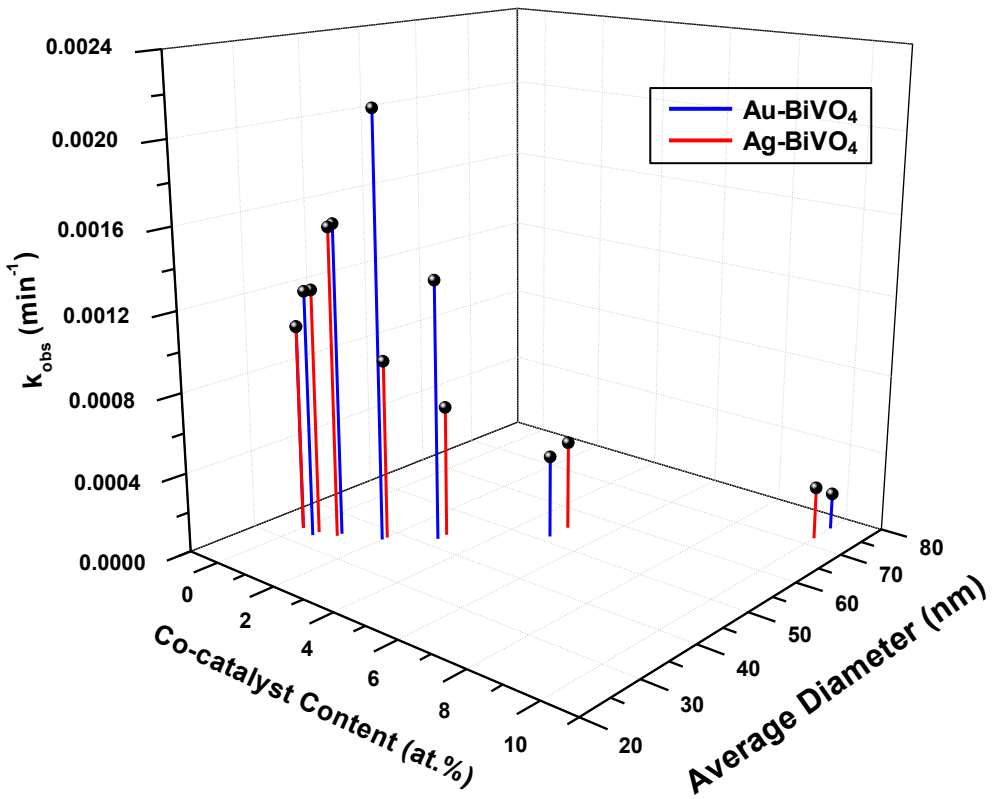

Figure 4-20: First order reaction rate constant (k_{obs}) as a function of co-catalyst content and average diameter of Ag- and Au-$BiVO_4$ nanofibers under VL irradiation ($\lambda > 395$ nm).

4.5 Conclusions

Although TiO_2 photocatalysts have shown to be a very efficient material for photo-oxidation throughout the years, its limitations in the solar spectrum have brought a push towards non-titania semiconductors, such as $BiVO_4$, for VL-activated photocatalysis. This study presents the facile synthesis of $BiVO_4$ nanofibers as a possible next-gen photocatalyst for the removal of organic contaminants in impaired water sources. Through strenuous experimental design, including solution properties, electrospinning parameters, ambient parameters and calcinations parameters, nanofiber size was optimized to 33 nm, showing controlled diameter tuning through the synthesis technique, as well as morphological and optical property control. Photocatalyic reactivity studies showed the greatest performance from the smallest sized nanofibers, due to the increased surface area-to-volume ratio. The addition of co-catalysts Ag and Au separately resulted in enhanced photoreactivity of the $BiVO_4$ in both solar and VL irradiation conditions. Although performance was diminutive compared to TiO_2 photocatalysts under solar irradiation conditions, the co-catalyzed $BiVO_4$ nanofibers outperformed TiO_2 under VL. The 2 at.% Au-$BiVO_4$ nanofibers, which showed the greatest photocatalytic performance, outperformed unmodified $BiVO_4$ nanofibers by a factor of 2. Electrospun $BiVO_4$ nanofibers, with their ease in synthesis and tenability and their high reactivity, have shown to be a novel material for VL-activated photocatalysis and potential adaptability in nanotechnology-integrated treatment systems.

4.6 References

[1] Biernat, K.; Malinowski, A.; Gnat, M. The Possibility of Future Biofuels Production Using Waste Carbon Dioxide and Solar Energy. In *Biofuels - Economy, Environment and Sustainability*; InTech: Rijeka, 2013.

[2] Zhang, L.; Long, J.; Pan, W.; Zhou, S.; Zhu, J.; Zhao, Y.; Wang, X.; Cao, G. Efficient Removal of Methylene Blue over Composite-Phase $BiVO_4$ Fabricated by Hydrothermal Control Synthesis. *Materials Chemistry and Physics* **2012**, *136*, 897–902.

[3] Hou, L.; Yang, L.; Li, J.; Tan, J.; Yuan, C. Efficient Sunlight-Induced Methylene Blue Removal over One-Dimensional Mesoporous Monoclinic $BiVO_4$ Nanorods. *Journal of Analytical Methods in Chemistry* **2012**, *2012*, 345247.

[4] Eastaugh, N.; Walsh, V.; Chaplin, T.; Sidda, R. *Pigment Compendium: A Dictionary of Historical Pigments*; Butterworth-Heinemen: Oxford, 2008.

[5] Smith, H. M. *High Performance Pigments*; Wiley-VCH: Weinheim, 2002.

[6] Pookmanee, P.; Kojinok, S.; Phanichphant, S. Bismuth Vanadate ($BiVO_4$) Powder Prepared by the Sol-Gel Method. *Journal of Metals, Materials and Minerals* **2012**, *22*, 49–53.

[7] Dunkle, S. S.; Helmich, R. J.; Suslick, K. S. $BiVO_4$ as a Visible-Light Photocatalyst Prepared by Ultrasonic Spray Pyrolysis. *Journal of Physical Chemistry C Letters* **2009**, *113*, 11980–11983.

[8] Zhou, L.; Wang, W.; Zhang, L.; Xu, H.; Zhu, W. Single-Crystalline $BiVO_4$ Microtubes with Square Cross-Sections: Microstructure, Growth Mechanism, and Photocatalytic Property. *Journal of Physical Chemistry C* **2007**, *111*, 13659–13664.

[9] Kudo, A.; Omori, K.; Kato, H. A Novel Aqueous Process for Preparation of Crystal Form-Controlled and Highly Crystalline $BiVO_4$ Powder from Layered Vanadates at Room Temperature and Its Photocatalytic and Photophysical Properties. *Journal of the American Chemical Society* **1999**, *121*, 11459–11467.

[10] Zhang, X.; Ai, Z.; Jia, F.; Zhang, L.; Fan, X.; Zou, Z. Selective Synthesis and Visible-Light Photocatalytic Activities of $BiVO_4$ with Different Crystalline Phases. *Materials Chemistry and Physics* **2007**, *103*, 162–167.

[11] Fan, H.; Jiang, T.; Li, H.; Wang, D.; Wang, L.; Zhai, J.; He, D.; Wang, P.; Xie, T. Effect of $BiVO_4$ Crystalline Phases on the Photoinduced Carriers Behavior and Photocatalytic Activity. *Journal of Physical Chemistry B* **2012**, *116*, 2425–2430.

[12] Walsh, A.; Yan, Y.; Huda, M. N.; Al-Jassim, M. M.; Wei, S.-H. Band Edge Electronic Structure of $BiVO_4$: Elucidating the Role of the Bi S and V D Orbitals. *Chemistry of Materials* **2009**, *21*, 547–551.

[13] Park, Y.; McDonald, K. J.; Choi, K.-S. Progress in Bismuth Vanadate Photoanodes for Use in Solar Water Oxidation. *Chemical Society Reviews* **2013**, *42*, 2321–2337.

[14] Zhou, L.; Wang, W.; Liu, S.; Zhang, L.; Xu, H.; Zhu, W. A Sonochemical Route to Visible-Light-Driven High-Activity $BiVO_4$ Photocatalyst. *Journal of Molecular Catalysis A: Chemical* **2006**, *252*, 120–124.

[15] Wang, X.; Li, G.; Ding, J.; Peng, H.; Chen, K. Facile Synthesis and Photocatalytic Activity of Monoclinic $BiVO_4$ Micro/nanostructures with Controllable Morphologies. *Materials Research Bulletin* **2012**, *47*, 3814–3818.

[16] Li, H.; Liu, G.; Duan, X. Monoclinic $BiVO_4$ with Regular Morphologies: Hydrothermal Synthesis, Characterization and Photocatalytic Properties. *Materials Chemistry and Physics* **2009**, *115*, 9–13.

[17] Jiang, H.; Dai, H.; Meng, X.; Zhang, L.; Deng, J.; Liu, Y.; Au, C. T. Hydrothermal Fabrication and Visible-Light-Driven Photocatalytic Properties of Bismuth Vanadate with Multiple Morphologies And/or Porous Structures for Methyl Orange Degradation. *Journal of Environmental Sciences* **2012**, *24*, 449–457.

[18] Pookmanee, P.; Pingmuang, K.; Kangwansupamomkon, W.; Phanichphant, S. Methylene Blue Degradation over Photocatalyst Bismuth Vanadate Powder Synthesized by the Hydrothermal Method. *Advanced Materials Research* **2010**, *93-94*, 177–180.

[19] Yu, J.; Kudo, A. Hydrothermal Synthesis of Nanofibrous Bismuth Vanadate. *Chemistry Letters* **2005**, *34*, 850–851.

[20] Liu, G.; Liu, S.; Lu, Q.; Sun, H.; Xiu, Z. $BiVO_4$/cobalt Phthalocyanine (CoPc) Nanofiber Heterostructures: Synthesis, Characterization and Application in Photodegradation of Methylene Blue. *RSC Advances* **2014**, *4*, 53402–53406.

[21] Liu, G.; Liu, S.; Lu, Q.; Sun, H.; Xiu, Z. Synthesis and Characterization of $Bi(VO_4)_{1-m}(PO_4)_m$ Nanofibers by Electrospinning Process with Enhanced Photocatalytic Activity under Visible Light. *RSC Advances* **2014**, *4*, 33695–33701.

[22] Wang, C.; Shao, C.; Wang, L.; Zhang, L.; Li, X.; Liu, Y. Electrospinning Preparation, Characterization and Photocatalytic Properties of Bi_2O_3 Nanofibers. *Journal of Colloid and Interface Science* **2009**, *333*, 242–248.

[23] Wang, H.-G.; Ma, D.-L.; Huang, Y.; Zhang, X.-B. Electrospun V_2O_5 Nanostructures with Controllable Morphology as High-Performance Cathode Materials for Lithium-Ion Batteries. *Chemistry – A European Journal* **2012**, *18*, 8987–8993.

[24] Kohtani, S.; Hiro, J.; Yamamoto, N.; Kudo, A.; Tokumura, K.; Nakagaki, R. Adsorptive and Photocatalytic Properties of Ag-Loaded $BiVO_4$ on the Degradation of 4-N-Alkylphenols under Visible Light Irradiation. *Catalysis Communications* **2005**, *6*, 185–189.

[25] Kohtani, S.; Tomohiro, M.; Tokumura, K.; Nakagaki, R. Photooxidation Reactions of Polycyclic Aromatic Hydrocarbons over Pure and Ag-Loaded $BiVO_4$ Photocatalysts. *Applied Catalysis B: Environmental* **2005**, *58*, 265–272.

[26] Kohtani, S.; Yoshida, K.; Maekawa, T.; Iwase, A.; Kudo, A.; Miyabe, H.; Nakagaki, R. Loading Effects of Silver Oxides upon Generation of Reactive Oxygen Species in Semiconductor Photocatalysis. *Physical chemistry chemical physics : PCCP* **2008**, *10*, 2986–92.

[27] Pingmuang, K.; Wetchakun, N.; Kangwansupamonkon, W.; Ounnunkad, K.; Inceesungvorn, B.; Phanichphant, S. Photocatalytic Mineralization of Organic Acids over Visible-Light-Driven Au/$BiVO_4$ Photocatalyst. *Internation Journal of Photoenergy* **2013**, *943256*, 1–7.

[28] Xu, H.; Li, H.; Wu, C.; Chu, J.; Yan, Y.; Shu, H.; Gu, Z. Preparation, Characterization and Photocatalytic Properties of Cu-Loaded $BiVO_4$. *Journal of Hazardous Materials* **2008**, *153*, 877–84.

[29] Ge, L. Novel Pd/$BiVO_4$ Composite Photocatalysts for Efficient Degradation of Methyl Orange under Visible Light Irradiation. *Materials Chemistry and Physics* **2008**, *107*, 465–470.

[30] Ge, L. Synthesis and Characterization of Novel Visible-Light-Driven Pd/$BiVO_4$ Composite Photocatalysts. *Materials Letters* **2008**, *62*, 926–928.

[31] Hosseini, S. N.; Borghei, S. M.; Vossoughi, M.; Taghavinia, N. Immobilization of TiO_2 on Perlite Granules for Photocatalytic Degradation of Phenol. *Applied Catalysis B: Environmental* **2007**, *74*, 53–62.

[32] Tunc, I.; Bruns, M.; Gliemann, H.; Grunze, M.; Koelsch, P. Bandgap Determination and Charge Separation in Ag@TiO_2 Core Shell Nanoparticle Films. *Surface and Interface Analysis* **2010**, *42*, 835–841.

[33] Pal, M.; Pal, U.; Jiménez, J. M. G. Y.; Pérez-Rodríguez, F. Effects of Crystallization and Dopant Concentration on the Emission Behavior of TiO_2:Eu Nanophosphors. *Nanoscale Research Letters* **2012**, *7*, 1.

[34] Guo, Z.; Ma, R.; Li, G. Degradation of Phenol by Nanomaterial TiO_2 in Wastewater. *Chemical Engineering Journal* **2006**, *119*, 55–59.

[35] Araña, J.; Doña-Rodríguez, J. M.; Portillo-Carrizo, D.; Fernández-Rodríguez, C.; Pérez-Peña, J.; González Díaz, O.; Navío, J. a.; Macías, M. Photocatalytic Degradation of Phenolic Compounds with New TiO_2 Catalysts. *Applied Catalysis B: Environmental* **2010**, *100*, 346–354.

[36] Parra, S.; Olivero, J.; Pacheco, L.; Pulgarin, C. Structural Properties and Photoreactivity Relationships of Substituted Phenols in TiO_2 Suspensions. *Applied Catalysis B: Environmental* **2003**, *43*, 293–301.

[37] Young, K. F.; Frederikse, H. P. R. Compliation of the Static Dielectric Constant of Inorganic Solids. *Journal of Physical and Chemical Reference Data* **1973**, *2*, 313–409.

[38] Sun, L.; Lin, Z.; Peng, J.; Weng, J.; Huang, Y.; Luo, Z. Preparation of Few-Layer Bismuth Selenide by Liquid-Phase-Exfoliation and Its Optical Absorption Properties. *Scientific reports* **2014**, *4*, 4794.

[39] Patil, S.; Puri, V. Electromagnetic Properties of Bismuth Oxide Thin Film Deposited on Glass and Alumina. *Archives of Applied Science Research* **2011**, *3*, 14–24.

[40] Patil, S.; Kulkarni, D.; Puri, V. Microwave Studies of Thermally Oxidized Vacuum Evaporated Bismuth Thin Films on Alumina. *Journal of Physics: Conference Series* **2008**, *114*, 012040.

[41] Beke, S.; Giorgio, S.; Kőrösi, L.; Nánai, L.; Marine, W. Structural and Optical Properties of Pulsed Laser Deposited V_2O_5 Thin Films. *Thin Solid Films* **2008**, *516*, 4659–4664.

[42] Zhang, A.; Zhang, J. Synthesis and Characterization of Ag/$BiVO_4$ Composite Photocatalyst. *Applied Surface Science* **2010**, *256*, 3224–3227.

[43] Zhang, A.; Zhang, J. Characterization and Photocatalytic Properties of Au/$BiVO_4$ Composites. *Journal of Alloys and Compounds* **2010**, *491*, 631–635.

[44] Loganathan, K.; Bommusamy, P.; Muthaiahpillai, P.; Velayutham, M. The Syntheses, Characterizations, and Photocatalytic Activities of Silver, Platinum, and Gold Doped TiO_2 Nanoparticles. *Environmental Engineering Research* **2011**, *16*, 81–90.

[45] Liu, K.; Chang, Z.; Li, W.; Che, P.; Zhou, H. Preparation, Characterization of Mo, Ag-Loaded $BiVO_4$ and Comparison of Their Degradation of Methylene Blue. *Science China Chemistry* **2012**, *55*, 1770–1775.

[46] Zhou, B.; Zhao, X.; Liu, H.; Qu, J.; Huang, C. P. Visible-Light Sensitive Cobalt-Doped $BiVO_4$ (Co-$BiVO_4$) Photocatalytic Composites for the Degradation of Methylene Blue Dye in Dilute Aqueous Solutions. *Applied Catalysis B: Environmental* **2010**, *99*, 214–221.

[47] Kim, T. W.; Choi, K.-S. Nanoporous $BiVO_4$ Photoanodes with Dual-Layer Oxygen Evolution Catalysts for Solar Water Splitting. *Science (New York, N.Y.)* **2014**, *343*, 990–4.

[48] Chaiwichian, S.; Inceesungvorn, B.; Pingmuang, K.; Wetchakun, K.; Phanichphant, S.; Wetchakun, N. Synthesis and Characterization of the Novel $BiVO_4$/CeO_2 Nanocomposites. *Engineering Journal* **2012**, *16*, 153–160.

[49] Obregón, S.; Colón, G. On the Different Photocatalytic Performance of $BiVO_4$ Catalysts for Methylene Blue and Rhodamine B Degradation. *Journal of Molecular Catalysis A: Chemical* **2013**, *376*, 40–47.

[50] Yu, J.; Kudo, A. Effects of Structural Variation on the Photocatalytic Performance of Hydrothermally Synthesized $BiVO_4$. *Advanced Functional Materials* **2006**, *16*, 2163–2169.

[51] Bian, Z.-Y.; Zhu, Y.-Q.; Zhang, J.-X.; Ding, A.-Z.; Wang, H. Visible-Light Driven Degradation of Ibuprofen Using Abundant Metal-Loaded $BiVO_4$ Photocatalysts. *Chemosphere* **2014**, *117C*, 527–531.

[52] Zhang, X.; Zhang, Y.; Quan, X.; Chen, S. Preparation of Ag Doped $BiVO_4$ Film and Its Enhanced Photoelectrocatalytic (PEC) Ability of Phenol Degradation under Visible Light. *Journal of Hazardous Materials* **2009**, *167*, 911–4.

[53] Chen, L.; Huang, R.; Ma, Y.-J.; Luo, S.-L.; Au, C.-T.; Yin, S.-F. Controllable Synthesis of Hollow and Porous Ag/$BiVO_4$ Composites with Enhanced Visible-Light Photocatalytic Performance. *RSC Advances* **2013**, *3*, 24354.

[54] Liang, A.; Liu, Q.; Wen, G.; Jiang, Z. The Surface-Plasmon-Resonance Effect of Nanogold/silver and Its Analytical Applications. *Trends in Analytical Chemistry* **2012**, *37*, 32–47.

[55] Cao, S.; Yin, Z.; Barber, J.; Boey, F. Y. C.; Chye, S.; Loo, J.; Xue, C. Preparation of Au-$BiVO_4$ Heterogeneous Nanostructures as Highly Efficient Visible-Light Photocatalysts. *ACS Applied Materials & Interfaces* **2012**, *4*, 418–423.

[56] Myung, N.; Lee, W.; Lee, C.; Jeong, S.; Rajeshwar, K. Synthesis of Au-$BiVO_4$ Nanocomposite through Anodic Electrodeposition Followed by Galvanic Replacement and Its Application to the Photocatalytic Decomposition of Methyl Orange. *ChemPhysChem* **2014**, *15*, 2052–7.

[57] Kaur, R.; Pal, B. Size and Shape Dependent Attachments of Au Nanostructures to TiO_2 for Optimum Reactivity of Au–TiO_2 Photocatalysis. *Journal of Molecular Catalysis A: Chemical* **2012**, *355*, 39–43.

[58] Seery, M. K.; George, R.; Floris, P.; Pillai, S. C. Silver Doped Titanium Dioxide Nanomaterials for Enhanced Visible Light Photocatalysis. *Journal of Photochemistry and Photobiology A: Chemistry* **2007**, *189*, 258–263.

[59] Lee, M. S.; Hong, S.-S.; Mohseni, M. Synthesis of Photocatalytic Nanosized TiO_2–Ag Particles with Sol–gel Method Using Reduction Agent. *Journal of Molecular Catalysis A: Chemical* **2005**, *242*, 135–140.

[60] Ke, S.-C.; Wang, T.-C.; Wong, M.-S.; Gopal, N. O. Low Temperature Kinetics and Energetics of the Electron and Hole Traps in Irradiated TiO_2 Nanoparticles as Revealed by EPR Spectroscopy. *Journal of Physical Chemistry* **2006**, *110*, 11628–11634.

[61] Zhou, X.; Liu, G.; Yu, J.; Fan, W. Surface Plasmon Resonance-Mediated Photocatalysis by Noble Metal-Based Composites under Visible Light. *Journal of Materials Chemistry* **2012**, *22*, 21337.

[62] Long, R.; Prezhdo, O. V Instantaneous Generation of Charge-Separated State on TiO_2 Surface Sensitized with Plasmonic Nanoparticles. *Journal of the American Chemical Society* **2014**, *136*, 4343–4354.

Chapter 5: Synthesis and Optimization of Fe_2O_3 Nanofibers

5.1 Abstract

In this work, α-Fe_2O_3 nanofibers were synthesized via electrospinning and characterized to observe optimal morphological and dimensional properties towards heavy metal removal. The Fe_2O_3 nanofiber samples were tested in aqueous solutions containing chromate (CrO_4^{2-}) to analyze their adsorption capabilities and compare them with commercially-available Fe_2O_3 nanoparticles. Synthesized Fe_2O_3 nanofibers were observed with a variety of different average diameters, ranging from 23 to 63 nm, while having a constant average grain size at 34 nm, point zero charge at pH 7.1, and band gap at 2.2 eV. BET analysis showed an increase in specific surface area with decreasing average diameter, from 7.2 to 59.2 m^2/g, due to the increased surface area-to-volume ratio with decreasing nanofiber size. Based on CrO_4^{-2} adsorption isotherms at pH 6, adsorption capacity of the Fe_2O_3 nanofibers increased with decreasing diameter, with the 23 nm sized nanofibers having an adsorption capacity of 90.9 mg/g, outperforming the commercially-available Fe_2O_3 nanoparticles by nearly 2-fold. Additionally, adsorption kinetics was also analyzed, increasing with decreasing nanofiber diameter. The enhanced performance of the nanofiber is suggested to be caused solely due to the increased surface area, impart by its size and morphology. Electrospun Fe_2O_3 nanofibers provide a promising solution for effective heavy metal removal through nanotechnology-integrated treatment systems.

5.2 Introduction

5.2.1 Iron Oxide (Fe_2O_3)

Iron (Fe) is the second most abundant metal (after aluminum) in the earth's crust and contributes to a third of the entire earth's mass.[1],[2] Due to its great natural abundance, its uses, such as tools and weapons, date back to the 2nd millennia BC during prehistoric times.[3] Through its use from then on into the industrial revolution and today's modern era, iron accounts for 95% of worldwide metal production, being the foundation of the steel industry for the construction of infrastructure, mobile machinery and other engineering applications. Iron ore minerals are the basic raw material used to produce iron and steel,[4] and come in the form of iron oxides, hydroxides or oxide-hydroxides, as these are the naturally occurring forms of iron on earth.[5] Collectively, the different oxidized forms of iron are all grouped together as iron oxides. The main ore minerals mined for iron consumption, as well as the three most widely used iron oxide species, are magnetite (Fe_3O_4), goethite (α-FeOOH), and, most importantly and sought after, hematite (α-Fe_2O_3)[4],[6].

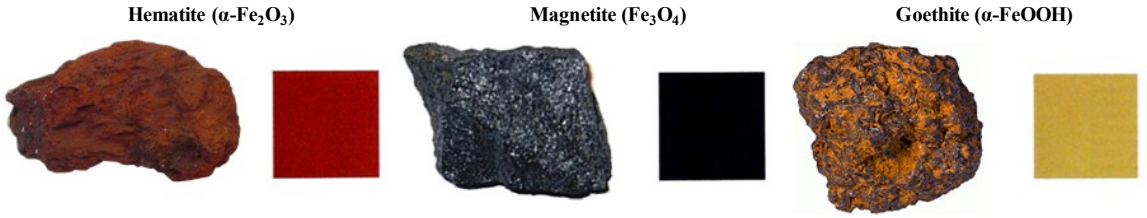

Figure 5-1: Common iron oxide minerals and their color plates.[7]

Hematite (α-Fe_2O_3) is one of the most abundant and most stable forms of oxidized iron minerals found on the Earth.[7] α-Fe_2O_3, alongside other iron oxides and hydroxides, can be introduced naturally into the pedosphere and hydrosphere from the lithosphere during rock weathering.[7] In these environments, iron oxides have shown to regulate the concentration of organic and inorganic constituents. In addition to its dominant usage in the iron and steel industry, α-Fe_2O_3 has also been used in a wide variety of applications, such as pigments, gas-sensors, field effect transistors, batteries, magnetic storages, and photoelectrolysis reactors.[8],[9] One prominent application of iron oxides, especially α-Fe_2O_3, is as an adsorbent for the removal of harmful heavy metals in water sources.[10]

5.2.2 Fe_2O_3 in Water Treatment

In addition to PPCPs, heavy metals present another prevalent water supply dilemma through their discovery in groundwater sources, a significant supply of available drinking water. Heavy metals have been used for thousands of years, so their emergence and adverse effects have been known and understood for a long time.[11] However, exposure to these contaminants continues around the world and increasingly in developing countries.[11] For example, arsenic (As) is a widely utilized element, as arsenic compounds have been heavily used in pesticides, herbicides, and wood preservation due to its recognized toxicity towards multicellular life.[12] Although it is also naturally occurring in inorganic and organic forms,[13] arsenic is a well-known carcinogen, can also cause gastrointestinal and cardiac damage,[12] and has been connected to human mortality.[14] In the United States, arsenic has been found in

groundwater sources in the southwestern states in concentrations well over the limits of the World Health Organization guidelines and the U.S. Environmental Protection Agency drinking water standards.[15] Chromium (Cr), another carcinogenic heavy metal, is very common in diverse metal industry processes, such as electroplating, leather tanning, wood preservations and chemical industries.[13],[16] It has been reported that occurrences of Cr entering the environment are due to leakage, poor storage or unsafe disposal practices from such metal industry processes.[13] Altogether, these heavy metals are found in water systems as anions (*e.g.*, chromate CrO_4^{2-}).

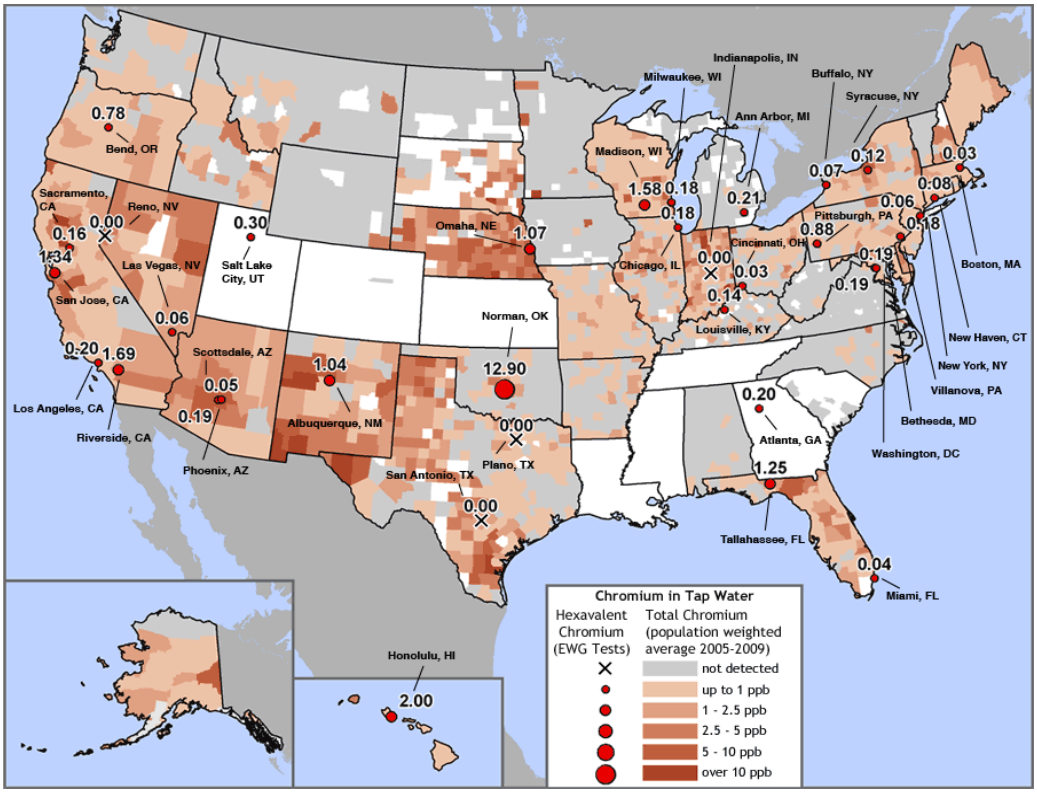

Figure 5-2: Chromium(VI) concentrations from different testing sites around the United States.[17]

Adsorption, the common treatment method for heavy metal removal, is the adhesion of atoms or molecules (adsorbate) on the surface of a highly porous material (adsorbent).[18] Fe_2O_3 is one of the most commonly used adsorbent materials for heavy metal removal. There has been extensive research on the performance of different iron minerals, such as iron oxides, iron hydroxides, iron oxide-hydroxides, and ferrihydrite, towards adsorption of heavy metals.[18] Of them all, α-Fe_2O_3 has attracted considerable attention as an adsorbent in water treatment due to its favorable properties, including its non-toxicity and being the most stable form of Fe_2O_3 under ambient conditions.[9] Additionally, research has shown that α-Fe_2O_3 has the greatest adsorption kinetics and capacity towards heavy metals compared to other Fe_2O_3.[14]

5.2.4 Fe_2O_3 Nanofibers

As with commercial TiO_2 used for photo-oxidation, Fe_2O_3 used for heavy metal removal is commonly in the form of nanoparticles. Fe_2O_3 nanoparticles are injected into the water supply, such as a groundwater basin, and slowly move with the flow of water flow while accumulating contaminants on its surface, and are subsequently captured by some filtration membrane at the endstream.[20] As previously stated, the use of nanoparticle suspensions is discouraged due to the possible inadvertent release into the environment. Therefore, it is imperative to establish systems that utilize immobilized nanomaterials to encourage the future use of nanotechnology for water quality applications.

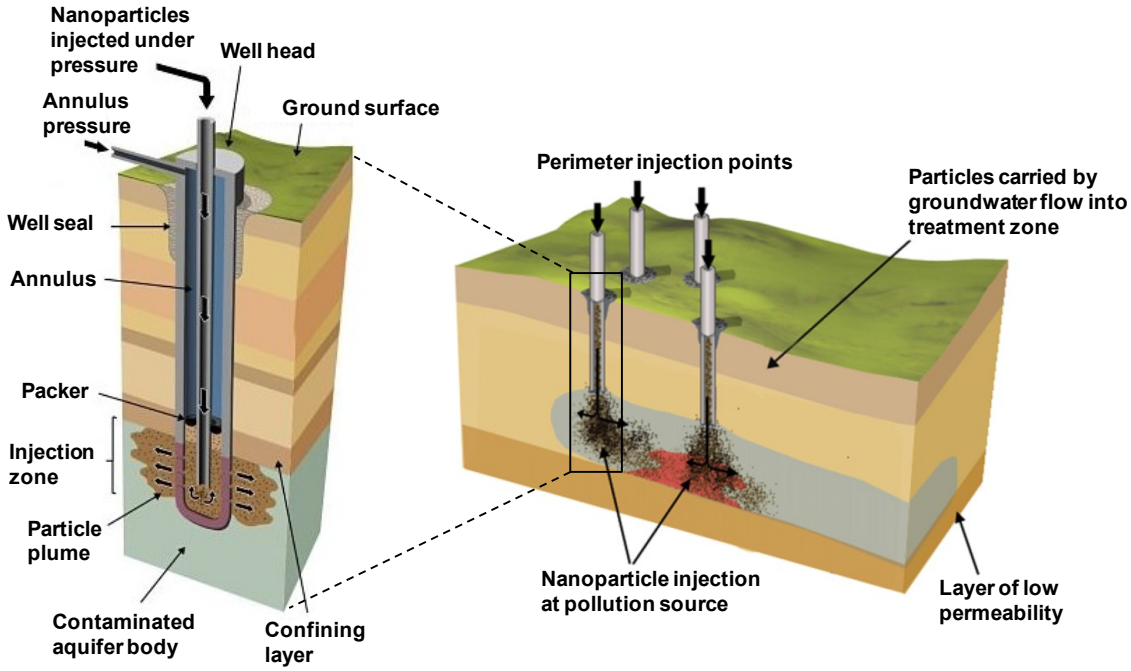

Figure 5-3: Schematic of nanoparticle injection well.[20]

For this work, electrospun Fe_2O_3 nanofibers were investigated as an adsorbent for heavy metals. Fe_2O_3 nanofibers have been synthesized by various methods and applied towards different applications, such as gas sensors, magnetic devices, and information storage.[8],[9],[21] Normally, iron(III) nitrate ($Fe(NO_3)_3$) is the popular iron precursor of choice during electrospinning, but precursors such as iron(II) acetate ($FeAc_2$) and iron(III) 2-ethylhexanoate diispropoxide ($C_{14}H_{29}FeO_4$) have also been used.[9],[20],[22]

Zheng et al.[8] studied the synthesis of Fe_2O_3 nanofibers via electrospinning using $Fe(NO_3)_3$ as the Fe precursor. The as-synthesized nanofibers were subsequently annealed at 800 °C to form Fe_2O_3 nanofibers. From dimensional and morphological characterization, the Fe_2O_3 nanofibers had an average diameter of 150 nm and an average grain size of 30 nm. The Fe_2O_3 nanofibers showed great gas sensing properties based on

response, recovery sensitivity and stability based on an array of different gases, including H_2, CH_3, CO and NO_2.

Zhu et al.[9] studied the synthesis of Fe_2O_3 nanofibers via electrospinning using $FeAc_2$ as the Fe precursor. Fe content was varied from 20 to 50 wt.% of $FeAc_2$ and annealing temperature was varied from 400 to 800 °C. The average diameter of the as-synthesized nanofibers prior to annealing increased from 70 to 150 nm with increased $FeAc_2$ content from 20 to 50 wt.%. At the 40 wt.% $FeAc_2$, the average diameter of the annealed nanofibers increased from 40 to 130 nm with increased annealing temperature from 400 to 800 °C, as well as nanofiber roughness. Hysteresis experiments determined that the Fe_2O_3 nanofibers exhibited tunable ferromagnetic properties.

Ren et al.[16] worked on the synthesis of Fe_2O_3 nanofibers via hydrothermal process using $FeCl_3$ as the Fe precursor. After synthesis, the nanomatierial powder was annealed at 400 °C to form Fe_2O_3 nanofibers. SEM and TEM analysis determined the average diameter to be 40 nm. Based on Cr(IV) adsorption studies, the Fe_2O_3 nanofibers outperformed its commercial counterpart, having over double the removal efficiency of Fe_2O_3 commercial powder. In addition to its superb adsorption kinetics and capacity, Fe_2O_3 nanofibers also exhibited great performance cyclability.

Shao et al.[21] worked on the synthesis of Fe_2O_3 and Fe nanofibers via electrospinning using $Fe(NO_3)_3$ as the Fe precursor. The as-synthesized nanofibers were annealed at 550 °C to form Fe_2O_3 nanofibers, which could then be annealed in a hydrogen environment at 750 °C to create Fe nanofibers. The average diameter of the Fe_2O_3 and Fe nanofibers was 350 and 180 nm, respectively.

Li et al.[22] studied the synthesis of $NiFe_2O_4$ nanofibers via electrospinning. The Fe precursor that was used during synthesis was $C_{14}H_{29}FeO_4$. The as-synthesized nanofibers were subsequently annealed at 550 °C. The $NiFe_2O_4$ nanofibers had an average diameter of 46 nm. Hysteresis studies showed significant changes in magnetic properties between the $NiFe_2O_4$ nanofibers and sol-gel synthesized $NiFe_2O_4$ powder.

Wu at al.[23] studied the synthesis of Fe_2O_3 nanofibers via sol-gel/electrospinning process using $Fe(NO_3)_3$ as the Fe precursor. The as-synthesized nanofibers were subsequently annealed at 500 °C. SEM analysis revealed that the Fe_2O_3 nanofiber diameter before and after annealing was 210 and 40 nm, respectively. The Fe_2O_3 nanofibers were annealed again at 400 °C in a hydrogen atmosphere to obtain Fe nanofibers, which had an average diameter of 25 nm.

Eid et al.[24] worked on the synthesis of Fe_2O_3 nanofibers via electrospinning using $FeAc_2$ as the Fe precursor. The ratio between $FeAc_2$ and the polymer PVP was varied. The as-synthesized nanofibers were subsequently annealed at 550 °C. Based diameter measurement from SEM images, the average diameter was controlled from 100 to 200 nm, increasing with increased $FeAc_2$ to PVP ratio. TEM analysis showed that the annealing process transformed the Fe_2O_3 nanofibers into hollow nanotubes, having a wall thickness ranging from 13 to 70 nm.

Chen et al.[25] studied the synthesis of Fe_2O_3 nanofibers via electrospinning using $Fe(NO_3)_3$ as the Fe precursor. The annealing temperature was varied from 200 to 500 °C. SEM analysis showed that the diameter of the nanofibers decreased with increased annealing temperature up to 300 °C. The average diameter plateaued after 300 °C, as

DSC/TGA measurements confirmed that all the PVP had evaporated appropriately by that temperature. The diameter of the Fe_2O_3 nanofibers ranged from 100 to 150 nm. TEM analysis showed that by 400 °C, the nanofibers obtained core transformation, becoming nanotubes.

Despite the large amount of research surrounding electrospun Fe_2O_3 nanofibers, the average diameter of these nanofibers is relatively large (100-300 nm)[8],[20],[24] and there is very little work on electrospun Fe_2O_3 nanofibers used for heavy metal adsorption.[16] As a result, there is little work on optimizing tunable nanofiber properties towards heavy metal removal. This project undertook the synthesis and optimization of electrospun Fe_2O_3 nanofibers for the removal of heavy metals in impaired water sources. Nanofiber morphology and dimensions were heavily exploited to take advantage of the greater surface area-to-volume ratio compared to that of nanoparticles and larger sized nanofibers, where surface adsorption can be optimized.

The overall objective of this study is to synthesize Fe_2O_3 nanofibers and optimize their adsorption capacity for the adsorption of heavy metal pollutants in water. Fe_2O_3 nanofibers were synthesized through the electrospinning process and synthesis parameters were manipulated to control the dimensional and morphological properties. Synthesized nanofibers were characterized via various techniques to first relate observed changes in nanofiber properties to specific adjustments in our electrospinning procedure. Different isotherm experiments were conducted to analyze the adsorption performance of the Fe_2O_3 nanofibers towards CrO_4^{2-}. Based on their adsorption capabilities, the structural modifications critical to optimizing treatment efficiency were identified.

5.3 Experimental Methods

5.3.1 Reagents

All chemicals were reagent grade or better and used as received. The synthesis of the Fe_2O_3 nanofibers involved iron(III) 2-ethylhexano-isopropoxide (Alfa Aesar, 10% w/v in isopropanol) as the iron precursor, acetic acid (Fisher Scientific, glacial 99.7%) as an additive and polyvinylpyrrolidone (PVP) (Sigma Aldrich, MW: 1,300,000 g/mol) as the polymer. A buffer prepared from 25 mM sodium chloride, NaCl (Sigma Aldrich, >99.0%) was used in all adsorption experiments. A buffer prepared from 10 mM NaCl was used in all zeta potential experiments. Lastly, potassium chromate (K_2CrO_4) (Fisher Scientific) was used as the heavy metal pollutant for the adsorption studies.

5.3.2 Synthesis of Fe_2O_3 nanofibers

The synthesis of Fe_2O_3 nanofibers began with the preparation of the polymer solution. 3 mL of iron(III) 2-ethylhexano-isopropoxide, 0.3 mL acetic acid and a designated amount (4-5 wt. %) of PVP were added in a 30 mL glass beaker and stirred with a magnetic stirrer at a rate of 300 rpm for an hour, insuring that all of the PVP has dissolved. For the electrospinning set-up, the needle was set at a distance of 10 cm from the drum collector, the feed rate was varied from 0.2-0.45 mL/hr and the voltage was varied from 10-24 kV. After electrospinning, the Fe/PVP nanofibers were annealed at 500 °C at rate of 3 °C/min and held for 3 hours. After annealing, the nanofibers were kept as dry samples in 20 mL glass vials for characterization and were later used to make 1 g/L stock suspensions in DI water for zeta potential and adsorption tests.

5.3.3 Nanofiber Characterization

Fe_2O_3 nanofibers were characterized using several different techniques to quantify their size, morphological and optical properties. Nanofiber diameter was examined by a Phillips XL30 FEG scanning electron microscopy (SEM). For SEM, samples were prepared by placing approximately a 0.5 cm x 0.5 cm area of nanofibers onto a SEM sample holder. SEM imaging of n = 40 nanofibers yielded average diameters (with standard deviation) that were used to create sizing histograms.

Crystal phase, crystal orientation and average grain size were determined by a Bruker D8 Advance x-ray diffraction (XRD) analyzer. XRD samples were prepared in the same manner as described for the TiO_2 nanofibers. The 1 x 1 cm^2 samples were analyzed from 20° to 80° for the Bragg angle with an interval of 0.03°. Grain size was quantified by means of the Scherrer-Debye equation, which relates grain size to the diffraction peak properties.[28] The prominent hematite peak (104) was used for this calculation.

Zeta potential was determined by a Brookhaven Instrumental Corporation ZetaPALS zeta potential analyzer. Just like the protocol for the TiO_2 nanofibers, 100 µL of the 1 g/L nanofiber stock suspension was added to 3.5 mL of 10 mM NaCl set at various pH values between 2 and 9. The point of zero charge (pzc) was calculated by interpolation between data points in which a zeta potential equal to 0 was achieved.

Band gap energy was quantified by a Thermo Scientific Evolution 300 UV-Vis spectrophotometer via diffuse reflectance infrared Fourier transform spectroscopy (DRIFTS). For analysis, the dry samples were analyzed over a wavelength scan from 200

to 800 nm and absorbance was measured. The band gap was calculated by taking the derivative of the absorbance curve, yielding a prominent negative peak.[29],[30] The wavelength value at the global minimum was converted into energy, thus yielding the band gap of the nanofibers.

Surface area was determined by BET analysis via Micromeritics ASAP 2020 Physisorption Analyzer in order to investigate any surface property change towards enhancement of adsorption. All samples were degassed at 300 °C for 3 hours prior to analysis.

5.3.4 Adsorption Experiments

Adsorption tests were conducted to quantify the performance capabilities of the Fe_2O_3 nanofibers. Six individual 10 mL vials contained 25 mM NaCl solution at pH 6, 0.1 g/L Fe_2O_3 nanofiber loading, and an initial CrO_4^{2-} concentration, which ranged from 5 to 200 μM. After the addition of the CrO_4^{2-} to the reactor vial, an initial sample of 0.5 mL is immediately withdrawn and passed through a 0.2 μm PFTE filter to remove the Fe_2O_3 nanofibers. Afterwards, the reaction vials are set on a circular rotator and mixed for 2 hours to reach equilibrium. After 2 hours of agitation, a 0.5 mL aliquot from reach vial is withdrawn and filtered as the final sample. The dissolved concentrations of CrO_4^{2-} were determined via atomic absorbance spectrometer (AAS) (Perkin Elmer AAnalyst 800). Prior to the adsorption experiments, a calibration curve was created to correlate the light absorbance from the AAS to CrO_4^{2-} concentration. The supernatant from the reaction vials was run through the flame and the light absorbance was recorded. Based on the

difference between the light absorbance of the initial and final sample, the amount of CrO_4^{2-} adsorbed by the Fe_2O_3 nanofibers was calculated. The data set was fitted into a Langmuir model isotherm to quantify adsorption properties (i.e., maximum adsorption capacity). Additionally, adsorption kinetics was analyzed by mixing a reaction vial, containing the NaCl solution, Fe_2O_3 nanofibers and an initial CrO_4^{2-} concentration of 50 μM. 0.5 mL aliquots were withdrawn and filtered with respect to time (0 to 120 min). Samples were analyzed via AAS and adsorption kinetic rates were calculated by fitting the data into a pseudo-second-order adsorption kinetic model.

5.4 Results and Discussion

5.4.1 Nanofiber Characterization

Average diameter was tuned by controlling several parameters: PVP polymer content, applied voltage and solution feedrate. Based on previous research, initial synthesis tuning was conducted with the following parameters: 4 and 5 wt.% PVP, 10 and 12 kV, and 0.25 and 0.3 mL/hr. Figure 5-4 shows the average diameter as a function of the three different parameters. Increased voltage and decreased polymer content led to decreased diameter as expected; however, higher feedrate yielded smaller nanofibers, although lower feedrate would normally decrease diameter. By these parameters, the average diameter was controlled from 62 (± 16) to 36 (± 7) nm, where the smallest sized nanofibers at 36 nm was synthesized at 4 wt.% PVP, 12 kV and 0.3 mL/hr.

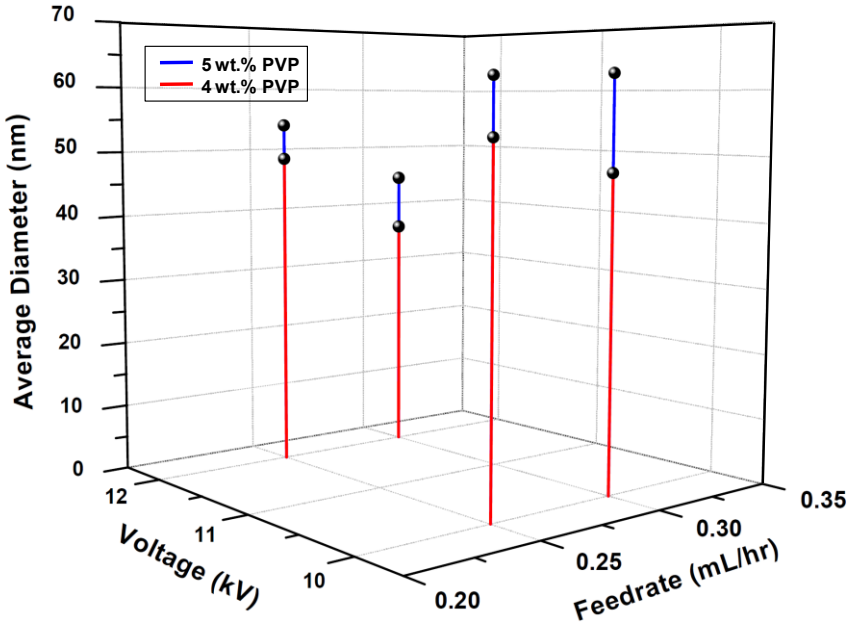

Figure 5-4: Average diameter of Fe_2O_3 nanofibers as a function of voltage and feedrate.

Subsequent synthesis tuning concentrated on only 4 wt.% PVP, as lower polymer content would lead to beaded non-uniform nanofibers, while extending the range of applied voltage (10-28 kV) and feedrate (0.2-0.45 ml/hr) to its limitations. Figure 5-5 shows a 3D plot of the effect of both applied voltage and feedrate on the average diameter of the Fe_2O_3 nanofibers. The plot conveys a bowl-shape trend, having an optimal value for both applied voltage and feedrate. It is known that increased voltage will decrease the nanofiber diameter in part by the increased electrostatic forces; however, too high of an applied voltage can lead to an unstable Taylor cone, which can lead to increased nanofiber diameter.[31] Decreased feedrate leads to smaller diameter, but, similar to the results seen in the initial synthesis tuning, diameter increased at a certain low feedrate. Applied voltage and feedrate are known to be interrelated, since at a certain voltage a corresponding feedrate is required to maintain a stable feedrate.[31] The

increase in nanofiber diameter seen at the lower feedrate could have been instigated by an unstable Taylor cone during electrospinning. Through the entire synthesis tuning, average nanofiber diameter was reduced to 23 (± 6) nm at an applied voltage of 20 kV and a feedrate of 0.3 mL/hr.

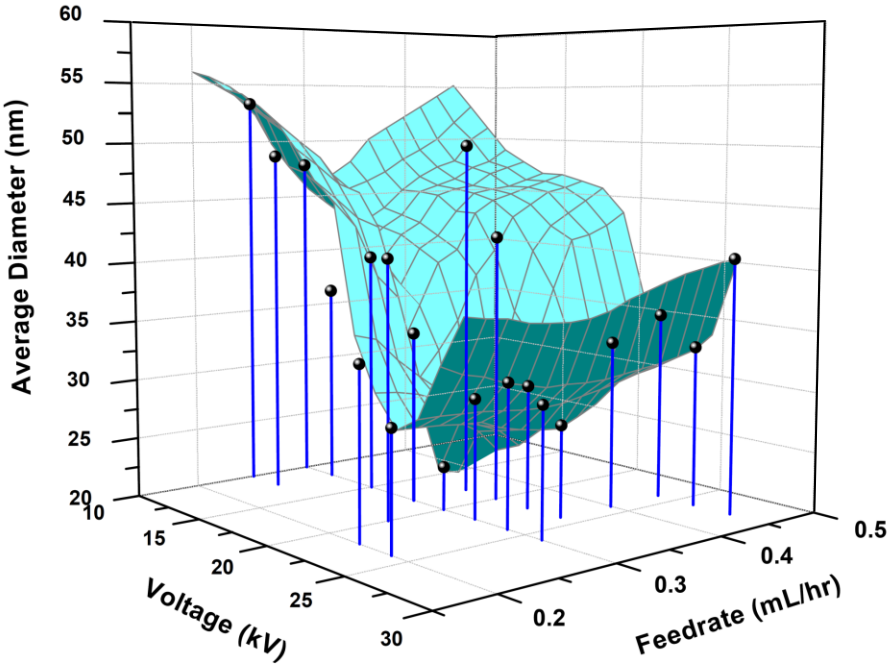

Figure 5-5: 3D surface plot of average diameter of Fe_2O_3 nanofibers as a function of voltage and feedrate.

For the subsequent analyses, select samples were utilized based on the synthesis experiments to analyze physical characteristics and performance as a function of different diameter sizes. Figure 5-6 provides the diameter histograms, and associated SEM images, of 5 selected nanofiber sample used henceforth. The samples, all synthesized at a feedrate of 0.3 mL/hr with select polymer content and applied voltage, were chosen based on varied average diameter and will be referenced as 62, 48, 40, 33 and 23 nm.

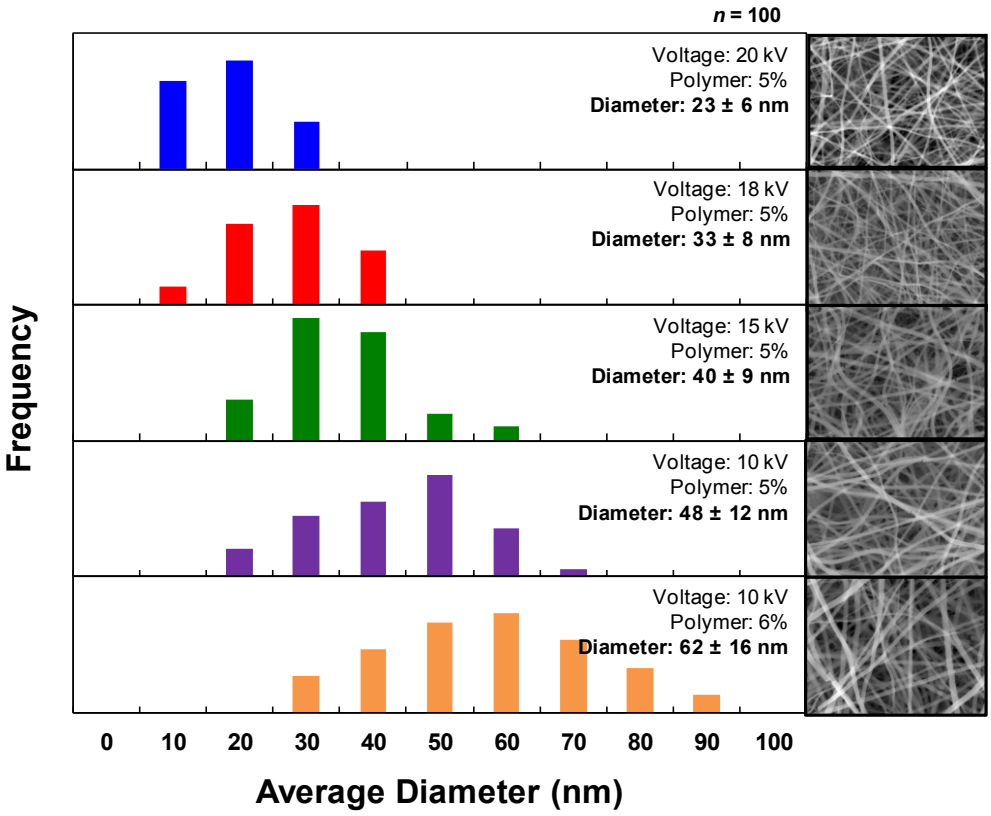

Figure 5-6: Histogram of Fe_2O_3 nanofiber average diameter with associated SEM images.

XRD characterization was conducted to analyze crystal phase and crystallinity of the Fe_2O_3 nanofibers (Figure 5-7). The XRD spectra of the synthesized Fe_2O_3 nanofibers at all diameter sizes were identified as hematite (α-Fe_2O_3) in conjunction with the JCPDS card (#33-0664). XRD analysis also identified the average grain size of the nanofibers to be 34 nm, independent of nanofiber average diameter, as seen in Figure 5-8. Interestingly, the average grain size was equal to or greater than some of the smaller nanofiber sizes, indicating the absence of dimensional confinement and possible ellipsoid grains. Additionally, texture coefficient calculations verified that the synthesis yielded random crystal orientation (Table 5-1).

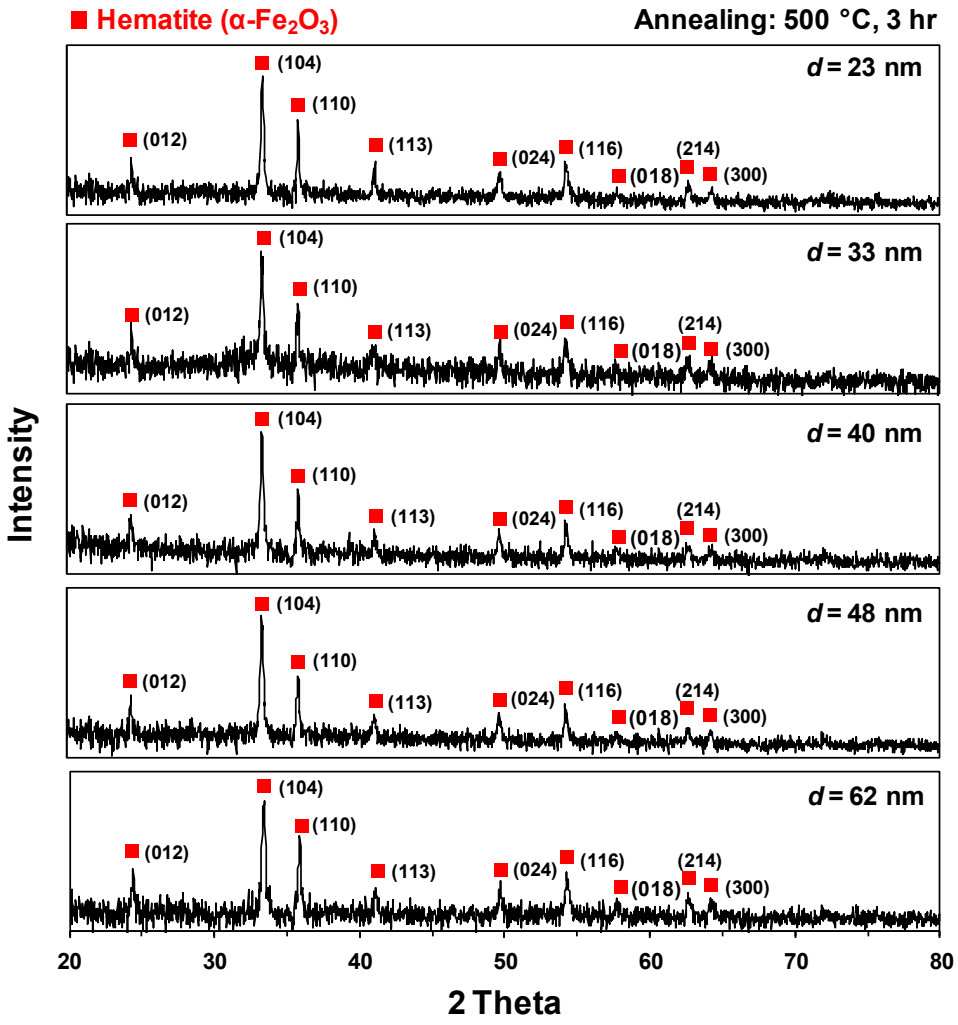

Figure 5-7: XRD patterns of the Fe_2O_3 nanofibers at different average diameter sizes.

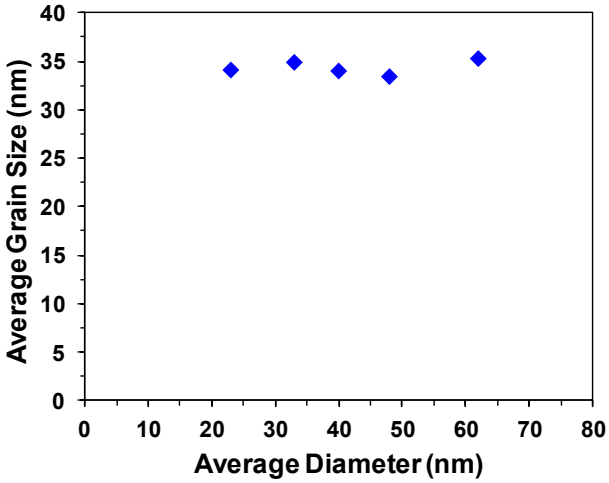

Figure 5-8: Average grain size as a function of Fe_2O_3 nanofiber diameter.

Table 5-1: Texture coefficients of Fe_2O_3 nanofibers.

XRD Parameters			Average Diameter (nm)				
Peak	2θ	Intensity	23	33	40	48	62
(012)	24.4	32	1.05308	1.03331	1.06515	1.08759	1.06731
(104)	33.4	100	1.00789	1.10962	1.10274	1.07739	1.01165
(110)	35.9	69	0.93903	0.85706	0.83211	0.83502	0.92105

Zeta potential measurements (Figure 5-9) showed little change in material surface charge among the different Fe_2O_3 nanofibers and commercial Fe_2O_3 nanoparticles. The average pH of pzc for all of the analyzed Fe_2O_3 nanofibers was 7.08 (±0.01), with no significant change based on average diameter. Additionally, the commercially-available Fe_2O_3 nanoparticles had a pzc value of 7.12. These results are comparable to values reported for Fe_2O_3, having an average pzc value of ~7.3.[32],[33]

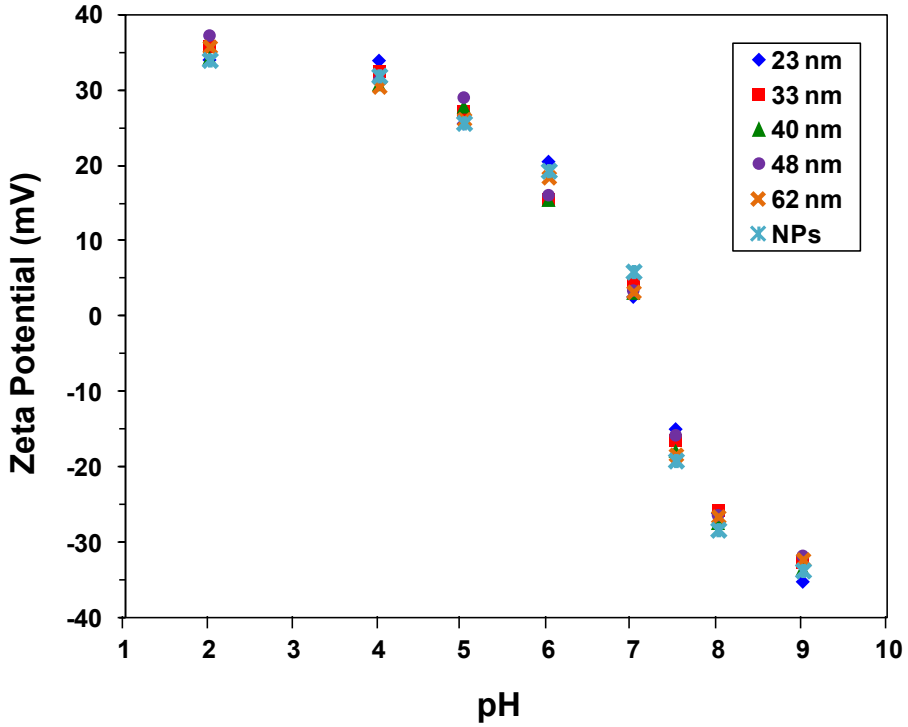

Figure 5-9: Zeta potential of Fe_2O_3 nanofibers at different average diameters.

Diffuse reflectance was conducted to characterize the band gap of the Fe_2O_3 nanofibers. Figure 5-10-A shows the absorbance curves of the nanofibers at different nanofiber diameters, showing little variation with nanofiber size. Regardless of average diameter, the band gap values of the Fe_2O_3 nanofibers were stable at an average of 2.18 (±0.01) eV, as seen in Figure 5-10-B, which is in accordance with the accepted range of 2.1-2.2 eV. [34],[35] There should not be any expected changes in band gap of the nanofibers since the Bohr radius of Fe_2O_3 is around 5 nm, roughly a quarter the size of the smallest nanofibers.[34]

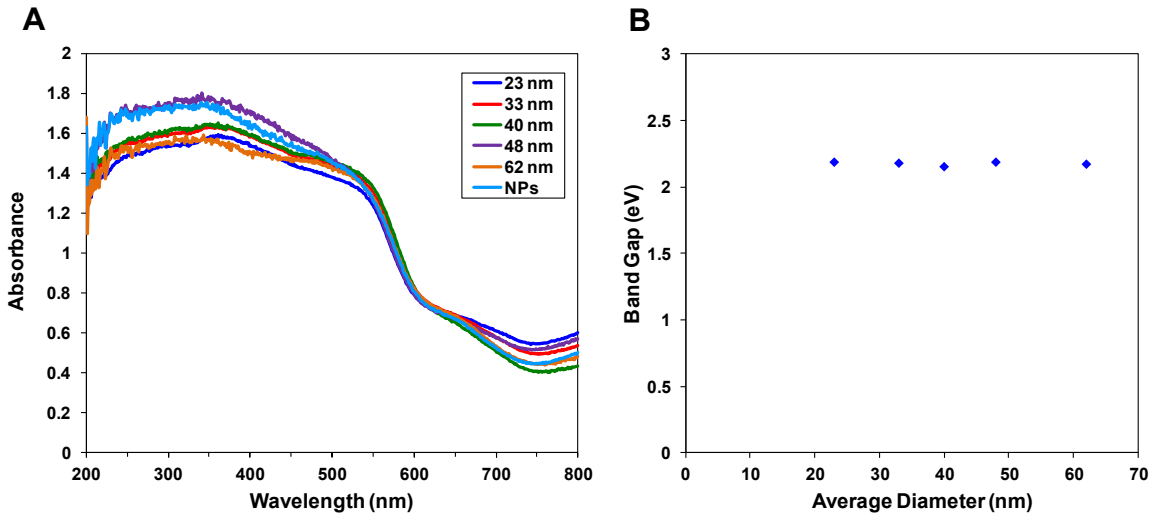

Figure 5-10: A) Diffuse reflectance absorbance curves of different nanofiber diameter and B) band gap energy as a function of average diameter of Fe_2O_3 nanofibers

BET analysis provided the information of specific surface area and pore dimension of the Fe_2O_3 and Al_2O_3-Fe_2O_3 composite nanofibers (Table 5-2). Based on the BET data, specific surface area increased with decreasing nanofiber diameter, as expected. As seen in Figure 5-11, the specific surface area increased from 7.2 to 59.2 m^2/g with decreased average diameter from 62 to 23 nm. These values were expected, as surface area-to-volume ratio would increase with decreasing nanofiber diameter while still within the range of hematite from published work (1-90 m^2/g).[19] Additionally, pore volume increased with decreasing diameter, while average pore width decreased accordingly. The specific surface area of the commercial Fe_2O_3 nanoparticles with an average diameter of ~25 nm was significantly lower, having a value of 28.4 m^2/g.

Table 5-2: BET analysis data of Fe_2O_3 nanofibers as a function of average diameter.

Average Diameter (nm)	SSA (m^2/g)	SSA_{Meso} (m^2/g)	SSA_{Micro} (m^2/g)	Pore Volume (cm^3/g)	Average Pore Width (nm)
23	59.2	43.2	16.0	0.198	13.4
33	35.0	27.0	8.0	0.156	17.8
40	23.4	18.5	4.9	0.131	22.4
48	13.2	11.4	1.8	0.098	29.6
62	7.2	6.6	0.6	0.085	36.2

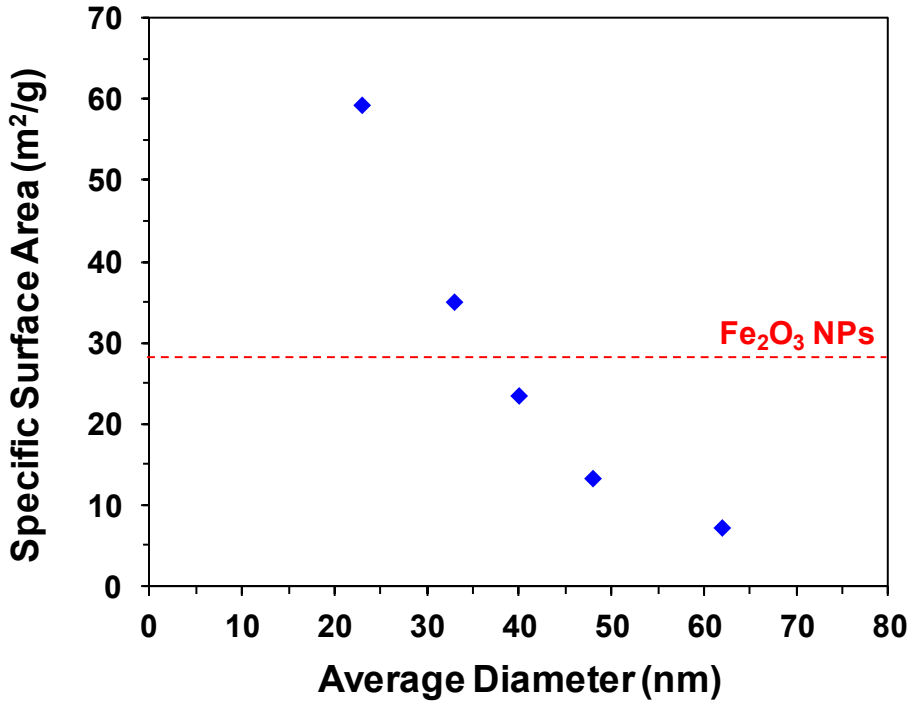

Figure 5-11: Specific surface area of Fe_2O_3 nanofibers and commercially-available Fe_2O_3 nanoparticles as a function of average diameter.

5.4.2 Adsorption Performance

Adsorption kinetics was determined to quantify adsorption rates of the Fe_2O_3 nanofibers. The adsorption of CrO_4^{2-} (C_0 = 50 μM) on synthesized Fe_2O_3 nanofibers and commercially-available nanoparticles with respect to time can be seen in Figure 5-12. Adsorption was initially rapid up to 30 minutes and plateaued gradually afterwards as adsorption reaches equilibrium. Furthermore, adsorption increased with decreasing diameter, indicating increased adsorption kinetics with decreasing diameter or increased surface area. The adsorption data was fitted into a pseudo-second-order adsorption kinetic model, described in the following equation:[27],[37]

$$\frac{dq_t}{dt} = k(q_e - q_t)^2 \tag{5.1}$$

where t is time in minutes, q_t is the amount of CrO_4^{2-} adsorbed at time t in mg/g, q_e is equilibrium adsorption capacity in mg/g, and k is the second-order adsorption rate constant in g/mg·min. The value of kq_e^2 can be defined as h, the initial adsorption rate in mg/g·min, and used to compare among the different nanofiber materials. After integrating equation 5.1 as a function of time, the integrated equation can be rearranged to obtain:

$$\frac{t}{q_t} = \frac{1}{kq_e^2} + \frac{1}{q_e}t \tag{5.2}$$

Plotting t/q_t as a function of time, as seen in Figure 5-13-A, will linearize the kinetic model to yield adsorption rate, h. The adsorption rate increased with decreasing diameter,

which indicates that the increase in surface area, and subsequently increase in surface sites, can promote faster adsorption kinetics (Figure 5-13-B).

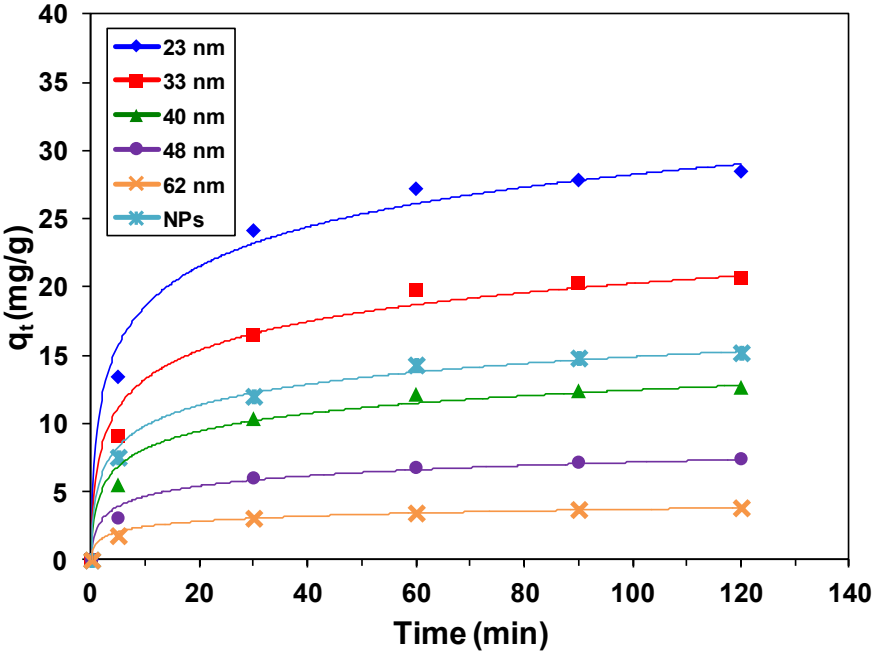

Figure 5-12: Adsorption of CrO_4^{2-} as a function of time of Fe_2O_3 nanofibers.

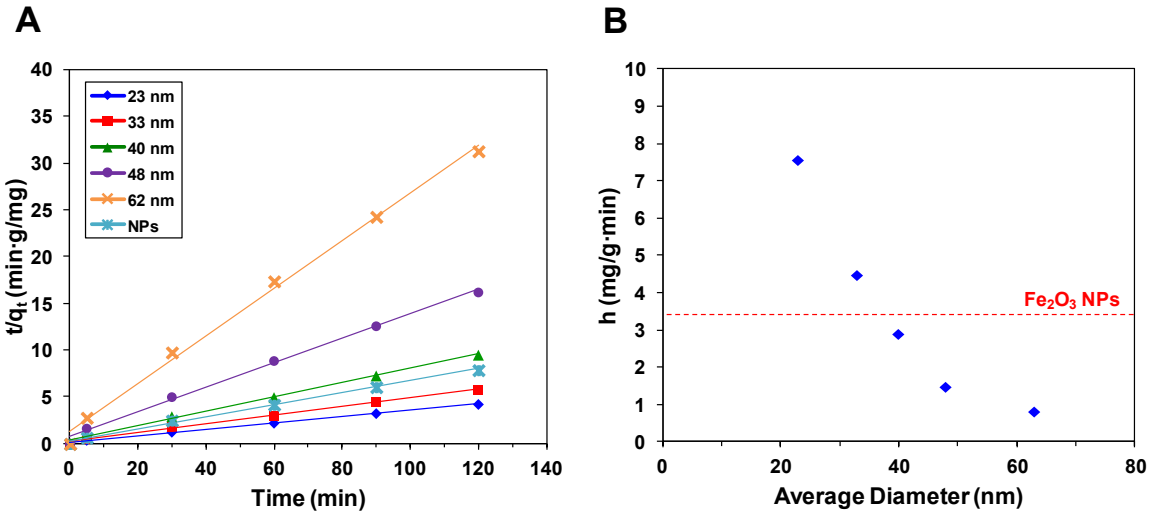

Figure 5-13: A) Pseudo-second-order adsorption kinetic fit of Fe_2O_3 nanofibers and B) initial adsorption rate *h* as a function of average diameter of Fe_2O_3 nanofibers.

Adsorption isotherms were conducted to analyze CrO_4^{2-} adsorption capacity of the Fe_2O_3 nanofibers. The isotherms based on mass of Fe_2O_3 showed an increase in CrO_4^{2-} adsorption with decreased nanofiber diameter, seen in Figure 5-14. The greatest adsorption performance came from the smallest nanofibers with an average diameter of 23 nm, having the greatest surface area-to-volume ratio. The 23 nm sized nanofibers, as well as the 33 nm sized nanofibers, noticeably outperformed the commercial Fe_2O_3 nanoparticles. Additionally, Figure 5-15 shows the CrO_4^{2} isotherms normalized by specific surface area. The normalized isotherms collapsed into a uniform curve, showing that the nanofibers all behaved similarly based on specific surface area. This illustrates that CrO_4^{2-} removal is solely specific surface area dependent, in which maximum surface area per unit of mass is optimal.

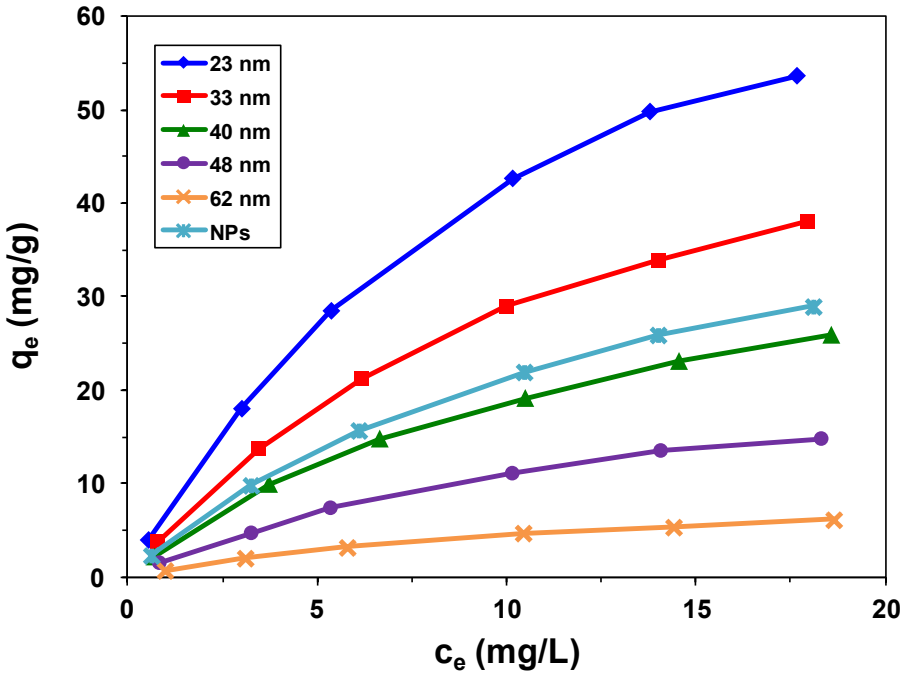

Figure 5-14: CrO_4^{2-} adsorption isotherm of Fe_2O_3 nanofibers.

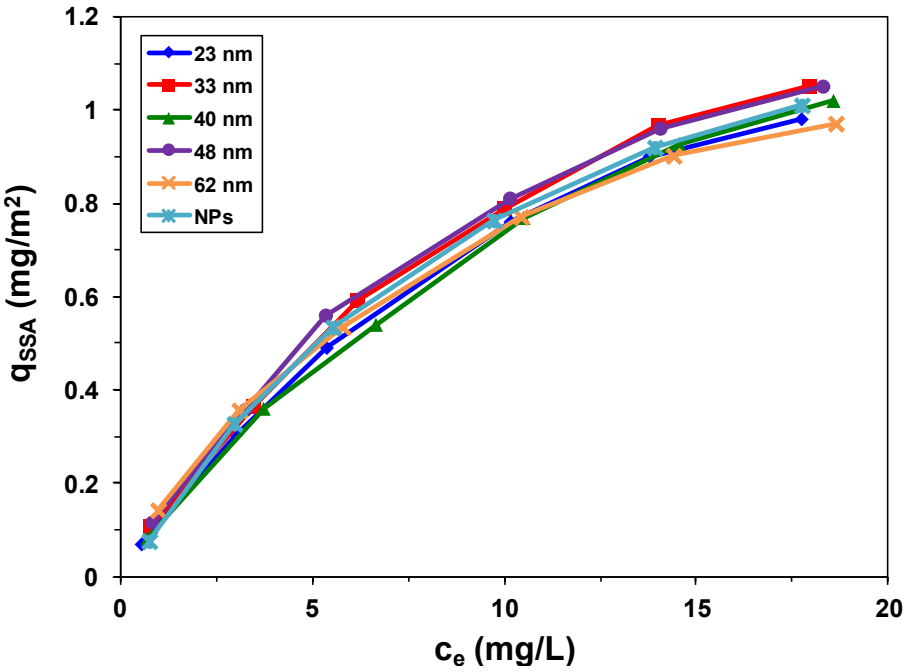

Figure 5-15: Specific surface area-normalized CrO_4^{2-} adsorption isotherm of Fe_2O_3 nanofibers.

The CrO_4^{2-} adsorption isotherms were then fitted towards an adsorption model to quantify the amount of the toxic adsorbate on the Fe_2O_3 adsorbent. The data curves behaved similarly to that of the commonly used Langmuir adsorption model, which is defined as:

$$q_e = q_m \frac{bc_e}{1 + bc_e} \tag{5.3}$$

where c_e is the equilibrium concentration of CrO_4^{2-} in mg/L, q_e is equilibrium adsorption capacity of CrO_4^{2-} on Fe_2O_3 in mg/g, q_m is the maximum adsorption capacity in mg/g, and b is the Langmuir equilibrium constant in L/mg.[16] The equation can be modified to linearize the adsorption isotherm curve and yield a maximum adsorption capacity value.

The adsorption data points were fitted to a Langmuir linear regression, which is defined as:

$$\frac{c_e}{q_e} = \frac{1}{bq_m} + \frac{c_e}{q_m} \tag{5.4}$$

Figure 5-16 shows the linearization of the Langmuir fitted isotherms of the different Fe_2O_3 nanofibers. The inverse of the slope of each linear fit provides the magnitude of the adsorption capacity. Therefore, a decrease in the slope would lead to a larger adsorption capacity value. Figure 5-17 provides the maximum adsorption capacity of the Fe_2O_3 nanofibers. Based on the linear Langmuir plots, the maximum adsorption capacity of CrO_4^{2-} increased with decreasing nanofiber diameter, which coincides with the increased specific surface area. Additionally, the adsorption capacity plot observed the same trend as the specific surface area plot shown earlier in Figure 5-11. The adsorption capacity of the Fe_2O_3 nanofibers increased from 10.2 to 90.9 mg/g with decreasing nanofiber average diameter from 62 to 23 nm. Additionally, the 23 nm sized nanofibers had a greater adsorption capacity than that of the commercially-available Fe_2O_3 nanoparticles, having value of 49.3 mg/g. The Langmuir constant *b* was stable as a function of nanofiber diameter with an average value of 0.079 ± 0.002 L/mg, similar to the value of the commercial nanoparticles (0.078 L/mg), indicating no change in adsorption bond strength of Fe_2O_3.[18],[36] Altogether, the enhanced adsorption of CrO_4^{2-} by the Fe_2O_3 nanofibers is attributed solely to the surface area effect. With the decrease in average diameter, the surface area-to-volume ratio increased, thus improving specific surface area and porosity to enhance the adsorption of the heavy metal anion.[19]

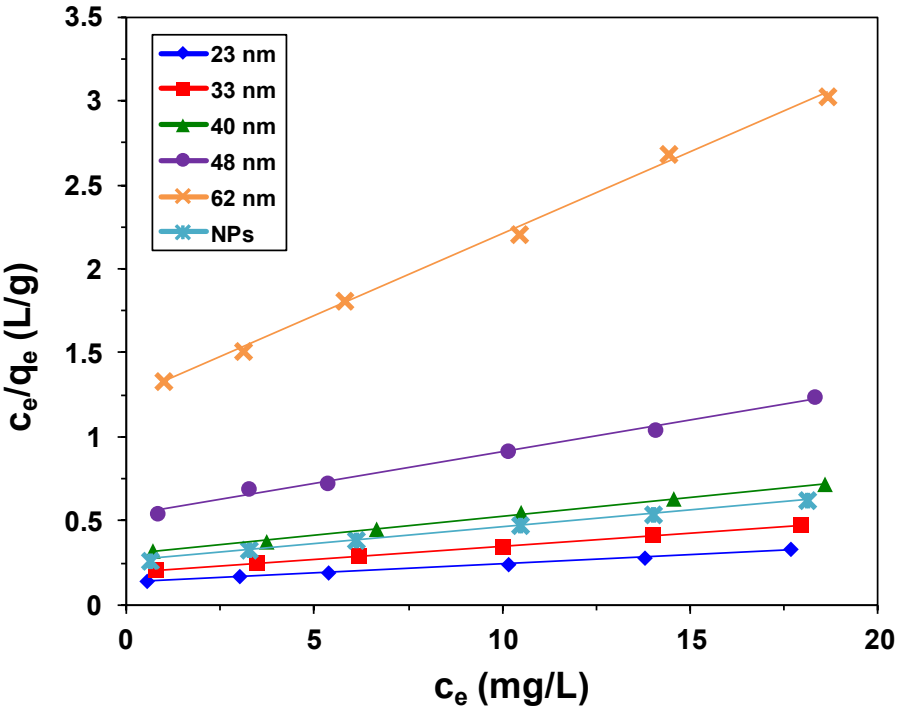

Figure 5-16. CrO_4^{2-} adsorption isotherm of Fe_2O_3 nanofibers fitted to linearized Langmuir model.

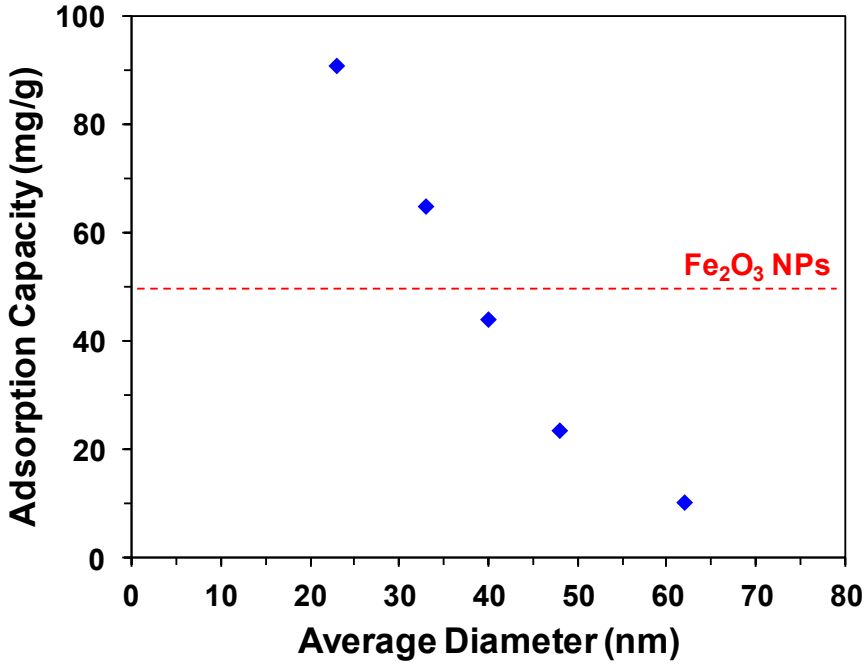

Figure 5-17. Maximum adsorption capacity of Fe_2O_3 nanofibers as a function of average diameter.

5.5 Conclusion

The results from this study show promise of metal oxide nanofiber materials for heavy metal treatment of water systems. Electrospinning provides a simple synthesis route to create nano-sized Fe_2O_3 nanofibers for contaminant adsorption applications. Tuning of different electrospinning parameters allows for control of nanofiber property manipulation towards performance optimization. Hematite Fe_2O_3 nanofibers with average diameters ranging from 23 to 64 nm and average grain size of 34 nm were developed. While most properties were stable (*e.g.*, such as crystallinity, band gap, and zeta potential), specific surface area was drastically augmented with the reduction of the nanofiber diameter. Adsorption isotherm studies were performed to connect the nanofibers' physical properties toward heavy metal adsorption. Results show the Fe_2O_3 nanofibers with average diameter of 23 nm provided the greatest CrO_4^{2-} adsorption capacity, outperforming commercial Fe_2O_3 powder. Additionally, the 23 nm sized nanofibers also had the greatest adsorption kinetics. Altogether, the smallest Fe_2O_3 nanofibers had optimal adsorption performance, solely dependent on surface area. With such results, electrospun Fe_2O_3 nanofibers are promising for nano-engineered heavy metal remediation systems, as they are more potent and pertinent to application systems than suspension-driven commercial Fe_2O_3 powders.

5.6 References

[1] Haxel, G. B.; Hedrick, J. B.; Orris, G. J. Rare Earth Elements-Critical Resources for High Technology. *United States Geological Survey* **2002**.

[2] Morgan, J. W.; Anders, E. Chemical Composition of Earth, Venus and Mercury. *Proceedings of the National Academy of Science USA* **1980**, *77*, 6973–6977.

[3] Weeks, M. E.; Leichester, H. M. *Discovery of the Elements*; Seventh Ed.; Journal of Chemical Education: Easton, 1968.

[4] Tuck, B. C. A.; Virta, R. L. Iron Ore. In *United States Geological Survey 2011 Minerals Yearbook*; 2013.

[5] Kuck, P. *Iron Ore Statistical Compendium*; United States Geological Survey, 1990.

[6] Junta-Rosso, J. L.; Hochella, M. F. The Chemistry of Hematite {001} Surfaces. *Geochmica et Cosmochimica Acta* **1996**, *60*, 305–314.

[7] Schwertmann, U.; Cornell, R. M. *Iron Oxides in Laboratory: Preparation and Characterization*; Second Edi.; Wiley-VCH: Weinheim, 2000; Vol. 156.

[8] Zheng, W.; Li, Z.; Zhang, H.; Wang, W.; Wang, Y.; Wang, C. Electrospinning Route for Alpha-Fe_2O_3 Ceramic Nanofibers and Their Gas Sensing Properties. *Materials Research Bulletin* **2009**, *44*, 1432–1436.

[9] Zhu, Y.; Zhang, J. C.; Zhai, J.; Jiang, L. Preparation of Superhydrophilic Alpha-Fe_2O_3 Nanofibers with Tunable Magnetic Properties. *Thin Solid Films* **2006**, *510*, 271–274.

[10] Streat, M.; Hellgardt, K.; Newton, N. L. R. Hydrous Ferric Oxide as an Adsorbent in Water Treatment Part 1. Preparation and Physical Characterization. *Process Safety and Environmental Protection* **2008**, *86*, 1–9.

[11] Jarup, L. Hazards of Heavy Metal Contamination. *British Medical Bulletin* **2003**, *68*, 167–182.

[12] Narayana, B.; Cherian, T.; Mathew, M.; Pasha, C. Spectrophotometric Determination of Arsenic in Environmental and Biological Samples. *Indian Journal of Chemical Technology* **2006**, *13*, 36–40.

[13] Chowdhury, S. R.; Yanful, E. K. Arsenic and Chromium Removal by Mixed Magnetite-Maghemite Nanoparticles and the Effect of Phosphate on Removal. *Journal of Environmental Management* **2010**, *91*, 2238–2247.

[14] Giménez, J.; Martínez, M.; de Pablo, J.; Rovira, M.; Duro, L. Arsenic Sorption onto Natural Hematite, Magnetite, and Goethite. *Journal of Hazardous Materials* **2007**, *141*, 575–80.

[15] Ramos, M. A. V; Yan, W.; Li, X.; Koel, B. E.; Zhang, W. Simultaneous Oxidation and Reduction of Arsenic by Zero-Valent Iron Nanoparticles : Understanding the Significance of the Core-Shell Structure. *Journal of Physical Chemistry C Letters* **2009**, *113*, 14591–14594.

[16] Ren, T.; He, P.; Niu, W.; Wu, Y.; Ai, L.; Gou, X. Synthesis of Alpha-Fe_2O_3 Nanofibers for Applications in Removal and Recovery of Cr(VI) from Wastewater. *Environmental Science and Pollution Research* **2013**, *20*, 155–62.

[17] Sutton, R. Chromium-6 in U.S. Tap Water. *Environmental Working Group* **2010**.

[18] Jeong, Y.; Fan, M.; Singh, S.; Chuang, C.-L.; Saha, B.; Hans van Leeuwen, J. Evaluation of Iron Oxide and Aluminum Oxide as Potential arsenic(V) Adsorbents. *Chemical Engineering and Processing: Process Intensification* **2007**, *46*, 1030–1039.

[19] Cornell, R. M.; Schwertmann, U. *The Iron Oxides: Structure, Properties, Reactions, Occurences and Uses*; Second Edi.; Wiley-VCH: Weinheim, 2003; pp. 3–527.

[20] Crane, R. A.; Scott, T. B. Nanoscale Zero-Valent Iron: Future Prospects for an Emerging Water Treatment Technology. *Journal of Hazardous Materials* **2012**, *211-212*, 112–25.

[21] Shao, H.; Zhang, X.; Liu, S.; Chen, F.; Xu, J.; Feng, Y. Preparation of Pure Iron Nanofibers via Electrospinning. *Materials Letters* **2011**, *65*, 1775–1777.

[22] Li, D.; Herricks, T.; Xia, Y. Magnetic Nanofibers of Nickel Ferrite Prepared by Electrospinning. *Applied Physics Letters* **2003**, *83*, 4586.

[23] Wu, H.; Zhang, R.; Liu, X.; Lin, D.; Pan, W. Electrospinning of Fe, Co, and Ni Nanofibers: Synthesis, Assembly, and Magnetic Properties. *Chemistry of Materials* **2007**, *19*, 3506–3511.

[24] Eid, C.; Brioude, A.; Salles, V.; Plenet, J.-C.; Asmar, R.; Monteil, Y.; Khoury, R.; Khoury, A.; Miele, P. Iron-Based 1D Nanostructures by Electrospinning Process. *Nanotechnology* **2010**, *21*, 125701.

[25] Chen, X.; Unruh, K. M.; Ni, C.; Ali, B.; Sun, Z.; Lu, Q.; Deitzel, J.; Xiao, J. Q. Fabrication, Formation Mechanism, and Magnetic Properties of Metal Oxide Nanotubes via Electrospinning and Thermal Treatment. *The Journal of Physical Chemistry C* **2011**, *115*, 373–378.

[26] Panda, P. K.; Ramakrishna, S. Electrospinning of Alumina Nanofibers Using Different Precursors. *Journal of Materials Science* **2007**, *42*, 2189–2193.

[27] Mahapatra, a; Mishra, B. G.; Hota, G. Electrospun Fe_2O_3-Al_2O_3 Nanocomposite Fibers as Efficient Adsorbent for Removal of Heavy Metal Ions from Aqueous Solution. *Journal of hazardous materials* **2013**, *258-259*, 116–123.

[28] Hosseini, S. N.; Borghei, S. M.; Vossoughi, M.; Taghavinia, N. Immobilization of TiO_2 on Perlite Granules for Photocatalytic Degradation of Phenol. *Applied Catalysis B: Environmental* **2007**, *74*, 53–62.

[29] Gilbert, B.; Frandsen, C.; Maxey, E.; Sherman, D. Band-Gap Measurements of Bulk and Nanoscale Hematite by Soft X-Ray Spectroscopy. *Physical Review B* **2009**, *79*, 035108.

[30] Shijie Wang, J. E. Dutrizac, Michael L. Free, James Y. Hwang, D. K. *T.T. Chen Honorary Symposium on Hydrometallurgy, Electrometallurgy and Materials Characterization*; John Wiley & Sons, Inc., 2012; p. 803.

[31] Ramakrisha, S.; Fujuhara, K.; Teo, W.-E.; Lim, T.-C.; Ma, Z. *An Introduction to Electrospinning and Nanofibers*; World Scientific Publishing Co.: Singapore, 2005.

[32] Kosmulski, M. The pH-Dependent Surface Charging and the Points of Zero Charge. *Journal of Colloid and Interface Science* **2002**, *253*, 77–87.

[33] Kosmulski, M. The pH-Dependent Surface Charging and Points of Zero Charge: V. Update. *Journal of Colloid and Interface Science* **2011**, *353*, 1–15.

[34] Vayssieres, L.; Sathe, C.; Butorin, S. M.; Shuh, D. K.; Nordgren, J.; Guo, J. One-Dimensional Quantum-Confinement Effect in Alpha-Fe_2O_3 Ultrafine Nanorod Arrays. *Advanced Materials* **2005**, *17*, 2320–2323.

[35] Kleiman-Shwarsctein, A.; Huda, M. N.; Walsh, A.; Yan, Y.; Stucky, G. D.; Hu, Y.-S.; Al-Jassim, M. M.; McFarland, E. W. Electrodeposited Aluminum-Doped

Alpha-Fe_2O_3 Photoelectrodes: Experiment and Theory. *Chemistry of Materials* **2010**, *22*, 510–517.

[36] Salmani, H. A Comparative Study of Copper (ii) Removal on Iron Oxide, Aluminum Oxide and Activated Carbon by Continuous down Flow Method. *Journal of Toxicology and Environmental Health Sciences* **2013**, *5*, 150–155.

[37] Li, R.; Li, Q.; Gao, S.; Shang, J. K. Enhanced Arsenite Adsorption onto Litchi-Like Al-Doped Iron Oxides. *Journal of the American Ceramic Society* **2011**, *94*, 584–591.

Chapter 6: Synthesis and Optimization of Al_2O_3-Fe_2O_3 Composite Nanofibers

6.1 Abstract

Al_2O_3-Fe_2O_3 composite nanofibers were synthesized via electrospinning and optimized towards enhanced heavy metal adsorption. The composite nanofibers were characterized for their morphological and dimensional properties and tested in aqueous solutions containing chromate (CrO_4^{2-}) to analyze their adsorption performance. Synthesized Al_2O_3-Fe_2O_3 nanofibers were observed with stable average diameter from 23 to 26 nm. Additionally, the composite nanofibers maintained other stable characteristics including average grain size at 35 nm, point zero charge at pH 7.1, and band gap at 2.2 eV. BET analysis showed an increase in specific surface area with increasing Al content from 59.2 to 92.8 m^2/g, which suggests a direct effect from the contribution of the highly porous Al_2O_3. Based on CrO_4^{-2} adsorption isotherms at pH 6, adsorption capacity of the Fe_2O_3 nanofibers increased with increased Al content, with the 32% Al/Fe composite nanofiber yielding an adsorption capacity of 169.5 mg/g, twice the value of the unmodified Fe_2O_3 nanfibers and over a 3-fold increase compared to the commercial Fe_2O_3 nanoparticles. Moreover, adsorption kinetics was also enhanced with increased Al content. The combination of Fe_2O_3 and Al_2O_3 promotes synergy in specific surface area and, in turn, enhanced adsorption properties. Electrospun composite nanofibers have great potential for removal of heavy metals compared to commercial materials due to their enhanced performance and integrability into hybrid treatment systems.

6.2 Introduction

Through the advancement of nanotechnology, iron oxide (Fe_2O_3) nanoparticles are finding homes in a large array of different application, with sensing, catalysis and water purification just being a few examples.[1]–[3] While facile syntheses of these materials are readily accessible, manipulation of nanotechnology, via size, shape, composition, etc., is increasingly more prevalent in order to take advantage of all the nano-scale properties can offer. Specifically for the removal of heavy metals, Fe_2O_3 nanomaterials, as well as other adsorbents like alumina (Al_2O_3), have garnered attention for their great treatment capabilities, yet there is large room for improvement, especially in terms of pollutant removal capabilities and kinetics. Modifications of Fe_2O_3 nanoparticles, most notably nanocomposites, are becoming more common in order to utilize their recognized adsorption properties and, through nanoscale synthesis, enhance their performance further than their unmodified counterparts can possibly achieve. There have been several reports on Fe_2O_3-containing nanocomposites for different applications including water treatment.

Li et al.[5] reported on the synthesis of $NiFe_2O_4$ nanofibers via electrospinning. The Fe precursor that was used during synthesis was $C_{14}H_{29}FeO_4$. The as-synthesized nanofibers were subsequently annealed at 550 °C. The $NiFe_2O_4$ nanofibers had an average diameter of 46 nm. Hysteresis studies showed significant changes in magnetic properties between the $NiFe_2O_4$ nanofibers and sol-gel synthesized $NiFe_2O_4$ powder.

Kleiman-Shwarsctein et al.[6] reported on Fe_2O_3 thin films doped with aluminum (Al) via electrodeposition. The thin films had particles ranging in size from 50 to 150 nm

at all Al content levels. Additionally, band gap of the thin films ranged from 2.05 to 2.15 eV with no clear trend as a function of Al content. Photoelectrochemical performance was shown to be enhanced due to Al doping, where 0.46 at.% Al showed optimal performance.

Li et al.[4] reported on Al-doped Fe_2O_3 nanoparticles via hydrothermal process for arsenite (As^{+3}) adsorption. Nanoparticles with molar ratios of 0 to 50% Al/Fe were synthesized, having an average diameter of 80 nm and protuberances within the nanoparticles with an average diameter of 10 nm. Surface area was shown to increase with increased Al content, starting from 23 m^2/g for the pure Fe_2O_3 nanoparticles to 52 m^2/g for the 50 mol.% Al/Fe nanocomposites. Adsorption capacity and kinetics were enhanced due to the addition of Al and correlated with the increase surface area, where optimal performance was observed by the 50 mol.% Al/Fe sample. The enhanced performance was attributed to the increase in adsorption sites by the addition of Al via X-ray photoelectron spectroscopy (XPS), which provided the increase in surface area and adsorption capabilities.

Li et al.[7] reported on the synthesis of Fe_2O_3-Al_2O_3 core-shell nanofibers via electrospinning for heavy metal adsorption. Nanofibers containing a core of Fe_2O_3 and a shell of Al_2O_3 were fabricated with an average diameter of 300 nm. The core-shell structures exhibited ferromagnetic properties and good adsorption performance towards hexavalent chromium (Cr^{+6}). El-Latif et al.[8] reported on Al_2O_3-Fe_2O_3 nanocomposites for the removal of Cd^{2+}. The nanocomposites were synthesized in a hydrothermal method and exhibited paramagnetic properties for magnetic adsorption. The nanocomposites

were around 25-29 nm in diameter and contained grains of Fe_2O_3 and Al_2O_3 ranging from 7 to 18 nm. Adsorption tests showed that the nanocomposites were excellent adsorbent for Cd^{+2}.

Mohapatra et al.[9] reported on Mg-doped Fe_2O_3 nanoparticles via sol-gel method for the removal of heavy metal ions, including Pb^{+2}, Cd^{+2}, Cu^{+2}, and Co^{+2}. The optimal sample of 0.38% Mg yielded structures of 2-10 nm in size and a surface area of 174 m^2/g, resulting in greater adsorption of heavy metal ions compared to the unmodified Fe_2O_3 nanoparticles. Increased Mg content above 0.38% led to decreased adsorption performance for Pb^{+2} and Cd^{+2} removal, but still relatively decent performance for Cu^{+2} and Co^{+2} removal. Mahapatra et al.[10] reported on Fe_2O_3-Al_2O_3 nanocomposite fibers via electrospinning for the removal of heavy metal ions. The nanofibers were synthesized in alpha phases for both metal oxides, having diameters ranging from 200 to 500 nm, and a surface area of 9.6 m^2/g. Adsorption tests regarding Cu^{+2}, Pb^{+2}, Ni^{+2}, and Hg^{+2} removal showed great adsorption capacity and kinetics for the nanocomposite fibers.

Although the amount of research surrounding composite Fe_2O_3 nanoparticles is reasonable, there is very limited work on nanocomposites towards water treatment, let alone work from electrospun nanofibers, which have great potential for treatment integration. And while there are a few reports on electrospun composite Fe_2O_3 nanofibers towards heavy metal adsorption, they don't offer extensive property and performance studies, alongside comparisons with commercial materials. Additionally, the reported composite nanofibers are also relatively large (200-500 nm), indicating necessary improvement to maximize surface area-to-volume ratio. The overall objective of this

study is to synthesize Al_2O_3-Fe_2O_3 composite nanofibers and optimize their adsorption performance for the removal of heavy metal pollutants in water. The composite nanofibers were synthesized through the electrospinning process, as synthesis parameters were manipulated to control the nanofiber's dimensional and morphological properties. Synthesized nanofibers were characterized via various techniques to first relate observed changes in nanofiber properties to specific adjustments in the electrospinning procedure. The composite nanofibers were run through different isotherm experiments to analyze the adsorption performance towards CrO_4^{2-}. Based on their adsorption capabilities, the structural modifications critical to optimizing treatment efficiency were identified.

6.3 Experimental Methods

6.3.1 Reagents

All chemicals were reagent grade or better and used as received. The synthesis of the Fe_2O_3 nanofibers involved iron(III) 2-ethylhexano-isopropoxide (Alfa Aesar, 10% w/v in isopropanol) as the iron precursor, acetic acid (Fisher Scientific, glacial 99.7%) as an additive and polyvinylpyrrolidone (PVP) (Sigma Aldrich, MW: 1,300,000 g/mol) as the polymer. The Al precursor used to fabricate Al_2O_3-Fe_2O_3 composite nanofibners was aluminum oxide hydroxide (AlOOH) nanopowder, which was synthesized based on previous research[10],[11] using aluminum isopropoxide (AlIP) (Sigma Aldrich, >98%), acetic acid, DI water and isopropanol (Fisher Scientific, Certified ACS Plus). A buffer prepared from 25 mM sodium chloride (NaCl) (Sigma Aldrich, >99.0%) was used in all adsorption experiments. A buffer prepared from 10 mM NaCl was used in all zeta

potential experiments. Lastly, potassium chromate (K_2CrO_4) (Fisher Scientific) was used as the heavy metal pollutant for the adsorption studies.

6.3.2 Synthesis of Al_2O_3-Fe_2O_3 nanofibers

The synthesis of unmodified Fe_2O_3 nanofibers began with the preparation of the polymer solution. 3 mL of iron(III) 2-ethylhexano-isopropoxide, 0.3 mL acetic acid and 4 wt. % of PVP were added in a 30 mL glass beaker and stirred with a magnetic stirrer at a rate of 300 rpm for an hour, insuring that all of the PVP has dissolved. For the composite nanofibers, a select amount of the AlOOH powder was added to the eletrospinning solution with content loading from 10 to 50 at.% Al to Fe. The total amount of metal precursor (Al and Fe) to the entire electrospinning solution was kept at 9 wt.%, just as the pure Fe_2O_3 nanofibers, in effort to prevent any increase of average diameter due to an increase in metal content.[12],[13] In short, the AlOOH powder was synthesized by mixing 1 g of AlIP, 6 μL of acetic acid, 353 μL of DI water and 7.1 mL of isopropanol in a beaker for 6 hours until a well-mixed suspension was formed.[10],[11] The AlIP sol-gel was then placed in an oven at 80 °C for 24 hours, forming the AlOOH powder.

For the electrospinning set-up, the needle was set at a distance of 10 cm from the drum collector, the feed rate at 0.3 mL/hr and the voltage at 20 kV, as described in Chapter 4. After electrospinning, the unmodified nanofibers were annealed at 500 °C at rate of 3 °C/min and held for 3 hours, while the composite nanofibers were annealed at 1000 °C in order for both metal oxides to crystallize.[10],[14] After annealing, the nanofibers were kept as dry samples in 20 mL glass vials for characterization and were

later used to make 1 g/L stock suspensions in DI water for zeta potential and adsorption tests.

6.3.3 Nanofiber Characterization

Fe_2O_3 nanofibers were characterized using several different techniques to quantify their size, morphological and optical properties. Nanofiber diameter was examined by a Phillips XL30 FEG scanning electron microscopy (SEM). For SEM, samples were prepared by placing approximately a 0.5 cm x 0.5 cm area of nanofibers onto a SEM sample holder. SEM imaging of n = 40 nanofibers yielded average diameters (with standard deviation) that were used to create sizing histograms. Energy dispersive x-ray (EDX) analysis was conducted following SEM imaging for the Al_2O_3-Fe_2O_3 nanofibers to quantify elemental composition.

Crystal phase, crystal orientation and average grain size were determined by a Bruker D8 Advance x-ray diffraction (XRD) analyzer. XRD samples were prepared in the same manner as described for the TiO_2 nanofibers. The 1 x 1 cm^2 samples were analyzed from 20° to 80° for the Bragg angle with an interval of 0.03°. Grain size was quantified by means of the Scherrer-Debye equation, which relates grain size to the diffraction peak properties.[15] The prominent hematite peak (104) was used for this calculation.

Zeta potential was determined by a Brookhaven Instrumental Corporation ZetaPALS zeta potential analyzer. Just like the protocol for the TiO_2 nanofibers, 100 μL of the 1 g/L nanofiber stock suspension was added to 3.5 mL of 10 mM NaCl set at

various pH values between 2 and 9. The point of zero charge (pzc) was calculated by interpolation between data points in which a zeta potential equal to 0 was achieved.

Band gap energy was quantified by a Thermo Scientific Evolution 300 UV-Vis spectrophotometer via diffuse reflectance infrared Fourier transform spectroscopy (DRIFTS). For analysis, the dry samples were analyzed over a wavelength scan from 200 to 800 nm and absorbance was measured. The band gap was calculated by taking the derivative of the absorbance curve, yielding a prominent negative peak.[16],[17] The wavelength value at the global minimum is converted into energy, thus yielding the band gap of the nanofibers.

Surface area was determined by BET analysis via Micromeritics ASAP 2020 Physisorption Analyzer in order to investigate any surface property change towards enhancement of adsorption. All samples were degassed at 300 °C for 3 hours prior to analysis.

6.3.4 Adsorption Experiments

Adsorption tests were conducted to quantify the performance capabilities of the composite nanofibers. Similar to the procedure explained in Chapter 4, six individual 10 mL vials contained 25 mM NaCl solution at pH 6, 0.1 g/L Fe_2O_3 nanofiber loading, and an initial CrO_4^{2-} concentration, which ranged from 5 to 200 μM. After the addition of the CrO_4^{2-} to the reactor vial, an initial sample of 0.5 mL is immediately withdrawn and passed through a 0.2 μm PFTE filter to remove the Fe_2O_3 nanofibers. Afterwards, the reaction vials are set on a circular rotator and mixed for 2 hours to reach equilibrium.

After 2 hours of agitation, a 0.5 mL aliquot from reach vial is withdrawn and filtered as the final sample. The dissolved concentrations of CrO_4^{2-} were determined via atomic absorbance spectrometer (AAS) (Perkin Elmer AAnalyst 800). Prior to the adsorption experiments, a calibration curve was created to correlate the light absorbance from the AAS to CrO_4^{2-} concentration. The supernatant from the reaction vials was run through the flame and the light absorbance was recorded. Based on the difference between the light absorbance of the initial and final sample, the amount of CrO_4^{2-} adsorbed by the Fe_2O_3 nanofibers was calculated. The data set was fitted into a Langmuir model isotherm to quantify adsorption properties (i.e., maximum adsorption capacity). Additionally, adsorption kinetics was analyzed by mixing a reaction vial, containing the NaCl solution, Fe_2O_3 nanofibers and an initial CrO_4^{2-} concentration of 50 μM. 0.5 mL aliquots were withdrawn and filtered with respect to time (0 to 120 min). Samples were analyzed via AAS and adsorption kinetic rates were calculated by fitting the data into a pseudo-second-order adsorption kinetic model.

6.4 Results and Discussion

6.4.1 Nanofiber Characterization

Al_2O_3-Fe_2O_3 composite nanofibers were synthesized using the protocol that yielded 23 nm-sized unmodified Fe_2O_3 nanofibers (4 wt.% PVP, 20 kV voltage, 0.3 mL/hr feedrate) Based on SEM analysis, there was no significant change in average diameter of the Al_2O_3-Fe_2O_3 composite nanofibers. As seen in Figure 6-1, the average

diameter slightly increased from 23 (± 6) to 25-26 (± 6-7) nm with the addition of Al, but was still well within the standard error of the unmodified nanofibers.

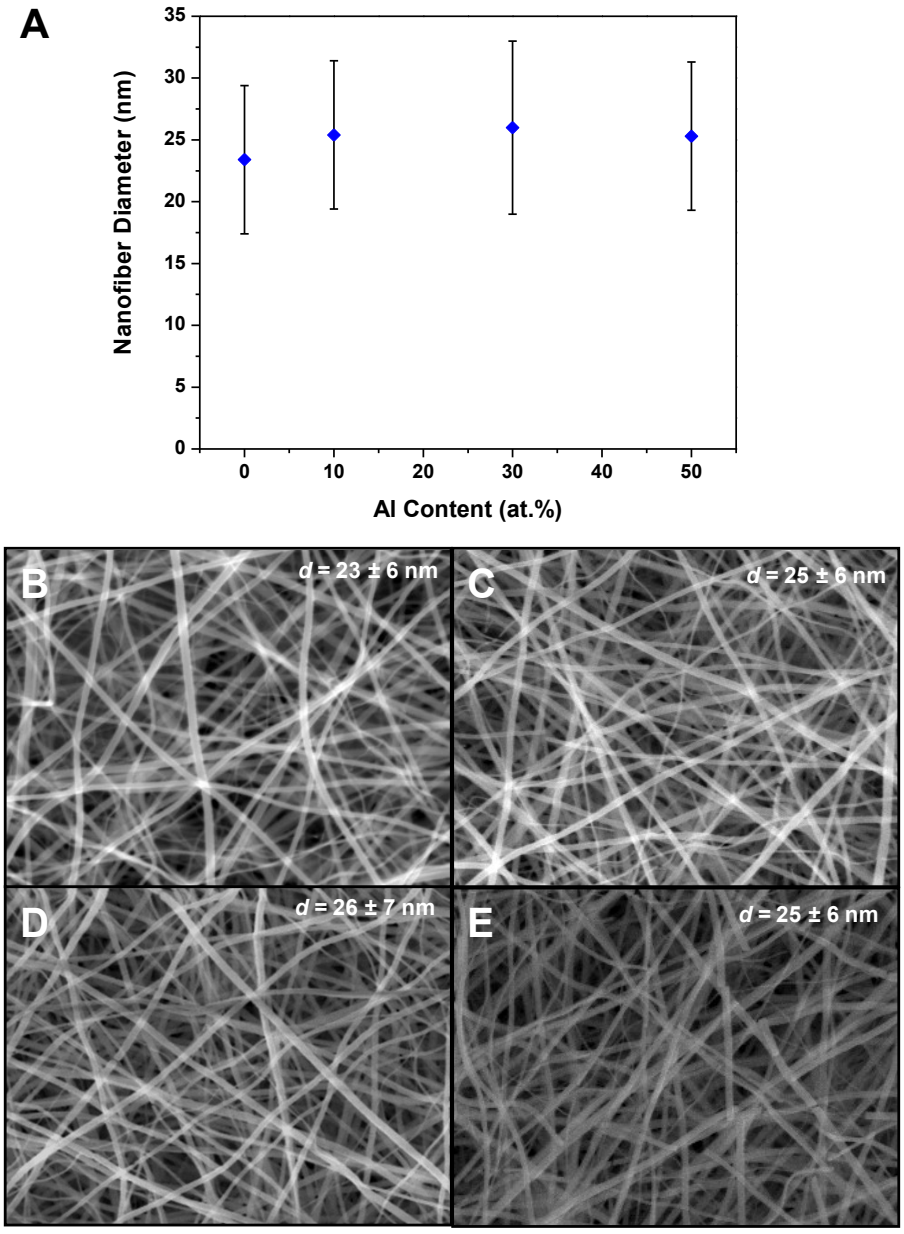

Figure 6-1: A) Average diameter as a function Al content for the Al_2O_3-Fe_2O_3 nanofibers and corresponding SEM images of B) 0, C) 10, D) 30, and E) 50 at.% Al content levels.

EDX was conducted to ensure the presence of Al in the composite nanofibers. Figure 6-2 provides the EDX spectra of the Al_2O_3-Fe_2O_3 nanofibers, showing the presence of Al with increasing Al content. In accordance with previous work,[4] the atomic percent of oxygen (O) reached around ~60 at.% while the atomic percentage of Al and Fe together was ~40 at.% The ratio of Al to Fe analyzed from EDX was slightly lower than anticipated from synthesis, with Al to Fe ratio values 9.7, 18.7, and 32.4 at.% for 10, 30, and 50 at.%, respectively. In addition, since the atomic percent of oxygen (O) stays stable at ~60 at.% with increased Al content, the species of Al oxide in the nanofibers is highly likely to be Al_2O_3. Henceforth, the composite nanofibers will be designated as 10, 19, and 32% Al/Fe.

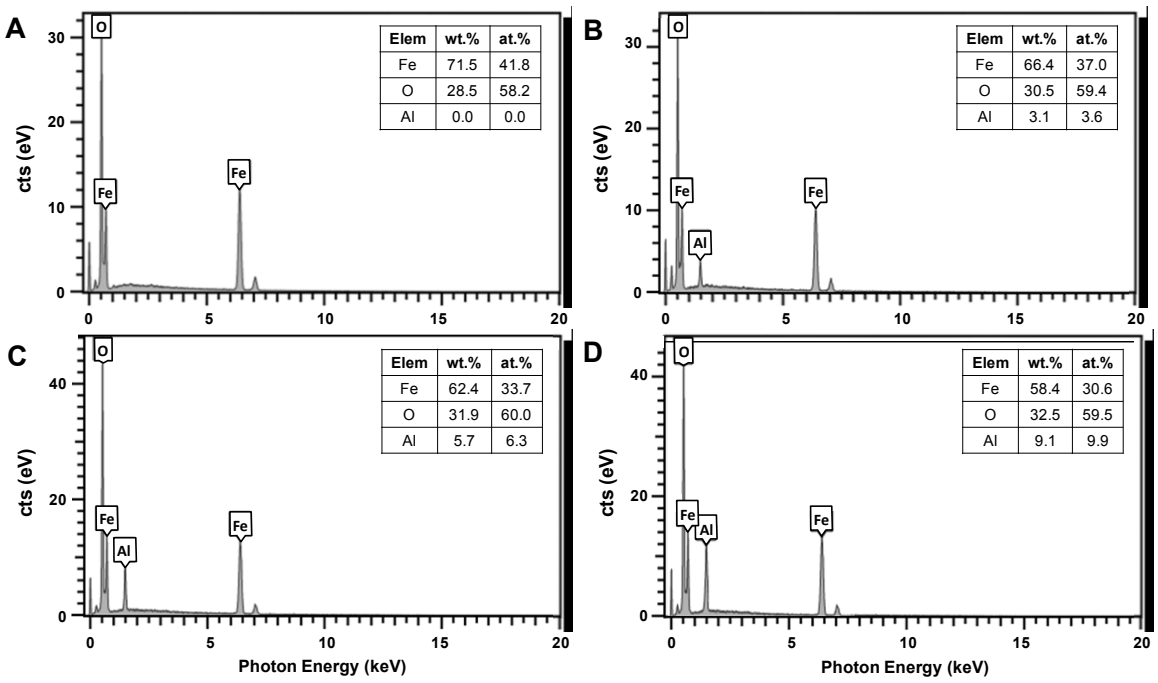

Figure 6-2: EDX spectra of the A) 0, B) 10, and C) 30, and D) 50 at.% Al_2O_3-Fe_2O_3 nanofibers.

XRD characterization was conducted to analyze crystallinity and crystal phase of the composite nanofibers. Firstly, XRD analysis was carried out on the AlOOH nanopowder to verify its crystal structure. The XRD spectra, seen in Figure 6-3, verified that the synthesized nanopowder was boehmite, γ-AlOOH (#21-1307) and, annealed at 1000 and 1200 °C, the nanopowder transformed into θ-Al_2O_3 (#11-0517) and α-Al_2O_3 (#10-0173), respectively, in accordance to previous work,[10],[18] although their intensities were nearly 10-20% that of hematite. In Figure 6-4, the Al_2O_3-Fe_2O_3 nanofibers showed hematite pattern (#33-0664) for all samples and a very small (230) alumina peak for both 19 and 32% Al/Fe ratio, possible due to the low intensity of the θ-Al_2O_3 spectra. Previous work has shown similar results, where no substantial Al peaks from XRD spectra were observed, even up to 50 mol% Al to Fe.[4] The 32 at.% Al/Fe nanofiber sample annealed at 1200 °C maintained the hematite pattern and exhibited several α-Al_2O_3 peaks (Figure 6-5). Additionally, there was no significant change in average grain size of the composite nanofibers despite the higher annealing temperature (Figure 6-6), where the average grain size was stable at 35 nm regardless of the Al/Fe ratio. Similar to the results seen in Chapter 4, the average grain sizes were slightly larger than the nanofiber diameter, indicating possible ellipsoidal grains existing within the nanofibers.

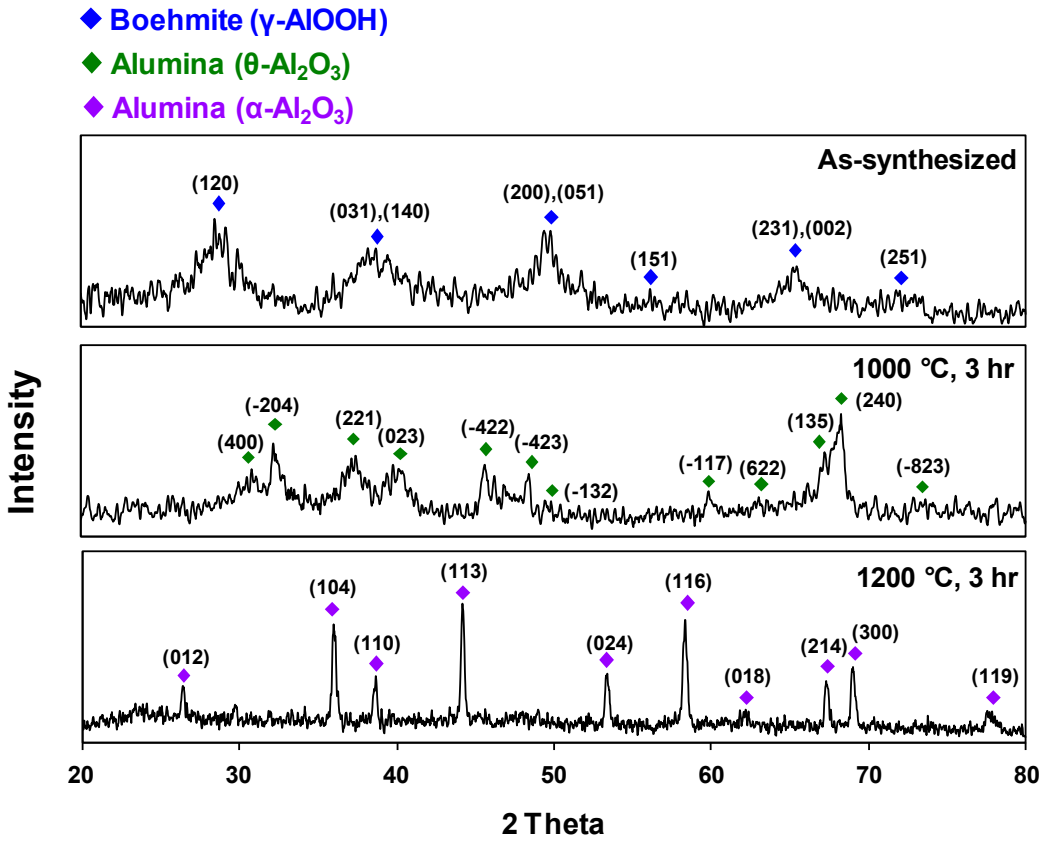

Figure 6-3: XRD pattern of the sol-gel synthesized boehmite (AlOOH) and annealed alumina (Al_2O_3) nanopowders.

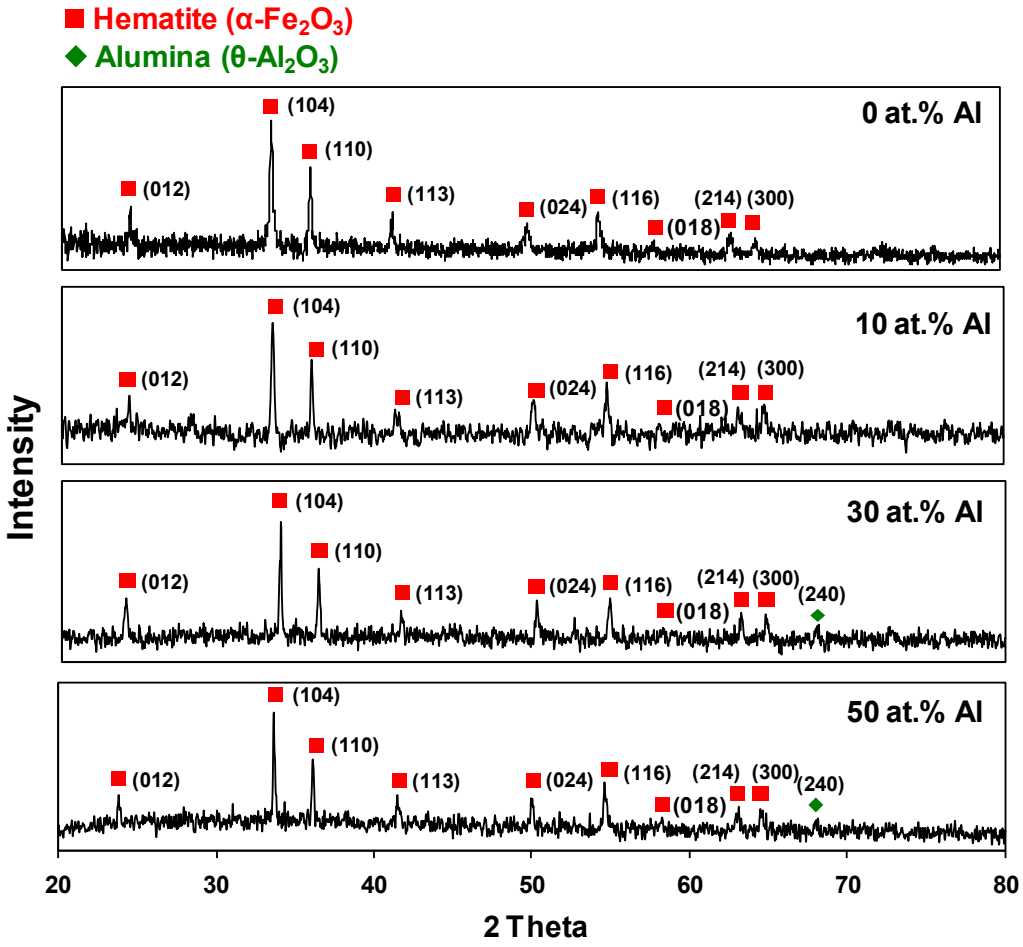

Figure 6-4: XRD patterns of the Al_2O_3-Fe_2O_3 nanofibers at different Al/Fe ratios.

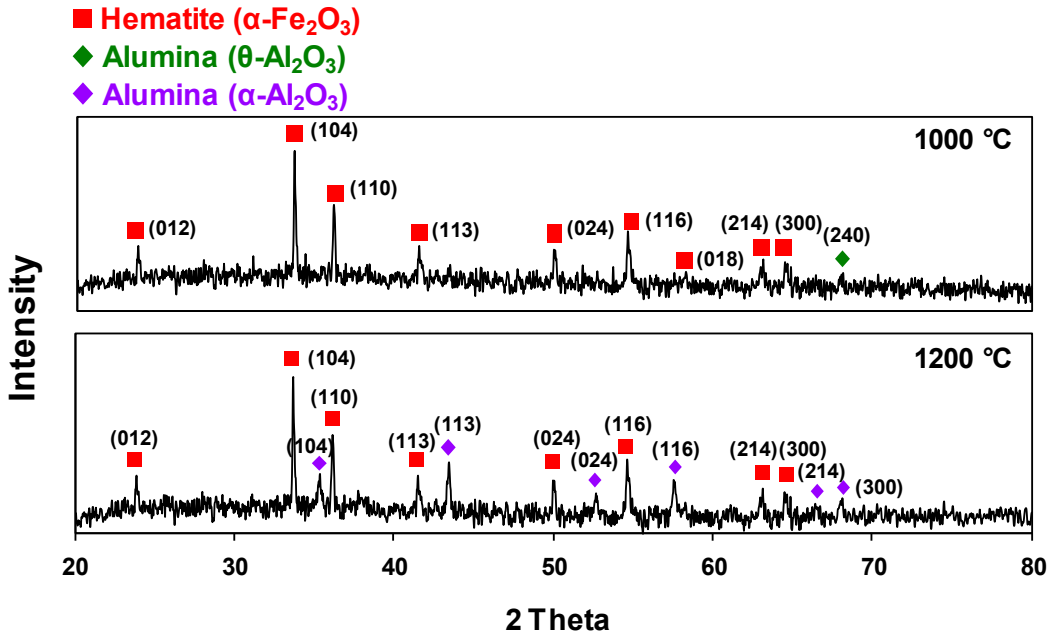

Figure 6-5: XRD patterns of 32% Al_2O_3-Fe_2O_3 nanofibers at different annealing temperatures.

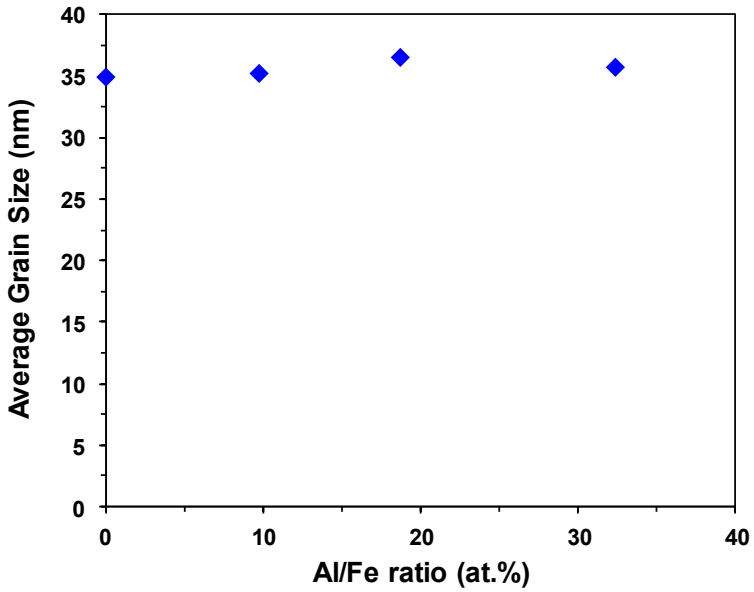

Figure 6-6: Average grain size as a function of Al/Fe ratio of the Al_2O_3-Fe_2O_3 nanofiber diameter.

Zeta potential measurements of the composite nanofibers were conducted to observe any change in the surface charge of the Fe_2O_3 nanofibers that could have occurred due to the addition of Al, possibly altering the pzc. As seen in Figure 6-7, zeta potential did not show any significant shift with the addition of Al. The pH of pzc increased from 7.08 for the pure nanofibers to 7.13-7.15 for the composite nanofibers, still within the value of the commercially-available Fe_2O_3 nanoparticles (7.12) and comparable to reported values.[19],[20]

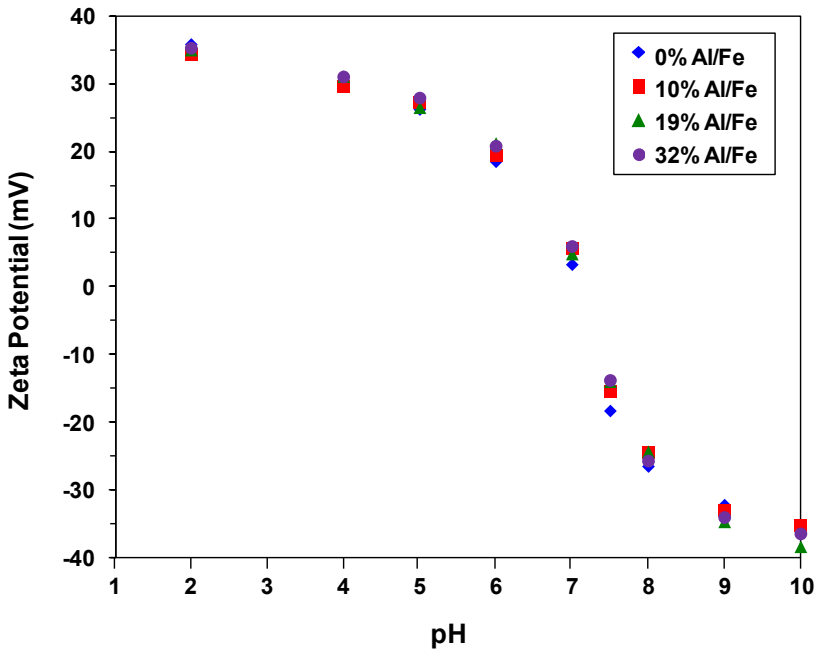

Figure 6-7: Zeta potential of Al_2O_3-Fe_2O_3 nanofibers at different Al content levels.

Diffuse reflectance was conducted to characterize the band gap of the composite nanofibers. The addition of Al did not alter the band gap of the composite nanofibers as the band gap value stayed at 2.17 eV with increasing Al content (Figure 6-8), which is accordance with the hematite band gap range of 2.1-2.2 eV. [6],[21] Although Al_2O_3 is very

insulating (5-8 eV),[22]–[24] the composite nanofibers maintained a band gap value to that of pristine hematite, which has been reported in previous work.[6],[25]

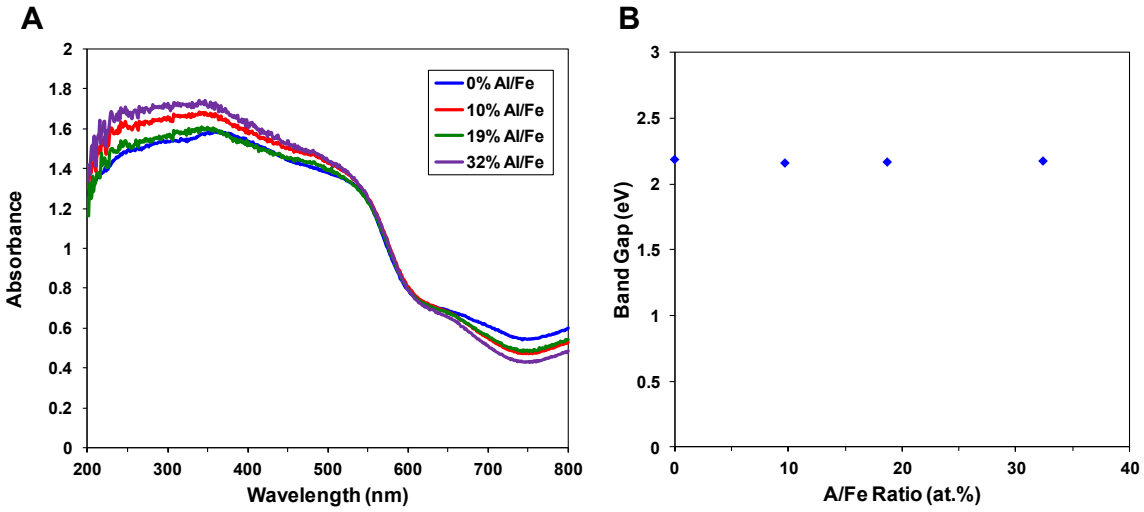

Figure 6-8: A) Diffuse reflectance absorbance curves of different Al_2O_3-Fe_2O_3 nanofibers and B) band gap energy as a function of Al/Fe ratio of Al_2O_3-Fe_2O_3 nanofibers

BET analysis provided information on specific surface area and pore dimension of the Al_2O_3-Fe_2O_3 composite nanofibers (Table 6-1). Specific surface area increased with increased Al/Fe ratio, indicating enhanced surface area due to the introduction of Al (Figure 6-9). The specific surface area increased from 59.2 m^2/g for the unmodified Fe_2O_3 nanofibers up to 92.8 m^2/g for the 32 at.% Al/Fe composite nanofibers. These results correlate with previous research,[4] where Al incorporation has a significant effect on enhancing specific surface area. It can be easily observed that the high surface area of the Al_2O nanopowder (134.2 m^2/g) greatly contributed to the overall enhanced surface area of the composite nanofibers. Additionally, pore volume increased and average pore width

decreased alongside increased Al/Fe ratio. Nevertheless, the surface area of the composite nanofibers is greater than the calculated surface area from the contributions of its two metal oxide components according to XRD and BET data, which suggests synergy between the Fe_2O_3 and Al_2O_3 to yield increased porosity and enhanced surface area. The different in average grain size of the Fe_2O_3 (~35 nm) and Al_2O_3 (~15 nm) within the nanofiber could lead to increased surface roughness and promote increased surface area. Comparatively, the composite nanofibers had significantly greater surface area than the commercially Fe_2O_3 nanoparticles (28.4 m^2/g).

Moreover, the BET analysis of the 32 at.% Al/Fe nanofibers provides more evidence of Al's strong influence on the surface area of the composite nanofibers. Annealed at a higher temperature of 1200 °C, the surface area of the 32 at.% composite nanofibers decreased significantly (53.3 m^2/g), most likely due to the phase transformation of the Al_2O_3 from theta to alpha (10.9 m^2/g). Similar to the other composite nanofibers, the surface area was greater than the calculated contributions, which could be due to the change different in grain size between the Fe_2O_3 and α-Al_2O_3 (~25 nm). However, the low surface area of the α-Al_2O_3 led to a considerable decrease in surface area of the α-composite nanofibers, which could be detrimental to adsorption performance.

Table 6-1: BET analysis data of A) Al_2O_3-Fe_2O_3 composite nanofibers as a function of Al/Fe ratio, and B) 32 at.% Al_2O_3-Fe_2O_3 composite nanofibers and alumina nanopowders as a function of alumina phase.

A

Al/Fe ratio (%)	SSA (m^2/g)	SSA_{Meso} (m^2/g)	SSA_{Micro} (m^2/g)	Pore Volume (cm^3/g)	Average Pore Width (nm)
0	59.2	43.2	16.0	0.198	13.4
9.7	66.4	48.3	18.1	0.201	12.1
18.7	75.6	57.1	18.5	0.206	10.9
32.4	92.8	72.3	20.5	0.217	9.3
NPs	28.4	22.5	5.9	0.094	13.2

B

Material	SSA (m^2/g)	SSA_{Meso} (m^2/g)	SSA_{Micro} (m^2/g)	Pore Volume (cm^3/g)	Average Pore Width (nm)
θ-Al_2O_3-Fe_2O_3	92.8	72.3	20.5	0.231	9.9
α-Al_2O_3-Fe_2O_3	53.3	35.0	18.2	0.115	8.6
θ-Al_2O_3	134.2	102.8	31.4	0.791	23.0
α-Al_2O_3	10.9	1.8	9.1	0.018	6.7

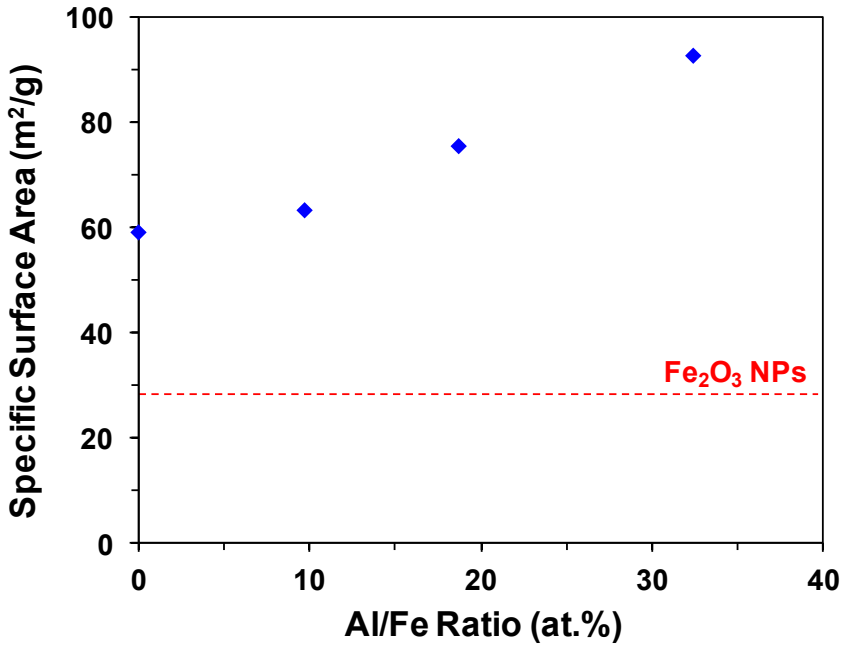

Figure 6-9: Specific surface area of Al_2O_3-Fe_2O_3 nanofibers as a function of Al/Fe ratio.

6.4.2 Adsorption Performance

Firstly, adsorption kinetics was determined to identify the rate of CrO_4^{2-} adsorption on the Al_2O_3-Fe_2O_3 composite nanofibers. The adsorption of CrO_4^{2-} (C_0 = 50 μM) on the composite nanofibers with respect to time can be seen in Figure 6-10. Adsorption was initially rapid up to 30 minutes and plateaued gradually afterwards as adsorption reaches equilibrium. The adsorption data was fitted into a pseudo-second-order adsorption kinetic model, described in the following equation:[4],[10]

$$\frac{dq_t}{dt} = k(q_e - q_t)^2 \tag{6.1}$$

where t is time in minutes, q_t is the amount of CrO_4^{2-} adsorbed at time t in mg/g, q_e is equilibrium adsorption capacity in mg/g, and k is the second-order adsorption rate constant in g/mg·min. The value of kq_e^2 can be defined as h, the initial adsorption rate in mg/g·min, and used to compare among the different nanofiber materials. After integrating equation 5.1 as a function of time, the integrated equation can be rearranged to obtain:

$$\frac{t}{q_t} = \frac{1}{kq_e^2} + \frac{1}{q_e}t \tag{6.2}$$

Plotting t/q_t as a function of time, as seen Figure 6-11-A, will linearize the kinetic model to yield adsorption rate, h. Initial adsorption rate of the composite nanofibers increased with increased Al content (Figure 6-11-B), similar to results described in previous

work.[4] The increased surface area brought upon by the introduction of Al in the composite nanofibers led to increased adsorption kinetics.

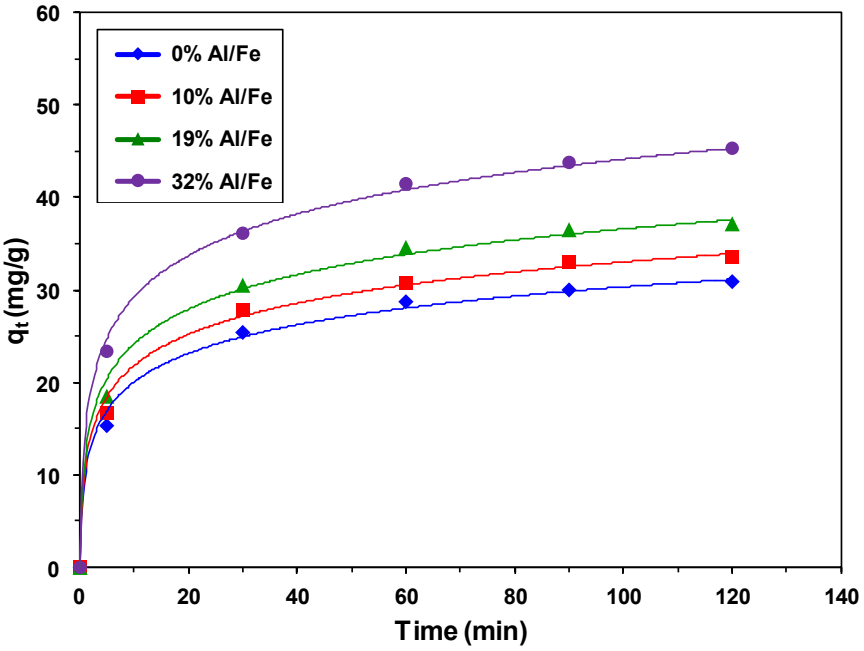

Figure 6-10: Adsorption of CrO_4^{2-} as a function of time of Al_2O_3-Fe_2O_3 composite nanofibers.

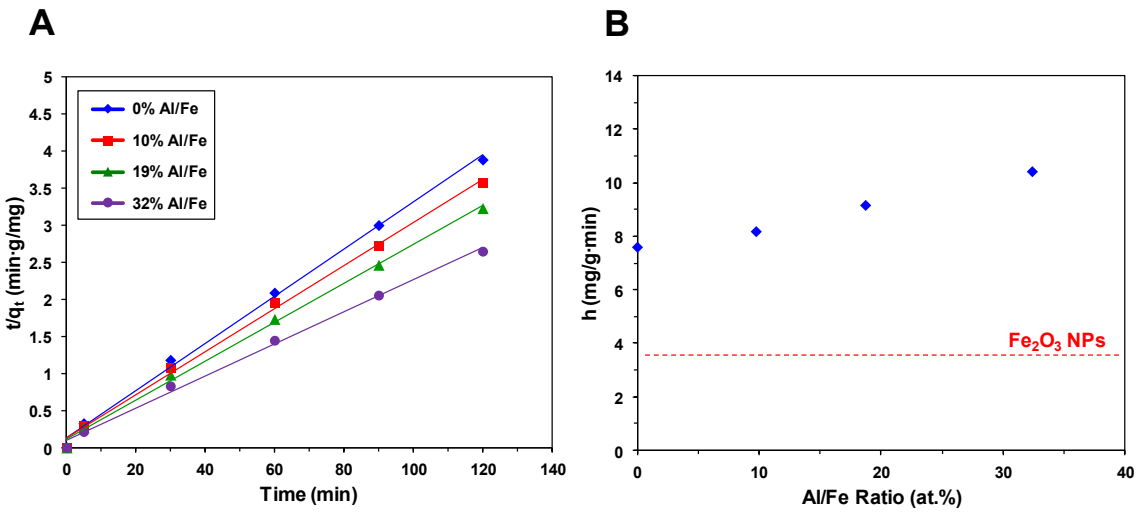

Figure 6-11: A) Pseudo-second-order adsorption kinetic fit of Al_2O_3-Fe_2O_3 nanofibers and B) initial adsorption rate *h* as a function of Al/Fe ratio of Al_2O_3-Fe_2O_3 nanofibers.

Additionally, adsorption isotherms helped quantify the CrO_4^{2-} adsorption capacity of the composite nanofibers. Figure 6-12 shows that the increasing Al content leads to greater adsorption according to the isotherm curves, which is expected due to the Al's contribution to surface area.[4] Furthermore, the adsorption isotherm curves normalized by specific surface area showed uniformity at all Al/Fe ratios (Figure 6-13), which also has been reported by previous work.[4] This indicates that adsorption performance is significantly linked to specific surface area.

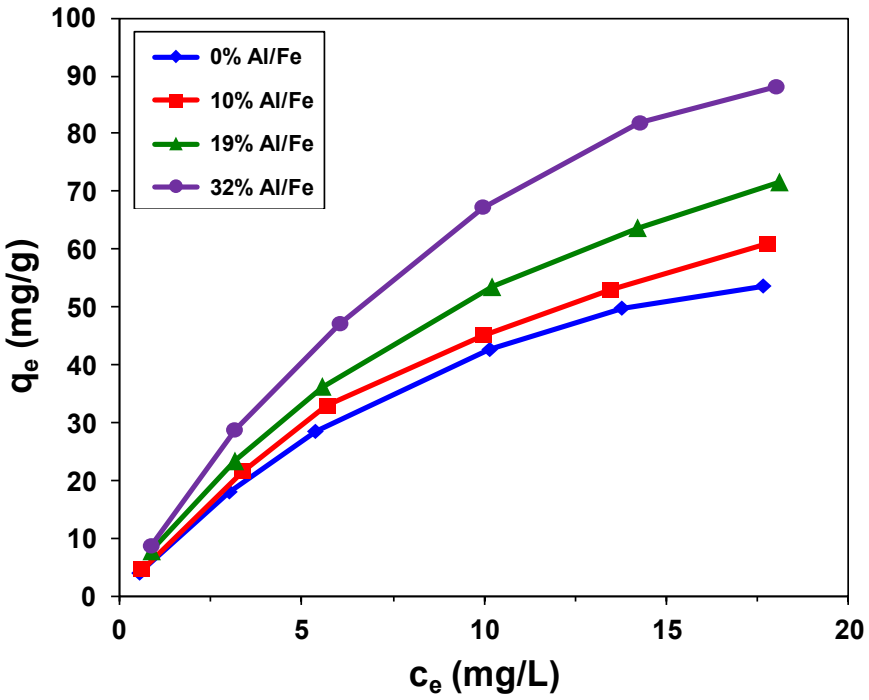

Figure 6-12: CrO_4^{2-} adsorption isotherm of Al_2O_3-Fe_2O_3 nanofibers.

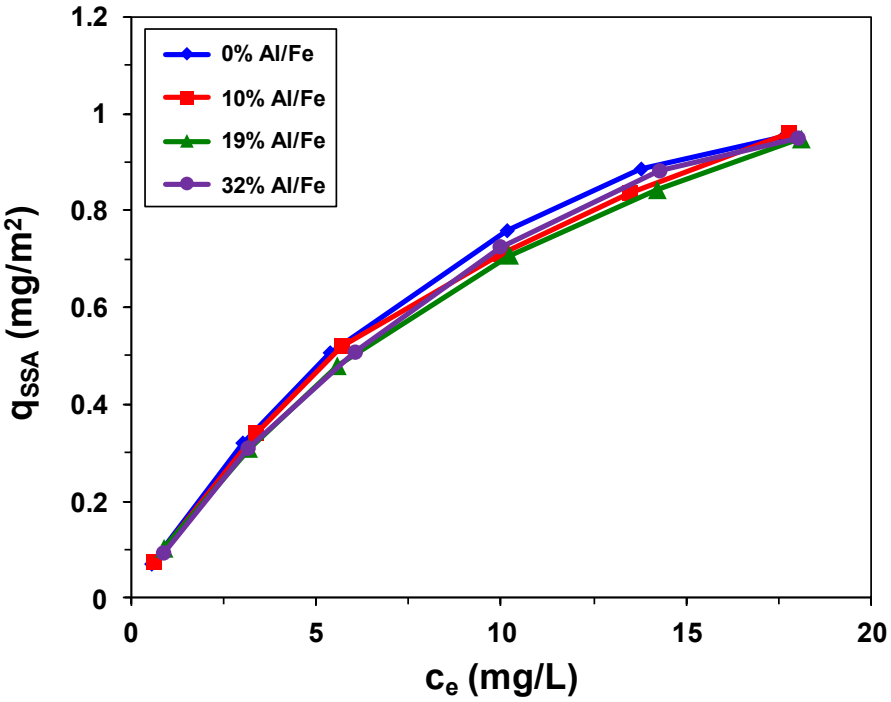

Figure 6-13: Specific surface area-normalized CrO_4^{2-} adsorption isotherm of Al_2O_3-Fe_2O_3 nanofibers.

The adsorption isotherms were then fitted towards the Langmuir adsorption model, which is defined as:

$$q_e = q_m \frac{bc_e}{1 + bc_e} \tag{6.3}$$

where c_e is the equilibrium concentration of CrO_4^{2-} in mg/L, q_e is equilibrium adsorption capacity of CrO_4^{2-} on Fe_2O_3 in mg/g, q_m is the maximum adsorption capacity in mg/g, and b is the Langmuir equilibrium constant in L/mg.[26] The Langmuir linear regression fit was utilized to yield a maximum adsorption capacity:

$$\frac{c_e}{q_e} = \frac{1}{bq_m} + \frac{c_e}{q_m} \tag{6.4}$$

As seen in Figure 6-15**,** the adsorption capacity increased dramatically due to Al introduction, where the maximum adsorption capacity value increased from 90.9 mg/g for the unmodified Fe_2O_3 nanofibers to 163.9 mg/g for the 32 at.% Al/Fe composite nanofibers.

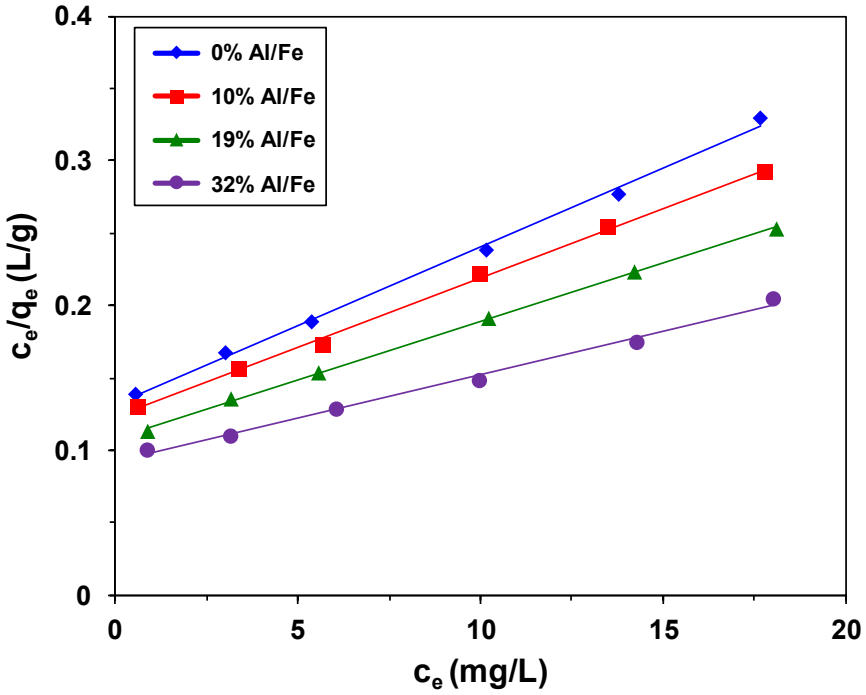

Figure 6-14: CrO_4^{2-} adsorption isotherm of Al_2O_3-Fe_2O_3 nanofibers fitted to linearized Langmuir model.

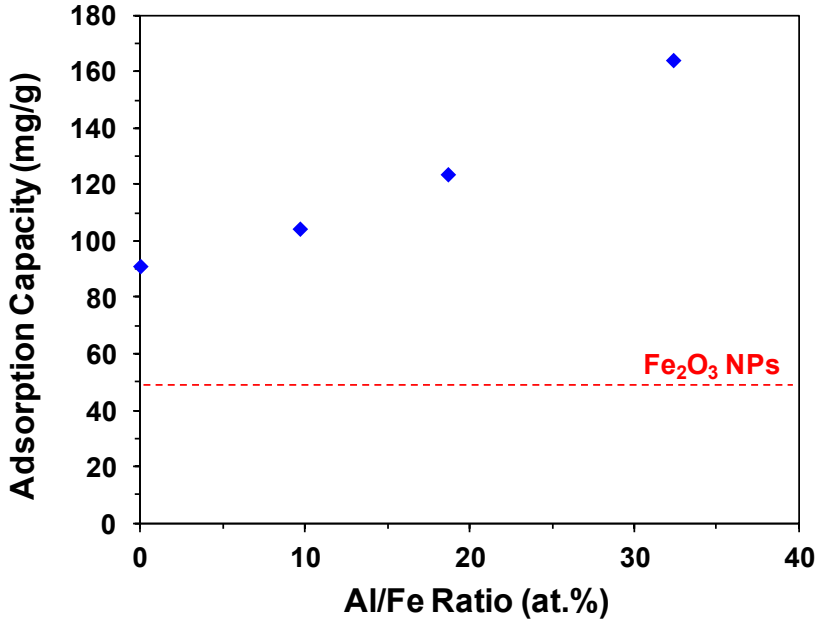

Figure 6-15: Maximum adsorption capacity of Al_2O_3-Fe_2O_3 nanofibers as a function of Al/Fe ratio.

Adsorption isotherms in Figure 6-16 show the performance of the 32 at.% Al/Fe composite nanofibers as well as the Al_2O_3 nanopowders. The alpha-composite nanofibers (77.5 mg/g) performed worse than the theta-composite (163.9 mg/g) and unmodified nanofibers (90.9 mg/g) on a mass basis, but all performed similarly when normalized by surface area, which again suggests surface area-driven adsorption. Similarly, α-Al_2O_3 nanopowder (11.7 mg/g) was outperformed by θ-Al_2O_3 (39.7 mg/g) nanopowder, but was significantly more efficient on a surface area-basis (Figure 6-17). This suggests that the Al_2O_3 nanoparticles in the composite nanofibers, regardless of crystal phase, provide their characteristic surface area substantially, but not their adsorption capabilities entirely. Therefore, there is likely synergy existing between the Al_2O_3 and Fe_2O_3 towards enhance adsorption performance (Figure 6-18).

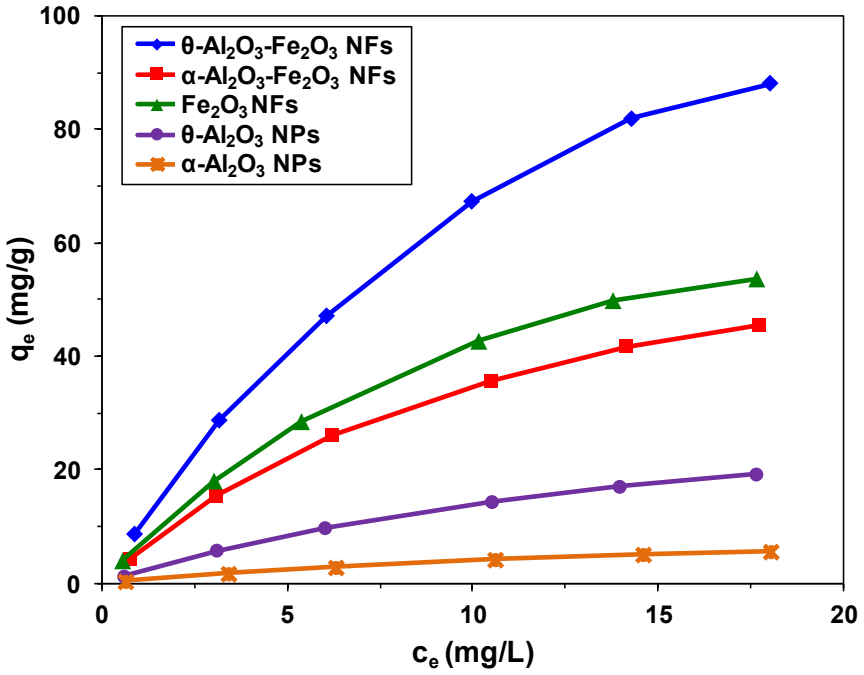

Figure 6-16: CrO_4^{2-} adsorption isotherm of 32% Al/Fe composite nanofibers and Al_2O_3 nanopowders.

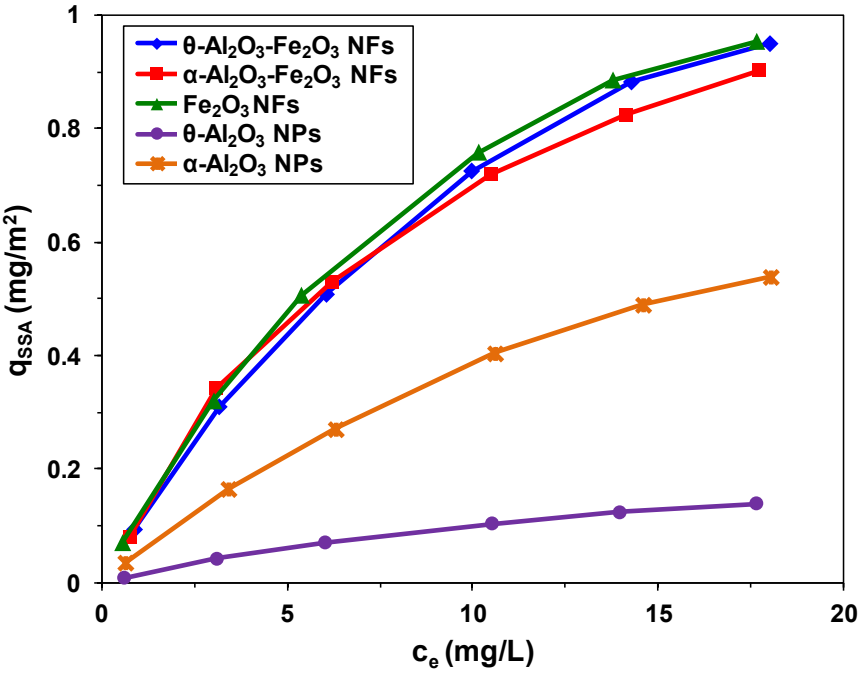

Figure 6-17: Specific surface area-normalized CrO_4^{2-} adsorption isotherm of 32% Al/Fe composite nanofibers and Al_2O_3 nanopowders.

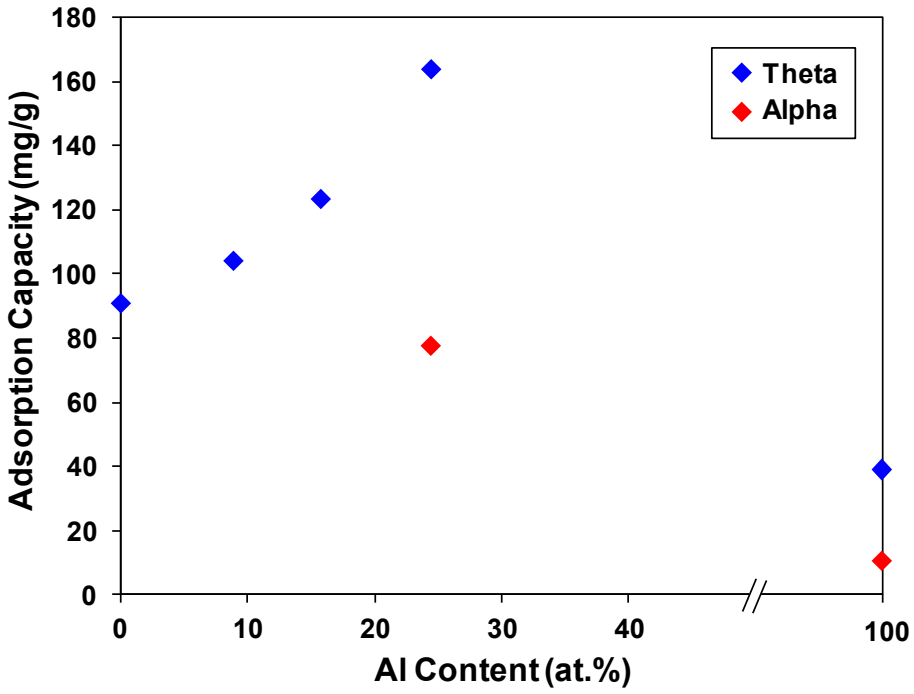

Figure 6-18. Maximum adsorption capacity of Al_2O_3-Fe_2O_3 nanofibers and Al_2O_3 nanopowders at different alumina phases as a function of Al content.

Overall, the Al_2O_3-Fe_2O_3 composite nanofibers exhibited enhanced adsorption of CrO_4^{2-} solely due to increased surface area. While the average diameter of the composite nanofibers was stable and independent of Al content, the increase in surface area is exclusively attributed to the introduction of Al_2O_3. Naturally, the increase in surface area is largely in part by the inherently high surface area of Al_2O_3 (100-200 m^2/g).[11],[18] Since the analyzed BET surface area was greater than the sum of the metal oxide contributions, the combination of Fe_2O_3 and Al_2O_3 augmented surface area synergistically. Reports suggest that increased Al content in the composite nanofibers will increase the specific surface area via increased and retainable adsorption sites (-OH).[4] Additionally, as

previously stated, the differences in average grain size between Al_2O_3 and Fe_2O_3 could introduce increased surface roughness, and subsequently, increased surface area.

The isotherm studies revealed that adsorption capacity of the composite nanofibers increased due to the addition of Al, and that the performance was directly related to surface area based on the normalized isotherms. Since the adsorption performance of Fe_2O_3 was greater than that of Al_2O_3, it is proposed that the combination of Al_2O_3 and Fe_2O_3 in the composite nanofibers provides enhanced adsorption of chromate synergistically. As previously stated, reports state that Fe_2O_3 is a better adsorbent than Al_2O_3 due to stronger adsorption bonds,[27],[28] which is in accordance with this work's adsorption isotherm data; the calculated Langmuir constant *b*, which is directly related to adsorption bond strength, was greater for the Fe_2O_3 (0.08 mg/L) nanofibers than it was for the Al_2O_3 nanoparticles (0.053 L/mg).

Interestingly, the Langmuir constants of the composite nanofibers they did not increase, but actually decreased steadily with Al content towards the value of the Al_2O_3 nanoparticles. Analysis of the Langmuir constants based on metal oxide composition suggests that the adsorption bond strength of both Al_2O_3 and Fe_2O_3 was not altered within the composite nanofibers. Given that adsorption performance increased while adsorption bond strength was stable with increased Al content, the number of adsorption sites on the composite nanofibers must have increased, resulting in greater adsorption capacity in relation to increased surface area.[4] Furthermore, since the Langmuir constant of the composite nanofibers steadily decreased towards the value of the Al_2O_3 nanoparticles, it is likely that further addition of Al content could disrupt or reduce the reactive adsorption

sites of Fe_2O_3 surface and disturb the adsorption performance, indicating an optimal Al_2O_3/Fe_2O_3 composition.[9]

6.5 Conclusion

Electrospun Al_2O_3-Fe_2O_3 composite nanofibers were fabricated to further enhance heavy metal removal of conventional Fe_2O_3 nanomaterials. Through facile property modifications via electrospinning parameter tuning, composite nanofibers were synthesized allows for control of nanofiber property manipulation towards optimization of CrO_4^{2-} adsorption. Al_2O_3-Fe_2O_3 nanofibers were developed with controlled average diameter (~25 nm), crystallinity (hematite), and average grain size (~35 nm). Additionally, band gap and zeta potential were unaltered with the addition of Al. However, specific surface area of the composite nanofiber was greatly enhanced due to the addition of Al, increasing surface area value with increased Al content. As a result, adsorption capacity and kinetics were enhanced based on adsorption studies with CrO_4^{2-}. With a specific surface area of 92.8 m^2/g, the 32 at.% Al/Fe composite nanofibers had outperformed the unmodified Fe_2O_3 nanofibers by nearly a factor of 2 and the commercially-available Fe_2O_3 nanoparticles by over a factor of 3. Based on the adsorption studies, synergy between Al_2O_3 and Fe_2O_3 resulted in greater adsorption performance, likely due to increased surface adsorption sites. Composite Al_2O_3-Fe_2O_3 nanofibers represent an innovative nanomaterial for future heavy metal removal systems, having greater treatment potential than conventional Fe_2O_3 materials.

6.6 References

[1] Zheng, W.; Li, Z.; Zhang, H.; Wang, W.; Wang, Y.; Wang, C. Electrospinning Route for Alpha-Fe_2O_3 Ceramic Nanofibers and Their Gas Sensing Properties. *Materials Research Bulletin* **2009**, *44*, 1432–1436.

[2] Zhu, Y.; Zhang, J. C.; Zhai, J.; Jiang, L. Preparation of Superhydrophilic Alpha-Fe_2O_3 Nanofibers with Tunable Magnetic Properties. *Thin Solid Films* **2006**, *510*, 271–274.

[3] Shao, H.; Zhang, X.; Liu, S.; Chen, F.; Xu, J.; Feng, Y. Preparation of Pure Iron Nanofibers via Electrospinning. *Materials Letters* **2011**, *65*, 1775–1777.

[4] Li, R.; Li, Q.; Gao, S.; Shang, J. K. Enhanced Arsenite Adsorption onto Litchi-Like Al-Doped Iron Oxides. *Journal of the American Ceramic Society* **2011**, *94*, 584–591.

[5] Li, D.; Herricks, T.; Xia, Y. Magnetic Nanofibers of Nickel Ferrite Prepared by Electrospinning. *Applied Physics Letters* **2003**, *83*, 4586.

[6] Kleiman-Shwarsctein, A.; Huda, M. N.; Walsh, A.; Yan, Y.; Stucky, G. D.; Hu, Y.-S.; Al-Jassim, M. M.; McFarland, E. W. Electrodeposited Aluminum-Doped Alpha-Fe_2O_3 Photoelectrodes: Experiment and Theory. *Chemistry of Materials* **2010**, *22*, 510–517.

[7] Li, X.; Zhao, R.; Sun, B.; Lu, X.; Zhang, C.; Wang, Z.; Wang, C. Fabrication of A-Fe_2O_3–γ-Al_2O_3 Core–shell Nanofibers and Their Cr(VI) Adsorptive Properties. *RSC Adv.* **2014**, *4*, 42376–42382.

[8] El-Latif, M. M. A.; Ibrahim, A. M.; Showman, M. S.; Hamide, R. R. A. Alumina/Iron Oxide Nano Composite for Cadmium Ions Removal from Aqueous Solutions. *International Journal of Nonferrous Metallurgy* **2013**, *2*, 47–62.

[9] Mohapatra, M.; Mohapatra, L.; Hariprasad, D.; Anand, S.; Mishra, B. K. Nano-Structured Mg-Doped Fe_2O_3-Ferrihydrite Powder--a New Adsorbent for Cation Removal from Aqueous Solutions. *Environmental Technology* **2014**, *33*, 1717–26.

[10] Mahapatra, a; Mishra, B. G.; Hota, G. Electrospun Fe_2O_3-Al_2O_3 Nanocomposite Fibers as Efficient Adsorbent for Removal of Heavy Metal Ions from Aqueous Solution. *Journal of hazardous materials* **2013**, *258-259*, 116–123.

[11] Kim, S.-M.; Lee, Y.-J.; Jun, K.-W.; Park, J.-Y.; Potdar, H. S. Synthesis of Thermo-Stable High Surface Area Alumina Powder from Sol–gel Derived Boehmite. *Materials Chemistry and Physics* **2007**, *104*, 56–61.

[12] Eid, C.; Brioude, A.; Salles, V.; Plenet, J.-C.; Asmar, R.; Monteil, Y.; Khoury, R.; Khoury, A.; Miele, P. Iron-Based 1D Nanostructures by Electrospinning Process. *Nanotechnology* **2010**, *21*, 125701.

[13] Eid, C.; Luneau, D.; Salles, V.; Asmar, R.; Monteil, Y.; Khoury, A.; Brioude, A. Magnetic Properties of Hematite Nanotubes Elaborated by Electrospinning Process. *Journal of Physical Chemistry C* **2011**, *115*, 17643–17646.

[14] Panda, P. K.; Ramakrishna, S. Electrospinning of Alumina Nanofibers Using Different Precursors. *Journal of Materials Science* **2007**, *42*, 2189–2193.

[15] Hosseini, S. N.; Borghei, S. M.; Vossoughi, M.; Taghavinia, N. Immobilization of TiO_2 on Perlite Granules for Photocatalytic Degradation of Phenol. *Applied Catalysis B: Environmental* **2007**, *74*, 53–62.

[16] Gilbert, B.; Frandsen, C.; Maxey, E.; Sherman, D. Band-Gap Measurements of Bulk and Nanoscale Hematite by Soft X-Ray Spectroscopy. *Physical Review B* **2009**, *79*, 035108.

[17] Shijie Wang, J. E. Dutrizac, Michael L. Free, James Y. Hwang, D. K. *T.T. Chen Honorary Symposium on Hydrometallurgy, Electrometallurgy and Materials Characterization*; John Wiley & Sons, Inc., 2012; p. 803.

[18] Lee, S. C.; Cho, M. S.; Jung, S. Y.; Ryu, C. K.; Kim, J. C. Effects of Alumina Phases on CO_2 Sorption and Regeneration Properties of Potassium-Based Alumina Sorbents. *Adsorption* **2013**, *20*, 331–339.

[19] Kosmulski, M. The pH-Dependent Surface Charging and the Points of Zero Charge. *Journal of Colloid and Interface Science* **2002**, *253*, 77–87.

[20] Kosmulski, M. The pH-Dependent Surface Charging and Points of Zero Charge: V. Update. *Journal of Colloid and Interface Science* **2011**, *353*, 1–15.

[21] Vayssieres, L.; Sathe, C.; Butorin, S. M.; Shuh, D. K.; Nordgren, J.; Guo, J. One-Dimensional Quantum-Confinement Effect in Alpha-Fe_2O_3 Ultrafine Nanorod Arrays. *Advanced Materials* **2005**, *17*, 2320–2323.

[22] Koo, J.; Kim, S.; Jeon, S.; Jeon, H.; Kim, Y. Characteristics of Al_2O_3 Thin Films Deposited Using Dimethylaluminum Isopropoxide and Trimethylaluminum

Precursors by the Plasma-Enhanced Atomic-Layer Deposition Method. *Journal of the Korean Physical Society* **2006**, *48*, 131–136.

[23] Mousavi, S. J.; Abolhassani, M. R.; Hosseini, S. M.; Sebt, S. A. Comparison of Electronic and Optical Properties of the A and K Phases of Alumina Using Density Functional Theory. *Chinese Journal of Physics* **2009**, *47*, 862–873.

[24] Fang, C. M.; de Groot, R. a The Nature of Electron States in AlN and A-Al_2O_3. *Journal of Physics: Condensed Matter* **2007**, *19*, 386223.

[25] Shinde, S. S.; Bansode, R. a; Bhosale, C. H.; Rajpure, K. Y. Physical Properties of Hematite Alpha-Fe_2O_3 Thin Films: Application to Photoelectrochemical Solar Cells. *Journal of Semiconductors* **2011**, *32*, 013001.

[26] Ren, T.; He, P.; Niu, W.; Wu, Y.; Ai, L.; Gou, X. Synthesis of Alpha-Fe_2O_3 Nanofibers for Applications in Removal and Recovery of Cr(VI) from Wastewater. *Environmental Science and Pollution Research* **2013**, *20*, 155–62.

[27] Jeong, Y.; Fan, M.; Singh, S.; Chuang, C.-L.; Saha, B.; Hans van Leeuwen, J. Evaluation of Iron Oxide and Aluminum Oxide as Potential arsenic(V) Adsorbents. *Chemical Engineering and Processing: Process Intensification* **2007**, *46*, 1030–1039.

[28] Salmani, H. A Comparative Study of Copper (ii) Removal on Iron Oxide, Aluminum Oxide and Activated Carbon by Continuous down Flow Method. *Journal of Toxicology and Environmental Health Sciences* **2013**, *5*, 150–155.

Chapter 7: Conclusions

In this work, electrospun nanofibers of different metal oxide materials were fabricated and optimized to analyze their performance towards several treatment applications and ultimately understand their functions for future approaches of nanofiber-integrated advanced treatment systems. Solution characteristics, electrospinning system parameters and calcination conditions were all varied and controlled in efforts to manipulate nanofiber properties best suited for their individual applications.

In Chapter 2, TiO_2 nanofibers were successfully synthesized as photocatalysts for organic degradation. Through systematic tuning, TiO_2 nanofibers were fabricated with controlled diameter, crystal phase, grain size and band gap. Through varying polymer content and applied voltage of the electrospinning system, average diameter was controlled from 33 to 209 nm. Through varying temperature and duration of the calcinations process, crystal phase was controlled from pure anatase to pure rutile and grain size was controlled from 19 to 49 nm. Through variation of crystal phase composition, band gap was controlled from 3.02 to 3.21 eV. Additionally, surface area, zeta potential and crystal orientation were characterized. Photoreactivity studies towards the model pollutant phenol were conducted to analyze nanofiber performance based on different property changes. Reactivity showed to increase with decreased nanofiber diameter, impart by the increased surface area-to-volume ratio; also, reactivity was optimal at the mixed phase ratio of 76/24 anatase/rutile, similar composition to commercially-available TiO_2 photocatalyst Aeroxide® P25. The optimal material, having

the smallest average diameter (d = 33 nm) nanofibers and mixed phase composition, outperformed the Aeroxide P25 nanoparticles, indicating that dimension and crystal phase were two prominent factors affecting photoreactive performance.

In Chapter 3, Ag-TiO_2 nanofibers were synthesized to yield enhanced performance due to the introduction of the co-catalyst Ag. The composite materials were fabricated from the optimal TiO_2 protocol, having a diameter of 33 nm and mixed phase of 76/24% anatase/rutile. Average diameter, crystal phase, grain size and band gap were all characterized to identify any changes in nanofiber properties due to the co-catalyst, which was added from 0.25 to 10 at.%. Average diameter increased very slightly with increased Ag content until reaching over 2 at.%, where nanofiber size increased substantially with Ag content. The introduction of Ag caused the composite nanofibers to come out nearly all anatase phase, which indicated inhibition of anatse-to-rutile transformation during calcinations. Grain size was not altered by the Ag co-catalyst, having a constant value of 32 nm. Band gap was readily reduced with increased Ag content to as low as 2.79 eV for the 10 at.% nanofibers. Ag-TiO_2 nanofibers were also recalcined to induce rutile phase in efforts to replicate the optimal crystal phase compositon. The band gap of these materials showed a decrease in band gap due to the increased rutile content, similar to findings seen in the unmodified TiO_2 nanofibers. Photoreactivity studies based on Ag content showed optimal performance at 0.5 at.% Ag, outperforming the unmodified nanofibers by nearly a factor of 3. This indicated an optimal Ag nanoparticle size correlating with enhanced performance. Additionally, a decrease in reactivity was observed with increased presence of rutile, indicating

maximum performance from only anatase phase while rutile maintained its inactivity. Altogether, enhanced reactivity was associated with increased electron traps due to the Ag co-catalyst, as these traps inhibit carrier recombination and facilitate carrier separation for augments surface reactions. While the interfacial connection of rutile and anatase provide activation for this mechanism in unmodified TiO_2, the connection between anatase and the Ag nanoparticles provide it for the composite material.

In Chapter 4, $BiVO_4$ nanofibers were successfully synthesized as visible light-activated photocatalysts. Through systematic tuning, $BiVO_4$ nanofibers were fabricated with controlled diameter, crystal phase, grain size and band gap. Through design of experiment that factored in solution chemistry (*i.e.*, viscosity, conductivity, surface tension) and electrospinning parameters (*i.e.*, applied voltage, feedrate), average diameter was controlled from 33 to 71 nm. Crystal phase was monoclinic $BiVO_4$ and stable throughout nanofiber diameter, along with grain size (24 nm) and band gap (2.39 eV). Photoreactivity studies towards phenol showed increased performance with decreased average diameter, indicating a strong surface area-to-volume ratio effect. $BiVO_4$ nanofibers with embedded co-catalysts (e.g., Ag, Au) were synthesized to enhance photocatalytic performance. While having stable morphological properties, the co-catalyzed nanofibers enhanced photo-induced characteristics as seen from diffuse reflectance analysis. Based on photocatalytic studies towards phenol, both Ag- and Au-$BiVO_4$ nanofibers yielded enhanced performance compared to unmodified $BiVO_4$. Under visible light irradiation, the co-catalyzed nanofibers outperformed synthesized TiO_2 nanofibers and commercially-available TiO_2 nanoparticles, with 2 at.% Au-$BiVO_4$ having

the greatest performance. The mechanisms attributed to the enhanced photocatalytic reactivity were increased carrier traps for the Ag-$BiVO_4$ nanofibers and surface plasmon resonance for the Au-$BiVO_4$ nanofibers.

In Chapter 5, Fe_2O_3 nanofibers were successfully synthesized for adsorption of heavy metals. Through varying polymer content, applied voltage and feedrate of the electrospinning system, average diameter was controlled from 23 to 63 nm. Crystal phase analysis revealed all the nanofibers to be hematite and grain size was stable at 34 nm. Specific surface area increased substantially with decreasing diameter due to the increased surface area-to-volume ratio. For example, the smallest sized (d = 23 nm) nanofibers yielded a surface area of 59.2 m^2/g. Additionally, zeta potential and bang gap characterization were also conducted. Adsorption isotherm studies of chromate showed increased adsorption capacity with decreased diameter. These findings are solely associated with increased specific surface area, as the isotherm results normalized by surface area showed negligible variation. The 23 nm sized nanofibers, with an adsorption capacity of 90.9 mg/g, outperformed commercially-available Fe_2O_3 nanopowder (49.3 mg/g) by a factor of ~2.

Finally, In Chapter 6, Al_2O_3-$Fe2O_3$ composite nanofibers were successfully synthesized and examined in order to enhance adsorption performance. Although most characteristics, such as diameter, grain size, band gap and zeta potential, were not altered, specific surface area dramatically increased with increased Al content, where the highest Al/Fe ratio of 32 at.% yielded a specific surface area of 92.8 m^2/g. As expected, adsorption performance was enhanced due to the introduction of Al, where the 32 at.%

Al/Fe composite sample (163.7 mg/g) outperformed the unmodified Fe_2O_3 nanofibers by nearly 2-fold and the commercial nanopowder by over 3-fold. Again, surface area was identified as the only factor that augmented adsorption performance of the composite nanofibers, as other properties stayed stable despite the introduction of Al. Based on BET analysis and adsorption studies, the introduction of Al in the composite nanofibers promoted synergy in surface area, which enhanced adsorption capabilities. The Al_2O_3 improved the surface area of the composite nanofibers in part by its own high surface area, yet resulted in higher surface area than anticipated, possibly due to increased increased surface roughness, which altogether resulted in a greater amount of adsorption sites. The adsorption performance of the composite nanofibers was far greater than the sum of its parts, indicating a synergy of adsorption between Al_2O_3 and Fe_2O_3. Considering that the adsorption energy was unchanged via isotherm results, the enhanced adsorption of the composite nanofibers was attributed to an increase in adsorption sites and an adsorption synergy between the two metal oxide components.